Title
Optimizing Transport Phenomena in Electrolytic Cells

Author
Fornaciari, Julie Christine

Publication Date
2022

Peer reviewed|Thesis/dissertation

Optimizing Transport Phenomena in Electrolytic Cells

By

Julie Christine Fornaciari

A dissertation submitted in partial satisfaction of the

requirements for the degree of

Doctor of Philosophy

in

Chemical Engineering

in the

Graduate Division

of the

University of California, Berkeley

Committee in charge:

Dr. Adam Z. Weber, Co-Chair
Professor Alexis T. Bell, Co-Chair
Professor Bryan McCloskey
Professor Philip Marcus

Summer 2022

Abstract

Optimizing Transport Phenomena in Electrolytic Cells

by

Julie Christine Fornaciari

Doctor of Philosophy in Chemical Engineering

University of California, Berkeley

Dr. Adam Z. Weber, Co-Chair
Professor Alexis T. Bell, Co-Chair

Electrolytic devices are energy-conversion technologies that can assist in decarbonizing essential industries that are hard to decarbonize. These systems use electricity to drive chemical transformations and generate valuable products, such as hydrogen gas. One promising device is a water electrolyzer that splits water into hydrogen and oxygen gases. These systems use membrane-electrode assemblies (MEAs) that are comprised of an ion-conducting membrane as the solid electrolyte and catalyst layers (CLs) where the electrochemical reaction proceeds. Each of these MEA layers has its own set of design parameters and can influence the device's performance. Specifically, the catalytic activity of the anode or oxygen-generating electrode of the MEA depends not only on the electrocatalyst, but also the reactant and product mass transport to/from the reaction sites. While one could increase performance via increasing catalyst loading, this is not cost-effective since in acid systems costly iridium oxide is the most common catalyst. Thus, to increase performance, we examine optimizing catalyst utilization via understanding multiphase and multiscale transport in the CL. Studying the multiscale transport helps determine how the reaction conditions in an MEA can dictate the performance of the catalyst and its surrounding microenvironment.

This dissertation focuses on exploring and elucidating the transport phenomena in electrolytic cells to diagnose their inherent issues and develop pathways to ameliorate them. This dissertation starts by investigating liquid-fed systems in the first two chapters and the rest of the chapters explore vapor-phase conditions. Chapter 2 investigates the transport within the anode CL of a proton-exchange-membrane water electrolyzer (PEMWE). The local transport within the anode CL depends strongly on its structure and how the species (i.e. water and oxygen) are transported throughout it. The structure of the CL depends on the catalyst ink from which it is formed. Correlating the ink properties, such as solvent ratio and aggregate size of the catalyst particles and ionomer, to the structure of the CL can help guide others in fabricating new CLs and elucidate how the physical structure changes the transport phenomena in porous electrodes. In Chapter 2, the large aggregates found in the alcohol-rich ink result in a denser CL (porosity = 20%, compared to a baseline porosity = 40%) and hence high mass-transport overpotentials, which govern cell performance. The best performing CL had double the porosity (40%), small aggregates (210 nm), and anisotropic tortuosity, in which the through-plane tortuosity was higher than in-plane. The structure plays a significant role in minimizing overpotentials.

In addition to the PEMWE device, other electrolyzer motifs are being explored to allow for a wider selection of catalysts and different operating strategies. Investigating different conditions, such as pH, can identify the differences in the kinetic mechanism of the oxygen evolution reaction and how species are transported throughout the cell. Chapter 3 uses a microkinetic model and experimental data to explore the kinetics of the oxygen-evolution reaction near the surface of the catalyst for three different pHs: 1, 9, and 13. Chapter 3 introduces liquid electrolytes to achieve the desired conditions and investigates the performance of the system both in a rotating disk electrode (RDE) and in an MEA. From the RDE experiments, the kinetic data can be inputted into the model and can identify how the ion species are influenced by different current densities and pH values, and provide the behavior at the catalyst surface. The local transport results in very different pH conditions at the catalyst surface compared to the bulk, which greatly impacts the reactivity at near-neutral pHs. MEA performance links these kinetic findings to relevant systems at high operating current densities (> 100 mA cm^{-2}) and reveals even more challenges for these systems when investigating ion transport, particularly large concentration gradients must be overcome.

Since the MEA systems are complex, balancing multiple species and phases, we can focus on a simpler system, where a single-phase water electrolysis can be examined. Chapter 4 explores vapor-fed PEMWEs through coupled experiments and mathematical modeling. While the literature showed low activity for water-vapor PEMWEs, Chapter 4 shows the best performing vapor-fed system to date within the literature, achieving >100 mA cm^{-2} performance at < 1.7 V. However, this system exhibited major limitations due to membrane dehydration. Thus, the decreased membrane water content at higher current densities is exacerbated by lower local relative humidity, resulting in poor CL utilization. Water is not only essential for the oxygen-evolution reaction, but also for ensuring good ion conductivity in the polymer electrolyte.

Finally, the last two chapters of this dissertation connect the findings of Chapter 4 to specific applications. Chapter 5 explores water-vapor-fed PEM unitized regenerative fuel cells (PEMURFCs). Vapor-phase operation simplifies the physics of the system, as shown in Chapter 4, and Chapter 5 explores the impact of different PEMs, feed gases, and relative humidity on URFC performance and durability. By tailoring operating conditions and membrane chemistry, the vapor-URFC achieves a roundtrip efficiency of 42% and a lifetime of 50,000 accelerated-stress-test cycles for fully humidified feeds. Chapter 6 builds on the simple vapor-fed PEMWE in Chapter 4 and introduces another reaction: methane partial oxidation. Using an electrolytic device for electrochemical synthesis directly can revolutionize and decarbonize the way chemical products are synthesized. However, there are significant challenges to overcome, including an electrocatalyst with high conversion and selectivity, high efficiency, and sufficient transport of the multiple reactants and products. This chapter explores the literature, the current status of the field, and recommendations for designing these systems for methane partial oxidation. Unfortunately, using the vapor-fed MEA and the promising catalysts, no methanol was found in the system and more work needs to be done within the electrocatalysis space.

In summary, electrolytic devices can be engineered better by modulating the transport of the reactants, products, and ion species to and from the reaction site. This dissertation uses experiments and simulations to explore species transport within various electrolytic devices at different length scales. The results provide guidelines and identify open questions to improve these devices and determine how to start using them for other electrochemical-conversion systems.

To my parents – for supporting me in all of my crazy adventures and being my best cheerleaders. Thank you for all of your support.

Contents

List of Figures v

List of Tables x

Acknowledgements xi

1. Introduction 1

    1.1 Motivation for Energy Conversion Devices 1
    1.2 Summary of Electrochemical Hydrogen Production Devices 2
    1.3 Literature on Membrane Electrode Assemblies 5
    1.4 Scope of Dissertation 6

2. Linking Catalyst-Layer Structure – From Inks to Performance for Water-Electrolysis 8

    2.1 Abstract 8
    2.2 Introduction 9
    2.3 Methods 11
        2.3.1 Catalyst-Ink Preparation and Characterization 11
        2.3.2 Catalyst-Coated-Membrane Fabrication 12
        2.3.3 Cell Assembly and Testing 13
        2.3.4 Applied-Voltage Breakdown 13
        2.3.5 Catalyst-Layer Characterization 14
    2.4 Results & Discussion 15
        2.4.1 Catalyst-Ink Behavior 15
        2.4.2 Catalyst-Layer Performance 16
        2.4.3 Linking Structure to Performance 19
    2.5 Conclusions 23
    2.6 Supplemental Information 24

3. The Impact of Species Transport in Near-Neutral and Hydroxide Exchange Water Electrolysis[†] 25

    3.1 Abstract 25
    3.2 Introduction 26
    Theoretical 29
        3.2.1 Microkinetics 29
        3.2.2 Transport Model 31

3.3 Experimental 32
3.3.1 Cell Materials and Electrolyte Solutions 32
3.3.2 Cell Preparation 33
3.3.3 Cell Testing 33
3.4 Results and Discussion 34
3.4.1 OER at various pHs 34
3.4.2 Microkinetic Analysis of the OER 37
3.4.3 Full-Cell Operation at Near-Neutral to Alkaline Conditions 39
3.5 Summary 44
Supplemental Information 45
4. The Role of Water in Vapor-fed Proton-Exchange-Membrane Electrolysis† 50
4.1 Abstract 50
4.2 Introduction 51
4.3 Experimental 52
4.3.1 Membrane-Electrode-Assembly Fabrication 52
4.3.2 Test Protocol 53
4.4 Mathematical Model 54
4.5 Theory: Role of Water 55
4.6 Results and Discussion 57
4.6.1 Vapor-Fed Electrolyzer Performance 57
4.6.2 Effects of difference in the RH of the anode and cathode feeds 61
4.7 Summary 66
4.8 Supplemental Information 67
4.8.1 Model Development 67
4.8.2 Characteristic Properties within Each Domain 71
4.8.3 Applied-Voltage Breakdowns 74
5. Performance and Durability of Proton-Exchange Membrane Vapor-Fed Unitized Regenerative Fuel Cells† 76
5.1 Abstract 76
5.2 Introduction 77
5.3 Methods 79
5.3.1 Catalyst-Coated-Membrane Fabrication 79
5.3.2 Cell Assembly 80

5.3.3 Cell Testing 81
5.4 Results and Discussion 82
5.4.1 Liquid-Water vs. Water-Vapor Performance 82
5.4.2 Membrane comparison (1100 vs. 980 vs. 870) 83
5.4.3 Relative-Humidity Experiments 84
5.4.4 Durability 86
5.4.5 Impact of oxygen carrier gas 87
5.5 Summary 88
5.6 Supplemental Information 89
5.6.1 Round-Trip-Efficiency (RTE) Calculation 89
5.6.2 Relative-Humidity Calculation 90
6. Electrochemical Oxidation of Methane to Methanol in Membrane Electrode Assemblies† 92
6.1 Abstract 92
6.2 Introduction 93
6.3 Evaluation of Cell Performance 97
6.4 Literature on Electrochemical Methane-to-Methanol Conversion Devices. 101
6.5 Current Status and Recommendations on Electrocatalysts 104
6.6 Experimental Efforts in a PEM MEA 107
6.6.1 Catalyst Screening and Membrane-Electrode-Assembly Testing 107
6.6.2 Methanol Crossover through the Membrane 110
6.7 Summary and Conclusions 112
7. Summary & Outlook 113
7.1 Future Directions 114
8. Nomenclature 117
9. References 121

List of Figures

Figure 1.1: A schematic showing Hydrogen at scale (H2@Scale) showing the various sectors hydrogen is used in. Figure modified from Pivovar *et al* 2018 Electrochem. Soc. Interface 27 47,[14] 2

Figure 1.2: Schematics of the three main types of low-temperature electrolyzers, liquid alkaline electrolysis, proton exchange membrane electrolysis, and hydroxide exchange membrane electrolysis and the corresponding reactions. 3

Figure 1.3:Membrane electrode assembly of a PEMWE, with each corresponding part blown up and zoomed in to show the components and morphology of the anode catalyst layer, porous transport layer, gas diffusion layer, the membrane chemistry, and the cathode catalyst layer. 4

Figure 2.1: Schematic showing the catalyst ink to catalyst layer and the unknown relationship on performance and structure..... 10

Figure 2.2: Average aggregate size of iridium oxide particles in catalyst inks measured by DLS for different solvent ratios (percent volume). All of the inks were held at a constant weight-percent-solids of 0.16%. 15

Figure 2.3: (a) polarization curves of the three different MEAs tested and the applied voltage breakdown of each. The (b) kinetic, (c) ohmic, and (d) mass transport overpotentials are compared for the three MEAs. For all three of these tests, a Nafion 117 membrane was used and the catalyst loading for the iridium oxide side was 0.35 ± 0.0023 mg cm^{-2} and the platinum loading was 0.1 ± 0.023 mg cm^{-2}..... 17

Figure 2.4: Characterization of the different anode Cls (aCL), 2:1:1 (a,d,g), 1:1 (b,e,h), and 3:1 (c,f,i). (a-c) FIB-SEM images of the cross section of each CL; (d-f) FIB-SEM reconstructions of the slide of the images shown in (a-c); (g-i) pore-size distribution of each of the CLs calculated using the reconstruction. 19

Figure 2.5: Through-plane porosity for the three CLs determined from FIB-SEM images. 20

Figure 2.6: The relationship between mass transport overpotential and porosity/tortuosity for the three different CLs; the through-plane tortuosity is used here. 21

Figure S2.1: Histograms for the five repetitions for the four different inks (n-propanol: water: ethanol) (a) 2:1:1, (b) 1:1:0, (c) 3:1:1, and (d) 0:1:3. The peaks of the histograms do not change over the course of the measurements (from the first set of data to the fifth) showing stability in the ink..... 24

Figure S2.2: FIB-SEM of CCMs revealing catalyst layer cross section. Image on the left shows the milled trench and image on the right shows the magnified cross section. 24

Figure 3.1: A schematic showing the catalyst and the active species for the various pH conditions (counterions are ignored). The surface state of the catalyst is determined by DFT and then is fed into the microkinetics, qualitatively depicted here. The preexponential factor and activation energy was calculated based on theory and experimental data.[114] 28

Figure 3.2: Conductivities of SELs used for KOH and K_2CO_3 in addition to others used in Kiessling *et al*.[35] 33

Figure 3.3: Linear-sweep voltammograms shown for (a) acidic pH (1 thru 5), (b) neutral to near neutral pH (6 thru 10), and (c) alkaline pH (11 thru 13). The most acidic and alkaline pH's, 1 and 13, respectively, and pH 9 are shown in comparison (d) and are investigated as representative cases in the modeling sections throughout this chapter..... 35

Figure 3.4: Oxygen-evolution overpotential as a function of bulk pH, for iridium oxide nanoparticles from experiments (circles) and simulations (squares). The potentials were reported at current densities of (a) 2 mA cm^{-2} and (b) 12 mA cm^{-2}. The current densities were reported at corresponding voltages of (c) 1.5 V and (d) 1.65 V. The pH's used in the simulation are pH 0, 2, 9, and 13. The red star indicates the pH at the surface of the electrode, 2.34, determined by the transport model with a bulk pH of 9..... 36

Figure 3.5 (a) the local pH as a function of current density for pH 0, 9 and 13. (b) The local proton concentration as a function of distance from the electrode at pH 9..... 37

Figure 3.6: The percent change in current density relative to that of the perturbation (0.1% change of the forward rate coefficient) on each of the eight forward rate coefficients at different applied potentials, 1.5 to 2 V, for a) pH 0, b) pH 9, and c) pH 13. 100% change represents that the overall current density (rate) changed by the same amount as that of the 0.1% perturbation. d) Surface coverage from 1.3 to 2.0 V vs RHE for all pHs..... 38

Figure 3.7: HEMWE sketch; Abbreviations: PTL – porous transport layer, CL – catalyst layer, HEM – hydroxide exchange membrane, anolyte – anodic supporting electrolyte. OER is performed in the anode CL and HER in the cathode CL..... 39

Figure 3.8: Polarization curves showing kinetic (inset, Tafel plot) and ohmic regions for DIW and KOH anolyte feeds. Current density range of DIW was limited so as to try and suppress HEM degradation..... 40

Figure 3.9: (a) Polarization curve showing the kinetic (inset, Tafel plot) and ohmic regions and (b) HFR resistances; for carbonate and hydroxide solutions. Numbers in brackets indicate the order in which the experiments were conducted consecutively, * denotes similar conductivities and § denotes similar pH at 60°C..... 41

Figure 3.10: Qualitative concentration profiles of carbonates and hydroxides within the HEM anode catalyst layer..... 43

Figure S3.1: a) Model geometry for the transport equations b) Surface species concentration for the total flux of protons at the disk. 45

Figure S3.2: The impact of current density and boundary-layer thickness on local pH at (a) pH change for 500μm boundary layer thickness for pH 0 and pH 13 and (b) pH 9 for varying boundary-layer thicknesses..... 46

Figure S3.3: 3D plots for each individual rate of reaction ($r_1 - r_8$)..... 47

Figure S3.4: Extent of reaction for pH 0, 9, and 13..... 48

Figure S3.5: Tafel slopes for (a) pH = 0 (b) pH =9 (c) pH = 13. Dashed lines are experimental values, solid lines are the microkinetic model. The change in slope for the experimental data and large mismatch at lower current densities is due to capacitance effects that are not considered in the microkinetics. 48

Figure S3.6: Cyclic voltammograms for iridium oxide at (a) pH 1-5, (b) pH 6-10, and (c) pH 11-13..... 49

Figure S3.7: HFR and polarization curves for DIW and KOH anolytes at 60 ^{o}C. 1.0 M KOH was flown first, followed by DIW, then KOH again. 49

Figure 4.1: Cell schematic of the vapor electrolyzer MEA 51

Figure 4.2: a) The nondimensionalized limiting current density as a function of β, the net water flux in the membrane normalized by the proton flux b) The current density for β=0 as a function of temperature assuming 98% RH in the anode gas channel. 56

Figure 4.3: Electrolysis at (a) 30°C, blue, (b) 80°C, red, and (c) the iR corrected curves for 80°C for both liquid-fed (circles) and vapor-fed (squares) cells. Operating conditions: Nafion 117 membrane; 1 mg cm^{-2} iridium loading on anode, and 0.3 mg cm^{-2} Pt from Pt/C on cathode, and vapor feed at 98% RH on both sides flowing at 200 mL min^{-1}. 57

Figure 4.4: a) Model fit of the vapor-fed MEA operating at 98% RH system at 80°C with the HFR data corresponding to the experiments (circles, right axis) and b) AVB for this system c) RH (green) and water content (purple), defined as moles of water per mole sulfonic acid site, throughout the cell at 150 mA cm^{-2} (dashed) and 680 mA cm^{-2} (solid)..... 58

Figure 4.5: Temperature distribution within the membrane electrode assembly at two different current densities. 59

Figure 4.6: (a) Difference in cell potential when the carrier gas is changed from helium (2 g/mol) to argon (MW = 40 g/mol), so a negative change is potential is a lower overpotential. The square points show experimental measurements and the solid line shows the predictions of the model (left axis). The difference in membrane water content, λ, is shown on the right axis for Nafion 117, where the increasing trend shows a higher λ in helium with increasing current density. (b) Electrolyzer performance for Nafion 117 (183 μm) vs. Nafion 211 (25 μm). Experiments were carried out at 80 °C with an iridium loading 1 mg cm^{-2} on the anode and a Pt from Pt/C loading of 0.3 mg cm^{-2} on the cathode. The anode and cathode feed flow rate were 200 mL min^{-1} and the RH was 98% for both feeds..... 60

Figure 4.7: Polarization curves at various RH for vapor electrolysis from 98% RH (dark blue), 50% RH (blue), and 30% RH (light blue). Points are experimental data; solid lines are from the model. Vapor electrolyzer experiments and model were ran and simulated at 80 °C, with Nafion 117 membrane; the anode had 1 mg cm^{-2} iridium loading, the cathode had 0.3 mg Pt cm^{-2} using Pt/C loading. 61

Figure 4.8: Vapor electrolysis tested at two different conditions. Wet and cold test of 98% RH at 30°C (blue) and hot and dry test of 30% RH at 80°C..... 62

Figure 4.9: a) AVBs at a constant current density of 150 mA cm^{-2} shown as a function of humidity. b) Percent contribution to the total cell voltage, simulated at 80°C. 63

Figure 4.10:a) Reaction distributions, b) water content and c) overpotential for varying RH conditions within the nondimensionalized anode catalyst layer at 150 mA cm^{-2}..... 64

Figure 4.11: a) Polarization curves for asymmetric study (triangles and circles) and the average cell RH humidity symmetric study (squares) for comparison. The cathode (circles) and anode (triangles) had the inlet RH of 30% while the other electrode was kept at 98% b)

Values of β as a function of current density for each of the three cases calculated using the model of a vapor-fed electrolyzer. 65

Figure 5.1: (a) Vapor-URFC schematic for constant-gas mode. (b) a cross section of the MEA used in the vapor-URFC. The water shown entering in the oxygen electrode is vapor phase and a hydrogen inlet is not needed for HER but could be fed in. 78

Figure 5.2: Vapor WE performance is compromised relative to the liquid WE due to greater ohmic losses. The left axis corresponds to WE performance, and the right axis shows the WE HFR. 82

Figure 5.3. (a) Polarization curves during both FC (solid) and WE (dashed) operation for MEAs using the three membranes tested (Solvay is the same as Aquivion). (b) RTE for MEAs using the three membranes tested. (c) HFR during WE operation for the MEAs using the three membranes. 84

Figure 5.4: a) Nafion™ 1100 WE performance between 81 to 122% RH, with a significant decrease at 52% RH. b) RTE for the different RH feeds. 85

Figure 5.5: AST cycles and performance compared to beginning of life (BOT) for the vapor-URFC at (a) 100% RH and (b) 75% RH. 86

Figure 5.6: The electrolyzer polarization curve and RTEs for vapor-URFC with a) nitrogen and air at the oxygen electrode and b) carbon dioxide and nitrogen. The FC performance remains the same for these tests. 87

Figure S5.1: Voltage-loss breakdown in FC operation for the beginning of test (BOT, squares), middle of test (MOT, triangles) and end of test (EOT, circles). The polarization curves are shown in a. The overpotentials are shown for (b) kinetics, (c) ohmic, and (d) mass transport. 90

Figure S5.2: Applied-voltage breakdown in WE operation for the beginning of test (BOT, squares), middle of test (MOT, triangles) and end of test (EOT, circles). The polarization curves are shown in (a). The overpotentials are shown for (b) kinetics, (c) ohmic, and (d) mass transport. 91

Figure 6.1: a) Half-cell set ups for three-electrode and gas diffusion electrode aqueous test cells. b) The testing MEA cell and in the insets, the vapor membrane electrode assembly and the exchange membrane electrode assembly. The desired and potential reactions are shown below for the PEM and HEM cases. 95

Figure 6.2: a) Gas and ion flows through the PEM MEA during electrolytic operation. b) Fluxes of each individual reactant and product and additional transport mechanisms. 98

Figure 6.3: Distribution of overpotentials within the MEA vs. current density for an electrolytic cell. The three main components are ohmic losses, mass transport losses, and kinetic losses. Thermodynamic potential is the minimum free energy required to drive the reaction. (Adapted from Ref.[145]). 99

Figure 6.4: Free energies of various metal oxides for the third step in the water oxidation process and methane activation step. The steps for oxygen evolution and methane activation are shown below. Data from Ref. [213]. 105

Figure 6.5: Testing Parameters: Flow rate: 200 ccm both sides, electrochemical test sweeping the voltage from 1.5 V – 2.0 V, at 2 min holds. Electrode Properties: Anode: Iridium Oxide (1 mg cm^{-2}), CH_4 or Ar with water vapor, Ti GDL. Cathode: Pt (0.3 mg cm^{-2}), 2% H_2 in Ar with water vapor, carbon GDL. Membrane: boiled Nafion, 183 mm dry. 108

Figure 6.6: Polarization curves for the various catalysts up to (a) 1200 mA cm^{-2} and (b) a magnified portion of a, only going up to 18 mA cm^{-2} from 0 to 2 V. Each of these membrane electrode assemblies were coated with the catalyst with a target loading of 1 mg cm^{-2} on a boiled Nafion 117 membrane. Pt/C at 0.3 mg cm^{-2} was the cathode..... 110

Figure 6.7: Schematic of the flux of methanol (N_{MeOH}) and water (N_{H2O}) when fed into the anode compartment. Argon was the carrier gas; 4% methanol vapor was fed in and the stream was saturated with water vapor at 100% RH at 80 °C. 111

List of Tables

Table 2.1: Catalyst-ink recipes and their constituent components. 11

Table 2.2: The loadings of each anode catalyst layer for the different ink formulations. 12

Table 2.3: The three different MEAs, 2:1:1, 1:1:0, and 3:1:0 and their structural properties from the FIB-SEM reconstruction and analysis. *Pore size distributions are shown in detail in Figure 2.4g-i. 20

Table 3.1: The mechanism step and the net reaction rate for all eight steps. Acidic steps shown by reactions 1 thru 4 (eqns. 3.7 thru 3.10) and alkaline steps shown by reactions 5 thru 8 (eqns. 3.11 thru 3.14). 30

Table 3.2: Transport Governing Equations 31

Table 3.3: Boundary Conditions for the RDE Model 32

Table 4.1:Catalyst Ink Recipes for the cathode and the anode inks. 53

Table S4.1: Governing equations for the electrolyzer model. 67

Table S4.2: Source Terms for heat balance equations. 68

Table S4.3: Source terms for conservation of chemical species. 69

Table S4.4: Boundary conditions for each variable. 70

Table S4.5: Characteristic properties of the subdomains. 71

Table S4.6: Binary diffusion coefficients for gas species (Pa cm^2 s^{-1}). Coefficients are taken from correlations in, Bird, Stewart, and Lightfoot, chapter 17. 72

Table S4.7: Thermodynamic and transport properties for the components of the gas. 73

Table S4.8: Relevant properties for the kinetic parameters for oxygen and hydrogen evolution. 73

Table S4.9: Ionomer and membrane properties relevant for ion and water transport. 74

Table S4.10: Applied voltage breakdown equations. 75

Table 5.1: The catalyst recipe for the hydrogen electrode and oxygen electrode. 80

Table 5.2: The equivalent weight, cell RTE (%), and HFR [Ω cm^2] for all three membranes at 1 A cm^{-2} 83

Table 6.1: Low Temperature Electrochemical Methane Oxidation, experimental findings. Energy efficiency and voltage efficiency was not reported for any of the following experimental results. 103

Table 6.2: The electrocatalysts tested for methane partial oxidation at > 1.5V 109

Acknowledgements

Many people helped me finish this dissertation. Some have no idea how much of an impact they had on me, others saw me day in and day out, through the tears, the late-night runs to check on my experiment so I wouldn't blow up the lab, etc. To all those who have touched my journey, thank you so much for the help, advice, support, and cheerleading I needed to get here. So many people say it takes a village to accomplish something this big – so thank you to this village.

I first want to thank my advisers, Alex Bell and Adam Weber. Alex, thank you for challenging me, supporting me, and assisting me in my research endeavors. Adam, thank you for seven long years of support, laughs, eye rolls, and advice. I appreciate you listening to all my feedback and complaints, gaining insight on science I have yet to consider, and being a champion and cheerleader throughout it all. I appreciate your constant reminders that science is hard, and failure is normal, and even if the science fails, I am not a failure. With that, thank you so much for all your support over the years.

Additionally, I need to thank my unofficial adviser, mentor, and friend, Nem Danilovic. Thank you for teaching me everything I know about electrolysis, and then some; thank you for being a role model on how to be a mentor, and thank you for sharing your own experience. From your example, I have been able to learn how to manage up, manage better, and take ownership of the work I have done. Also, thank you so much for giving me the dog time I always need, I will miss my walks with Haven (or lack thereof).

I want to thank my past mentors, Yvette Moore, David Sanchez, Daniel Armenios, Meagan Mauter, Sneha Shanbhag, Julie Albert, and Jan Genzer. You all gave me the foundation to believe in myself, remember my worth was not in my work, and be my cheerleaders through this all. While time and distance have prevented reunions, I appreciate the emails, the updates, and the support.

To the Energy Conversion Group, thank you for being such amazing lab mates. I am so lucky I got to spend the last five years (and then some) with such inspiring people. Each and every one of you who has passed through the ECG group made this Ph.D. enjoyable and worthwhile – while I didn't list everyone here, I truly am grateful for every iteration of this group during my time here. Specific thanks include: Pete Dudenas, Ahmet Kusoglu, Andy Crothers, Meron Tesfaye, Kelsey Hatzell, and Iryna Zenyuk, I met you all as a SULI and am so grateful to have gotten some more time with you during my Ph.D. Thank you for all the help, guidance, and confidence. Philomena Weng, you have been such a source of patience, light, and guidance. Thank you for answering my questions, hearing me vent, and just being an amazing person (and all the cat time). Xiong Peng, Zac Taie, Yagya Regmi, and Mike Gerhardt, thank you so much for being amazing friends, role models, and colleagues. Yagya and Mike – if it were not for you two, I would have never finished my first paper or understood the Office Space reference without you – I'm excited to cross paths in Europe soon. To the friends I made first over zoom, Arthur Dizon, Andrew Tricker, Jason Lee, and Hailey Boyer – I am glad it has moved past zoom and I am so glad to have you all as dear friends. And to the people who have been with me through it all: Claire Arthurs, Grace Lau, Oyin Romiluyi, Doug Kushner, words cannot describe how much fun I have had with you all and how much you helped me get to this point. Doug – you taught me everything I know I know about test stands and Swageloks, and while I wish I only had to build a lab once in my Ph.D., I am glad you were there to commiserate with both times. And last but certainly not least are Johnny Petrovick,

Sarah Berlinger, and Anamika Chowdhury – my confidants, my pep squad, and my lifelong friends – I couldn't have imagined my Ph.D. without you. From delicious baked goods, to arguing about whether they should be eaten in mugs, and the countless reminders to relax, I am so grateful to have you all as my friends.

I want to thank my amazing undergraduates, Ashley Werre, Maria Rochow, Samay Garg, and Elizabeth Greenberg. You all made this experience exciting, fun, and meaningful. You all taught me more than I ever could teach you and then some – I cannot wait to see the amazing things you all accomplish.

I want to thank the organizations that I was a part of during my time at Berkeley: Community Resources for Science, Berkeley Science Review, Science at Cal, ComSciCon, Expanding Your Horizons, Skype a Scientist, Joint Undertaking for an African Materials Institute, Women Supporting Women in Science, and Chemical Engineering Graduate Advisory Committee. Thank you for the community, the space to learn how to communicate my science better, and to find ways to make an impact locally and globally.

I would not have been able to survive this experience if it were not for the local friends who helped me forget my failing experiments, helped me finish problem sets, hiked with me (begrudgingly), drank margaritas with me (less begrudgingly), and gave me hugs on the bad days. I have to thank the San Pablo House – David Brown, Sarah Yang, Kara Fong, Nat Goh, and Wyatt Ochs– living with you for three years and quarantining together was a blast and I am grateful to have shared this time with you. Let's find time to watch West World season 4 from our new adventures together. Lorena Grundy, Elyse Kedzie, Jade Fostvedt – I am so grateful for your friendship and the memories we share and I am glad Berkeley brought us together. To those in the department, past and present, particularly, Angelo Bonzanini, Bridgette Lafaye, Jeremy Adams, Ana Carneiro, Julie Rorrer, Kyle Diederichsen, Natalie Lefton, Branden Leonhardt, Paul Kim, Helen Bergstrom, and many others – thank you for the advice, the fun times, and the interesting conversations. And to the friends not in my Ph.D. program – Jen Braschakyo, Natalie Dall, Kayee So, Josh Su, and Shavonne Stanek – you all have been a source of inspiration, balance, and fun. Thank you for putting up with my crazy camping ideas, hikes that are far too long, and the climbing sends.

I also have to thank the friends who were not physically here day in and day out but were a source of support throughout this all: Hannah Dominiak, Peter Larson, Jon Dietz, Alvaro Castelan, Ashley Robbins Irwin, Emily Klonicki-Ference, Chris Ference, Zach Margolies, Macy Yu, Cam Beichner, Paige Lumley Beichner, Caren Dieglio Stokes, Kim Sklener Lynch, Sarah Trossman Jacobs, Melissa Smith, Erin Sarosi, Maya McKeown, Kimmai Tran, and Jennifer Wenker. You all cheered me on, reminded me to be proud of my accomplishments, and loved me regardless of a successful experiment. I am so grateful for your friendship and with friends like these – who doesn't feel loved.

I truly would not be here without my family – Mom, Dad, Nick, Luke, Steph, Mila, (lil) Luke, Uncle Hank, Aunt Wendy, Uncle Slugger, Nana, Papa, Grandma, and the rest of the family (and dogs of the households)– thank you for your support and your love. Your patience and understanding for being so far away has meant the world to me. Thanks for letting me (attempt) to teach you what I do and learning to ask me how lab is instead of school. I want to thank my partner, Ryan. I am lucky to have found you in time to be quarantined together for two years. Your never-

ending support and love have made the last part of my Ph.D. all that much easier and I promise to repay you for all the meals you made me, someday. Thank you for always reminding me to take it easy, take care of myself, enjoy the present moment, and celebrate the small accomplishments.

Additionally, I need to acknowledge the 500+ miles I have hiked in my Ph.D. Nature is a powerful therapy and the sense of awe I felt after every hike always kept things into perspective. The beauty of California helped motivate me to continue my research, gave me much needed breaks and perspective during the last five years, and provided time with great friends and family, even if I somehow always choose the steepest, hilliest hike of them all.

Last but not least, this work would not have been able to be conducted if it weren't for the following funding: Shell's New Energies Research and Technology (NERT) and the Energy & Biosciences Institute through the EBI-Shell Program, HydroGen Energy Materials Network, H2New Consortium and the Department of Energy – Office of Energy Efficiency and Renewable Energy – Hydrogen and Fuel Cell Technologies Office (DOE-EERE-HFTO) for funding under Contract Number DE-AC02-05CH11231. All of these funding sources came with collaborators who I have learned a lot from and am happy to have engaged with over my time at Berkeley. I would like to acknowledge support from the Graduate Research Fellowship program by the National Science Foundation under Grant No. DGE 1752814. Lastly, I would like to acknowledge that Lawrence Berkeley Laboratory operates on Huichin, the unceded lands of the Ohlone people.

1. Introduction

1.1 Motivation for Energy Conversion Devices

A zero or negative carbon future requires a diverse set of renewable and sustainable resources.[1,2] No single technology can solve the climate crisis but a portfolio of technologies to generate, store, and convert green electricity can help.

Technologies such as solar cells or wind turbines can generate electricity without emitting any greenhouse gases.[3–6] These technologies have decreased in price dramatically but are still burdened with two major issues: intermittency and location dependence.[1,2,6] If there is no sun or wind, whether seasonally or daily, the electricity will not be generated. There are other options, such as hydropower and nuclear, but both come with their own obstacles.[2]

Storing electricity is a research area that is vital for a zero or negative carbon future. Typical storage of electricity uses batteries, typically lithium-ion batteries.[7] These devices are abundant in our everyday life, from the phone we use to the computer used to write this dissertation to electric vehicles. However, they can only store electricity for so long, on average 4-6 hours, and become increasingly expensive as they get larger since they cannot separate energy and power.[8] Additionally, the need for lithium and cobalt is another obstacle in sourcing these materials sustainably and ethically. Another option is using chemical energy to convert chemicals to electricity, especially for larger or longer capacities.

Chemical conversion, and specifically electrochemical energy conversion, provides ample benefits, such as modularity and on-demand power.[9] Fuel cells and redox flow batteries are two ways to use electrochemical energy conversion and storage.[10–12] While these devices are not fully commercialized like the gas engine or a lithium-ion battery, their costs are feasible within a few industries and with ongoing research, the cost can continue to decrease. Additionally, they have the advantage to decouple energy and power. An issue with these devices, particularly with fuel cells, is they depend on hydrogen gas for the feedstock.

Hydrogen gas is typically made via steam-methane reforming, where methane is heated to high temperatures and reacts with steam to form hydrogen and carbon dioxide.[13–15] The dependence of such hydrogen gas production on natural gas is huge. While fuel cells are known to be "emission-free" systems, the upstream process of making hydrogen is polluting, releasing greenhouse gases in the process. Steam-methane reforming generates a lot of carbon dioxide, and the natural gas pipelines lead to issues like leaks to the environment and flaring of methane.[13,14] If there is a future in using hydrogen gas as a carbon-free energy storage and conversion medium, different technologies need to be used to make it.

Luckily, hydrogen (H) is the most abundant element in the universe. Unfortunately, hydrogen gas (H_2) needs to be created, bonding two hydrogen atoms together. Hydrogen gas is an essential component in many different industries, as shown in Figure 1.1.[14–21] Decarbonizing hydrogen gas production can make a huge difference in hard-to-decarbonize sectors, such as plastics, fertilizer, and other areas.

Within this dissertation, the electrochemical production of hydrogen gas is explored in electrolytic devices. Experiments and simulations were conducted to explore various transport phenomena within these devices. The transport of water, oxygen, and ions becomes vitally important for the performance and durability of these cells and is explored within this dissertation. Additionally, these electrolytic devices could be used for different technologies, such as the electrochemical conversion of more complex reactions. Applications of these devices for the exploration of novel and impactful decarbonization are explained in this dissertation.

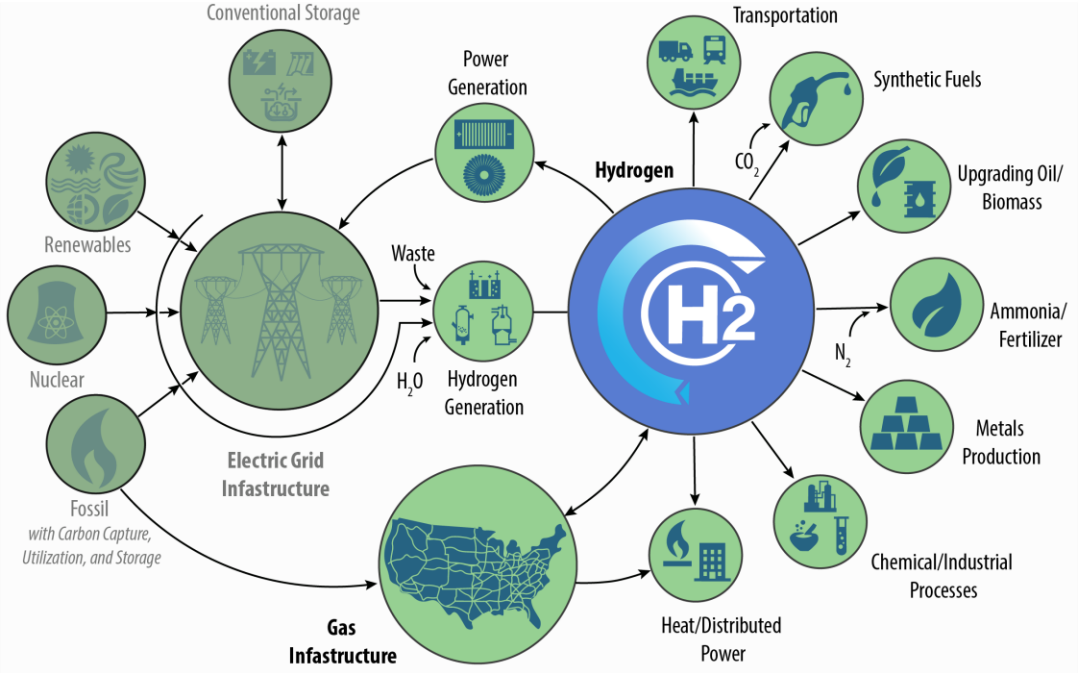

Figure 1.1: A schematic showing Hydrogen at scale (H2@Scale) showing the various sectors hydrogen is used in. Figure modified from Pivovar *et al* 2018 Electrochem. Soc. Interface 27 47,[14]

1.2 Summary of Electrochemical Hydrogen Production Devices

Electrochemical hydrogen production uses electricity and splits water into oxygen gas and hydrogen gas through a water electrolyzer.[13,14,20–24] Creating hydrogen gas in this way is very advantageous since the excess electricity from solar during the summer can be converted to hydrogen gas and then stored for days or months in cylinders, tanks, and even large caverns.[8] Then when there is an electricity demand, hydrogen can be used to make electricity via a fuel cell and combustion in hydrogen turbines.[25,26] As long as the water electrolyzer uses electricity from solar or wind energy, this entire process can be completely emission-free.

This process is advantageous as hydrogen can be used in so many sectors, as shown in Figure 1.1 and removing the dependence on natural gas can help reduce overall emissions. The issue currently is the cost of the system. The cost of hydrogen via electrolysis is $4/kg of hydrogen, unlike steam-

methane reforming which is only ~$1-2/kg.[14,15] There are initiatives started by the Department of Energy that is working towards the goal of producing green hydrogen at $1 per kilogram of hydrogen in one decade (111) via the Hydrogen Shot initiative.[15,23] While this is a lofty goal, there are promising routes providing that there are improvements within the electrochemical hydrogen production field.

There are many ways to convert water to hydrogen gas electrochemically. As shown in Figure 1.2, the three main low-temperature ways are liquid alkaline electrolysis, proton exchange membrane electrolysis, and hydroxide exchange membrane electrolysis.[21,22] These three ways are specifically for low-temperature electrolysis and this dissertation does not take into account the high-temperature methods, although there are many.

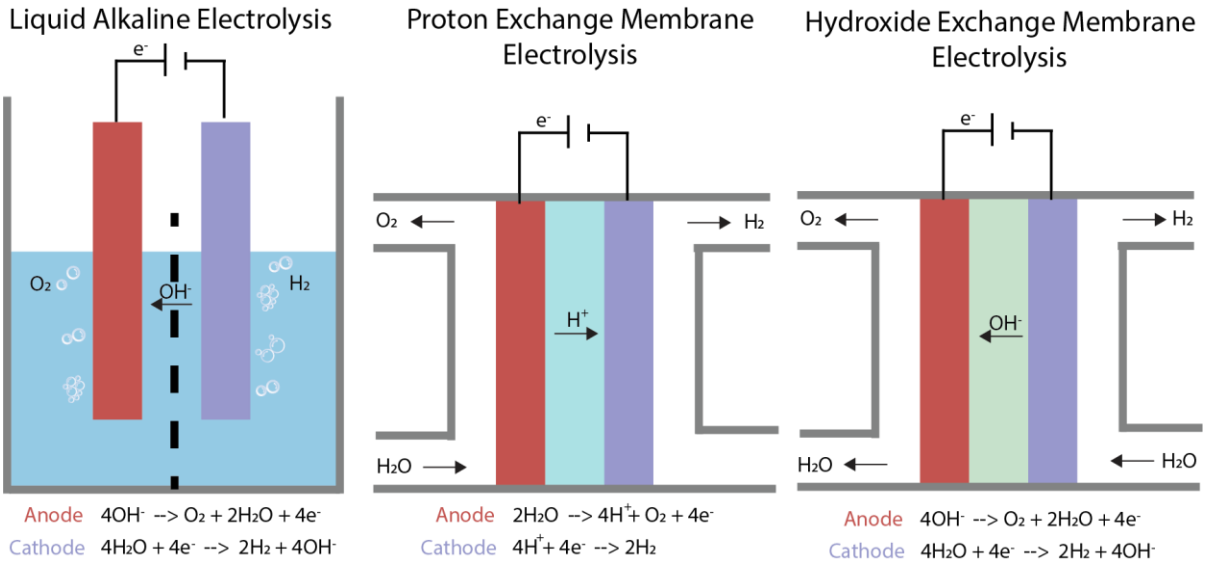

Figure 1.2: Schematics of the three main types of low-temperature electrolyzers, liquid alkaline electrolysis, proton exchange membrane electrolysis, and hydroxide exchange membrane electrolysis and the corresponding reactions.

Liquid-alkaline water electrolysis (LAWE) is the oldest method of producing hydrogen and the most commercialized to date. It uses a liquid electrolyte, potassium hydroxide, and a nickel catalyst to generate hydrogen and oxygen.[21,22,27] It is an established technology that has a long lifespan and uses readily available materials which lower the cost. However, the issues with this system come in separating the hydrogen and oxygen from the liquid electrolyte, being able to operate intermittently and generate pressurized hydrogen, and operating only at low current densities due to thick electrolyte layers, thereby increasing cell size and cost. While it is the oldest way to generate hydrogen electrochemically, there is still a lot of research to be done on this system. However, for the context of this dissertation, the liquid alkaline electrolysis system will not be discussed further.

Proton-exchange-membrane water electrolysis (PEMWE) is a solid-state system that uses a membrane-electrode assembly (MEA) to transport the liquid, gases, and ions, shown in detail in Figure 1.3.[16,20–22,28] This technology is becoming the state of the art as it can efficiently produce

very pure hydrogen at high current densities and higher pressures. Additionally, the system is very compact, utilizing the catalyst in the MEA efficiently. The entire cell, including gas-diffusion layers (GDLs), porous-transport layers (PTLs), a membrane, and two catalyst layers (CLs) is less than 1 mm thick. Stacking multiple cells yields high amounts of ultra-pure hydrogen at high efficiencies.[21] However, the cost of the system, lifetime, and the degradation in performance at high current densities lead to setbacks within the field. Understanding how to reduce the amount of catalyst and the origins of some of the losses within the cell and MEA is key to making these state-of-the-art electrolyzers cost effective. The typical catalysts used for PEMWE are platinum and iridium oxide, to generate hydrogen and oxygen respectively. These catalysts are expensive and are part of the platinum-group metals (PGMs) so they are not abundant.

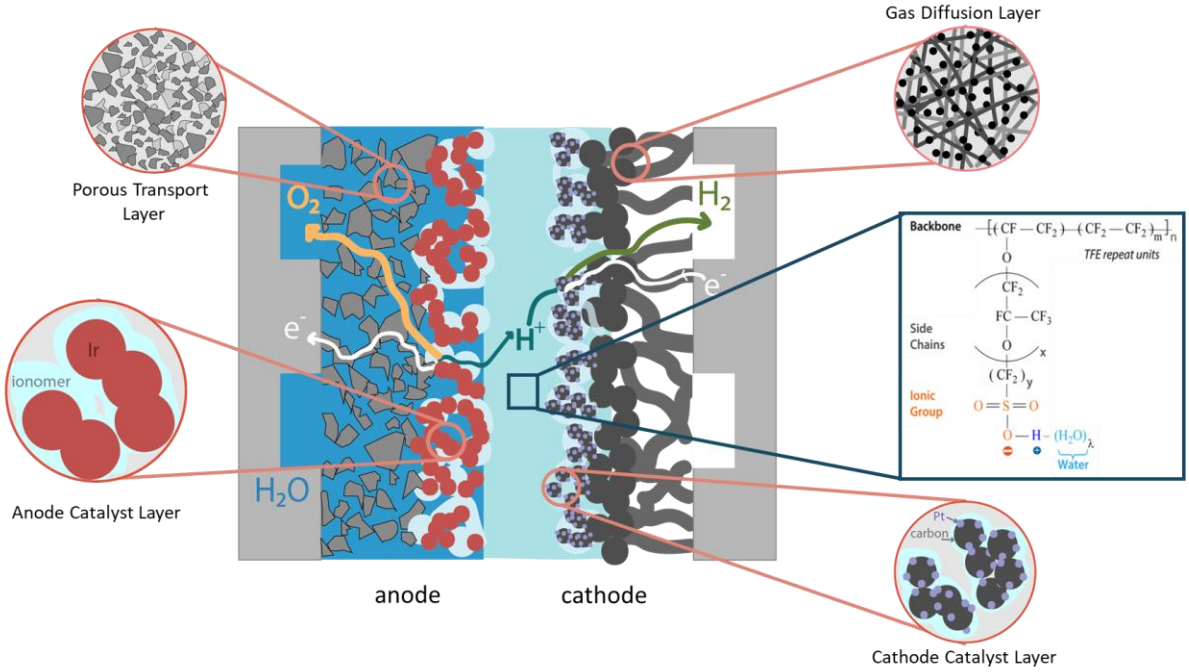

Figure 1.3:Membrane electrode assembly of a PEMWE, with each corresponding part blown up and zoomed in to show the components and morphology of the anode catalyst layer, porous transport layer, gas diffusion layer, the membrane chemistry, and the cathode catalyst layer.

The last low-temperature electrolyzer is hydroxide-exchange-membrane water electrolysis (HEMWE).[21,22,29] While this system is very similar to LAWEs, the biggest change is using a hydroxide exchange membrane (HEM), which makes the design more similar to PEMWEs.[29–34] The compact design reduces the ohmic losses seen within the LAWE system and HEMWEs can use more inexpensive alkaline catalysts compared to PEMWEs. However, the HEMs are in their infancy, as there is not a stable membrane that is used universally within the field; research and development are underway to find new polymer chemistries to conduct hydroxide anions efficiently through the membrane and remain stable for long operation.[29,30] The ideal scenario would be to use deionized water or water vapor instead of a supporting electrolyte for these systems.[35,36] HEMWEs are the newest technologies but there is an abundance of research understanding the pitfalls of these systems.

The above electrolysis systems show there are many ways to make hydrogen gas, but these MEA technologies can be applied for other applications. The knowledge can be transferred these devices and can be translated into different applications. Additionally, manipulating the transport the MEA experiences can help identify the areas hydrogen gas can play the most important role, including disadvantaged, water scarce, and off-grid communities. Identifying the trade-offs for these different applications and their impact within communities can provide an incentive for deploying the systems. The MEA system is being explored for carbon dioxide reduction systems[37] and could be potentially used for promising new chemistries, including nitrogen reduction and hydrocarbon oxidation[38–40]. This dissertation will explore a few applications, including methane to methanol partial oxidation and a unitized regenerative fuel cell for energy storage.

1.3 Literature on Membrane Electrode Assemblies

Low-temperature electrolysis systems have been studied for many decades, with the PEMWEs becoming the dominant technology over the last two decades.[14,15,20] Publications on PEMWEs have increased tremendously from 2000 to 2010, with a continued trend over the past decade.[13] The field is broad, since most of the research has been focused on the components of the MEAs and more recently looking at how to scale the systems better for manufacturing, long lifetimes, and large-scale deployment.[41–43] The main motivation for most of the field is how to reduce the cell voltages seen at high current densities while decreasing the expenses of the individual cell stack and operate more dynamically for intermittent operation. The most expensive parts of the electrolyzer systems are in the stack, accounting for 53% of the total cost.[21] The stack costs are mostly due to the MEA and the precious metal catalysts that are used, and then flow fields and membranes. The majority of this dissertation focuses on the MEA and how different transport phenomena can manipulate cell and eventual stack performance.

There is a plethora of research focused specifically on the MEA, some of the main topics include new electrocatalysts,[44–47] transport layers,[48–50] fundamental catalyst-ink studies,[51,51–54] and fabrication techniques.[41,52,55] PEMWEs are complex and systematic studies of how transport impacts the performance of the system is crucial when scaling up to necessary high-volume production. Scaled-up systems rely heavily on different ink formulations and not much work has been done investigating how the ink properties impact structure and how that structure impacts performance. While there is still a large amount of work to be done in PEMWEs, the issue comes with the PGM catalyst that is used for the oxygen evolution reaction, iridium oxide. Due to the limited supply of iridium oxide around the world, the low-temperature electrolysis field is moving towards more HEMWEs systems. In HEMWEs, there is a lot more to learn about the membrane chemistries, the stability, the ink formulations, and the overall MEA fabrication.[22,29] In contrast, the HEMWE field is still in its infancy, as the membrane stability and operation without a supporting electrolyte are areas that still need to be overcome.[32,34–36] Additionally, the catalysts used need to be better understood during operation and better integrated into the MEA. While larger issues, like stability and reaching comparable performance to the PEMWE, are still required, identifying important transport limitations under the typical operating conditions will help move the field forward rapidly.

While the field has numerous initiatives in producing green hydrogen gas, many studies expanded these MEAs to be used for different reactions.[2,19,37,38,56] Carbon-dioxide reduction is already using the MEA systems to make promising commodity fuels using electrochemistry.[57] However, with

more push from different stakeholders, different reactions are starting to show up within the literature, including hydrocarbon partial oxidation, ammonia synthesis, and other chemical transformations via electrochemistry.[38,40,56,58]

1.4 Scope of Dissertation

The six following chapters in this dissertation highlight transport in electrolytic devices, including fundamental and applied applications for various uses. Each chapter provides a review into the current literature on the respective topic and introduces the experimental and modeling protocols done, and discusses the findings of the study.

Chapter 2 focuses on PEMWE and the transport of reactants and products through the catalyst layer. The catalyst layer, which is a porous electrode comprised of catalyst particles, ionomer, and void space is a key component in the MEA as shown in Figure 1.3. This chapter highlights how catalyst ink properties can influence the structure of that catalyst layer and what properties (e.g., porosity, tortuosity, ionomer distribution) the catalyst layer should have to reduce the overpotentials in the cell.

Chapter 3 continues to look at the transport of these systems, extending to different pHs to better explore other applications like photoelectrochemical and alkaline electrolysis. The acidic systems are more developed and understood, and this chapter focuses on expanding the knowledge of the oxygen-evolution reaction (OER) in better detail for alkaline and near-neutral systems. This chapter uses simulations and experiments to determine the microkinetics at and transport to the catalyst surface. The findings from this chapter are informative for acidic and alkaline electrolyzers and near-neutral photoelectrochemical systems at operating current densities (<100 mA cm^{-2}).

Chapter 4 takes what has been understood for water electrolysis and investigates vapor electrolysis, feeding in water vapor instead of liquid water for the OER. This system can be seen as a model system for more complex reactions, including carbon-dioxide reduction or methane to methanol oxidation (see Chapter 6). In this chapter, we further explore the role of water as the reactant but look at bulk transport to the catalyst layer and its impact on membrane hydration. Water is a crucial element in these electrolytic systems as it is not only a hydrating agent for the membrane and ionomer but also the reactant for the OER. Within the chapter, coupled experiments and simulations investigate different relative humidities and cell configurations, and applied voltage breakdowns provide a detailed understanding of the challenges and promises for vapor-electrolysis systems.

Chapters 5 and 6 start to explore case studies and applications of some of the technology that has been explored in Chapter 4. Chapter 5 looks at using the vapor electrolyzer in a unitized regenerative fuel cell (URFC), making the entire system vapor and increasing the switch over time between fuel-cell and electrolysis operation. In this chapter, looking at constant gas mode for URFCs, the learnings from Chapter 4 are used to explore different membrane chemistries, different relative humidities, and different carrier gases for specific applications. By tailoring operating conditions and the membrane chemistry, the vapor-URFC achieves a roundtrip efficiency of 42% and a lifetime of 50,000 accelerated-stress-test cycles for fully humidified feeds.

Chapter 6 is another case study focused on the prospect of using an electrolytic device as a potential reactor for partial oxidation of methane to methanol at high conversion and selectivity. In this chapter, we describe why MEAs are well suited for the electrochemical oxidation of methane, define the metrics for assessing MEA performance, and review the progress in the field. However, through experiments, evaluating the literature, and theory from others, the pitfall comes in the design and nature of the electrocatalyst. There have been many catalysts tested for partial oxidation but none yield significant amounts of methanol; this chapter provides a guidepost of what has been learned and directions for future MEA systems for these reactions.

The final chapter summarizes the dissertation and the main outcomes of the work conducted. Additionally, future directions and avenues are included to consider in the next steps of electrolytic devices and other applications.

2. Linking Catalyst-Layer Structure – From Inks to Performance for Water-Electrolysis

2.1 Abstract

Proton-exchange membrane water electrolyzers (PEMWE) depend on various components in a membrane-electrode assembly (MEA) to achieve high rates of reaction. The most important part of the MEA is the anode catalyst layer, as the oxygen-evolution reaction is limiting within this system. The catalyst layer must manage multiple phases (i.e. gas and liquid) and maintain ion and electron transport within this porous electrode. However, the complexity of understanding how liquid inks form a solid, porous electrode has been underexplored in the PEMWE literature. Within this chapter, the connection between ink properties, the structure of the resulting catalyst layer, and the performance of the MEA is elucidated. This study focuses on how the solvent ratio of the catalyst ink impacts the aggregate sizes and the resulting structure of the catalyst layer. We find that large aggregates in the ink result in denser catalyst layers and resultant high mass-transport overpotentials. The best performing catalyst layer had relatively high porosity (40%), small aggregates (210 nm), and anisotropic tortuosity. Correlations are drawn between ink properties and catalyst-layer structure that can assist the field in understanding the limiting factors in these complex porous electrodes.

2.2 Introduction

There is a need for deep decarbonization in chemical, food, and steel manufacturing processes, which is enabled through a decarbonized energy vector like low carbon-intensity hydrogen (aka green hydrogen).[9,59–61] A prominent technology for producing such hydrogen is proton-exchange-membrane water electrolyzers (PEMWEs).[13–15,20,21,30] In water electrolysis, the oxygen- and hydrogen-evolution reactions (OER and HER, respectively), shown in eqs 2.1 and 2.2, respectively, work together to produce hydrogen gas.

$$2H_2O \rightarrow O_2 + 4H^+ + 4e^- \qquad U = 1.23\ V\ vs\ SHE \qquad (2.1)$$

$$4H^+ + 4e^- \rightarrow 2H_2 \qquad U = 0.00\ V\ vs\ SHE \qquad (2.2)$$

PEMWEs can operate at high cell efficiencies (~80%) and offer a lot of advantages compared to traditional liquid alkaline electrolyzers or hydroxide-exchange membrane water electrolyzers (HEMWEs), particularly high performance, reliability, and long lifetimes.[21,62,63] However, PEMWEs require iridium oxide as the catalyst for the OER, which is a platinum-group metal (PGM) that is rare and expensive. By contrast, alkaline systems use more abundant, non-PGM catalysts.

In PEMWE systems, a lot of iridium oxide is used since they require high loadings to sustain high catalyst activity and high electronic conductivity through the catalyst layer.[51,59,64] While there have been attempts at reducing the loading and using a metal support, such as titanium dioxide for the iridium to help increase conductivity, typical PEMWEs in industry still operate at 1-3 mg cm^{-2} total PGM loading.[20,41,59] Recent studies have shown that performance can be maintained at lower loadings, between 0.1-0.4 mg cm^{-2} to even as low as 0.05 mg cm^{-2},[50,59] but the tradeoff is shorter operational lifetimes. Regardless of loading, the anode catalyst layer is the most important component of the membrane-electrode assembly (MEA).

Since the catalyst layer (CL) used to promote the OER exhibits a significantly higher overpotential than the catalyst used to promote the HER, there is considerable interest understanding how the structure of the OER CL influences the overpotential and what might be done to minimize it.[21,41,54,55] Unfortunately, due to the complexity and location of the OER CL, the needed understanding is limited. The CL is fabricated using an ink, which includes the catalyst and an ionomer dispersed in a solvent mixture of alcohol and water.[51,53,54,65] There have been numerous studies of catalyst inks, particularly platinum catalyst inks that are used in fuel cells.[52,53,55,65–72] Researchers have studied the solids loading,[53–55,65] aggregation behavior,[54,66] and the conformation of the ionomer in different solvents,[68,69,71,73] in order to understand how the CL is formed. In a recent current opinion, Berlinger *et al* correlated the key catalyst ink with CL variables and analyzed the recent literature to gain better connections between the liquid ink and the solid layer. They found several trends linking the ink's solvent's ratio to the diameter of the aggregates, the stability of the ink, the limiting current density in fuel cells, and the electrochemically active surface area. With each of the parameters, solvent ratio influenced interactions in the CL and the performance for fuel cells. However, even with all of these studies done for fuel cells, nothing is conclusive on the direct effects of the catalyst-ink properties to the structure of the CL.

Catalyst inks are highly complex, and require a detailed understanding of the different types of interactions: particle/particle, particle/solvent, particle/ionomer, and ionomer/solvent.[51,53] Many of these interactions are hard to measure and isolate. Additionally, there has been little work done for PEMWEs CLs thus far, and linking the relationship between ink-catalyst layer-performance, as shown in Figure 2.1. Khandavalli *et al* studied the rheological properties of iridium inks and saw the addition of ionomer helps to stabilize the inks when investigating n-propanol and water solvent systems, particularly for high solids-percent inks.[54] Alia *et al* systematically evaluated different catalyst-ink variables and empirically linked the variables to performance. They found that ionomer/catalyst segregation, which they saw was due to both solvent composition and ionomer content, significantly reduced the kinetic performance.[55] Many reports have looked at empirical correlations between PEMWE performance and the ionomer content, solids percent, and/or solvent ratio of the inks.[41,54,55,64]

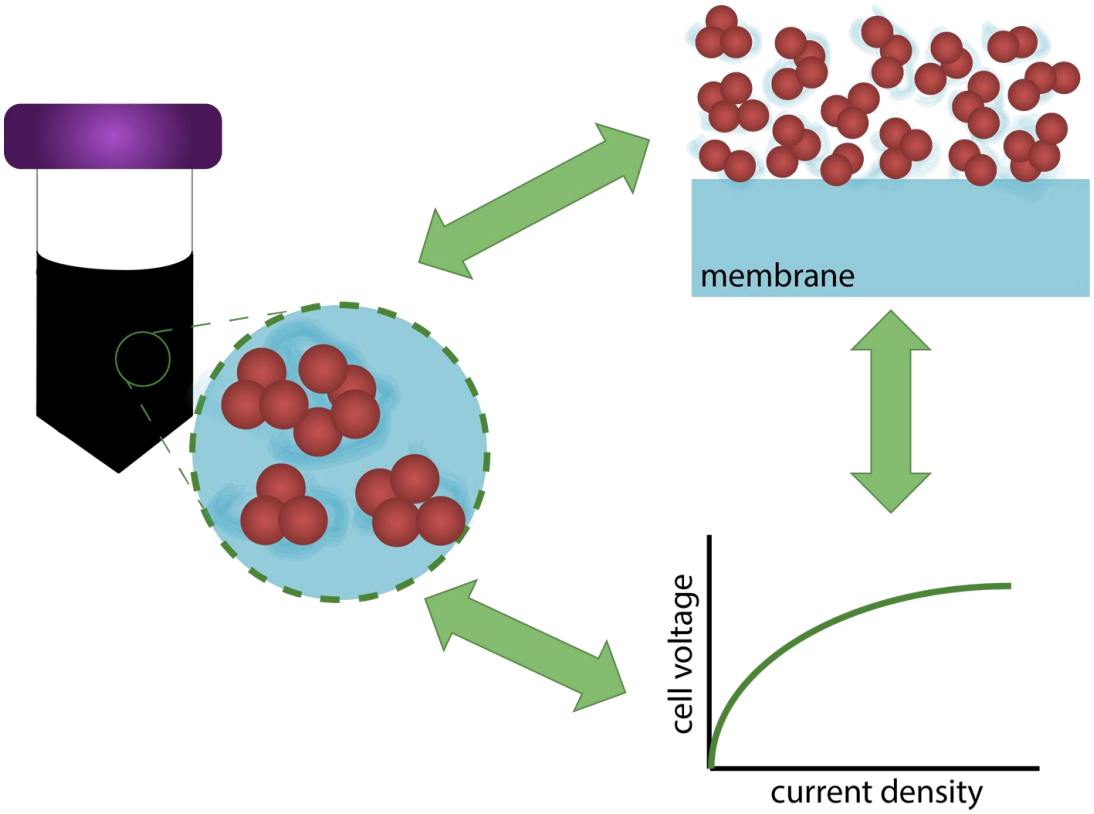

Figure 2.1: Schematic showing the catalyst ink to catalyst layer and the unknown relationship on performance and structure.

In this chapter, we explore the impact of solvent ratio in a catalyst ink and on the catalyst-layer structure. Solvent ratio was chosen in order to keep the solids percent and ionomer content the same as what is found in the literature,[54,55,68,69,71,73] and to investigate only one parameter of the ink. Cell performance, applied-voltage breakdowns, and characterization of the catalyst ink and layer are explored to provide information on how the solvent ratio plays a role in the structure of the catalyst layer and eventually performance. Thus, we correlate aggregation size to CL structure,

for the same fabrication method. Additionally, we show that the structure of the CL (i.e. tortuosity, porosity, and pore-size distribution) can be manipulated by changing the ink solvent. This result indicates that the interaction between solvent and aggregates of catalyst particles and ionomer is a strong force in the CL fabrication process and impact overall performance.

2.3 Methods

2.3.1 Catalyst-Ink Preparation and Characterization

The anodic ink was prepared by adding 50 mg of iridium oxide (Alfa Aesar, Massachusetts, USA, 50 nm primary particle size) to the appropriate volume of deionized water in a vial, followed by addition of the designated volumes of alcohol, either n-propanol, ethanol, or both (see Table 2.1). In this study, we investigated different solvent ratios, including 2:1:1, 1:1:0, 3:1:0, and 0:1:3 of n-propanol (200 proof, Koptec, Pennsylvania, USA): deionized water (DI, 18.2 MΩ, Milli-Q, EMD Millipore, Massachusetts, USA): ethanol (Sigma Aldrich, Missouri, USA), all by volume. The solvent ratios were chosen based on previous literature studies (i.e. 2:1:1 and 1:1:0 are common solvent ratios in the PEMWE literature and empirically show stable, dispersed inks[41,50,59]) and to determine if the catalyst ink and CL change based on amount of alcohol or the composition of the specific alcohols used. The 0:1:3 ink was made to verify the impact of ethanol on the system. A 5 wt% ionomer dispersion in a 1:1 weight ratio of n-propanol and water (Nafion™, D521, Chemours, Delaware, USA) was added to achieve a 0.116 ionomer-to-catalyst weight ratio. This ionomer-catalyst-ratio was chosen from the literature as it yielded the best performance for these loadings.[74] Each ink was sonicated for 30 min using a probe tip sonicator (CPX500, Cole-Parmer, Illinois, USA).

Table 2.1: Catalyst-ink recipes and their constituent components.

Components	**Ink Recipe**			
	2:1:1 Ink	1:1:0 Ink	3:1:0 Ink	0:1:3 Ink
Iridium oxide	50 mg	50 mg	50 mg	50 mg
Nafion (5 wt% solution)	116 mg	116 mg	116 mg	116 mg
N-propanol	16 g	16 g	24 g	--
Water	10 g	20 g	10 g	10 g
Ethanol	7.898 g	--	--	23.67 g

Dynamic light scattering (DLS) was used to characterize the aggregation of the suspended iridium-oxide particles in order to determine the average aggregate size and the stability of the ink to settling, as shown in Figure S2.1. Five measurements were completed within fifteen minutes for each ink to achieve good statistics and also determine the ink stability. The average aggregate

radius was determined via the Stokes-Einstein equation, converting the measured diffusion coefficient to a hydrodynamic radius via Stoke-Einstein Equation. The Stokes-Einstein equation is only valid for spheres; therefore, the results are qualitative in nature since the aggregates are not necessarily spheres. The measurements are helpful to compare qualitatively between the different tested inks.

For the cathodic inks, platinum inks were prepared by adding 65 mg of Pt/C catalyst (46.2wt% of Pt on Vulcan carbon, Tanaka, Japan) to a 1:1 volume ratio solution of n-propanol (200 proof, Koptec, Pennsylvania, USA) and deionized water (18.2 MΩ, Milli-Q, EMD Millipore, Massachusetts, USA). The ionomer dispersion (Nafion™, D521, Chemours, Delaware, USA) was added to this catalyst suspension in order to achieve a 0.6 ionomer-to-carbon ratio, which is based off of results from the fuel cell and electrolysis literature.[74,75] This ratio was chosen as it exhibited the lowest overpotentials for HER in the literature, presumably showing sufficient ionomer coverage for the electrochemical reaction. These inks were then hand-shaken for 30 s, and bath sonicated (M1800, Branson, Connecticut, USA) for 30 min at 10°C. The inks were sprayed via the SonoTek to achieve the loading of 0.1 mg cm^{-2}.

2.3.2 Catalyst-Coated-Membrane Fabrication

To fabricate 5 cm^2 catalyst-coated membranes (CCM), the platinum and iridium oxide inks were coated onto Nafion™ membranes (N117, Chemours, Delaware, USA) by ultrasonic spray coating. The membranes were pretreated by boiling in DI water at 100°C for one hour before being cooled to room temperature and stored in DI water. The membranes were removed from the DI water and placed on the heated (at 80°C) vacuum plate of the spray coater (Sono-Tek, Exacta Coater, New York, USA) to dry. A fiberglass mask and a rubber gasket were used to protect the membrane, prevent it from moving during spraying, and assure the exact 5 cm^2 area was sprayed. For the cathode, ~2.5 mL of the Pt/C ink was deposited at 0.3 mL min^{-1} for a target loading of 0.1 mg cm^{-2}. On the anode side, ~14 mL of the iridium oxide ink of interest was deposited at 0.35 mL min^{-1} for a target loading 0.35 mg cm^{-2}. The platinum side was coated first, followed by the iridium oxide electrode. The loadings and standard deviation of the CCMs are shown in Table 2.2. X-ray fluorescence (XRF) was used to determine the exact loading of both electrodes. The XRF was calibrated using platinum and iridium standards (MicroMatter Technologies Inc., Canada).

Table 2.2: The loadings of each anode catalyst layer for the different ink formulations.

CCM	2:1:1	1:1	3:1
Loading (mg cm^{-2})	0.3803	0.3477	0.3515
Standard Deviation	±0.021	±0.064	±0.077

2.3.3 Cell Assembly and Testing

The cathode side of the electrochemical cell utilized a Teflon-coated carbon-paper gas-diffusion layer (Toray 120, 5% PTFE content, Fuel Cell Store, Texas, USA). The anode was equipped with a titanium porous transport layer (Nel Hydrogen, Connecticut, USA), cut using a laser cutter (Full Spectrum Laser Fiber50FC, Nevada, USA) to achieve the exact 5 cm^2 active area. PTFE gaskets (McMaster-Carr, Illinois, USA) were used on both sides. The electrochemical cells (Fuel Cell Technologies, New Mexico, USA) consisted of a graphite flow field on the cathode and a platinized titanium flow field on the anode. Both current collectors in the electrochemical cell were gold-plated copper and are placed between the flow fields and end plates of the cell. One cell was used to test all CCMs in this study. The cell was connected to a lab-built test stand consisting of a heated water bath and a recirculation pump for the anode and gas flow and temperature controlled via a fuel-cell test stand for the cathode (Fuel Cell Technologies Inc, New Mexico, USA).

Once the cell was assembled, it was heated to 50°C by running DI pre-heated in a water bath through the anode side of the electrolyzer at 100 mL min^{-1}. The cell was then connected to an auxiliary heater and the temperature was increased to the operating temperature, 80°C. Humidified H_2 (at 100% relative humidity) was supplied to the cathode at 100 mL min^{-1} and at ambient pressure to establish a pseudo-steady reference potential. All electrochemical measurements were accomplished using a potentiostat (VSP300, Biologic, France) equipped with a 20 A booster and an electrochemical impedance analyzer. The cell was cycled 10 times between 1.2 V and 2 V at 50 mV s^{-1}. To generate a polarization curve, the current via chronopotentiometry (CP) was swept from 5 to 3.2 A cm^{-2} in 30 steps, holding at the specific currents for 2 min and averaging the last for 300 s. Following the CP measurements, electrochemical impedance was measured at each of current in galvanostatic mode. The impedance was measured by applying an AC current perturbation between 200 kHz and 100 mHz to the cell and measuring the voltage response. The amplitude of the current was determined for each step to assure there is a sufficient signal-to-noise ratio but assuring the perturbation remained small. A Nyquist plot was used to find the y-intercept at high frequency in order to obtain the high-frequency resistance (HFR) of the cell, which corresponds to the membrane, solid, and contact resistances.

2.3.4 Applied-Voltage Breakdown

The applied-voltage breakdown (AVB) follows the same empirical protocol used by Peng *et al.*[50] Further details concerning AVBs are described by Gerhardt *et al.*[76] The overall cell voltage (E_{cell}) is the sum of all the overpotentials (η_i) and the reversible cell potential (E_{rev}),

$$E_{cell} = E_{rev} + \eta_{kinetic} + \eta_{Ohmic} + \eta_{MT} \tag{2.3}$$

where $\eta_{kinetic}$, η_{Ohmic}, and η_{MT} are the kinetic, ohmic, and mass-transport overpotentials, respectively. This AVB only considers the OER side of the PEMWE since HER is more facile and essentially negligible under PEMWE operating conditions, accounting for < 10 mV of the total voltage from calculations at all currents.[77] The temperature-dependent E_{rev} was calculated to be 1.168 V at 80°C.[78] The kinetic overpotential was determined assuming Tafel kinetics for the OER,

$$\eta_{kinetic} = b \log\left(\frac{i}{i_0}\right) \quad (2.4)$$

where i is the operating current density, i_o is the exchange current density, and b is the Tafel slope, which was extracted via the linear fit of the experimental data points from 5 to 100 mA cm^{-2}. This range assures we are in the kinetic regime and the Tafel slope remains linear in a Tafel plot.

The ohmic overpotential was determined measurement using the HFR obtained from the electrochemical impedance. The HFR represents the total cell resistance (R_{tot}), which can be related to the voltage loss through the membrane. η_{Ohmic}:

$$\eta_{Ohmic} = I * R_{tot} \quad (2.5)$$

where I is the total current running through the cell at a given step in the CP.

The mass-transport overpotential is the remainder of the losses within the cell, including the gas or liquid transport through the MEA and other transport phenomena not covered in the other overpotentials. η_{MT} is determined by subtracting the E_{rev}, $\eta_{kinetic}$, and η_{Ohmic} from the cell voltage (E_{cell}) at each current density.

2.3.5 Catalyst-Layer Characterization

Focused-ion-beam scanning electron microscopy (FIB-SEM) of the anode CLs was done on a FEI Quanta 3D dual beam microscope with a Ga focused ion beam. The FIB allows micro- and nano-scale cutting of surfaces, slice by slice to obtain an image stack that can be stitched together to form a 3D reconstruction. Hence, sub-surface features of the CL such as pore network and its distribution can be visualized.

After the sample is loaded in the instrument, it is tilted 52° such that the surface is perpendicular to the FIB gun. A probe is then used to deposit a several hundred nm layer of Pt on the area to be milled. This process protects underlaying surface features and helps prevent heat damage from ion beam milling. The FIB is then used to mill front and side trenches to prepare a region of interest with a width of 9 um, height of 2 um and depth of 8 um as seen in Figure S2.2. After the trenches are milled, the CL cross section is exposed and an image is taken with the electron beam at 10 kV accelerating voltage. The FIB then mills another 20 nm into the exposed cross section at 30 kV accelerating voltage, and another image is taken. This process is repeated to obtain 40 image slices that are stitched and aligned in ImageJ software. A bandpass filter is applied to the resulting image stack to improve the relative contrast of pores. The image stack is then thresholded to expose the pore structure. Porosity is obtained using an ImageJ macro that uses area measurements along the stack. The pore-size distribution is obtained using the Local Thickness option within the BoneJ plugin, which uses an inscribed sphere approach. The plugin calculates mean and standard deviation of the trabecular thickness (Tb.Th) and trabecular spacing (Tb.Sp) directly from pixel values in the resulting thickness map. The thickness map values are then represented as a pore-size distribution using a probability density function fitting.

2.4 Results & Discussion

2.4.1 Catalyst-Ink Behavior

Figure 2.2 shows the size of the aggregates of iridium oxide particles (50 nm in diameter for the primary particles) in the as-prepared inks (constant weight-percent-solids of 0.16%). The aggregates vary from 200 to 330 nm.

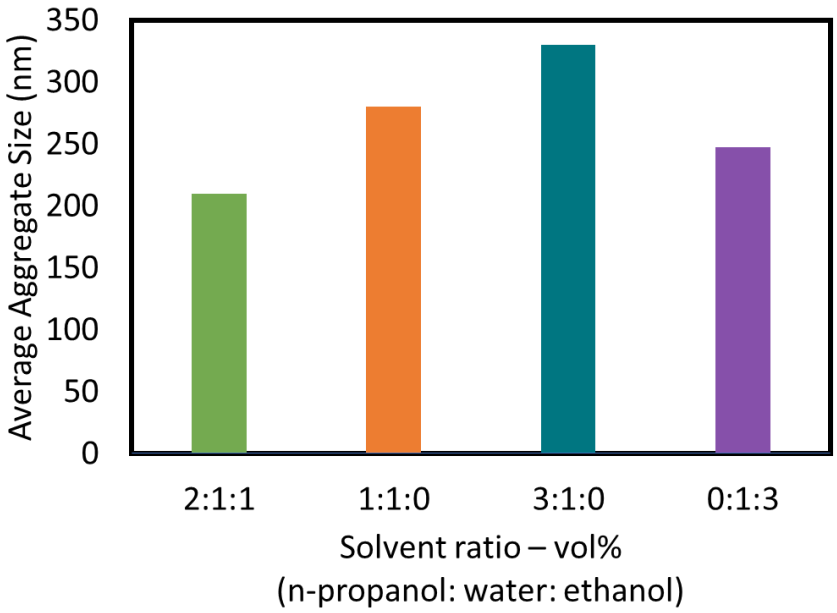

Figure 2.2: Average aggregate size of iridium oxide particles in catalyst inks measured by DLS for different solvent ratios (percent volume). All of the inks were held at a constant weight- percent-solids of 0.16%.

The aggregate size of all four of the inks was stable over the measurement time (~15 min), as shown in Figure S2.1. A stable ink assures that phase separation does not occur between the catalyst particles and the ionomer/solvent mixture,[51] and that the ink is well mixed. All of the inks exhibited a monomodal distribution in aggregates size after the ink was probe-tip sonicated and pumped through the SonoTek. This procedure was used to be as similar to the fabrication process as possible.

The data in Figure 2.2 show that in the absence of ethanol, the aggregate size increases as the proportion of n-propanol to water increases, and that at constant alcohol to water ratio (3:1), the partial replacement of n-propanol by ethanol reduces the aggregate size. These results demonstrate that an alcohol-rich ink does not necessarily result in large aggregates, compared to the baseline 2:1:1 ink, but the composition of the alcohols matters as well. Interestingly, introducing ethanol changes the interactions within the ink. This finding is consistent with previous studies carried out with Pt/C, which showed that the presence of ethanol leads to a more homogenous ink.[79] Ethanol and water alone do not lead to smaller aggregation behavior, as shown in Figure 2.2. The aggregate sizes are 246 nm, larger than the 2:1:1 ink (aggregate size is 210 nm). This result shows that the interactions with the three solvents, n-propanol, water, and ethanol, lead to different interactions with the Nafion film and the iridium oxide catalyst inks. Further research must be done to identify

better the driving forces controlling aggregation, which is beyond the scope of this chapter. It would also be interesting to identify how Nafion interacts with more complex solvents (tertiary or higher), since most of the literature looks only at binary solvents, or even non-aqueous solvents.

2.4.2 Catalyst-Layer Performance

The inks characterized by DLS in section 2.4.1, were sprayed onto membranes and the resulting CCMs were evaluated for performance in a PEMWE. The polarization curves for all three inks at the same iridium oxide loading (0.35 ± 0.0023 mg cm^{-2}) are shown in Figure 2.3a. The variation between the three different CCMs is at most 100 mV at 3 A cm^{-2}. These data demonstrate that for a given operating current density, the overpotential increases with increasing aggregate size, indicating that the smallest overpotential occurs for a CL prepared using an ink containing n-propanol:water:ethanol in proportions of 2:1:1.

To gain more insight into the origins of losses, the AVB is shown in Figure 2.3b-d. The kinetic overpotential, shown in Figure 2.3b, varies the least out of the three overpotentials. Since the Tafel slope and kinetic overpotential is determined at low current densities (< 100 mA cm^{-2}), the difference in overpotential is expected to be low. Additionally, the Tafel slopes are nearly identical, 41.8 ± 0.0020, 42.2 ± 0.053, 40.1 ± 0.0014 mV dec^{-1}, for 2:1:1, 1:1:0, and 3:1:0, respectively, showing that the intrinsic rate of reaction is effectively the same for all three CCMs. This result is expected as the kinetic overpotential is limited by the kinetics of the reaction and how much catalyst is in the electrode. Interestingly, the structure has no impact on the kinetics of the catalyst layer.

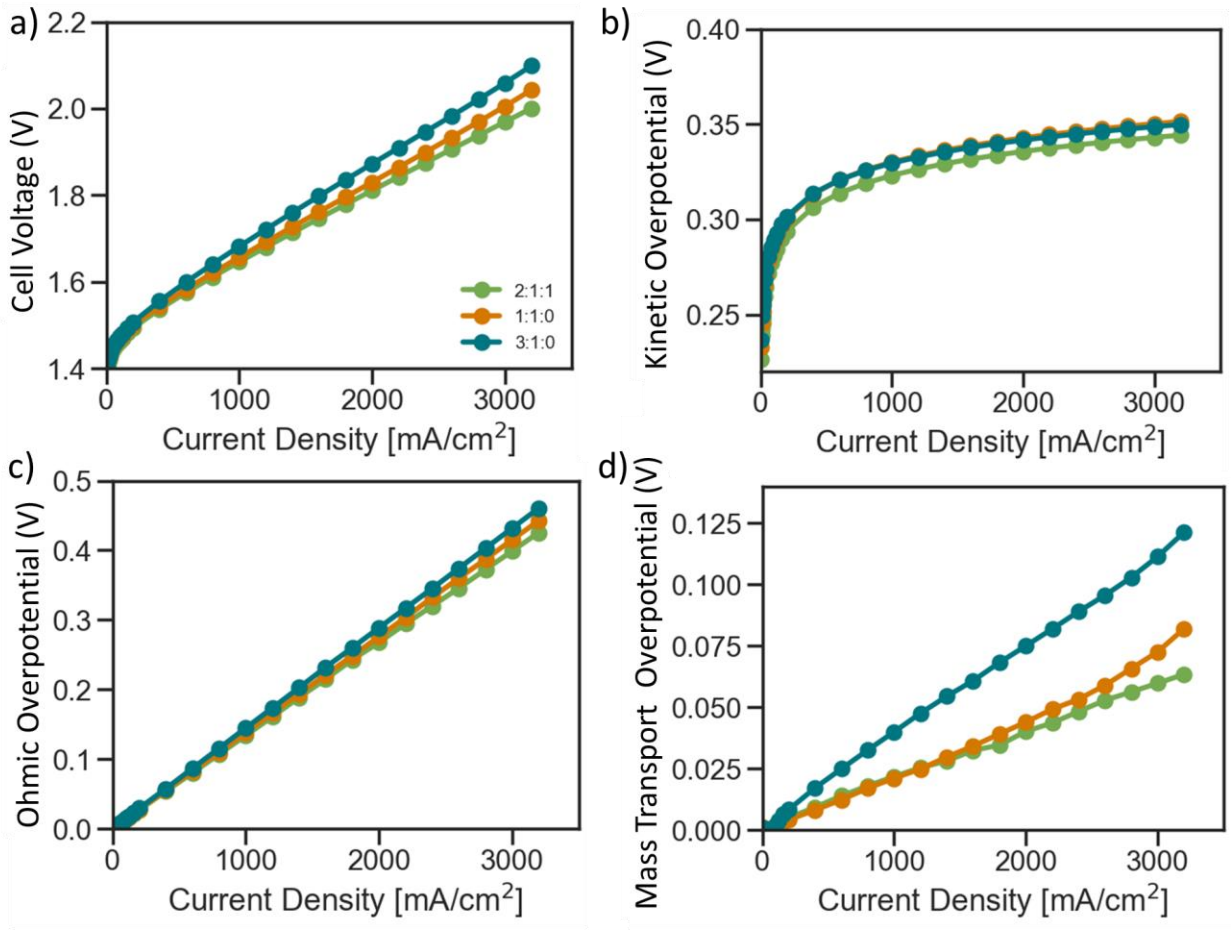

Figure 2.3: (a) polarization curves of the three different MEAs tested and the applied voltage breakdown of each. The (b) kinetic, (c) ohmic, and (d) mass transport overpotentials are compared for the three MEAs. For all three of these tests, a Nafion 117 membrane was used and the catalyst loading for the iridium oxide side was 0.35 ± 0.0023 mg cm^{-2} and the platinum loading was 0.1 ± 0.023 mg cm^{-2}

Likewise, the ohmic resistance changes slightly between CCMs (see Figure 2.3c): 1.33 ± 0.0026, 1.39 ±0.0061, and 1.43 ± 0.0026 Ohm-cm^2 for 2:1:1, 1:1:0, and 3:1:0, respectively. Typically, ohmic overpotential loss is dominated by the ionic resistance in the membrane and contact resistances within the cell. Since the same cell and membrane are being used, the values should be similar, as seen. However, converting this ohmic resistance to an overpotential at 3 A cm^{-2} there is a 32-mV difference between the 2:1:1 sample and the 3:1:0 sample. This difference could be due to changes in ionomer distribution, as the solvent ratio will yield different ionomer configurations in the ink. The ionomer distribution would influence the ionic resistance measured within the cell. A recent study showed that the interface between the catalyst layer and the porous-transport layer (CL|PTL) is important, and ohmic overpotentials, even if they are small, could be due to a small change in the CL|PTL interface since oxygen and water are simultaneously moving towards and away from the membrane.[50] If this finding is true for this work, and the PTLs are all the same, then the observed ohmic overpotential difference may be due primarily to a change in the oxygen/water transport through the catalyst layer and at the interface. The contact resistance at the CL|PTL interface could be different, which influences the HFR. The structure of the catalyst

layers is different, which would lead to different contact resistances and will be discussed in the next section 2.4.3.

Finally, as shown in Figure 2.3d, the mass-transport overpotential, makes up the majority of the difference in the overpotential for the three CCMs (~52 mV at 3 A cm^{-2}). The largest mass-transport overpotential occurs for the 3:1:0 CCM. The mass-transport contribution to the overpotential can be attributed to different phenomena. These include water transport within the CL, poor catalyst utilization, oxygen bubbles blocking the reaction sites, evaporation rate of the ink, etc. Typically, mass transport losses exponentially increase with current density, which is shown only in 1:1:0 and not for the other two, as 2:1:1 and 3:1:0 increase linearly with current density. This difference in dependence on current density may indicate different phenomena occurring. The mass-transport loss also indicates that there is something different between the three CCMs, since the anode CL is the only thing varied. The different solvents ratios that were used for the three CCMs could have led to a different distribution of the ionomer and thus different CL utilization or electrochemical surface area (ECSA). Various studies have looked at how Nafion changes shape and interactions with catalyst particles under different solvent conditions.[55,67,69,80,81] In fuel cells, Orfanidi *et al* showed changing the solvent (n-propanol to i-propanol) and solvent ratio with water resulted in drastically different ionomer distributions.[69] ECSA could be helpful in identifying if these three CCMs differ in the maximum sites available for the reaction due to the structure and ionomer distribution. Unfortunately, determining the ECSA for an iridium oxide electrode is intrusive and typically requires destructive techniques, such as mercury underpotential deposition or zinc adsorption measurements.[82,83] Additionally, the ECSA is the number of sites available, typically at low current and can be accessible – however that does not mean they are active under operating conditions. Bubble formation, water movement throughout the system, and other physical differences in the layer could change which sites are actually available to operate.[84,85] In addition to the solvent ratio changing the ionomer distribution throughout the CL, the solvent could have also changed the structure of it since the evaporation rate would be different for all three solvents.[69,79]

2.4.3 Linking Structure to Performance

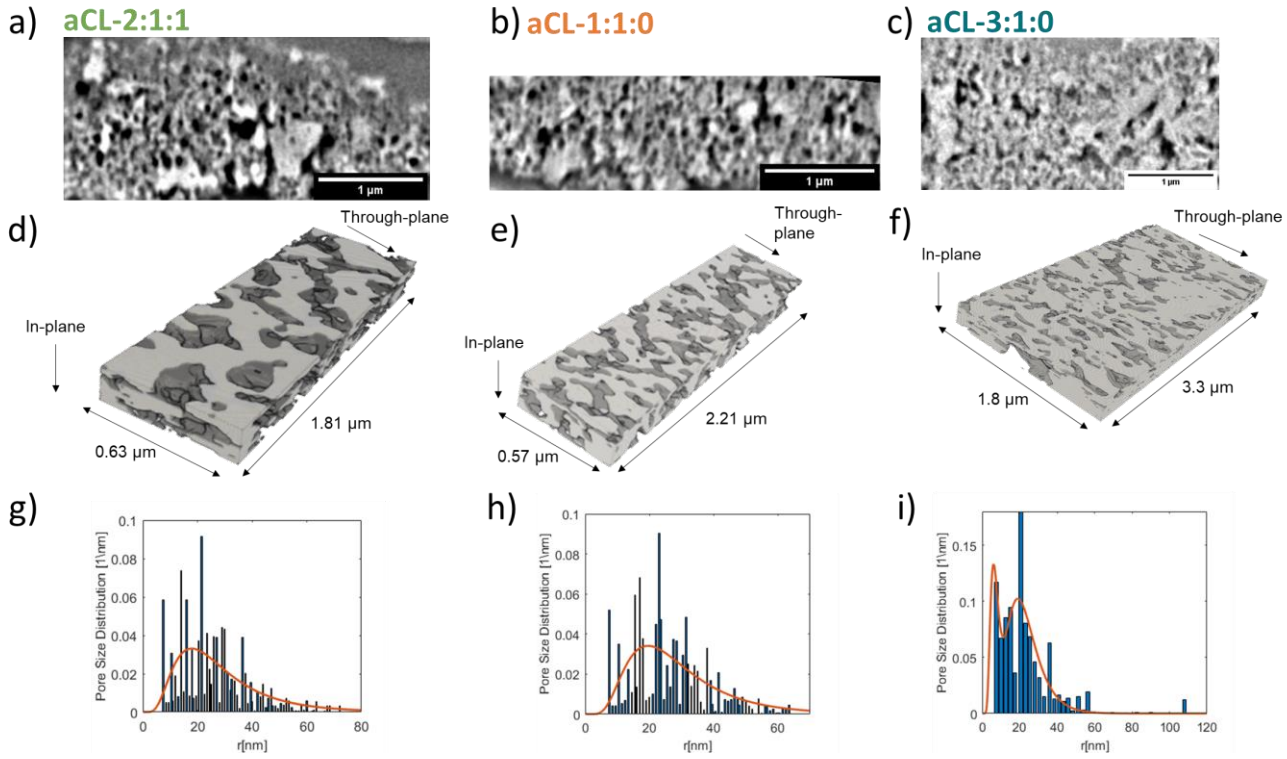

Figure 2.4: Characterization of the different anode Cls (aCL), 2:1:1 (a,d,g), 1:1 (b,e,h), and 3:1 (c,f,i). (a-c) FIB-SEM images of the cross section of each CL; (d-f) FIB-SEM reconstructions of the slide of the images shown in (a-c); (g-i) pore-size distribution of each of the CLs calculated using the reconstruction.

FIB-SEM tomography was performed on all three CCMs in order to obtain structural information, such as porosity, average pore size, and tortuosity (see Figure 2.4). Figures 2.4 and 2.5 display the structure and through-plane porosity for all three CLs. The aCL-3:1:0 shows the lowest porosity, 20%, which is substantially lower than the other two. Interesting, although the 3:1:0 ink has the largest agglomerates of the three, the lowest porosity suggest a different packing mechanism and that perhaps the solvent is the driving force for the porosity. This could be due to a higher evaporation rate leading to a less porous layer since there is less time for rearrangement and settling after spraying. However, since the CLs are spray coated, the CL structure builds layer by layer and the interaction between the membrane-bound aggregates the free aggregates may define the ultimate porosity of the CL. There could have been some collapsing of large agglomerates onto the membrane as the subsequent layers were sprayed on, which led to a denser catalyst layer. As they were sprayed, bound layers sit on the heated surface and more ink is being deposited, reconfiguration of the catalyst particles can occur within the time scale of spraying.[51,52,79] Since there are multiple driving forces for CL formation, identifying the main driving force is difficult and may change during the process. This area of research is being actively pursued in the electrolysis and fuel cell area. Modeling attempts to understand the fundamental forces at play are being investigated and additional studies like the one shown are also trying to elucidate this difficult, complex question.

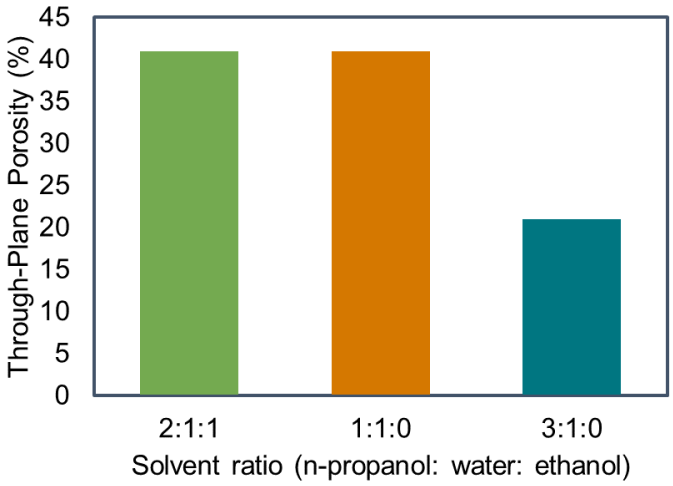

Figure 2.5: Through-plane porosity for the three CLs determined from FIB-SEM images.

Interestingly, as shown in Table 2.3, while porosity varies among the three CLs, the pore-size distribution is very similar. For all the aCLs, the average pore size is about 24 ± 2 nm. For the aCL-3:1:0, the pore-size distribution was bimodal, in addition to having pores of ~24 nm, this layer also has smaller pores of about 7 nm (see Figure 2.4i), perhaps showing the pore size is more dependent on the fabrication technique and the porosity is dependent on the solvents used in the ink. Comparing a CL that was slot-die or doctor bladed could help clarify if the pore-size distribution is fabrication dependent; but that is out of the scope of this chapter.

Table 2.3: The three different MEAs, 2:1:1, 1:1:0, and 3:1:0 and their structural properties from the FIB-SEM reconstruction and analysis. *Pore size distributions are shown in detail in Figure 2.4g-i.

Solvent Ratio	**Porosity (through-plane)**	**Porosity (in-plane)**	**Tortuosity (through-plane)**	**Tortuosity (in-plane)**	**Average Pore radius (nm)***
2:1:1	40%	40%	1.45	1.16	24.7
1:1:0	40%	40%	1.1	1.09	25.6
3:1:0	20%	20%	1.89	1.15	6.91 and 23.5

The last, and perhaps most important, structural factor that can provide information about the mass-transport losses within the catalyst layer is the tortuosity. The tortuosity is the ratio between the actual path the fluid is moving and the straight-line path between two points.[11,86] The less tortuous a layer is, the more connected the pores are and a shorter path for the oxygen or water to travel. However, if the pore space tortuosity is low, the solid phase, including the catalyst and ionomer, is more separated and may have fewer pathways or connections for the reaction to easily proceed within the catalyst layer. These catalyst layers need a triple percolated pathway The in-

plane tortuosity shown in Table 2.3 shows that within error, all three aCLs are the same. In contrast, the through-plane porosity does vary between 1.1 to 1.89 for 1:1:0 to 3:1:0, respectively. The through-plane tortuosity is typically the most important for these aCLs as the water and oxygen typically flow through-plane. The in-plane tortuosity does play an influence on the transport of species. The difference in tortuosity between the two different directions may yield different effects in the fluid transport in the layer.

Understanding how the fluid (gas or liquid) is transported through the CL and how the transport may differ from bulk conditions is crucial in understanding the role of structure on performance. This understanding is traditionally exemplified by the effective transport property (e.g., permeability or diffusivity),

$$K_{eff} = K\frac{\varepsilon}{\tau}, \tag{2.6}$$

where K is the bulk transport property, ε is the porosity, and τ is the tortuosity of the CL, respectively. The ratio between porosity and tortuosity provides an idea on the anisotropy of the catalyst layer. Typically, within the field, various studies have shown that the larger this ratio is, the higher the effective transport.[48,50,87] However, the highest effective transport of the fluid may not mean the best performance or smallest losses. While previously this trend is true, the results shown in Figure 2.6 do not follow this trend.

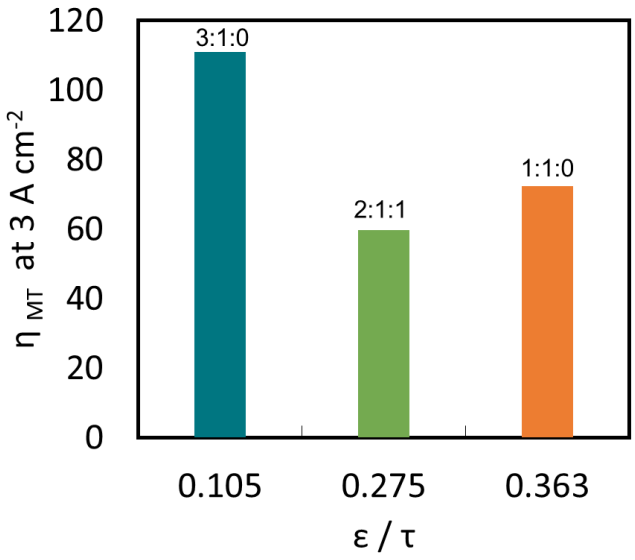

Figure 2.6: The relationship between mass transport overpotential and porosity/tortuosity for the three different CLs; the through-plane tortuosity is used here.

Figure 2.6 correlates the mass-transfer overpotential vs the ratio of porosity to tortuosity. There is a local minimum in the mass-transport overpotential at 3 A cm^{-2} for the aCL-2:1:1. Unlike a previous study where the highest ratio of these properties led to the lowest mass transport, the aCl-1:1:0 has the highest ratio but the second highest overpotential.[50] There are two potential explanations for this nonmonotonic behavior. First, the aCL-1:1:0 is the only one that had

symmetric tortuosity and porosity for in-plane and through-plane directions. While symmetry should not impact the system, anisotropic transport of the fluid may be helpful since the fluid wants to travel in the path of least resistance. When the water is being fed through-plane, there are only so many pathways it can travel for a given tortuosity and porosity. If there are more available pathways (i.e. a less tortuous path) in-plane, the fluid can utilize that part of the CL and potentially mitigate any transport losses in the system. Second, the ratio of porosity to tortuosity may be higher for the aCL-1:1:0 and the fluid is more effectively being transported, but the solid phase may be structured differently, especially how the ionomer and catalyst particles interact. The ionomer distribution, which is expected to be different between the different solvent ratios,[67,79,88] could be significantly different and could yield higher mass-transport losses. Since the mass-transport overpotential increases above 2 A cm^{-2} the difference between the aCL-1:1:0 and the aCL-2:1:1 could be due to different solid-phase interactions, such as the catalyst:ionomer interactions. Further imaging and analysis would need to be done to verify if the ionomer distribution is significantly different.

Additionally, the interface between the MEAs and the PTLs will be different due to the varying structures of the fabricated CLs as shown in Figure 2.4. Generally speaking, the interface between the PTL and the CL becomes increasingly important as catalyst loading decreases. As the catalyst loading decreases, the CL is not as interconnect in-plane and the CL|PTL interface is the only way to assure enough utilization within the layer.[50,59] However, even at higher loadings, the interface can play a role on how much catalyst is being utilized within the layer. Unfortunately, there is a tradeoff, since more contact area with the PTL could mean less open pore space for the fluids to transport. There have been many studies that have shown that a microporous layer (MPL) on a PTL will increase the interfacial contact area between the PTL and CL.[50] But because the MPL is thin, the benefits outweigh the negatives; if the PTL was as dense as the MPL throughout its thickness, then the utilization would suffer due to worse water and oxygen transport.

The PTL for this study stays the same and has a porosity of 36%, which is not very porous compared to other commercial PTLs (which can range from 50 to 78%).[50,89] Changing the porosity, the CL structure impacts the interfacial contact area and the viable pathways for the water and oxygen to move. The aCL-3:1:0 may have the most amount of contact with the PTLs based on the low density of pore space, but due to the lower ratio of porosity to tortuosity through-plane, mass transport still suffers, which the nonmonotonic behavior can be attributed to. There are only a limited number of pathways the oxygen and water can move through and thus attempting to understand the movement of the fluids is as important, if not more important than the CL/PTL interfacial contact area.

2.5 Conclusions

In this chapter, we showed a direct correlation between manipulating the catalyst ink to the catalyst-layer structure and linking to the electrolyzer performance. Changing the solvent ratio of the inks changes how the particles, ionomer, and solvent interact and results in different CL structures. The exact driving force is still unclear for this relationship and multiple phenomena may be at play, including aggregation size, solvent composition, and evaporation rates. More fundamental studies need to be conducted to further parse out the direct correlations with these phenomena and our observations. A tertiary solvent ink (2:1:1 n-propanol:water:ethanol) yielded the best performance with the smallest aggregates and the highest porosity (40%). The worse performance contained only n-propanol and water (3:1:0, respectively), with a through-plane porosity and tortuosity of 20% and 1.89, respectively. The differences in ink composition show direct changes in aggregation behavior and are suspected to influence the ionomer distribution – since studies have shown more homogeneous dispersions when ethanol is introduced. Interestingly all three CLs had the same in-plane tortuosity. Since the best performing CL had slightly different tortuosity through-plane than in-plane, the different pathways in varying directions helps distribute the water and oxygen more efficiently, leading to better effective transport in the CL. However, there could be other reasons for the difference in performance which requires more characterization to better identify. Lastly, we see that the highest effective transport property did not correlate to the best performing MEA, showing that some other phenomena are at play in terms of mass-transport losses. A possible reason is that CL utilization and interfacial contact area with the membrane and PTL varies for the different layers, and thus contributes to the performance differences seen in this chapter. This chapter provides examples that show ink properties can result into different CL structure and performance. Continued studies on understanding more parameters, like ionomer content or other solvent ratios, can provide clearer guidance in fabricating specific CL structures to yield a desired performance.

2.6 Supplemental Information

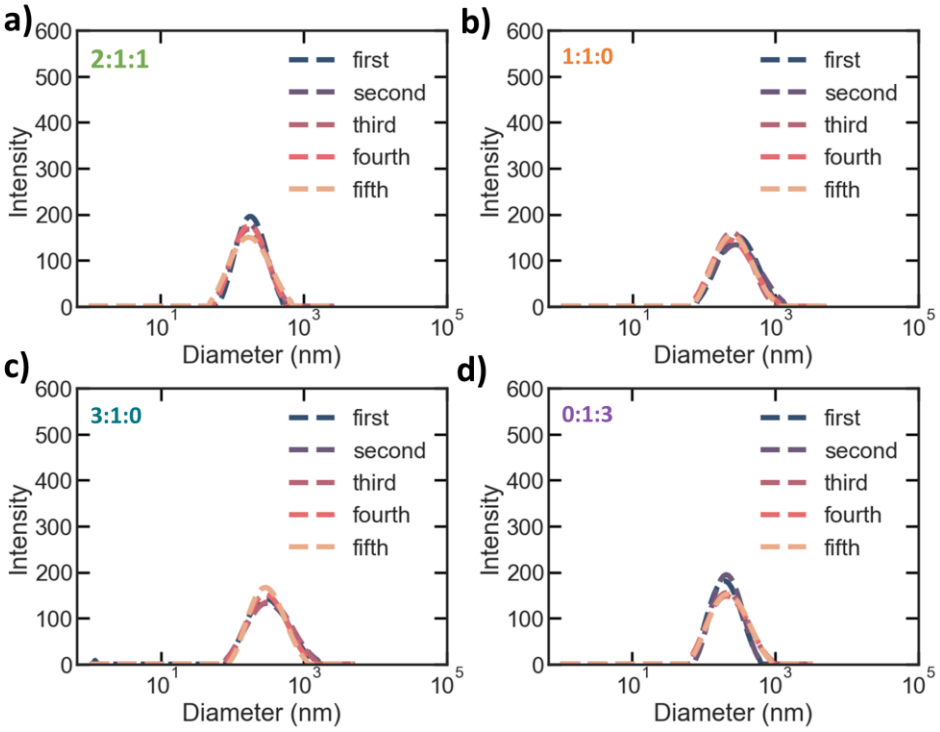

Figure S2.1: Histograms for the five repetitions for the four different inks (n-propanol: water: ethanol) (a) 2:1:1, (b) 1:1:0, (c) 3:1:1, and (d) 0:1:3. The peaks of the histograms do not change over the course of the measurements (from the first set of data to the fifth) showing stability in the ink.

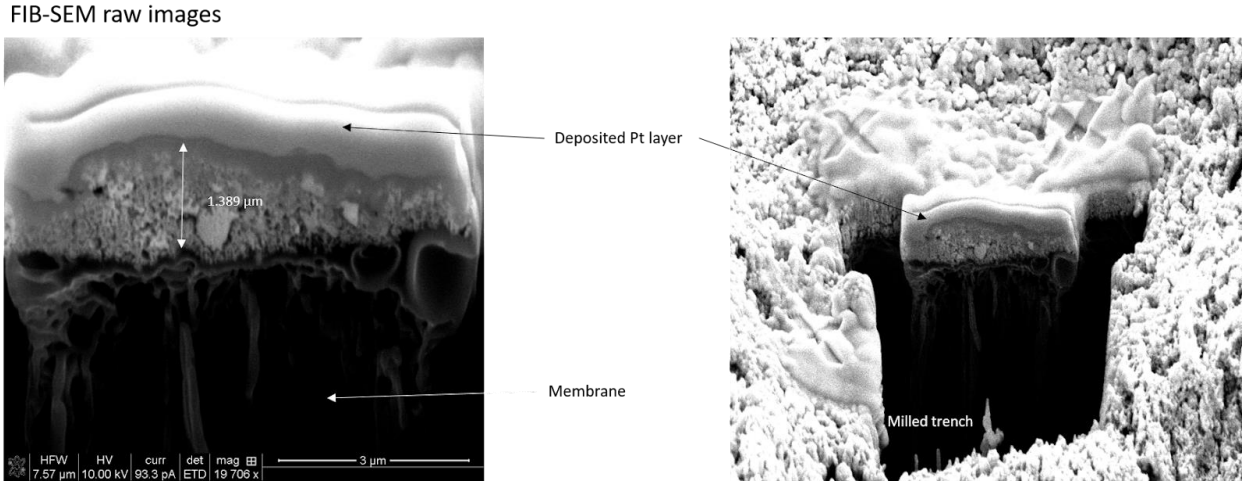

Figure S2.2: FIB-SEM of CCMs revealing catalyst layer cross section. Image on the left shows the milled trench and image on the right shows the magnified cross section.

3. The Impact of Species Transport in Near-Neutral and Hydroxide Exchange Water Electrolysis[†]

3.1 Abstract

The oxygen-evolution reaction (OER) is pivotal in many energy-conversion technologies as it is an important for making cost-effective green hydrogen. The local microenvironment and pH for the anode OER can vary from acidic to neutral to alkaline depending on the system being explored, making definitive mechanistic insights difficult, since the mechanism may be changing. In this chapter, we couple microkinetics, transport modeling, and experiments to explore the entire pH range of the OER. At low current densities, neutral pH values unexpectedly perform better than the acidic and alkaline conditions, and this trend is reversed at higher current densities (> 20 mA cm^{-2}). Using continuum modeling, this switch is rationalized by a change from a dual-reaction mechanism to a single rate-determining step. It is also shown how the alkaline reaction rates dominate in the middle to high pH range. Furthermore, we explore that the local pH for near-neutral conditions is much different (*e.g.*, 2.4 at the reaction surface vs. 9 in the bulk) than the pH extremes, demonstrating the criticality that transport phenomena plays in kinetic activity. The transport effects at near-neutral pHs are shown when we test the full cell at lower pHs and lower conductivities, showing the effect and importance of the supporting electrolyte for hydroxide-exchange membranes.

[†] Portions of this chapter were previously published as "Fornaciari, J.C.; Weng, L.C., Alia, S., Zhan, C., Pham, T.A., Bell, A.T., Ogitsu, T., Danilovic, N., Weber, A.Z. Mechanistic Understanding of pH Effects on the Oxygen Evolution Reaction. Electrochimica Acta, 2022, 405 139810" and "Kiessling, A., Fornaciari, J.C., Anderson, G., Peng, X., Gerstmayr, A., Gerhardt, M.R., McKinney, S., Serov, A. Kim, Y.S., Zulevi, B., Weber, A.Z., Danilovic, N. Influence of Supporting Electrolyte on Hydroxide Exchange Membrane Water Electrolysis Performance: Anolyte. Journal of Electrochemistry Society, 2021, 168 084512" and are adapted with permission from all co-authors.

3.2 Introduction

As renewable-energy generation grows, it is predicted that there will be an excess of inexpensive electrical energy, and storing this excess electricity in chemical bonds provides a viable pathway for long-duration storage and decarbonizing various energy sectors.[17,24,90–92] The key and often limiting reaction in this process is the oxygen-evolution reaction (OER), which is required as water is the traditional proton source. The OER occurs in multiple environments (e.g., across the pH range) depending on the specific cell and applications.[21,44–46,93–95] Of particular interest is the near-neutral range as it avoids corrosive solutions (strong acids and bases), and is compatible with photoelectrochemical water splitting among other technologies.[90,96–99] Additionally, for high pH (>11), hydroxide-exchange-membrane water electrolyzers (HEMWEs), which can use precious-group-metal-free catalysts and less expensive non-titanium stack components, such as stainless steel, while retaining the beneficial aspects of membrane-based technologies.[100] Although the OER has been studied in various pH conditions, there are is still a lack of mechanistic understanding of how it proceeds, especially when not under highly acidic or alkaline conditions.

The OER is shown in acidic and alkaline conditions in eqs 3.1 and 3.2, respectively.

$$2H_2O \rightarrow O_2 + 4H^+ + 4e^- \qquad 1.23 \text{ vs. SHE} \tag{3.1}$$

$$4HO^- \rightarrow O_2 + 2H_2O + 4e^- \qquad 0.40 \text{ vs. SHE} \tag{3.2}$$

Electrochemical and photoelectrochemical systems have studied the OER by investigating catalyst nanoparticles (films and single- and poly- crystals)[44,45,64,93,101] in half-cell (rotating disk electrode)[93,94,102,103] or full-cell (membrane electrode) experiments.[33,104] These types of studies are used to elucidate the effect of either the electrocatalyst or the electrolyte composition (identity of cations, anions, and pH) on the OER rate. Conventionally, product or reactant transport limitations to or from the reaction site are assumed to be negligible, and experiments are typically conducted at extreme pHs, where there is significant concentration of either H^+ and OH^-. There is a dearth of work at near-neutral pHs, which are especially relevant to photoelectrochemical water splitting and electrosynthesis.

To understand the OER mechanism, density functional theory (DFT) has often been used to determine reaction free energies for different surface states, which provides insight into surface coverage and transition states.[105,106] DFT calculations require specific catalyst surfaces and due to computational complexity are carried out for small system sizes and ideal crystals and for conditions that might not adequately represent experimental ones. In addition, existing DFT calculations largely focus on providing the energy and free energy between different states, while neglecting other important effects, such as adsorbate coverages by different species at the electrode.

Microkinetic analysis can be used to identify limiting steps and evaluate mechanisms. This approach can be combined with DFT and thermodynamic analyses tuned by experimental data for the energy-barrier predictions, since direct measurements of these multi-step processes remains inaccessible. Rates of reaction and surface coverages can be determined by microkinetic analysis and several studies have shown how the rates change with potential and, in some cases, with pH.[95,107] The recent study by Nishimoto *et al.*[107] examined how the kinetics change over the entire

pH range based on an in-depth kinetic analysis for the OER using an iridium oxide electrocatalyst. Their work suggests the O-O bond formation step is the rate-determining step and examines how anode potential impacts the kinetics for acidic, alkaline, and neutral conditions up to a current density of 20 mA cm^{-2}. [107] While many studies have shown the fundamental interactions of adsorbates and ions on catalyst surfaces using theory, modeling, and experiments, the effects of transport are often neglected in these studies.[95,107] Furthermore, the length scales involved in the OER, including the movement of ions near the surface and the actual reactions at the surface, are very different and concomitantly modeled with different approaches; minimal work has been done to bridge the gap between these phenomena, particularly in the neutral to near-neutral range. An initial effort towards this end demonstrated the importance of transport phenomena, in that it shifted the dominant reaction pathway under operation away from the lowest energy one predicted by the reaction barriers alone.[108] For the mid-pH range, transport is expected to perhaps be more important due to the lack of high proton and hydroxide concentrations in the bulk, especially at higher current densities or reaction rates.

Looking at longer length scales, the membrane-electrode assembly (MEA) shows additional hurdles to overcome. HEMs are the crucial component that is currently limiting the performance and durability of HEMWEs. HEMWEs are typically operated with only an anode (anolyte) feed to leverage proton-exchange membrane (PEMWE) systems and ease product separation.[109] When HEMWEs operate with deionized water (DIW) on the anode side, as is standard operation for PEMWEs, their performance (overpotential) and durability suffer.[30,63,110] This is mitigated with the use of supporting electrolytes (SEL), regardless of the HEM chemistry chosen; the most commonly used SELs are KOH and NaOH (at concentrations of up to 1 M) and K_2CO_3.[111,112] While detailed mechanistic understanding of SEL effects is still being investigated, the SEL is hypothesized to: 1) provide additional ion-conducting transport pathways within the pores of the catalyst layer as well as in the HEM ionomer on the anode; 2) change the bulk and local pH in the anode catalyst layer; 3) the SEL anions and cations have been shown to affect the electrocatalysis of the OER in rotating disk electrode (RDE, half-cell measurements) studies.[21,42,113]

In this chapter, we investigate the OER under controlled pH using a rotating-disk electrode half-cell and interpret the results using a microkinetic model, as illustrated in Figure 3.1. Free energies of the different states were calculated using DFT and the barriers from combined thermodynamic, DFT, and experimental studies. The modeling also examines the effects of ionic transport, to obtain a more complete picture of the OER for different pH regimes. Additionally, from the modeling results we are able to see how a full HEMWE system performs under similar conditions at different pHs. The results of this work provide insight into the effects of kinetics and transport and data of the OER across the entire pH range that will aid the design of better electrolytic and photoelectrolytic devices.

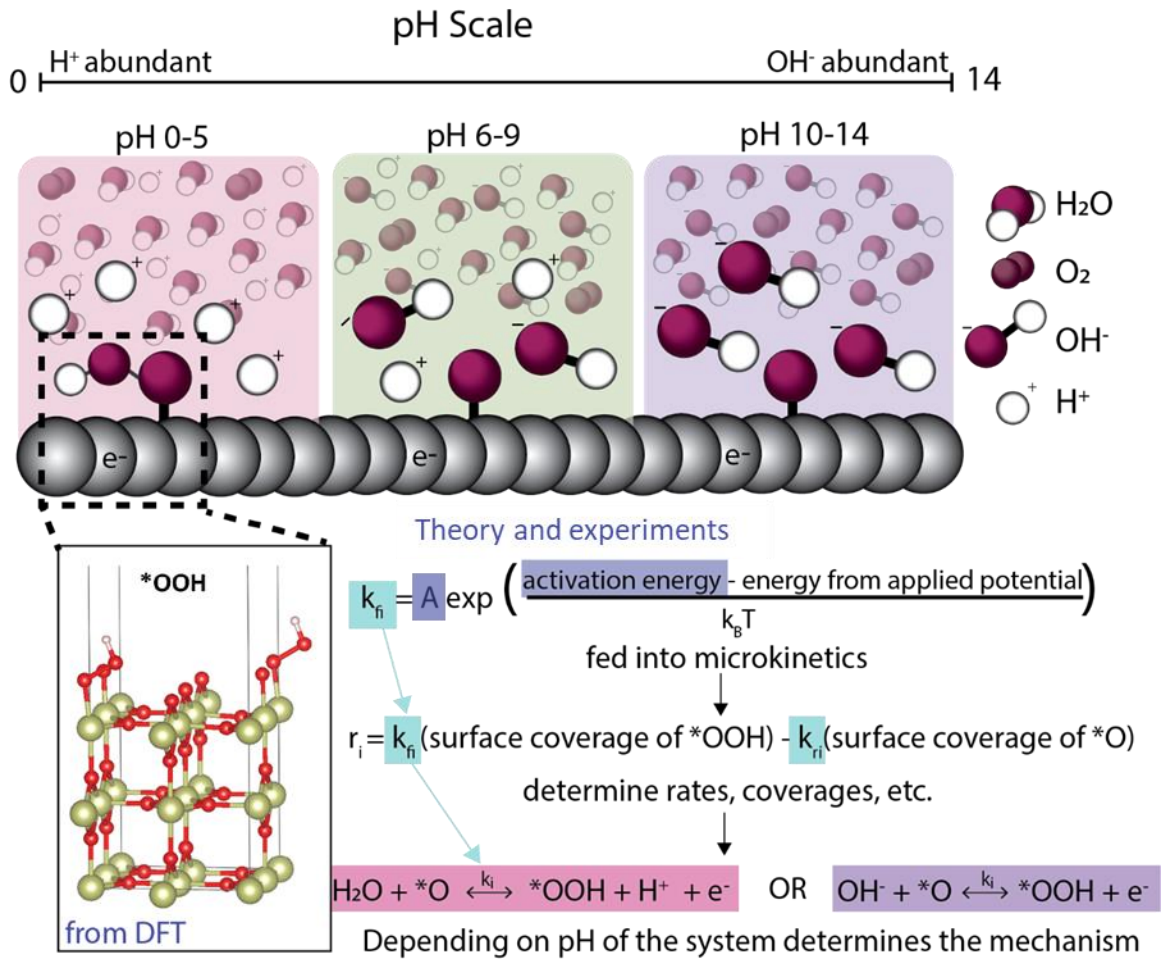

Figure 3.1: A schematic showing the catalyst and the active species for the various pH conditions (counterions are ignored). The surface state of the catalyst is determined by DFT and then is fed into the microkinetics, qualitatively depicted here. The preexponential factor and activation energy was calculated based on theory and experimental data.[114]

Theoretical

3.2.1 Microkinetics

Table 3.1 shows the eight-step kinetic mechanism used for all simulations. The reaction mechanism is based on Nørskov's OER mechanism for both H^+ and OH^- elementary steps.[114,115] All eight steps were considered simultaneously throughout the potential range (1.2 – 2.0 V vs. RHE) and the pH range (0 to 14). In eqs 3.7 thru 3.14, the net rate of formation of species *i* (r_i) is defined by the differences in the rates of the forward and reverse reactions for each of the eight elementary steps. The activity for water (a_0) is assumed to be 1 and the activity for the H^+ (a_{H^+}) is calculated using the bulk pH of the given simulation. The activity for OH^- (a_{OH^-}) was calculated based on the water dissociation constant, using the standard Gibbs Free Energy of reaction, and the activity for H^+.

The surfaces coverages were calculated by

$$\frac{\partial \theta_*}{\partial t} = -r_4 + r_3 - r_8 + r_7 \tag{3.3}$$

$$\frac{\partial \theta_{*OH}}{\partial t} = r_4 - r_1 + r_3 - r_8 \tag{3.4}$$

$$\frac{\partial \theta_{*O}}{\partial t} = r_1 - r_2 + r_5 - r_6 \tag{3.5}$$

$$\theta_* + \theta_{*OH} + \theta_{*O} + \theta_{*OOH} = 1 \tag{3.6}$$

where θ_{*OH}, θ_{*O}, θ_{*OOH} and θ_* denote surface adsorbed species or empty sites. The initial conditions for these ordinary differential equations are $\theta_* = 1$, and an activity of oxygen (a_{O_2}) of zero, as there is no reaction at $t = 0$.

Table 3.1: The mechanism step and the net reaction rate for all eight steps. Acidic steps shown by reactions 1 thru 4 (eqns. 3.7 thru 3.10) and alkaline steps shown by reactions 5 thru 8 (eqns. 3.11 thru 3.14).

Mechanism Step	Net Reaction Rate	
$*OH \leftrightarrow *O + H^+ + e^-$	$r_1 = k_{f1}\theta_{*OH} - k_{r1}a_{H^+}\theta_{*O}$	(3.7)
$H_2O + *O \leftrightarrow *OOH + H^+ + e^-$	$r_2 = k_{f2}a_0\theta_{*O} - k_{r2}a_{H^+}\theta_{*OOH}$	(3.8)
$*OOH \leftrightarrow * + O_2 + H^+ + e^-$	$r_3 = k_{f3}\theta_{*OOH} - k_{r3}a_{H^+}a_{O_2}\theta_*$	(3.9)
$H_2O + * \leftrightarrow *OH + H^+ + e^-$	$r_4 = k_{f4}a_0\theta_* - k_{r4}a_{H^+}\theta_{*OH}$	(3.10)
$OH^- + *OH \leftrightarrow *O + H_2O + e^-$	$r_5 = k_{f5}a_{OH^-}\theta_{*OH} - k_{r5}a_0\theta_{*O}$	(3.11)
$*O + OH^- \leftrightarrow *OOH + e^-$	$r_6 = k_{f6}a_{OH^-}\theta_{*O} - k_{r6}\theta_{*OOH}$	(3.12)
$*OOH + OH^- \leftrightarrow * + H_2O + O_2 + e^-$	$r_7 = k_{f7}a_{OH^-}\theta_{*OOH} - k_{r7}a_0a_{O_2}\theta_*$	(3.13)
$OH^- + * \leftrightarrow *OH + e^-$	$r_8 = k_{f8}a_{OH^-}\theta_* - k_{r8}\theta_{*OH}$	(3.14)

Rate coefficients, free energies, and activation energies are required to define the system. The forward reaction rate coefficients in Table 3.1 can be written as

$$k_{fi} = A \exp\left(\frac{\Delta E_{0V} - \beta n_i eV}{k_B T}\right) \tag{3.15}$$

where A is the pre-exponential factor, β is the transfer coefficient, k_B is the Boltzmann constant, T is the absolute temperature, n_i is the number of electrons in the reaction, eV is the applied voltage, and ΔE_{0V} is the activation energy (ΔE_{0V}) assuming 0 V free energy change. The transfer coefficient describes the activation energy dependence on applied potential, which in theory can be obtained from first-principles simulations. However, in these simulations, the various rate parameters for each reaction were obtained from an analytical model developed by Exner *et al.* that combines DFT calculation and experimental data,[116] and the reaction free energies were computed by first-principles thermodynamics as described below.

The reverse reaction rate coefficient is obtained from DFT calculations and the equilibrium constant,

$$\frac{k_{f_i}}{k_{r_i}} = K_i = \exp\left(\frac{\Delta G_{rxn,0V} - n_i eV}{k_B T}\right), \tag{3.16}$$

where $\Delta G_{rxn,0V}$ is the Gibbs Free Energy of reaction at 0 V calculated using DFT.

To solve the system of equations, the reaction rate constants (eqs. 3.15 and 3.16) were substituted into the reaction rate expressions (eqs. 3.7 thru 3.14) and then into the differential equations for species' coverage (eqs. 3.3 thru 3.6), where were solved simultaneously using MATLAB to predict the current density for the OER given the bulk pH value, the calculated rate constants, and the operating potential. All thermodynamic inputs into the microkinetic model used the DFT results from Lawrence Livermore Laboratory and highlighted in Fornaciari *et al* .[117]

3.2.2 Transport Model

To simulate mass-transport phenomena within the RDE, a two-dimensional, transient, isothermal transport model was used. The model domain consisted of the electrolyte with a boundary of bulk conditions and a rotating disk as shown in Figure S3.1a. The governing equations consisted of the species (H^+, O_2, ClO_4^-, K^+, OH^-) mass balances with the Nernst-Planck equation describing the various transport equations. For the convective velocity to the rotating disk, in both the *z* and *r* directions, a von Karmen and Cochran expression is used. Finally, the rate of reaction for the OER is given based on the local current density as determined from the microkinetic model. All governing equations and associated boundary conditions are in Tables 3.2 and 3.3. The model was solved using COMSOL Multiphysics.

Table 3.2: Transport Governing Equations

Nernst Planck equation, accounting for diffusion, migration and convection for all species, H^+, O_2, ClO_4^-, K^+, OH^-	$$N_i = D_i \nabla c_i - z_i \frac{D_i}{RT} F c_i \nabla \phi_l + c_i v$$	(3.17)
Overall mole balance	$$\nabla \cdot N_i = R_i$$	(3.18)
von Karmen and Cochran velocity profile, in the *z* direction	$$v_z = (\omega \nu)^{\frac{1}{2}} * (-0.5103\gamma^2 + \frac{\gamma^3}{3} - 0.6159\frac{\gamma^4}{6})$$	(3.19)
von Karmen and Cochran velocity profile, in the *r* direction	$$v_r = (r\omega) * (-0.5103\gamma + \frac{\gamma^2}{2} - 0.6159\frac{\gamma^3}{3})$$ Where $$\gamma = \frac{\omega^{1/2}}{\nu} z$$	(3.20)
Rate of reaction for OER, where i_{loc} is obtained from experiments and microkinetics	$$R_i = \frac{-\nu\, i_{loc}}{nF}$$	(3.21)

Table 3.3: Boundary Conditions for the RDE Model

Electrode boundary	$N_{H^+} = \frac{-\nu\, i_{O_2}}{nF}$ $N_{O_2} = \frac{\nu\, i_{O_2}}{nF}$ at the electrode surface
Bulk electrolyte boundary	Axisymmetric at r = 0 r = 5 mm, no flux L = 500 μm, $c_i = c_{bulk}$ L = 500 μm, $\phi_l = 0V$

3.3 Experimental

3.3.1 Cell Materials and Electrolyte Solutions

Tokuyama A201 membrane (28 μm dry thickness) and AS-4 ionomer were used in this study to allow replicable operation with DIW and SEL. MEAs were acquired from Pajarito Powder LLC (PP), (Albuquerque, NM, USA) and received as catalyst-coated membranes (CCMs) using Tokuyama A201 and AS-4 ionomer with loadings of ~0.8 mg_{Ir} cm^{-2} iridium oxide (~150 m^2 gr^{-1}, PP) and 0.5 mg_{Pt} cm^{-2} 50 wt% Pt/C (~130 m_{Pt}^2 gr^{-1}, PP). CCMs were spraycoated using ultrasonic Sono-Tek *ExactaCoat*, loadings and uniformity were characterized by XRF. Respective AS-4 ionomer-to-catalyst ratios were 10 and 15 wt% for iridium oxide and Pt/C electrodes. Prior to testing, CCMs were ion-exchanged to hydroxide form in ~50 mL 1 M KOH at ambient temperature inside a polyethylene bag for 1 hour, rinsed and then mounted into the cell.

Electrolytes were prepared under ambient conditions using Milli-Q water (DIW) and the solutes, KOH, K_2CO_3, and KNO_3. Electrolytes were stored in PET bottles and exposure to ambient air was limited as much as possible whenever electrolytes were connected to the cell or electrolyte conductivity measurements were taken. Electrolyte conductivity and pH were measured using a Thermo Fischer Scientific *Orion Starr A215* pH/conductivity meter with an *Orion 013005MD* conductivity probe and *Orion 8157BNUMD Ross Ultra pH/ATC* triode. Figure 3.2 shows the electrolyte conductivities. Throughout the figures for the cell studies in this chapter, * denotes similar conductivities and § denotes similar pH at 60°C.

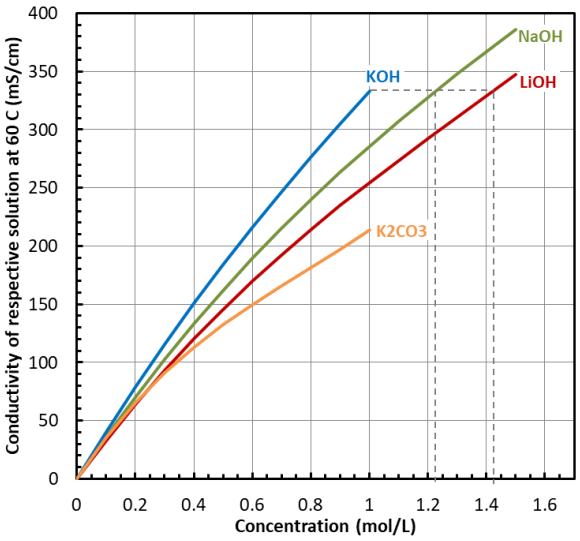

Figure 3.2: Conductivities of SELs used for KOH and K_2CO_3 in addition to others used in Kiessling *et al.*[35]

3.3.2 Cell Preparation

The electrochemical cell used in these experiments was a customized cell procured from NEL Hydrogen (Connecticut, USA), performance was functionally equivalent to the standard Fuel Cell Technologies Inc. (New Mexico, USA) cell. The nominal hardware active area was 25 cm^2, however we isolated it to 5 cm^2 using gaskets. Platinized-titanium serpentine flow fields were used on the anode and graphitic serpentine flow fields were used on the cathode. PTFE gaskets were used for both anode and cathode to assure the cell was sealed completely. Platinum-coated titanium porous-transport layers (PTLs, NEL Hydrogen) were used on the anode and carbon gas-diffusion layers (Toray, Fuel Cell Store, Texas, USA) were used on the cathode to help SEL and gas transport to the catalyst layers. To assure proper sealing, 3.05 N·m was applied using a torque wrench in incremental ~1 N·m steps. Cells were assembled in ambient air.

Cells were connected to a *KNFUSA NFB25 KPOCB-4A* membrane pump at the anode and operated at 5 % of maximum pumping power equaling a flow rate of 22 mL min^{-1}. Cells were heated using a *Digi-Sense TC6500* temperature control and heater to a temperature of 60°C. Heating was never applied when the cell was fully dry but only if there was at least DIW or a supporting electrolyte supplied to the anode side. Electrolytes were indirectly preheated by immersing in beakers and using heating plates (VWR). The cathode inlet remained closed, while the outlet vented into the fumehood for the duration of the entire experiment. Before SEL experiments began, cells were rinsed with DIW to check for leaks.

3.3.3 Cell Testing

When electrolytes were changed, heating was turned off to prevent severe dry out and the feeding tube was removed from the electrolyte bottle. After the tubing was free of electrolyte, the cell was rinsed with up to 4 batches of 500 mL DIW until the conductivity of rinsing water dropped below

1 μS cm^{-1}. DIW rinsing was omitted when the same or highly similar electrolyte at higher concentrations was subsequently used.

Biologic *VMP3B-10* potentiostats were used for polarization curves and electrochemical impedance spectroscopy (EIS) with a 10 A current booster. Cyclic voltammetry from 1.23 to 2 V at 50 mV/s were recorded to assess the MEA before polarization curves were recorded. Polarization curves were recorded at constant currents for each MEA. Thereafter, cell voltage was monitored for 2 minutes before the EIS script was started. EIS was recorded from 1 MHz to 100 mHz with 6 points per decade. Tests for multiple SELs were run for each MEA; to assure MEA degradation was not substantial, 1M KOH was tested in between of other electrolytes and its performance was used to quantify degradation as a baseline.

Polarization curves were recorded at 60°C after some pre-electrolysis to remove any trapped gas or contaminant species in the cell. Typical equilibration time was approximately 2 min, but the time was altered if it was observed that cell voltage did not level off within the 2 min. This time alteration was necessary for the case for nitrate and carbonate containing electrolytes or hydroxide at very low concentrations. For DIW, only currents for voltages <~1.85 V were investigated, and polarization curves has a lower cutoff current of 120 mA cm^{-2} was used. Data was processed using MATLAB. EIS data was automatically fitted to a R-RQ-RQ circuit using the ZFit MATLAB script found online and fits achieved good results.[35]

3.4 Results and Discussion

3.4.1 OER at various pHs

The OER performance via linear sweep voltammetry (LSV) was evaluated across the pH range on commercial iridium oxide nanoparticles as shown in Figure 3.3. These half-cell experiments were accomplished while holding the bulk pH constant, which was achieved through titrating the electrolyte. It should be noted that the bulk electrolyte conditions, which are monitored through titration, are taken as the RHE baseline. In the acidic and neutral range, Figures 3.3a and b, increasing pH seemingly results in worse performance in terms of a lower current density for a given potential. For higher pH shown in Figure 3.3c, however, the trend is not monotonic. Figure 3.3d compares the neutral (pH = 9), acidic (pH = 1), and alkaline (pH = 13) cases. From that figure, it is readily apparent that at low current densities the more neutral pH demonstrates more current for a given potential, although this better performance disappears at higher current density, where the high and low pH yield more current than the pH = 9 case.

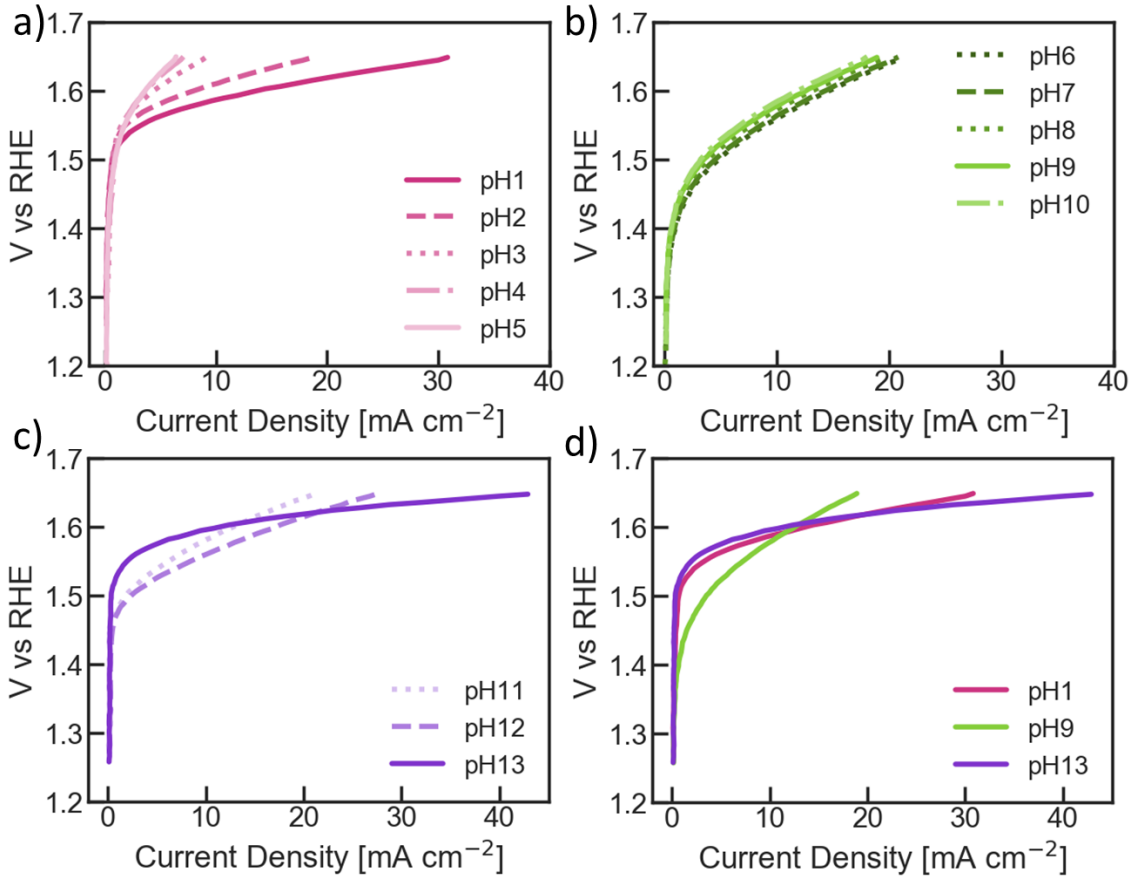

Figure 3.3: Linear-sweep voltammograms shown for (a) acidic pH (1 thru 5), (b) neutral to near neutral pH (6 thru 10), and (c) alkaline pH (11 thru 13). The most acidic and alkaline pH's, 1 and 13, respectively, and pH 9 are shown in comparison (d) and are investigated as representative cases in the modeling sections throughout this chapter.

Figure 3.4 provides a different perspective on this unexpected outcome by displaying the experimental and the simulation results for four different scenarios: (a) low current density, (b) high current density, (c) low potential, and (d) high potential. As shown in Figure 3.4a, at 2 mA cm^{-2}, and in Figure 3.4c, it is clear that the more neutral pH range demonstrates increased performance compared to either pH extreme. Interestingly, in all of curves, the performance (either current density at fixed potential or potential at fixed current density) demonstrated a seeming discontinuity around pH = 6. This is particular seen when examining performance at fixed potential (Figure 3.4c, d), where the current density initially decreases with increasing pH, then exhibits an increase around pH = 6 followed by a decrease again. As discussed later, this pH results in ideal conditions for both acidic and alkaline reactions mechanisms to occur. The seemingly large increase in performance at pH 6 is interesting, and was consistent throughout these experiments. Further experiments, perhaps with buffers, is required to understand fully the reasons for this value, which may stem from the sensitivity to logarithmic nature of pH and near neutral conditions. However, at higher current density (Figure 3.4b) or higher potential (Figure 3.4d), this trend is reversed with the extreme pH's outperforming the middle pH range, which is somewhat consistent with literature,[118,119] although in that case the alkaline provided the highest current density for a

given potential. This discrepancy can perhaps be related to the way in which those systems used buffers instead of titration to maintain pH, as was done here. Although beyond the scope of the current study, the use of buffers could lessen the impact of the pH changes during operation, however this will depend on device design, buffer concentrations, current density, etc.; surface pH would still vary due to interplay between buffer reaction rates and capacities and generation rates, as seen in simulations for CO_2 electrolysis in RDEs.[120] Finally, it should be noted that the low current-density comparison (Figure 3.4a, c) aligns nicely with the expected low current densities and need for near neutral pH (to avoid degradation) in photoelectrochemical water-splitting and related solar-fuel technologies.[117]

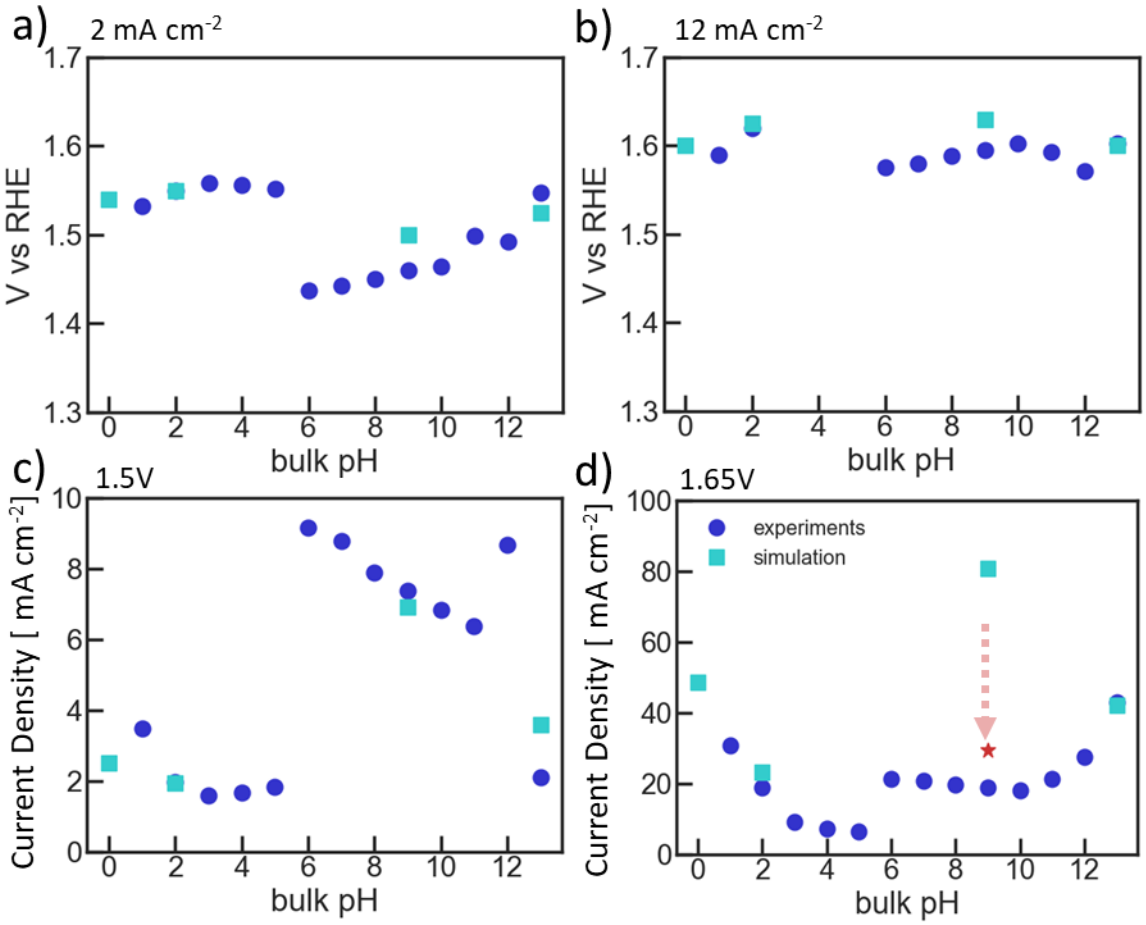

Figure 3.4: Oxygen-evolution overpotential as a function of bulk pH, for iridium oxide nanoparticles from experiments (circles) and simulations (squares). The potentials were reported at current densities of (a) 2 mA cm^{-2} and (b) 12 mA cm^{-2}. The current densities were reported at corresponding voltages of (c) 1.5 V and (d) 1.65 V. The pH's used in the simulation are pH 0, 2, 9, and 13. The red star indicates the pH at the surface of the electrode, 2.34, determined by the transport model with a bulk pH of 9.

To further interpret the data, simulations were carried out for several different pHs at low and high current densities (applied potentials). As shown in Figure 3.4, decent agreement was realized with the model except for pH 9 at 1.65 V (>20 mA cm^{-2}) (see Figure 3.4d). To ascertain the cause of

the discrepancy, a transport model of the RDE was used to explore how the local pH at the reaction site varies as a function of bulk pH, especially since the bulk pH was held constant by titration. As shown in Figure 3.5a, the local pH at 13 and 0 is the same as the bulk, but at pH 9 it deviates quite significantly, changing by orders of magnitude as the current density (applied potential) increases. Figure 3.5b shows that virtually all of this change occurs within the mass-transfer boundary layer near the electrode surface, which can be varied to modulate the pH (see Figure S3.2). Accounting for this concentration-polarization effect shifts the simulation at pH 9 to be in better accord with the experimental data, as shown in the translated point in Figure 3.4d following the arrow from the square to the star.

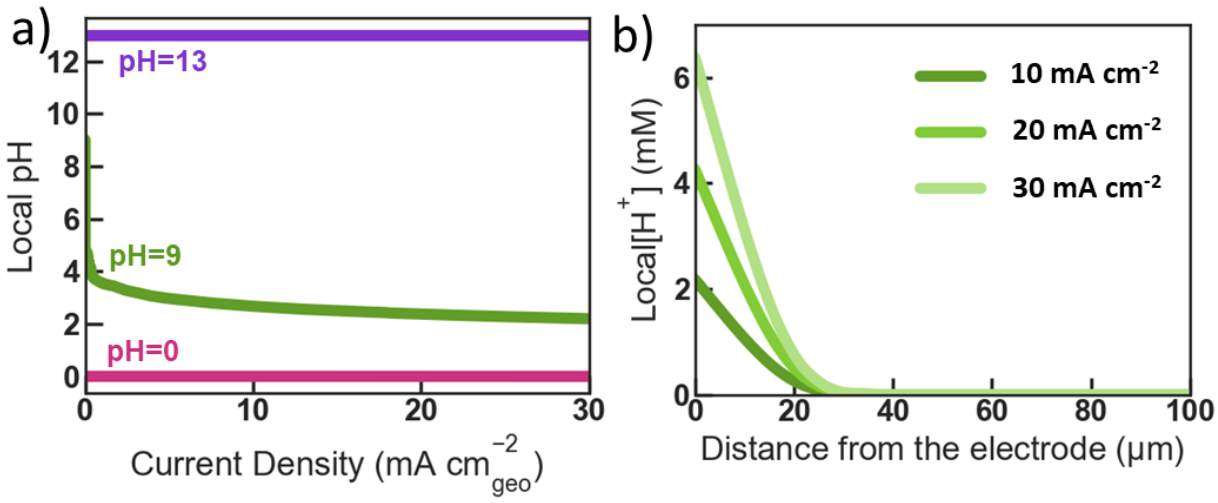

Figure 3.5 (a) the local pH as a function of current density for pH 0, 9 and 13. (b) The local proton concentration as a function of distance from the electrode at pH 9.

3.4.2 Microkinetic Analysis of the OER

To understand the trends in Figures 3.3 and 3.4, microkinetic simulation results are used to ascertain the rate-determining step(s) via a perturbation analysis. The analysis entails perturbing each individual reaction-rate constant by a small amount (~0.1%) and calculating the net change in the overall reaction rate or current density (see Figure S3.3 for the individual reaction rate plots). Figure 3.6a-c shows the results from the perturbation analysis at three different pHs: 0, 9, and 13, respectively. For pH 0, two different rate-determining steps are identified at low applied voltages, namely *OOH formation (eqn. 3.8) and O_2 formation (eqn. 3.9). However, at higher potentials (> 1.6V), only one rate determining step occurs, *OOH formation (eqn. 3.8), which is related to the change in the surface coverages at higher potential and agrees with previous studies.[116,121] For pH 13, shown in Figure 3.6c, the rate-determining step is clearly *OOH formation (eqn. 3.12). It is interesting to note that this rate-determining step persists to relatively low pH, owing perhaps to the use of converting OH^- and not needing to break the H-OH bond in water.

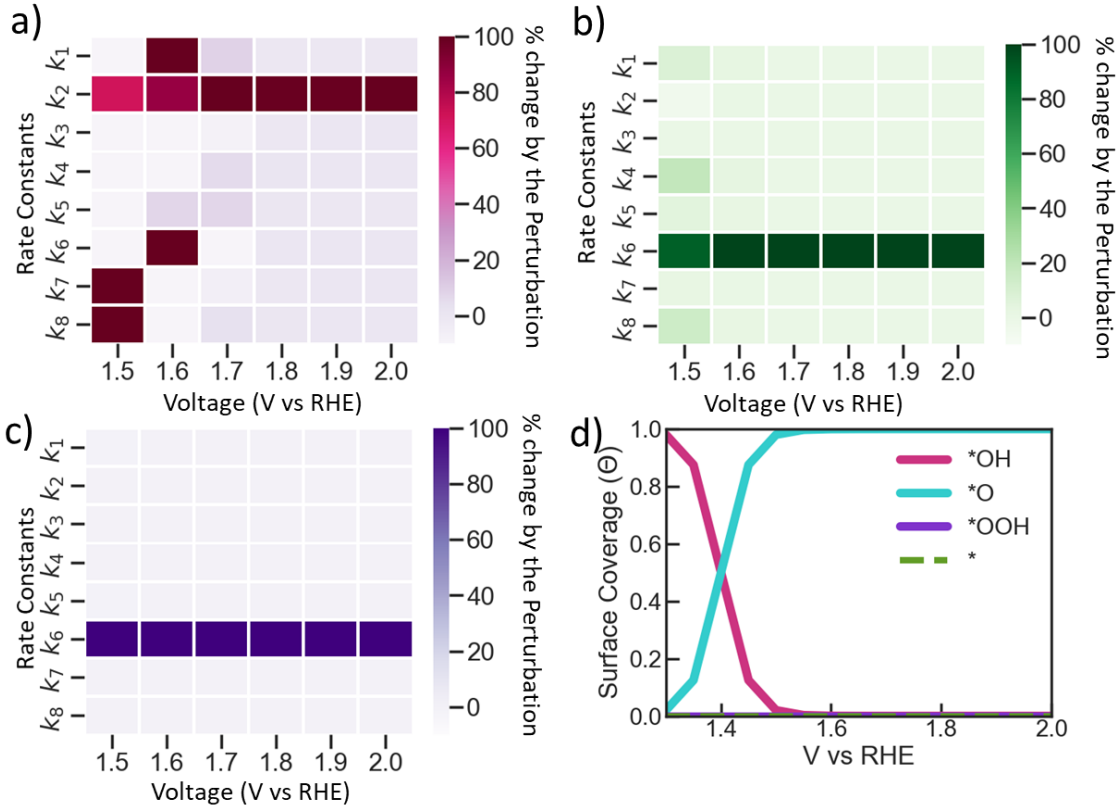

Figure 3.6: The percent change in current density relative to that of the perturbation (0.1% change of the forward rate coefficient) on each of the eight forward rate coefficients at different applied potentials, 1.5 to 2 V, for a) pH 0, b) pH 9, and c) pH 13. 100% change represents that the overall current density (rate) changed by the same amount as that of the 0.1% perturbation. d) Surface coverage from 1.3 to 2.0 V vs RHE for all pHs.

At neutral pH, both acidic and alkaline mechanisms may occur appreciably, with the alkaline pathway slightly dominating (eqn. 3.8 and 3.12) as shown in Figure 3.6b and Figure S3.4 from perturbation analysis and extent of reaction analysis, respectively. This finding also helps to rationalize the enhanced low current-density performance at neutral pHs. It is also consistent with the change in Tafel slope at middle pHs (see Figure S3.5), which suggest a mechanistic change is occurring. Although the Tafel slope does increase for the middle pH range, the onset potential is lower than at the extreme pHs, as explained by the above rate-limiting step changes. Furthermore, at low overpotential for near-neutral pH, it is also believed that in addition to having both types of charge carriers, there may also be altered adsorption/desorption, as suggested by the increased response at low potential (< 1.5 V) in the cyclic voltammograms (see Figure S3.6) and in Figure 3.6d for the surface species. This influence goes away at higher current densities where the local microenvironment changes to be much more acidic. This increased response may result in differences in intermediate binding, the rate-determining step, or transition-state energy, and are not reflected in the DFT or microkinetics herein; to verify such surface coverages *operando* requires careful ambient pressure XPS measurements in conjunction with more detailed theoretical calculations.[122–124] Finally, it should be noted that for these comparisons the local pH is being

interrogated and, as mentioned above, this deviates more to lower pH for near neutral bulk pH due to species transport.

3.4.3 Full-Cell Operation at Near-Neutral to Alkaline Conditions

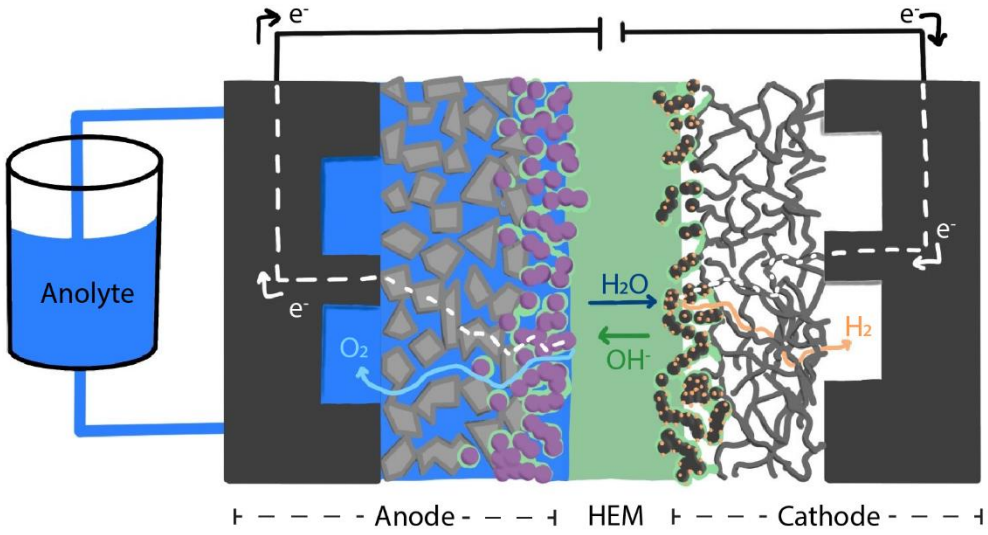

Figure 3.7: HEMWE sketch; Abbreviations: PTL – porous transport layer, CL – catalyst layer, HEM – hydroxide exchange membrane, anolyte – anodic supporting electrolyte. OER is performed in the anode CL and HER in the cathode CL.

To determine the consistency of these fundamental findings in real systems, full-cell testing, the diagram shown in Figure 3.7, of HEMWEs was accomplished. Testing these systems helps elucidate how feeding a bulk SEL influences the practical system. Ideally HEMWEs would operate on pure water, and thus neutral conditions. While the Tokuyama A201/AS-4 system used in this study is a relatively old chemistry,[29] it often serves as the baseline and compared with emerging HEM systems (Fumion, Sustanion, Ionomr (AEMION), Orion, Versogen (PIPERION), LANL, and Georgia Tech (PENTION)).[30,31,112,125] Operating with DIW solely utilizes catalyst sites covered with the HEM ionomer, in our case AS-4. However, in all cases, when HEMWEs operate with DIW, their performance (overpotential) suffers. We show this tradeoff between electrolytes for the Tokuyama MEAs in Figure 3.8, where we compare DIW and 1 M KOH anolytes. Note that current ranges from 0 to 50 mA cm^{-2} are referred to as kinetic region and from 250 to 2000 as ohmic region throughout this section. For each of the polarization curves, the numbers in parentheses give the order of conducted experiment. Intermediate KOH curves from the test series were omitted whenever they did not provide any additional insights to decrease plot clarity.

First, the performance of the 1 M KOH HEMWE is nearly equivalent to PEMWE operation on Nafion™ 117 (N117), achieving roughly 2A cm^{-2} below 2V.[41] Next, after adequate circulation of DIW as anolyte a polarization curve was obtained, there is a ~150 mV penalty at 250 mA cm^{-2} and high current densities are not sustainable as with SELs. The inset in Figure 3.8 shows that the kinetics of the reaction are severely affected, with a 150 mV overpotential increase, which can be attributed to a combination of reaction mechanism (based on the slope change) and

electrochemically active surface-area changes. Figure S3.7 shows the HFR and polarization resistance obtained during the testing. As the plots show, both the polarization and the HFR are much higher while operating in DIW. Interestingly the ohmic resistance decreases with increasing current density, which is starting to approach the KOH anolyte condition. One would expect the opposite trend in ohmic resistance; if dehydration of the polymer were occurring at higher current densities via electroosmosis. However, it is not enough to overcome the kinetic limitation. After operating on DIW and returning to 1 M KOH operation, there is irreversible degradation in the MEA, suggesting that the onset of degradation is swift, even though the voltage and current used to operate on DIW were low and cumulative capacity throughout was much smaller than for 1 M KOH. While rigorous durability assessment is beyond the scope of our study, it has been suggested that the durability of HEMWEs is affected not only by alkaline stability but also electrochemical stability of HEM and ionomer.[32,34] Clearly an SEL is important at least with this polymer/ionomer materials set, to overcome kinetic limitations, presumably imposed solely at the anodic side of the cell.

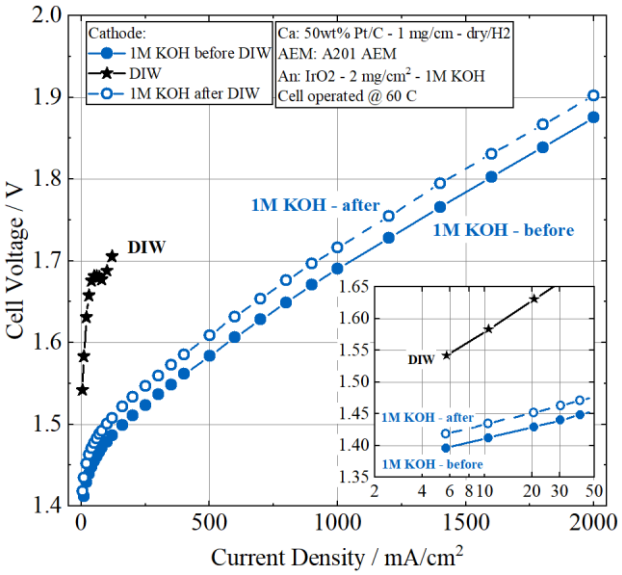

Figure 3.8: Polarization curves showing kinetic (inset, Tafel plot) and ohmic regions for DIW and KOH anolyte feeds. Current density range of DIW was limited so as to try and suppress HEM degradation.

Based on half-cell measurements in literature and above, the electrolyte anions and their concentration also play a role in the OER.[117,126] At the same time, K_2CO_3 is frequently used as an SEL in HEMWE's, but the role of the carbonate anion on the charge carrying species in the membrane is poorly understood.[127] Especially compared to HEMFCs where it is detrimental to membrane conductivity. We compare the SELs at the same conductivity and the same pH in order to elucidate the difference between the anion's themselves on the full-cell performance. To match conductivities, a concentration of 0.5 M instead of 1 M KOH was used because if we had had matched for conductivity with 1 M KOH, the K_2CO_3 solubility limit would have been exceeded. Thus, K_2CO_3 at 0.82 M was compared with 0.5 M KOH for nearly equivalent conductivity (189 mS cm^{-1}) but different pH (11.35 and 13.65, respectively) at 60°C; and with 18 mM KOH at

the same solution pH (11.22), but different conductivities (189 and 7.4 mS cm^{-1}, respectively). To note, we are looking at pH 11 which is slightly more basic than we previously explored above in Figure 3.3, but the concentration of charge carriers still is decreased compared to pH 13 or 14. Additionally, we are not accounting for changes in osmotic pressure or activity, which are beyond the scope of our study.

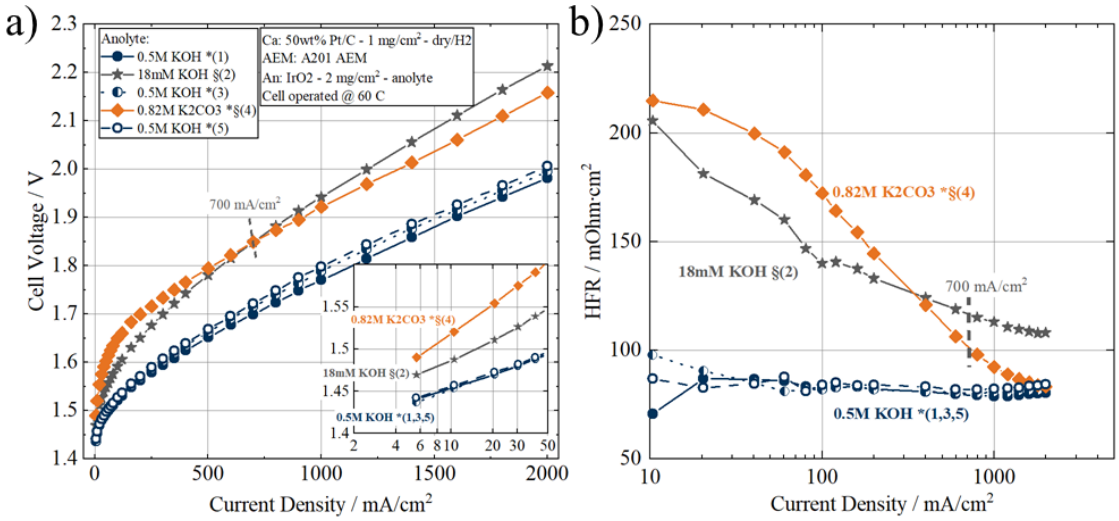

Figure 3.9: (a) Polarization curve showing the kinetic (inset, Tafel plot) and ohmic regions and (b) HFR resistances; for carbonate and hydroxide solutions. Numbers in brackets indicate the order in which the experiments were conducted consecutively, * denotes similar conductivities and § denotes similar pH at 60°C.

First, looking at just the effect with a hydroxide anion of decreasing conductivity (and pH) of KOH in Figure 3.9a, the cell voltage increased going from 500 to 18 mM KOH. This increase intuitively makes sense, as the SEL's OH^- charge carrying species is decreased and even in the RDE we see a lower performance for pH 11 compared to pH 13.5. The HFR plot in Figure 3.9b also supports this finding, showing an increase in HFR at low current densities that increases linearly until it almost matches that of the 0.5 M KOH at higher current density, similar to what was found for pure DIW (Figure 3.8). At the same time the kinetics are slowed, with an almost 50 mV increase corresponding to the pH and conductivity decrease (Fig 3.9a inset). Decreasing the pH, regardless of anion (18 mM KOH and 0.82 M K_2CO_3), decreased the performance at relevant voltages explored, even though the 0.82 M K_2CO_3 solution conductivity is the same as the 0.5 M KOH. This result implies that the higher pH may have a greater degree of influence on performance over that of solution conductivity, or that there is a secondary effect as the cation/hydroxide ratio is also changing. Comparing the differences between carbonate and hydroxide at the same pH the major difference is in the kinetic region (Figure 3.9a inset), where the KOH outperformed K_2CO_3 by 25 mV. The HFR behaved similarly, starting high and decreased with increasing current density, as shown in Figure 3.9b. These two lower pH tests show HFR approaching that of the higher pH test (0.5 M KOH). Examining the polarization curve, the 0.82 M K_2CO_3 is worse than 18 mM KOH at low current densities, but exceeds the hydroxide SEL at high ones. Since the kinetics of both the low pH SELs remained poor even at high current density, where the HFR matches the 0.5 M KOH, the full-cell performance trend remains.

We hypothesize that there are several effects occurring. First, the concentration, pH and conductivity change of the KOH solution results in both kinetic (Tafel region) and polarization (from impedance at higher currents) loss from a decrease in charge carrying species, thereby allowing more access to the catalyst surface area. Second, the lower anode SEL conductivity results in higher HFR of the full-cell. This intuitively makes sense, the lower the hydroxide concentration and conductivity, the lower the full-cell performance. Third, even though the conductivity of the carbonate SEL is the same as the 0.5 M KOH, there is a significant loss in HFR of the full-cell (Figure 3.9b). The HFR improves with increasing current density matching that of 0.5 M KOH. This may be due to due to self-purging effect.

As current increases, the ohmic resistance can change due to self-purging of CO_3^{2-} and NO_3^-. This self-purging effect occurs at high current densities, when the high hydroxide flux removes other anions (e.g. CO_3^{2-} and NO_3^-) from the HEM at the anode and replaces them with hydroxide from the cathode.[57,128] The result is a recovery of high HEM conductivity and a decrease in HFR.[29,35,109] At high current densities, the HFR decreases for CO_3^{2-} and NO_3^-, however only the CO_3^{2-} matches the 0.5 M KOH HFR, while remaining more than twice as high for NO_3^-. This is because CO_3^{2-} (and NO_3^-) can be removed from the anode SEL after self-purging by forming CO_2 via eq. 3.22 and 3.23.

Carbonate: $$CO_3^{2-} + H_2O \rightarrow HCO_3^- + OH^- \quad (3.22)$$

Bicarbonate: $$HCO_3^- + H_2O \rightarrow H_2CO_3 + OH^- \quad (3.23)$$

Additionally, local pH can change due to the consumption of OH^-. The change in local pH can yield more CO_2 as time increases. CO_2 may then follow the oxygen gas flux towards the PTL end of the electrode. This mechanism dissipates the accumulation of CO_3^{2-} near the electrochemical interface at the anode allowing faster OH^- flow (depicted in Figure 3.10). This might have kinetic implications as well, since the CO_2 evolution could affect the kinetics at reaction sites for OER, i.e. why the polarization resistance is three times higher than OH^- at the same flux through the membrane supporting a lower cell voltage. Whereas NO_3^- has no pathway for removal and accumulate at the interface slowing OH^- flow via repulsive interactions. A concentration gradient would build for NO_3^- which could drive these ions into the membrane via back diffusion.

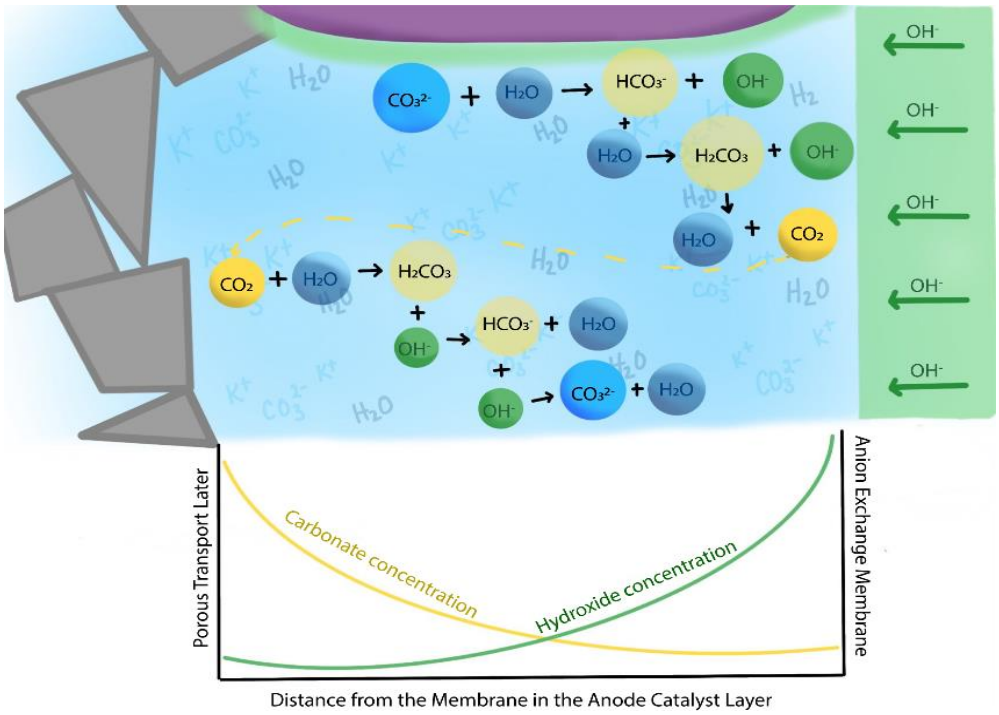

Figure 3.10: Qualitative concentration profiles of carbonates and hydroxides within the HEM anode catalyst layer.

3.5 Summary

In this chapter, microkinetics, transport modeling, and cell testing provide a multiscale picture of the oxygen-evolution reaction (OER) over a large pH range. This analysis provides informative findings for acidic and alkaline electrolyzers and near-neutral photoelectrochemical systems at operating current densities <100 mA cm^{-2}. For near-neutral pH systems at low current densities or applied potential, enhanced performance is witnessed due to the availability of both acid and alkaline reaction pathways, as shown via a perturbation analysis. However, at higher current densities, transport dominates and the local pH rapidly drops at the electrode surface as shown via transport modeling. We determined that the local pH deviates significantly from the bulk pH for cases of intermediate pH, and decreases significantly near the anode. Additionally, for low (pH=11) and high (pH=13) pH values, they performance is similarly at higher applied potentials and current densities. Through the perturbation analysis and evaluating the surface coverage, we demonstrate that there is only one rate determining step for the three pHs at these higher potentials. For full-cell testing, transport of species at relevant current densities are limiting when the pH decreases; further work can be done in understanding counter ions near the surface of the catalyst. The findings of this chapter will assist in designing more efficient electrochemical and photoelectrochemical systems that address the observed transport limitations.

Supplemental Information

The transport modeling for the rotating disk electrode was model in COMSOL Multiphysics and the modeling domain and geometry is shown in Figure S3.1.

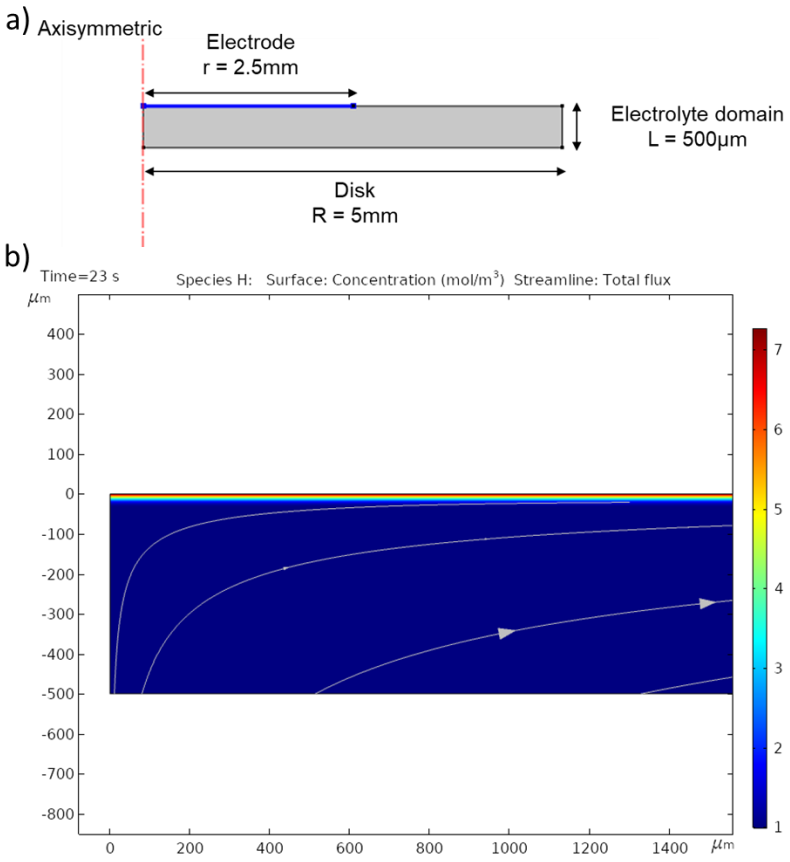

Figure S3.1: a) Model geometry for the transport equations b) Surface species concentration for the total flux of protons at the disk.

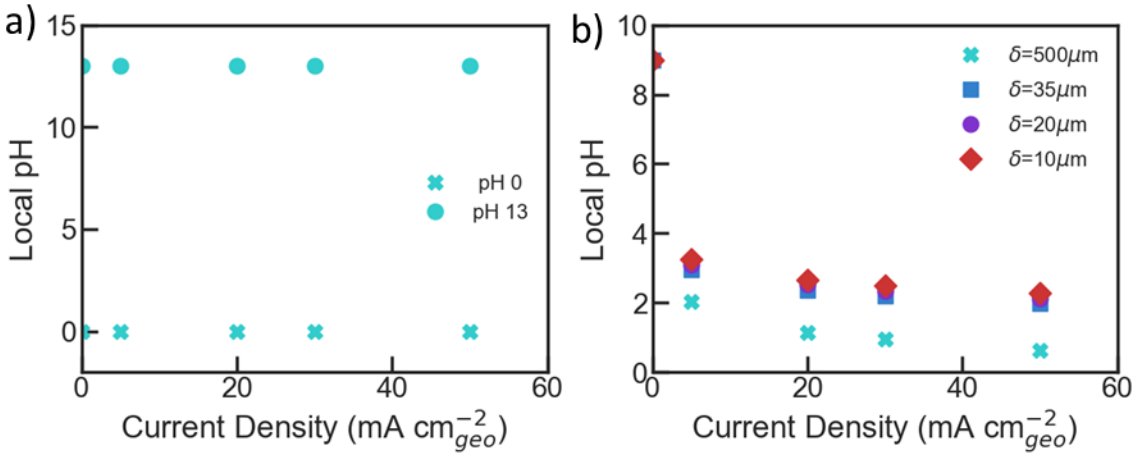

Figure S3.2: The impact of current density and boundary-layer thickness on local pH at (a) pH change for 500μm boundary layer thickness for pH 0 and pH 13 and (b) pH 9 for varying boundary-layer thicknesses

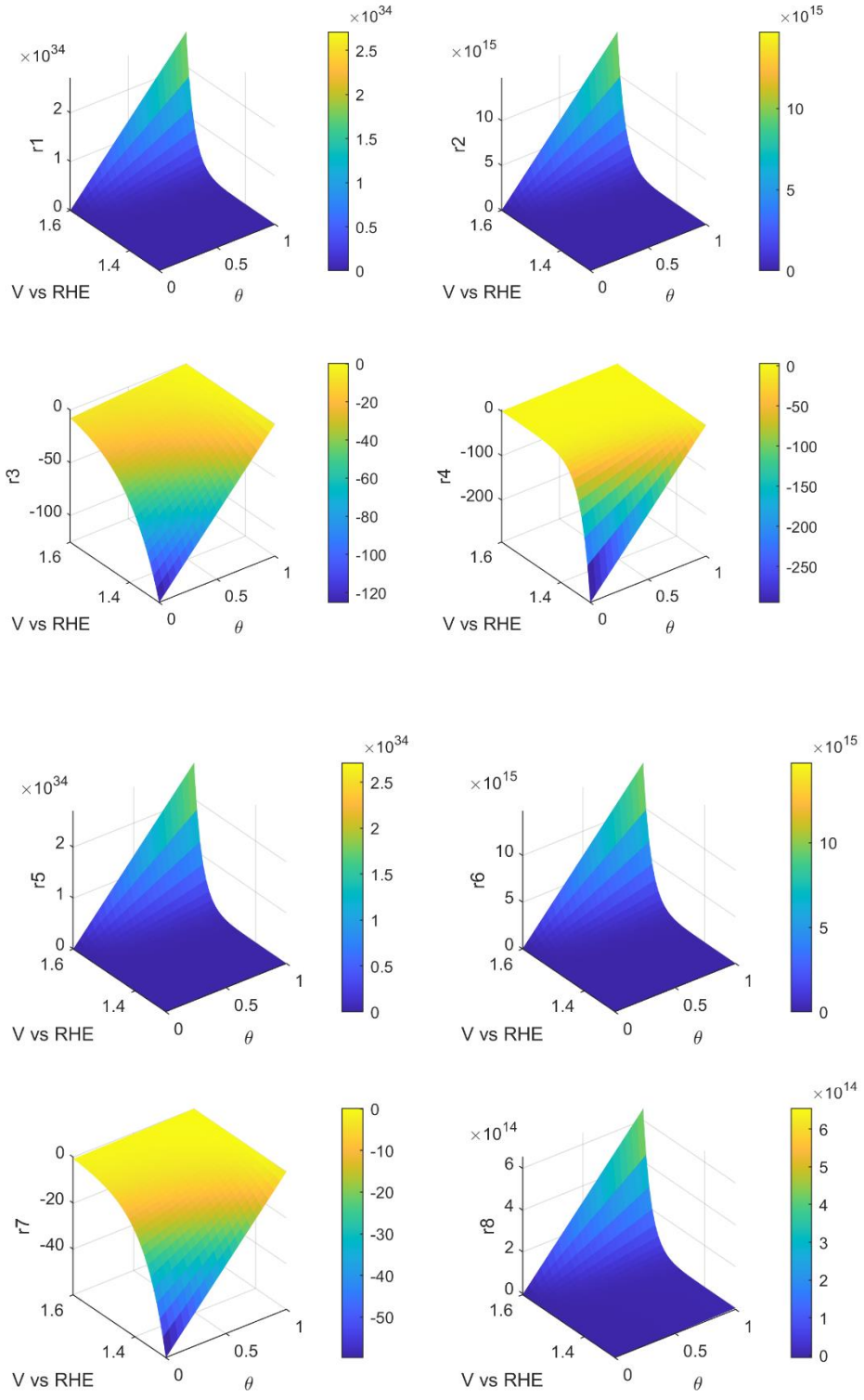

Figure S3.3: 3D plots for each individual rate of reaction ($r_1 - r_8$)

	V vs RHE	1.3	1.4	1.5	1.6	1.7	1.8	1.9	2
pH0	* --> *OH	1	1	1	1	1	1	0.98	0.04
	*OH --> *O	1	1	1	1	1	1	1	1
	*O --> *OOH	2E-04	1E-06	9E-09	7E-11	6E-13	4E-15	4E-17	3E-19
	*OOH --> *	0.12	3E-06	6E-11	1E-15	3E-20	6E-25	1E-29	7E-33

	V vs RHE	1.3	1.4	1.5	1.6	1.7	1.8	1.9	2
pH9	* --> *OH	1	1	1	1	1	1	0.46	0.002
	*OH --> *O	1	1	1	1	1	1	1	1
	*O --> *OOH	4E-05	1E-07	5E-10	3E-12	1E-14	6E-17	3E-19	1E-21
	*OOH --> *	0.44	3E-05	1E-09	4E-14	1E-18	5E-23	4E-27	4E-29

	V vs RHE	1.3	1.4	1.5	1.6	1.7	1.8	1.9	2
pH13	* --> *OH	1	1	1	1	1	0.94	0.03	5E-05
	*OH --> *O	1	1	1	1	1	1	1	1
	*O --> *OOH	7E-04	3E-06	2E-08	8E-11	4E-13	2E-15	9E-18	4E-20
	*OOH --> *	0.03	9E-07	3E-11	1E-15	4E-20	2E-24	2E-27	4E-29

Figure S3.4: Extent of reaction for pH 0, 9, and 13.

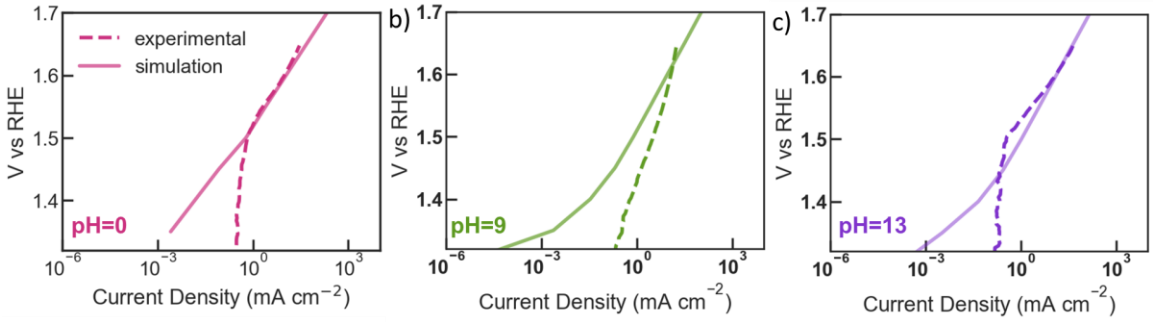

Figure S3.5: Tafel slopes for (a) pH = 0 (b) pH =9 (c) pH = 13. Dashed lines are experimental values, solid lines are the microkinetic model. The change in slope for the experimental data and large mismatch at lower current densities is due to capacitance effects that are not considered in the microkinetics.

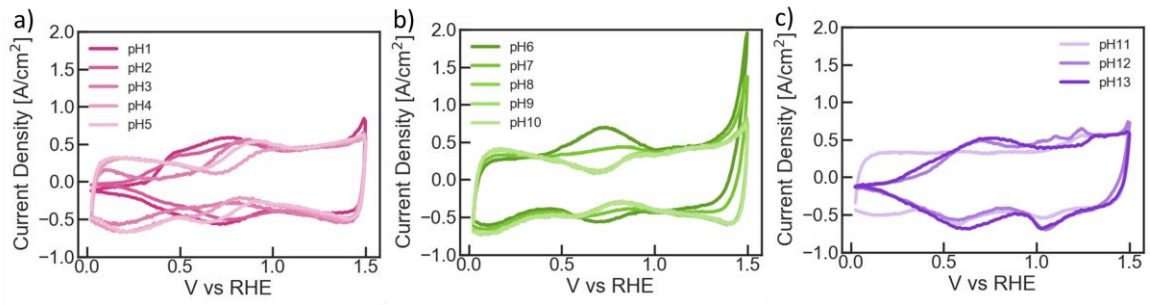

Figure S3.6: Cyclic voltammograms for iridium oxide at (a) pH 1-5, (b) pH 6-10, and (c) pH 11-13

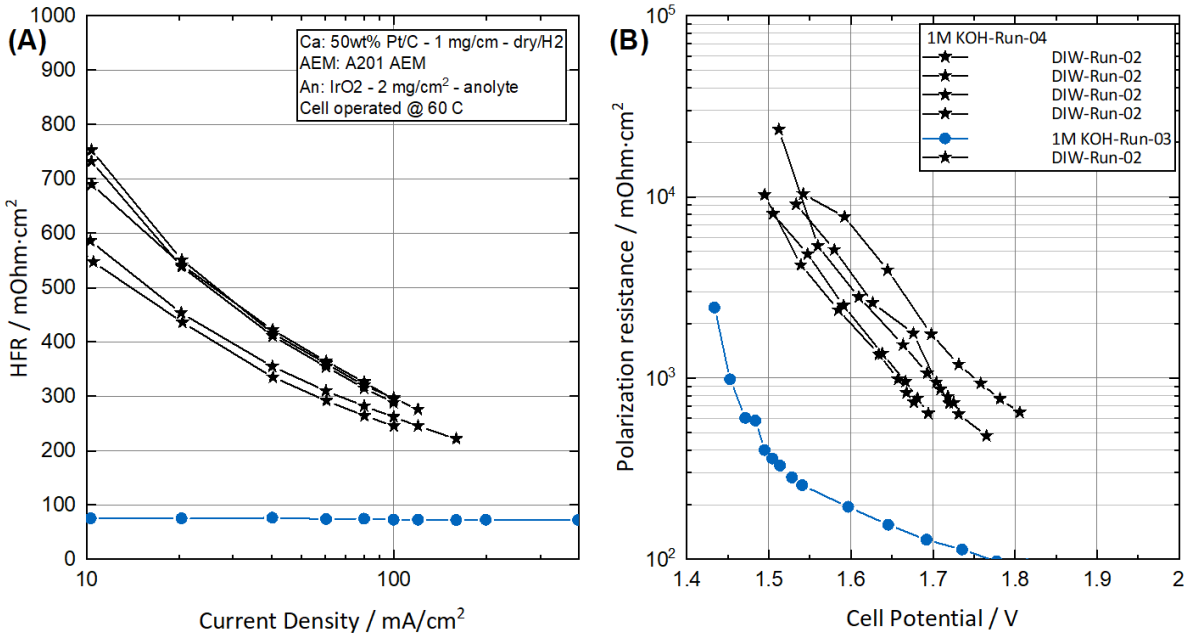

Figure S3.7: HFR and polarization curves for DIW and KOH anolytes at 60 ºC. 1.0 M KOH was flown first, followed by DIW, then KOH again.

4. The Role of Water in Vapor-fed Proton-Exchange-Membrane Electrolysis[†]

4.1 Abstract

Water-vapor-fed electrolysis, a simplified single-phase electrolyzer using a proton-exchange membrane-electrode assembly, achieved >100 mA cm^{-2} performance at <1.7 V, the best for water-vapor electrolysis to date, and was tested under various operating conditions (temperature and inlet relative humidity (RH)).To further probe the limitations of the electrolyzer, a mathematical model was used to identify the overpotentials, local water activity, water content values, and temperature within the cell at these various conditions. The major limitations within the water-vapor electrolyzer are caused by a decreased water content within the membrane, indicated by increased ohmic and mass-transport losses as observed in applied-voltage breakdowns. Further investigations show the water content (λ, mole of water/mole of sulfonic acid) can decrease from 13 at low current densities down to 6 at high current densities. Increasing the temperature or decreasing RH exacerbates this dry-out effect. Using the mathematical model, we show how these mass-transport limitations can be alleviated by considering the role of water as both a reactant and a hydrating agent. We quantify how low cathode RH can be tolerated as long as the anode RH remains high, showing equivalent performance as symmetric RH feeds.

[†] Portions of this chapter were previously published as "Fornaciari, J.C.; Gerhardt, M.R.; Zhou, J; Regmi, Y.N.; Danilovic, N; Bell, AT; Weber, A.Z. The Role of Water in Vapor-fed Proton-Exchange-Membrane Electrolysis. Journal of the Electrochemistry Society, 2020, 167 104508" and are adapted with permission from all co-authors.

4.2 Introduction

Hydrogen is garnering increasing attention for multiple applications, such as heavy-duty transportation and long-term storage of electrical energy.[16,18,62,129,130] Green hydrogen can be produced from renewable electricity via water electrolysis, where the half-reactions are the oxygen-evolution reaction (OER) and hydrogen-evolution reaction (HER)

$$2H_2O \rightarrow O_2 + 4H^+ + 4e^- \qquad U = 1.23\ \text{V vs SHE}, \tag{4.1}$$

$$4H^+ + 4e^- \rightarrow 2H_2 \qquad U = 0.00\ \text{V vs SHE}. \tag{4.2}$$

at the anode and cathode at standard conditions and in an acid environment, respectively. Recent studies have shown that high current densities (up to 5 A cm^{-2}) can be achieved using a membrane-electrode assembly (MEA), shown in Figure 4.1.[21,28,131]

The MEA comprises a solid-state electrolyte, typically a proton-exchange membrane (PEM), catalyst layers, and diffusion or transport media. Each component assists in transporting the reactants/products and protons and electrons to/from the reaction sites.[21] The MEA architecture, which originated from polymer-electrolyte fuel cells, optimizes mass and ohmic transport through its various porous layers and enables use of high-surface-area catalysts within the porous catalyst layers, while concomitantly minimizing cell ohmic losses through the use of thin, conductive PEMs.[131–133] Thus, it is a preferred design for use in vapor electrolysis.

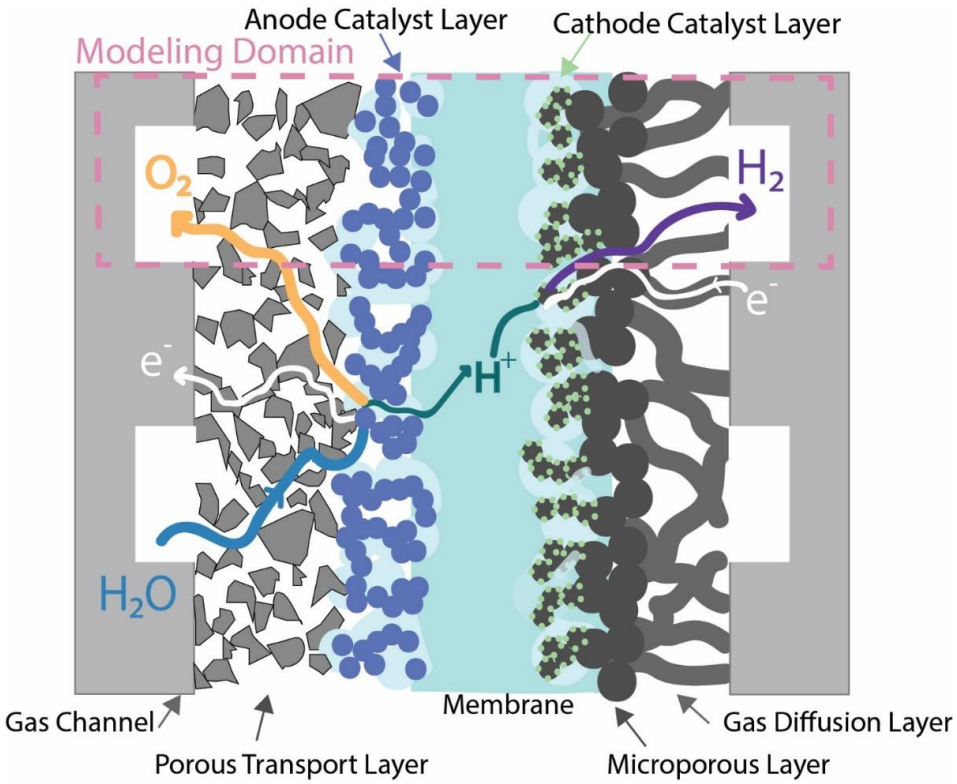

Figure 4.1: Cell schematic of the vapor electrolyzer MEA

Conventional electrolyzers utilize liquid water, which needs to be ultra-pure because contaminants can poison and degrade the electrocatalysts and the membrane.[134,135] Moreover, liquid-fed electrolyzers exhibit a high electro-osmotic flow of water from anode to cathode, which results in a saturated hydrogen stream that must be dried before compression and storage.[21] Furthermore, the use of this architecture for more complex reactions (e.g., carbon dioxide or nitrogen reduction) encounters problems due to the low solubility of the gaseous reactants.[37,136] Another issue is that bubble formation in liquid feeds can introduce transport problems and light scattering when the MEA architecture is used for photo-electrochemical water splitting.[98,137,138] The above issues can be ameliorated by using a water-vapor instead of a liquid-water feed.

Vapor-fed electrolysis significantly simplifies the physics and operation of MEA cells. It also provides the opportunity to use non-conventional water inputs, such as seawater-vapor,[139,140] and opens up the possibility of electrolysis in semiarid regions or locations where clean liquid water is not readily accessible.[141] Compared to liquid feeds, operating with water vapor is expected to result in significant mass-transport and nonlinear ohmic limitations, with the latter stemming from decreased membrane and ionomer hydration with water vapor due to the dependence of ionic conductivity on hydration for traditionally used proton-exchange membranes like Nafion.[142,143] There have been limited investigations of water-vapor fed electrolysis. The systems reported to date exhibit stable performance for several hours but low current densities (<100 mA cm^{-2}).[137,138,140,144] Therefore, there is a need for detailed exploration of the possibilities and limitations of this operating paradigm, especially as it concerns the interplay of water consumption, diffusion, and electro-osmosis within an MEA system.

In this chapter, we explore vapor-fed electrolysis with a focus on cell operating conditions and the role of water within the MEA. Our objective is to explore the causes of high overpotentials within the cell. Detailed understanding of global and local effects is accomplished through combined experimental and theoretical investigations of the underlying phenomena. First, the experimental and modeling methodologies are introduced. Next, the measured performance of a vapor-fed electrolyzer operated at room and elevated temperature is demonstrated and discussed. Then a model is used to dissect the results using an applied voltage breakdown in order to describe the impact of relative humidity and potential losses in different parts of the cell. Finally, the role of water vapor supply is investigated by examining the effects of supplying the anode and cathode compartments with feeds differing in relative humidity.

4.3 Experimental

4.3.1 Membrane-Electrode-Assembly Fabrication

The MEA (Figure 4.1) comprises a catalyst-coated membrane (CCM). The two catalyst layers (CLs) were formed by spray coating the respective sides of a Nafion 117 membrane (Ion Power, Delaware, USA) using a Sono-Tek ultrasonic spray coater (Sono-Tek Exacta Coat, New York, USA). For all tests, the Nafion membrane was pre-soaked in 95°C water for one hour and pre-treated in room temperature 0.5 M nitric acid bath for one hour to remove any impurities. Then, the membranes were stored in deionized water before the spray coating of catalyst layers, which were dried while on the heated vacuum plate of the spray coater. The MEA is sandwiched between

a 255-μm thick titanium porous transport layer (PTL) (Proton OnSite, Connecticut, USA) on the anode CL and a 190 μm-thick carbon gas-diffusion layer (GDL) covered by a 45 μm-thick microporous layer (MPL) (Sigracet 29BC, SGL Wiesbaden, Germany) on the cathode CL. Gas is supplied to both the PTL and the GDL using two graphite single-serpentine flow channels (Fuel Cell Technologies Inc., 1 mm thick land and channel). Although graphite is not thermodynamically stable at the anode potentials used in this study,[145] none of the tests in this chapter were held for longer than 2 h. No degradation of the graphite flow-fields was observed in the 2 h tests, as there was no CO_2 formed at 500 mA cm^{-2} for 16 h when the outlet of the cell was monitoring gas evolution with a real-time-gas-analyzer mass spectrometer (Diablo Analytical, California, USA). To minimize contact resistance, the carbon GDL was compressed to 20%, and to assure no gas leaks throughout the cell, PTFE (McMaster-Carr) or Tefzel™ gaskets (CS Hyde, Illinois, USA) of 0.18- and 0.254-mm thickness were used on the cathode and anode sides of the assembly, respectively.

The catalyst inks were composed of catalyst nanoparticles, iridium black for the anode and 45.9 wt.% platinum on Vulcan carbon for the cathode (both from TKK, Tokyo Japan), Nafion ionomer (Ion Power, Delaware), water, n-propanol, ethanol mixtures for the iridium ink and n-propanol and water mixture for the platinum ink (exact recipes are given in Table 4.1). These inks were spray-coated directly onto the Nafion 117 membrane using a 120 kHz nozzle. The target loadings were ~1 mg cm^{-2} iridium on the anode and ~0.3 mg cm^{-2} platinum/carbon on the cathode. A relatively high platinum loading was used for the cathode to ensure that the cell was not limited by the hydrogen-evolution reaction. The total active area (geometric) was 5 cm^2 for each electrode.

Table 4.1:Catalyst Ink Recipes for the cathode and the anode inks.

Component	**Cathode Platinum on Carbon Ink**	**Anode Iridium Ink**
Catalyst	48 mg	30 mg
n-Propanol	12 g	9.65 g
Water	12 g	6.0 g
Ethanol		4.73 g
Nafion (5wt% dispersion)	108 mg	54 mg

4.3.2 Test Protocol

Electrochemical tests were performed using a commercial test stand (Fuel Cell Technologies Inc. (FCT), New Mexico, USA). Ultra-high purity argon (99.999%) was bubbled through a temperature-controlled bubbler with 18.2 MΩ deionized water (EMD Millipore, Billerica MA). The gas flow rates, cell temperature, and bubbler temperature were controlled independently to

achieve a cell relative humidity (RH) of 30 to 98%. All tests were at ambient pressure and either 30 or 80°C. The flowrates of the gases to each side of the cell were 200 mL min^{-1}. For liquid-fed electrolysis, liquid water was introduced into the anode compartment using an external diaphragm pump (KNF NF25) at a flow rate of 100 mL min^{-1}. Electrochemical testing was performed using a Biologic VSP-300 potentiostat with 5 A booster (Seyssinet-Pariset, France). Electrochemical impedance was measured in potentiostatic mode, by imposing a 10 mV perturbation between 200 kHz – 100 mHz at several cell voltages in order to generate a Nyquist plot, where the intercept with the real axis is the measured high-frequency resistance (HFR) of the cell.

Each MEA was conditioned by flowing humidified argon (98% RH) to both sides of the cell for at least one hour at open circuit voltage. Chronopotentiometric steps were then applied, starting from 10 mA cm^{-2} and increasing to 1000 mA cm^{-2}, or until the MEA reached the upper cutoff potential 2.3 V, chosen to prevent corrosion of cell flow fields, endplates, and current collectors. A step size of 10 mA cm^{-2} was used at low current densities, and 50 mA cm^{-2} was used for higher current densities. Each current density step was 2 min or until a stable response was reached (± 50-100 mV), and the voltage response data were averaged over the last 20 s for the polarization curve point. Two polarization curves were collected for each MEA, with multiple MEAs tested for each set of electrolyzer test conditions.

4.4 Mathematical Model

A mathematical model of vapor-fed electrolysis in an MEA was used to interpret the experimental data. A 2-D view of the model domain is shown in Figure 4.1. The governing differential equations and their boundary conditions are given in Tables S4.1-S4.4. The characteristic properties for each domain (materials properties, dimensions, etc.) are detailed in Tables S4.5-S4.9.

This model was adapted from fuel-cell models developed by Balliet et. al.[146] and Zenyuk, Das, Weber.[147] Mass transport within each component domain is governed by the same mechanisms as those considered for the modeling of fuel cells, namely multicomponent diffusion and convection via Darcy's law for the porous media and concentrated-solution theory for the membrane and ionomer. In contrast to the fuel-cell models, the model is single phase and thus assumes no liquid water in the cell, which is justified due to an RH less than 100%, heat being generated, and water being consumed as a reactant. If water does condense, its influence is expected to be minimal although this could be a topic for future investigation and model refinement. Additionally, the fuel-cell model's reactions are changed to OER and HER (eq (4.1) and (4.2)) occurring at the anode and cathode, respectively. These two changes impact water movement within the system, as water is consumed at the anode in an electrolyzer, thereby limiting the flux of water to the anode side of the membrane. Water flux can still occur from the cathode side of the membrane to the anode depending on the balance between back transport and electro-osmosis in the membrane. Additionally, the model is nonisothermal and the effects of heat generation within the MEA are taken into account with an overall energy balance and appropriate boundary conditions (see Table S4.1 eq S4.10, Table S4.2, and Table S4.4). Heat generation and consumption occurs through ohmic heating, vaporization of water, and heat released in the electrochemical reactions. In the vapor-fed system, one expects more severe temperature nonuniformities and local dehydration due

to the increases temperature in the MEA, whereas in a liquid-fed cell, the water acts as a coolant and temperature excursions are minimal.

The model was used to calculate various properties and characteristics of the MEA that are not accessible by experiments. An important characteristic is the net water flux through the membrane,

$$N_{H_2O,PEM} = \frac{\xi\, i}{F} - \alpha\, \nabla \mu_{H_2O}, \tag{4.3}$$

where ξ is the electro-osmotic coefficient, **i** is the current density, *F* is Faraday's constant, α is the transport coefficient, and μ_{H_2O} is the chemical potential of water within the membrane. The first term on the right side of this equation represents water transport by electro-osmosis and the second term represents water transport by nominally diffusion.

The model is also used to determine the water content, temperature distribution and the contribution to the applied voltage within the MEA cell. Using the methodology of Gerhardt *et al*.[148] the applied-voltage breakdown (AVB) is given by

$$V = U^{ref} + \eta_{HER,BV} + \eta_{OER,Tafel} + \eta_{MT} + \eta_{cathode,ionomer} + \eta_{anode,ionomer} + \eta_{PEM,} \tag{4.4}$$

where U^{ref} is the Nernstian thermodynamic potential (referenced to the conditions in the gas channel), $\eta_{HER,BV}$ and $\eta_{OER,Tafel}$ are the kinetic overpotentials for the cathode and anode reaction, respectively, $\eta_{i,ionomer}$ is the ohmic loss from the ionomer within the CL, η_{MT} is the mass-transport loss within the anode CL, and η_{PEM} is the ohmic loss across the membrane. The dependence of these terms on current density and properties of different parts of the MEA are given in Table S4.10. The cathode CL has negligible mass-transport losses as the reactant protons are at fixed concentration set by the reaction rate and any transport losses are ohmic in nature. The electronic losses are assumed minimal due to the high conductivity of the electronically-conducting materials.

4.5 Theory: Role of Water

Before examining the data, it is important to identify the different types of water flux occurring in the system and their impact on the maximum possible performance of the MEA. In polymer-electrolyte water electrolysis, water is not only a reactant, but also a hydrating agent. Furthermore, water transport through the system is complex due to the various driving forces (see, for example, eq. (4.3)). At steady state, a water mass balance at the anode catalyst layer results in

$$N_{H_2O,PTL} - N_{H_2O,PEM} = \frac{i}{2F}, \tag{4.5}$$

where $N_{H_2O,PTL}$ is the water flux through the PTL from the water-vapor feed stream and $N_{H_2O,PEM}$ is the net water flux through the membrane. The extent to which water leaves or comes through the membrane can be described by the net electro-osmotic coefficient, β,[11,148]

$$\beta = \frac{N_{H_2O,PEM}\, F}{i}. \tag{4.6}$$

A positive value of β means that the net water movement is from anode to cathode and a negative value of β corresponds to water moving from cathode to anode. With no net water flux in the membrane (i.e., $\mathbf{N}_{H_2O,PEM} = 0$, β=0), a current density can be defined as

$$i_{\beta=0} = 2FN_{H_2O,PTL} = 2F\frac{(C_o-0)D^{eff}}{t_{PTL}} \quad (4.7)$$

where c_o is the concentration in the gas channel, D^{eff} is the effectivity diffusivity of water within the gas phase of the porous media in the anode, and t_{PTL} is the thickness of the PTL. $i_{\beta=0}$ is a function of temperature, as shown in Figure 4.2b (at 98% RH), because both D^{eff} and c_o are functions of temperature. eq. (4.7) is written assuming limiting current and a linear gradient from the channel to the reaction site. Combining eqs. (4.5)-(4.7) and normalizing by $i_{\beta=0}$ we obtain an expression for the nondimensionalized maximum current density

$$\frac{i_{max}}{i_{\beta=0}} = \frac{1}{(1+2\beta)}, \quad (4.8)$$

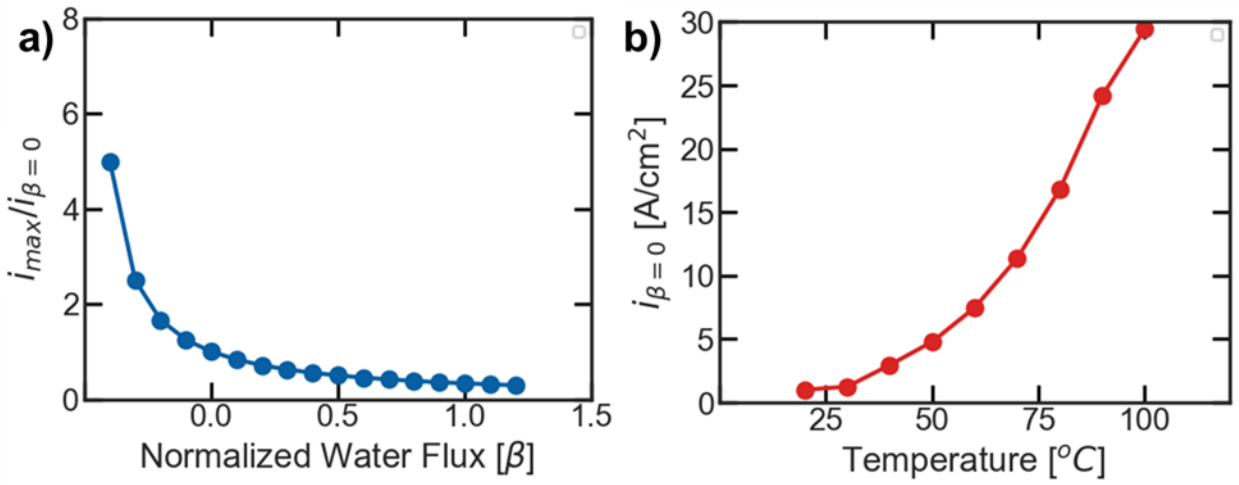

Figure 4.2: a) The nondimensionalized limiting current density as a function of β, the net water flux in the membrane normalized by the proton flux b) The current density for β=0 as a function of temperature assuming 98% RH in the anode gas channel.

Figure 4.2a plots eq. (4.8). Eq. 4.8 can also be written as a function of chemical potential as shown in the SI. The critical impact of water flux through the membrane is evident by its influence on the maximum achievable current density. Since the electro-osmotic flux of water through the membrane influences how much water is available to react in the anode catalyst layer, the maximum current density is a function of current, which dictates the magnitude of the electro-osmotic flux. For example, i_{max} goes from 1.22 A cm^{-2} for 98% RH feed at 30°C for β = 0 to ~400 mA cm^{-2} for β = 1, corresponding to pure electro-osmotic flow. The reason for this trend is that an increase in β results in a reduction in the availability of water for reaction. Conversely, if there is net water transport from the cathode (e.g., due to different membrane design or operating

conditions), a higher-than-expected maximum current is possible. It should be noted that for anode and cathode feeds with identical RH, β is typically negative and sufficiently large in magnitude, which can complicate the analysis of water management in electrolyzers. Precision and care are needed when analyzing experimental data. Overall, Figure 4.2 provides a metric for experimentalists to determine how close to mass-transport-limiting conditions their system operates, since the water balance and the value of β are accessible experimentally. The water balance can be determined by measuring the inlet and outlet RH of both streams and accounting for the consumption of water by reaction.

4.6 Results and Discussion

4.6.1 Vapor-Fed Electrolyzer Performance

Figure 4.3a compares the polarization curve for liquid- and vapor-fed electrolysis at 30°C. The liquid-fed MEA requires a lower voltage for a given current density. The voltage versus current-density curves are similar up to about 100 mA cm^{-2}. Above this current density, the voltage for the vapor-fed cell rises substantially relative to that for the liquid-fed cell and grows rapidly with increasing current density. This divergence between the vapor- and liquid-fed cases is mainly due to a loss of ion conductivity within the membrane brought about by inadequate membrane hydration (which includes RH changes due to water mass transport from the channel to the membrane surface) for the case of vapor-fed electrolysis. This finding is in agreement with the calculated HFR from the EIS data and the subsequent iR-corrected voltage vs current density plots in Figure 4.3c of the SI. We note that the iR-corrected plots are essentially the same for the vapor-fed and liquid-fed cases, indicating the supply of water does not limit the rate of reaction, which is consistent with the current being lower than i_{max} as calculated via Eq. 4.8 (see Figure 4.2).

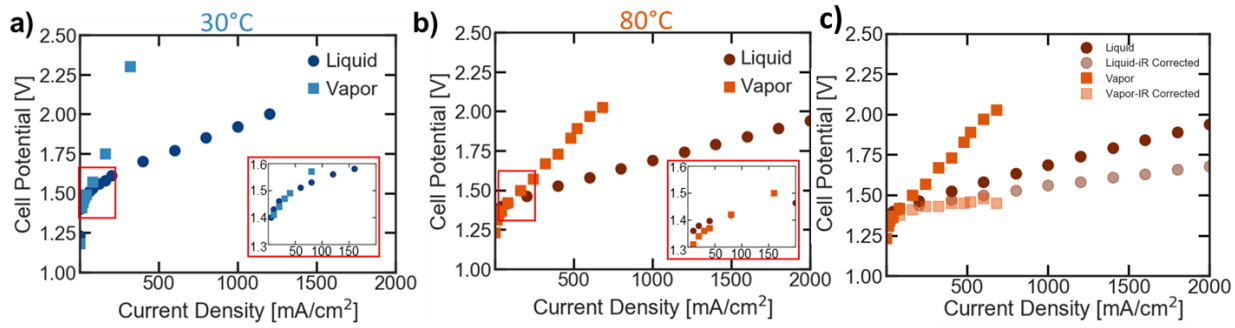

Figure 4.3: Electrolysis at (a) 30°C, blue, (b) 80°C, red, and (c) the iR corrected curves for 80°C for both liquid-fed (circles) and vapor-fed (squares) cells. Operating conditions: Nafion 117 membrane; 1 mg cm^{-2} iridium loading on anode, and 0.3 mg cm^{-2} Pt from Pt/C on cathode, and vapor feed at 98% RH on both sides flowing at 200 mL min^{-1}.

Temperature has a significant impact on performance of the vapor-fed electrolyzer. The maximum current density increases, as shown in Figure 4.2, which shows the dependence of temperature on water vapor concentration. Additionally, kinetic and transport properties are also a function of temperature in the membrane and ionomer. Figure 4.3b compares the polarization curves for liquid-fed electrolysis with vapor-fed electrolysis at 80°C. Increasing the temperature decreases

the voltage required for a given current density for both liquid and vapor cells. For example, the voltage required for a current density of 1000 mA cm^{-2} is 1.92 V at 30°C, but decreases to 1.76 V at 80°C for the liquid-fed system. The same is true for the vapor-fed MEA, but in this case, the voltage difference for required for a current density of 320 mA cm^{-2} at 30°C (2.3 V) and 80°C (1.67 V) is greater.

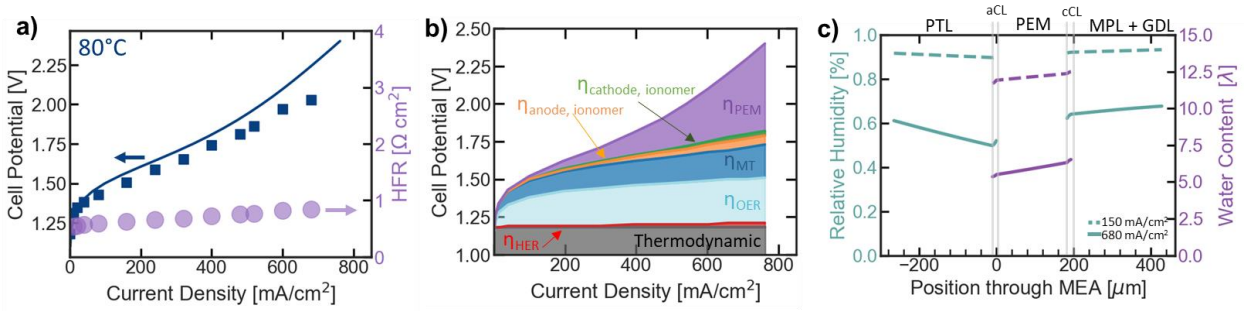

Figure 4.4: a) Model fit of the vapor-fed MEA operating at 98% RH system at 80°C with the HFR data corresponding to the experiments (circles, right axis) and b) AVB for this system c) RH (green) and water content (purple), defined as moles of water per mole sulfonic acid site, throughout the cell at 150 mA cm^{-2} (dashed) and 680 mA cm^{-2} (solid).

To identify the reasons for the large voltage required by the vapor-fed system, the total cell voltage versus current density and the AVB were calculated using the model of the 80°C vapor-fed MEA. Figure 4.4a shows that the model accurately describes the overall cell voltage versus current density measured experimentally. Figure 4.4b illustrates the AVB at 80°C. The largest voltage losses are associated with the OER kinetics, the ohmic resistance of the membrane, and the mass-transport loss through the anode CL. The potential loss due to the OER kinetics is a characteristic of the iridium catalyst. As expected, the OER overpotential is larger than that for the HER, reflecting the slower kinetics of OER.[21] The ohmic loss in the membrane increases rapidly with current density, and is a function of water activity within the membrane phase (as shown in Table S4.9). The mass-transport loss within the anode CL (see eq. 4.19 in Table S4.10) corresponds to the influence of changes in the reactant water concentration between the gas pathways, reaction sites, and ionomer. The origin of these mass-transport losses is caused by a combination of CL underutilization (discussed in further detail below), and local temperature rise.

The effects of current density on the distribution of water in the electrolysis cell is shown in Figure 4.4c. As the current density increases, the local cell temperature increases, as shown in Figure 4.5, which exacerbates the mass-transport-related decrease in RH at the CL; the membrane water content (λ) or moles of water per sulfonic acid site, is similarly depressed. For 150 mA cm^{-2}, λ is about 13, whereas for 680 mA cm^{-2} the value of λ is about 6. For reference, a maximum value of λ=16 for fully hydrated at 100% RH Nafion has been observed previously.[142,149,150] Thus, at the operating current densities at which the vapor electrolyzer is running, the value of λ is far from the fully hydrated value.

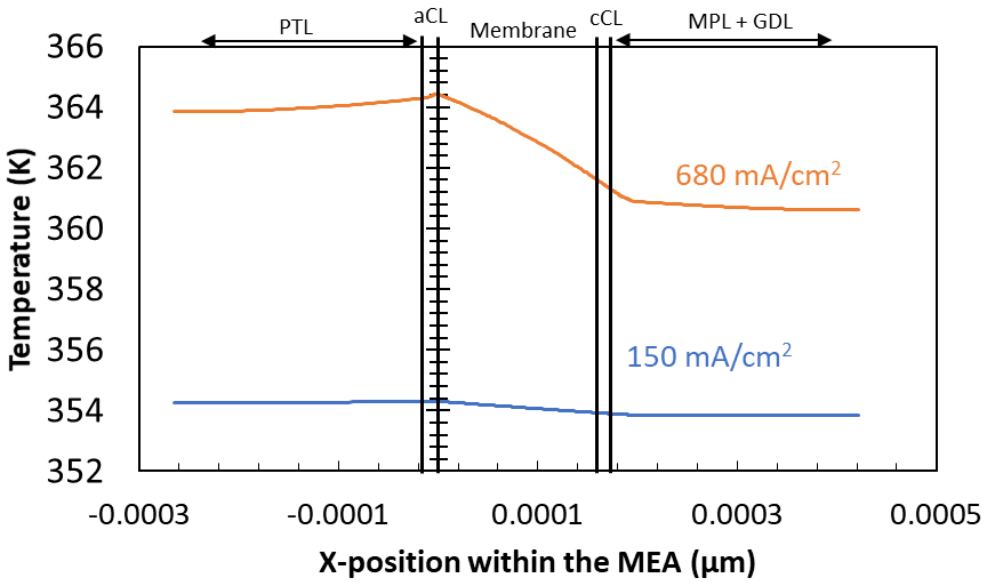

Figure 4.5: Temperature distribution within the membrane electrode assembly at two different current densities.

To explore the effects of overall water transport in more detail, the carrier gas was changed from argon to helium in order to decrease any bulk transport effects in the PTL since the water-vapor diffusivity through helium is three times larger than that through argon. As shown in Figure 4.6a, going from argon to helium results in a monotonic, nonlinear decrease in the overall cell voltage with current density. Although the gradient within the PTL is small, the higher diffusivity provides better water transport to the reaction sites, which leads to a higher local RH on both sides of the membrane at a given current density. The higher local RH leads to higher water content within the membrane phase (Figure 4.6a, right axis), demonstrating that helium results in better hydration. Since the membrane is better hydrated, secondary effects, such as water transport from the cathode to the anode and maximum cell temperature, further assist in mitigating overpotential losses. The maximum cell temperature when argon and helium are used is 91.4°C and 89.9°C, respectively, which is enough to reduce the overpotential by 150 mV. The reduction in overpotential is primarily ohmic, mainly due to the increase in hydration, with only a secondary effect on kinetics due to higher reactant concentration.

Figure 4.6b shows that decreasing the membrane thickness (from 183 to 25 µm) has a substantial impact on performance. The thinner membrane exhibits a lower ohmic loss because it promotes back transport of water in the membrane and thus a more negative value of β (see eqs. 4.6 and 4.8 and Figure 4.2), which helps to keep the membrane better hydrated,[151,152] in addition to simply being thinner. However, the decrease in membrane thickness is known to increase product gas crossover and thus lower cell efficiency.[21,153,154] Such effects become compounded by the fact that most electrolyzers operate with pressure differentials, as pressurized hydrogen is desired.[153] The tradeoffs between electrolyzer performance, gas crossover, and optimal operating pressure must be considered by system designers and is an active area of research.

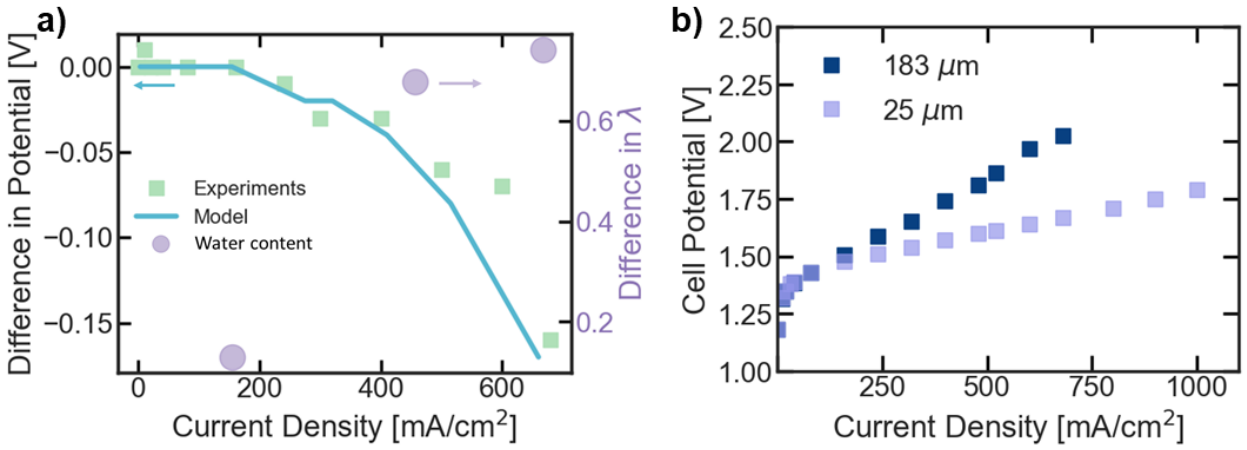

Figure 4.6: (a) Difference in cell potential when the carrier gas is changed from helium (2 g/mol) to argon (MW = 40 g/mol), so a negative change is potential is a lower overpotential. The square points show experimental measurements and the solid line shows the predictions of the model (left axis). The difference in membrane water content, λ, is shown on the right axis for Nafion 117, where the increasing trend shows a higher λ in helium with increasing current density. (b) Electrolyzer performance for Nafion 117 (183 μm) vs. Nafion 211 (25 μm). Experiments were carried out at 80 °C with an iridium loading 1 mg cm^{-2} on the anode and a Pt from Pt/C loading of 0.3 mg cm^{-2} on the cathode. The anode and cathode feed flow rate were 200 mL min^{-1} and the RH was 98% for both feeds.

4.6.2 Effects of difference in the RH of the anode and cathode feeds

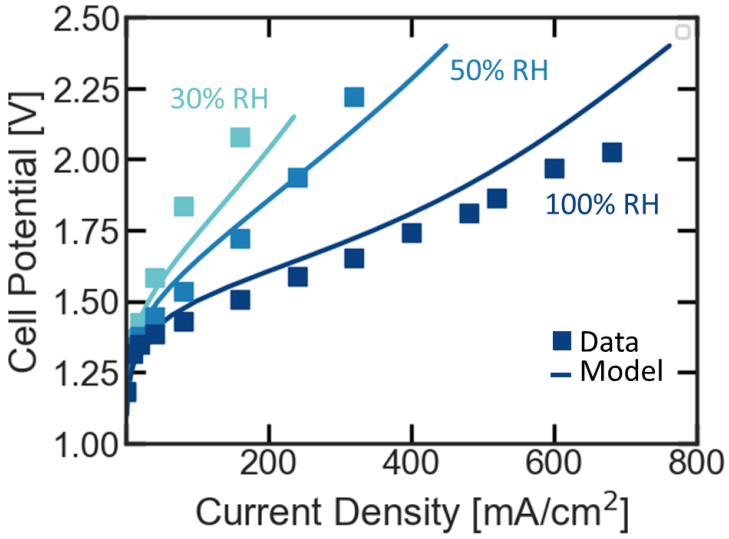

Figure 4.7: Polarization curves at various RH for vapor electrolysis from 98% RH (dark blue), 50% RH (blue), and 30% RH (light blue). Points are experimental data; solid lines are from the model. Vapor electrolyzer experiments and model were ran and simulated at 80 °C, with Nafion 117 membrane; the anode had 1 mg cm^{-2} iridium loading, the cathode had 0.3 mg Pt cm^{-2} using Pt/C loading.

Many of the proposed applications for vapor-fed electrolyzers are expected to have inlet streams that are not fully humidified or involve a water-vapor-feed to only one electrode. Different humidity levels in the anode and cathode feeds can help prevent excess water reaching the cathode, where wet hydrogen is difficult to store and use, as discussed earlier. To explore these effects and further comprehend the role of water on cell performance, the feed RH was varied, as shown in Figure 4.7. As expected, the cell voltage increased with reduced feed RH. Nevertheless, even at 30% RH and 80°C, a current density of 160 mA cm^{-2} is achieved at 2.08 V, comparable to the low-temperature study shown in Figure 4.3a. Interestingly, the inlet water-vapor concentrations are comparable for a feed with a 30% RH at 80°C (0.0049 mol L^{-1}) and a feed with a 98% RH at 30°C (0.0017 mol L^{-1}). Nevertheless, the measured voltage is not the same above 50 mA cm^{-2}. As shown in Figure 4.8, a feed with 30% RH at 80°C requires higher voltage for a given current density. This observation demonstrates that cell voltage is more dependent on water activity than water concentration: at 80°C, the activity is 0.30 ($\lambda = 4.47$), but at 30°C, the activity is 0.98 ($\lambda = 14.94$). This finding agrees as well with our modeling assumption and hypothesis that activity drives the reaction.

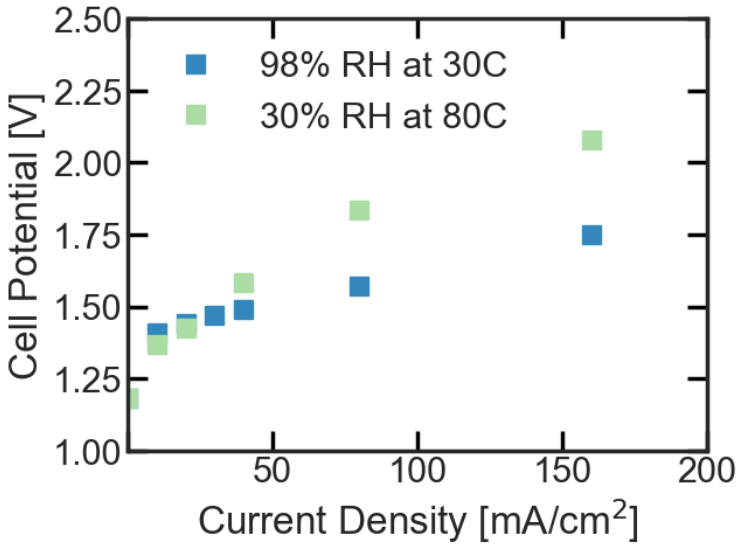

Figure 4.8: Vapor electrolysis tested at two different conditions. Wet and cold test of 98% RH at 30°C (blue) and hot and dry test of 30% RH at 80°C

AVBs obtained from the model of the vapor-fed electrolysis cell operated at 150 mA cm^{-2} are shown in Figure 4.9 as a function of the feed RH at 80°C. Figure 4.9a shows the absolute values of each component of the overpotential and Figure 4.9b shows the relative contributions of each component. The impact of anode mass transport and ohmic losses are evident at 30% RH, where mass transport accounts for 31% and ohmic accounts for 28% of the total overpotential. Interestingly, at 98% RH, the mass-transport losses are still high, accounting for 43% of the total overpotential, but the ohmic overpotential only makes up only 7% of the total overpotential loss. This result further highlights the importance of water activity within the membrane phase on the overall cell performance. At lower RHs, the low level of membrane and ionomer hydration significantly impact conductivity of these phases, resulting in increased ohmic loss within both components.

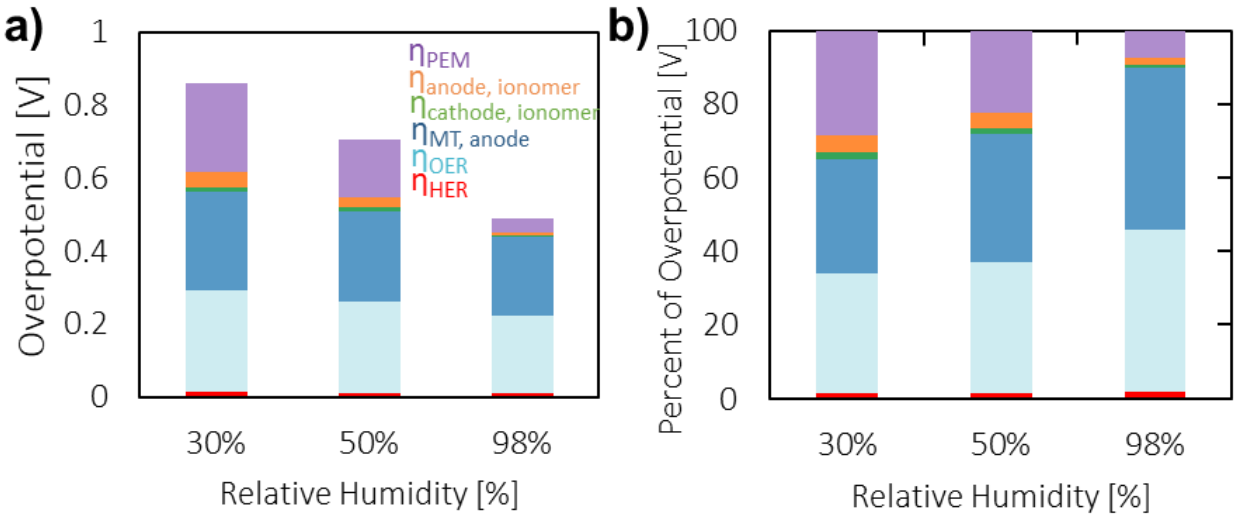

Figure 4.9: a) AVBs at a constant current density of 150 mA cm^{-2} shown as a function of humidity. b) Percent contribution to the total cell voltage, simulated at 80°C.

The CL is a heterogeneous, multicomponent structure that requires percolation pathways for water, ions, and electrons to reach the embedded catalyst sites. Due to this complexity and the interrelation of phenomena in the CL, unambiguous deconvolution of the mass-transport overpotentials is difficult, especially as the properties of all components depend on the state of their hydration.[142,151] As shown in Figure 4.10a, the reaction-rate distribution within the anode CL shifts from being uniform throughout the catalyst layer at 98% RH, to being localized near the membrane:anode CL boundary at 30% RH. Such a change is indicative of going from conditions where the rate of the OER is kinetically limited to one where this reaction is limited by ionic transport. In the latter case, the reduced water activity limits the availability of water, resulting in a lower water content in the ionomer, as shown in Figure 4.10b. Another consequence of the reduction in ionomer hydration with decreasing feed RH is that the total overpotential loss in the anode CL increase in order to maintain constant current density.[145,151] This effect is shown in Figure 4.10c.

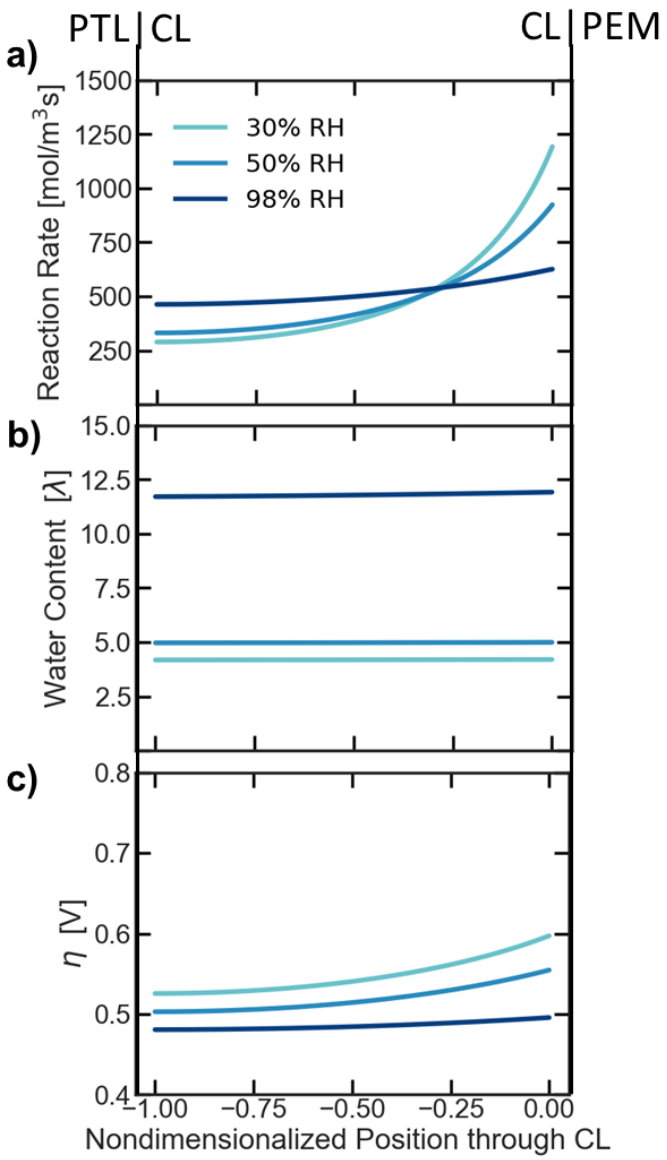

Figure 4.10:a) Reaction distributions, b) water content and c) overpotential for varying RH conditions within the nondimensionalized anode catalyst layer at 150 mA cm^{-2}.

Water moves through the cell in different phases and with different driving forces, as discussed above. To explore the effects of water transport further, experiments were conducted with unequal ("asymmetric") humidities in the anode and cathode feeds. The results of these experiments are shown in Figure 4.11a. Comparison of cell polarization curves reveals that water supply to the anode is more important than water supply to the cathode, because at 2 V, the current density is markedly higher when the anode feed is at a higher RH than the cathode feed. Also shown in Figure 4.11a is the "symmetric" case, in which the RH of each feed is set to the average RH of the asymmetric RH experiment. This experiment affirms that at low current densities kinetic losses dominate (i.e., the symmetric RH curve is aligned with that for the drier anode asymmetric curve, as shown in the inset), while at higher current densities mass transport and ohmic effects dominate

(i.e., the symmetric RH curve aligns closer to the drier cathode asymmetric curve). These trends agree with the AVBs presented in Figure 4.9.

Insights into the mechanism of water-transport and its effects on overall cell polarization were obtained by calculating the value of β, the net water flux through the membrane normalized by the proton flux (see eq. 4.6), i.e., a net electro-osmotic coefficient. The results for three cases are presented in Figure 4.11b. This calculation was done using the model of the vapor-fed electrolyzer. For the cases in which asymmetric RH is used in the anode and in the cathode feed, back transport via diffusion dominates the response, regardless of the direction of the electro-osmotic flow. At lower current densities, the lower RH anode case benefits from this transport, as β helps move water to the anode and the cell has similar performance as the symmetric RH case. However, at higher current densities, electro-osmosis drives β to be more positive and move water away from the anode reacting site. Even though β continues to be negative for the low RH anode case, this experiment shows that lower local RH at the anode CL can reduce the achievable current density at 2.0 V, emphasizing the importance of anode RH on performance. The experiments also demonstrate that there is little benefit of feeding the anode and the cathode with the same RH. A high RH in the feed to the anode is sufficient to provide water to the cathode and can sustain reasonable current densities.

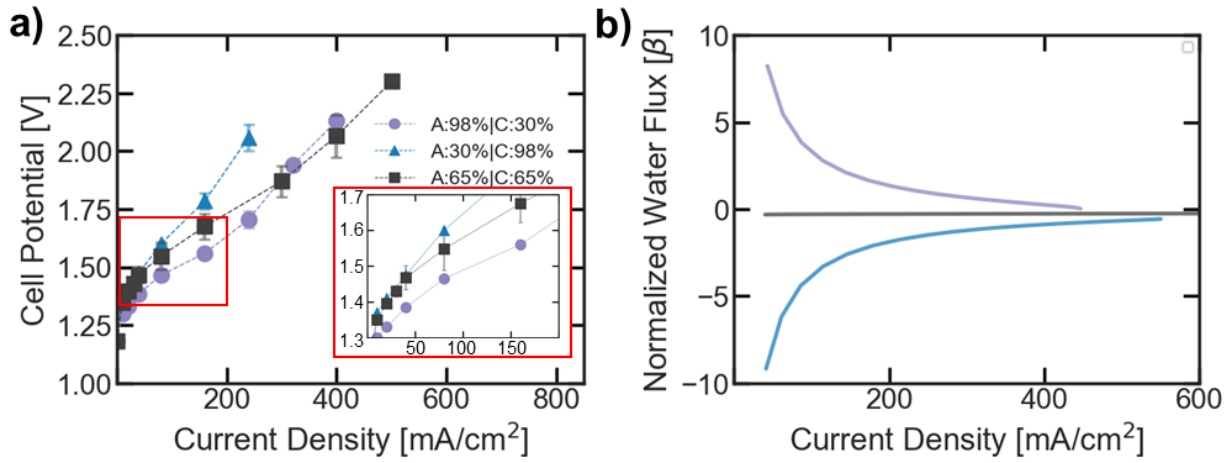

Figure 4.11: a) Polarization curves for asymmetric study (triangles and circles) and the average cell RH humidity symmetric study (squares) for comparison. The cathode (circles) and anode (triangles) had the inlet RH of 30% while the other electrode was kept at 98% b) Values of β as a function of current density for each of the three cases calculated using the model of a vapor-fed electrolyzer.

4.7 Summary

We have shown that a vapor-fed MEA system for the electrolysis water can be operated at current densities above 100 mA cm^{-2}. In contrast to liquid-fed electrolyzers, in which water supply is not an issue, the water content of the vapor-fed plays a significant role as both a hydrating agent and a reactant. This dependence on water content is especially true under conditions where the maximum achievable current densities are compromised due to electro-osmotic flows in the system that further decrease water activity at the reaction site. Analysis of the vapor-fed electrolyzer, using a mathematical model, demonstrates conclusively that the most important role of water is in hydrating the ionomer in the catalyst layers and the membrane, with higher humidity and temperatures leading to higher current densities for a given applied voltage. The computed reaction distribution with the anode catalyst layer suggests underutilization of this catalyst layer (where the OER occurs), especially at low anode feed humidities. We have also demonstrated that a high relative humidity in the anode feed is critical for good electrolyzer performance. Our study illustrates how feed composition and operating conditions affect the performance of a vapor-fed electrolyzer, information that will be useful for the design of vapor-fed electrolyzers for practical applications.

4.8 Supplemental Information

4.8.1 Model Development

The model was developed using a similar fuel cell model used Balliet *et al.*[146] The fitting parameters used in this model are the mass-transport coefficient $\left(k_{M,V}\right)$ and the anode electrochemically active surface area (a_{Ir}).

Table S4.1: Governing equations for the electrolyzer model.

Variable	Governing Equation	Eq	Region
Gas pressure	$\mathbf{N}_{\mathrm{G}} = -\frac{\rho_{\mathrm{G}} k_{\mathrm{G}}^{\mathrm{eff}}}{\mu_{\mathrm{G}}} \boldsymbol{\nabla} \mathrm{P}_{\mathrm{G}}$	[S4.1]	PTL, GDL, MPL, CL
Gas species flux	$\frac{\rho_{\mathrm{G}} k_{\mathrm{G}}^{\mathrm{eff}}}{\mu} \nabla \cdot \mathbf{N}_{\mathrm{G}} = \sum \mathrm{s}_{\mathrm{i}}$	[S4.2]	PTL, GDL, MPL, CL
Mass Fractions	$\nabla \cdot (-\rho_{\mathrm{G}} \omega_{\mathrm{i}} \sum_{\mathrm{j}}^{\mathrm{n}} \overline{\mathrm{D}}_{\mathrm{ij}}^{\mathrm{eff}} (\boldsymbol{\nabla} \mathrm{y}_{\mathrm{j}} + (\mathrm{y}_{\mathrm{j}} - \omega_{\mathrm{j}}) \frac{\boldsymbol{\nabla} \mathrm{P}_{\mathrm{G}}}{\mathrm{P}_{\mathrm{G}}}) + \rho_{\mathrm{G}} \omega_{\mathrm{i}} \mathbf{v}_{\mathrm{G}}) = s_i$	[S4.3]	PTL, GDL, MPL, CL
Electronic current density	$\nabla \cdot \mathbf{i}_1 = -i_h^{rxn}$	[S4.4]	Plate, GDL, MPL, CL
Electronic potential	$\mathbf{i_1} = -\sigma^{eff} \boldsymbol{\nabla} \Phi_1 = -\sigma_{bulk} \epsilon_s^{1.5} \boldsymbol{\nabla} \Phi_1$	[S4.5]	Plate, PTL, GDL, MPL, CL
Ionic current density	$\nabla \cdot \mathbf{i}_2 = i_h^{rxn}$	[S4.6]	CL, PEM
Ionic Potential	$\mathbf{i_2} = -\left(\kappa_V \boldsymbol{\nabla} \Phi_2 + \frac{\kappa_V \xi_V}{F} \boldsymbol{\nabla} \mu_{\mathrm{H_2O}}\right)$	[S4.7]	CL, PEM

Water flux†	$\nabla \cdot \mathbf{N}_{\mathrm{H_2O},PEM} = -R_{M,V} - \frac{i_{OER}^{rxn}}{2F}$	[S4.8]	CL, PEM
Water chemical potential in the membrane	$\mathbf{N}_{\mathrm{H_2O},PEM} = \left(\mathbf{i_2}\frac{\xi_V}{F} - \alpha_V \boldsymbol{\nabla}\mu_{\mathrm{H_2O}}\right)$,	[S4.9]	CL, PEM
Temperature	$-k_{T,eff}\nabla \cdot (\boldsymbol{\nabla}T) = Q_{V,M} + Q_J + Q_{rxn}$	[S4.10]	Plate, PTL, GDL, MPL, CL, PEM

† i_{OER}^{rxn} = 0 at the cathode

Table S4.2: Source Terms for heat balance equations.

Source Term	Domains				
	Plate	PTL, GDL, MPL	aCL	cCL	M
Energy-Balance					
$Q_{V,M}$			$-\Delta\widehat{H}_{L,V} \cdot R_{M,V}$		
Q_J	$\frac{\mathbf{i}_1 \cdot \mathbf{i}_1}{\sigma_{eff}}$	$\frac{\mathbf{i}_1 \cdot \mathbf{i}_1}{\sigma_{eff}}$	$\frac{\mathbf{i}_1 \cdot \mathbf{i}_1}{\sigma_{eff}} + \frac{\mathbf{i}_2 \cdot \mathbf{i}_2}{\kappa_{H^+}}$		$\frac{\mathbf{i}_2 \cdot \mathbf{i}_2}{\kappa_{H^+}}$
Q_{rxn}			$i_h^{rxn}(\eta_{s,h} + \Pi_h)$		

Table S4.3: Source terms for conservation of chemical species.

Mass Conservation, Gas Phase	
Species	
H_2	$s_{H_2} = \frac{i_{HER}^{rxn} M_{\mathrm{H_2}}}{2F}$
O_2	$s_{O_2} = \frac{i_{OER}^{rxn} M_{\mathrm{O_2}}}{4F}$
H_2O	$s_{H_2O} = R_{M,V} = k_{M,V}\,(\mu_{M,\mathrm{H_2O}} - \mu_{V,\mathrm{H_2O}})\exp(4.48 a_{\mathrm{H_2O},M})$
Electrochemical Reaction Rates	
i_{OER}^{rxn}	$a_{Ir} i_{0,OER}\left(a_{\mathrm{H_2O},M}\exp\left(\frac{\alpha_{A,OER}F}{RT}(\Phi_1 - \Phi_2 - U^{ref}\right)\right)$
i_{HER}^{rxn}	$a_{Pt} i_{0,HER}\left(-\frac{p_{\mathrm{H_2}}}{p^{ref}}\exp\left(\frac{\alpha_{A,HER}F}{RT}(\Phi_1 - \Phi_2 - U^{ref}\right) + \exp\left(-\frac{\alpha_{C,HER}F}{RT}\Phi_1 - \Phi_2 - U^{ref}\right)\right)$

No-flux boundary conditions are imposed on the top and bottom boundaries in the 2D model due to symmetry. No-flux boundaries are also assumed at each CL/membrane and land/GDL interface for gaseous species, at each CL/GDL interface for ions and membrane-bound water, and at CL/membrane and channel/GDL interfaces for electronic current. The land/PTL or GDL are all set to the cell temperature at the respective anode and cathode. The channel/PTL or GDL are set to the inlet gas pressure and specified weight fraction, ω_i, of each gas (water vapor, inert, and product gases of oxygen and hydrogen at the anode and cathode, respectively). The electronic potential, Φ_1, is set to 0 V at the cathode land/GDL interface and to the cell operating potential at the anode land/PTL interface. The specific boundary conditions for the various phenomena are detailed explicitly in Table S4.4.

Table S4.4: Boundary conditions for each variable.

Variable	Boundary condition	Boundary
Gas pressure, P_G	$P_G = P_G^{in}$	Anode channel/PTL Cathode channel/GDL
Mass Fractions ω_i		
Reactant mass fraction, ω_R	$\omega_R = \frac{y_R^{in} M_R}{\sum_j y_j^{in} M_j}$, $y_R^{in} = y_R^{in,dry}\left(1 - y_V^{in}\right)$	Anode channel/PTL Cathode channel/GDL
Water vapor mass fraction, ω_V	$\omega_v = \frac{y_v^{in} M_v}{\sum_j y_j^{in} M_j}$	Anode channel/PTL Cathode channel/GDL
Diluent mass fraction, ω_D	$\omega_D = \frac{y_D^{in} M_D}{\sum_j y_j^{in} M_j}$, $y_D^{in} = 1 - y_R^{in} - y_V^{in}$	Anode channel/PTL Cathode channel/GDL
Temperature, T	$T = T_{cell}$	Anode land/PTL Cathode land/GDL
Electronic potential	$\Phi_1 = 0$ V	Cathode land/GDL
Electronic current	$\Phi_1 = \Phi_{cell}$ (potentiostatic) $i_1 = i_{cell}$(galvanostatic)	Anode land/PTL
Ionic potential	$-\mathbf{n} \cdot \boldsymbol{\nabla \Phi_2} = 0$	MPL/CL (cathode) PTL/Cl (anode)
Water within the membrane chemical potential	$-\mathbf{n} \cdot \boldsymbol{\nabla \mu_{H_2O}} = 0$	MPL/CL (cathode) PTL/Cl (anode)

All equations for the 2D model were solved using COMSOL Multiphysics version 5.3a with the MUMPS solver. The mesh comprised 10,000 rectangular domain elements and 700 boundary elements, with the mesh density increasing within the CLs, the membrane, and at the CL/membrane interface; a mesh independence study was carried out and confirmed that the solutions do not depend on the mesh. Parametric sweeps from 1.0 V up to 2.4V with 50 mV step-size were conducted to generate polarization curves.

4.8.2 Characteristic Properties within Each Domain

The following Tables S4.5-S4.9 detail the characteristic properties of the model for each component to provide further details on what has been included in the model.

Table S4.5: Characteristic properties of the subdomains.

	Plate	PTL/GDL	MPL	CL	M	Units
Tortuosity exponent, β_τ (exponent in gas-phase volume fraction, $\varepsilon_G^{-\beta_\tau}$)		3	1.5	1.5		
Effective thermal conductivity, $k_{T,eff}$	17	1.4	1.4	0.27	see Table S4.9	W m^{-1} K^{-1}
Effective electric conductivity, σ_{eff}	144	120	120	120		S cm^{-1}
Modified Bruggeman coefficient for gas transport, $\beta_G, k_{r,G} = S_G^{\beta_G}$		3	3	3		
Porosity (ϵ)		0.36*(PTL)/0.7 (GDL)	0.62	0.5		
Solid volume fraction (ϵ_s)		$1-\epsilon$	$1-\epsilon$	$1-\epsilon-\epsilon_M$		
Thickness		Anode- 255 Cathode - 190	45	Anode – 10 Cathode – 10	183 (dry)	μm
Carman-Kozeny Diameter		7.6	2.5	0.1		μm
Carman-Kozeny Constant		4.06	9.375	9.375		

Table S4.6: Binary diffusion coefficients for gas species (Pa cm^2 s^{-1}). Coefficients are taken from correlations in, Bird, Stewart, and Lightfoot, chapter 17.

pD_{ik}	N_2	H_2O
H_2	$4900\left(\frac{T}{64.83\ \mathrm{K}}\right)^{1.823}$	$24700\left(\frac{T}{146.82\ \mathrm{K}}\right)^{2.334}$
O_2	$5200\left(\frac{T}{139.59\ \mathrm{K}}\right)^{1.823}$	$29100\left(\frac{T}{316.14\ \mathrm{K}}\right)^{2.334}$
Ar	n/a	$24100\left(\frac{T}{285.81\ \mathrm{K}}\right)^{2.334}$
H_2O	--	n/a

The binary diffusion coefficients in Table S4.7 are converted to effective diffusion coefficients,

$$\overline{\mathrm{D}}_{\mathrm{ik}}^{\mathrm{eff}} = \frac{pD_{ik}\epsilon_G^4}{p_G}. \tag{S4.11}$$

The effective diffusion coefficients are used in eq. S4.3 in Table S4.1. The relationship between the different gases can be found using this relationship.

$$\overline{\mathrm{D}}_{\mathrm{ik}}^{\mathrm{eff}} = \frac{x_i x_k}{\omega_i \omega_k} \frac{\sum_{j\neq i} \overline{D_{ij}} (\mathrm{adj}\ B_i)_{jk}}{\sum_{j\neq i} (\mathrm{adj}\ B_i)_{jk}}, \tag{S4.12}$$

where B_i is a matrix of diffusivities such that the jk component of matrix B_i is defined as:

$$(B_i)_{jk} = -\overline{D_{jk}} + \overline{D_{ik}} \tag{S4.13}$$

and $\mathrm{adj}\ (B_i)$ is the matrix adjoint to B_i. The matrix adjoint is done within COMSOL.

Table S4.7: Thermodynamic and transport properties for the components of the gas.

Component	Molar Mass (g mol^{-1})	Enthalpy (J/g)	Heat Capacity (J gK^{-1})	Viscosity (Pa s)
$H_2O_{(v)}$	18	2500.8	1.854	8.02 x 10^{-6}
H_2	2	-	0.917	8.39 x 10^{-6}
O_2	32	-	14.176	1.92 x 10^{-5}
Ar	40	-	0.52	2.1 x 10^{-5}

Table S4.8: Relevant properties for the kinetic parameters for oxygen and hydrogen evolution.

Symbol	**Name**	**Value**
a_{Pt}	Specific surface area for Platinum electrode	8.18×10^6 m^2 m^{-3}
a_{Ir}	Specific surface area for Iridium electrode	2.17×10^7 m^2 m^{-3} (Fitting parameter)
$i_{0,HER}$	Exchange current density for HER	$\left(1 \times 10^{-3} \frac{\mathrm{A}}{\mathrm{m}^2}\right) \exp\left(\frac{17000 \frac{\mathrm{J}}{\mathrm{mol}}}{R}\left(\frac{1}{T_t} - \frac{1}{T}\right)\right)$
$i_{0,OER}$	Exchange current density for OER	215 A m^{-2}
U^{ref}	Reference potential	$1.229\ \mathrm{V} - 0.0008456\ (T - 298.15\ \mathrm{K})$
p^{ref}	Reference pressure	1×10^5 Pa
$\alpha_{A,OER}$	Anodic charge transfer coefficient for OER	0.6
$\alpha_{A,HER}$	Anodic charge transfer coefficient for HER	0.5
$\alpha_{C,HER}$	Cathodic charge transfer coefficient for HER	0.5

Table S4.9: Ionomer and membrane properties relevant for ion and water transport.

Symbol	Name	Value
κ_{H^+}	Proton conductivity (S/m)	$40(\epsilon_{\mathrm{H_2O}} - 0.057)^{1.5} - \exp\left(\frac{14408\,\frac{\mathrm{J}}{\mathrm{mol}}}{R}\left(\frac{1}{310\ K} - \frac{1}{T}\right)\right)$
ξ_{H^+}	Electro-osmotic coefficient	1
$\epsilon_{\mathrm{H_2O}}$	Water volume fraction	$\frac{\lambda \bar{V}_{H_2O}}{\bar{V}_m + \lambda \bar{V}_{H_2O}}$
λ	Number of water molecules per sulfonic acid group	$31.273 a_{\mathrm{H_2O},M}{}^3$ - $33.74 a_{\mathrm{H_2O},M}{}^2$ + $16.089 a_{\mathrm{H_2O},M}$ + 1.8409
$\bar{V}_{H_2O}$	Molar volume of water	1.8016×10^{-2} L mol^{-1}
ϵ_M	Ionomer volume fraction	Anode – 0.18 Cathode – 0.22 Membrane – 1
$\bar{V}_M$	Molar volume of membrane	$\frac{EW}{\rho_M} = 0.55\,\frac{\mathrm{L}}{\mathrm{mol}}$
EW	Equivalent Weight	1100 g mol^{-1}
ρ_M	Density of dry ionomer	2000 kg m^{-3}
$D_{\mathrm{H_2O},M}$	Water diffusivity in membrane	2.26 x 10^{-9} m^2 s^{-1}
$k_{T,eff}$	Thermal conductivity	$0.569\epsilon_{H_2O}^{1.5} + 0.2\left(1 - \epsilon_{H_2O}\right)^{1.5}$ W m^{-1} K^{-1}

4.8.3 Applied-Voltage Breakdowns

The mathematical model enables one to define the various contributions to the applied voltage. As detailed in the manuscript, there are several components to the applied-voltage breakdown, where each of these terms are defined in Table S4.10.

Table S4.10: Applied voltage breakdown equations.

Variable	Equation	[Eq]
Cathode overpotential	$\eta_{HER,BV} = \frac{1}{H\, i_{cell}} \int_0^{L_{cathode,CL}} \int_0^{H} i_{rxn}\, \eta \, dxdy$	[S4.14]
Ionomer ohmic loss (for each CL)	$\eta_{i,ionomer} = \frac{1}{H\, i_{cell}} \int_0^{L_{CL}} \int_0^{H} \left(\frac{(i_{H^+})^2}{\kappa_{H^+}} \right) dx\, dy$	[S4.15]
Membrane ohmic loss	$\eta_{PEM} = \frac{1}{H\, i_{cell}} \int_0^{L_M} \int_0^{H} \left(\frac{(i_{H^+})^2}{\kappa_{H^+}} \right) dx\, dy$	[S4.16]
Anode Overpotential	$\eta_{anode} = \frac{1}{H\, i_{cell}} \int_0^{L_{anode,CL}} \int_0^{H} i_{rxn}\, \eta \, dxdy$	[S4.17]
Anode Tafel Overpotential	$\eta_{OER,Tafel} = \ln\left(\frac{i_{cell}}{a_{Ir} i_{0,OER} a_{H_2O} L_{CL}} \right) \left(\frac{RT}{\alpha_{A,OER} F} \right)$	[S4.18]
Mass Transport Overpotential	$\eta_{MT} = \eta_{anode} - \eta_{OER,Tafel}$	[S4.19]

5. Performance and Durability of Proton-Exchange Membrane Vapor-Fed Unitized Regenerative Fuel Cells[†]

5.1 Abstract

With a growing demand on electricity, clean hydrogen production and usage can be an asset not only to mitigate emissions, but for long-term energy storage as well. Hydrogen, a high-density energy carrier, can be made through electrolysis in charging mode and generate electricity via a fuel cell in discharging mode in a unitized regenerative fuel cell (URFC). While URFCs reduce cost, number of cells, and balance of plant by combining the charging and discharging modes into a singular device, switching between modes becomes burdensome, and water management is a major challenge. One way to mitigate these issues is to operate the entire system in the vapor phase. Vapor-phase operation simplifies the physics of the system, but will introduce additional losses within the system, primarily ohmic and mass transport during the charging mode. In this chapter, we explore the performance of a proton-exchange membrane (PEM) URFC under vapor-phase conditions and the impact of different PEMs, feed gases, and relative humidity has on the performance and durability. By tailoring operating conditions and membrane, the vapor-URFC achieves a roundtrip efficiency of 42% and a lifetime of 50,000 accelerated-stress-test cycles for fully humidified feeds. Discussion of vapor-URFC for energy storage and extensions to look at various applications shows the promise of this technology.

[†] Portions of this chapter were previously published as "Fornaciari, J.C.; S. Garg, X. Peng, Y. N. Regmi, A. Z. Weber, N. Danilovic. Performance and Durability of Vapor-Fed Unitized Regenerative Fuel Cells, 2022 J. Electrochem. Soc. 169 054514" and is adapted with permission from all co-authors.

5.2 Introduction

The prevalence of distributed renewable energy sources, primarily wind and solar, is growing rapidly, and so is the need for energy storage of these inherently intermittent resources. These energy-storage systems are a necessity to provide reliable, on-demand electricity, even seasonally, where solar energy can be stored from the summer to winter months.[155,156] Typical batteries, such as lithium ion, are well-suited for short-term energy storage, on the scale of hours, but to scale them up for long-term energy storage is cost prohibitive.[7] Electrochemical generation of hydrogen gas is an attractive medium for long-duration energy storage due to high energy and power densities, and excellent long-term stability of hydrogen gas.[155] Using hydrogen gas as an energy carrier also decouples energy storage from the energy-conversion device, which is especially advantageous for large-scale energy storage due to the lower aggregated costs.[155–160] This decoupling helps to store large amounts of energy without the need of a large balance of plant. Affording the flexibility to make hydrogen gas when surplus renewable electricity is available at lower price and deploying it at a moment's notice is another advantage to these systems. Potentially, the most cost-effective route to utilize hydrogen gas as the renewable energy carrier is by using a low-temperature unitized regenerative fuel cell (URFC).[25,26,157–159,161–165] Specifically, exploring vapor-fed URFCs can provide insight into the feasibility of these hydrogen batteries to solve energy resiliency issues in off-grid and water-scarce applications.

In a reversible fuel cell (RFC), a fuel cell (FC) and water electrolyzer (WE) are combined to form a hydrogen battery system.[166–168] A unitized regenerative fuel cell (URFC) combines the FC and WE functionality into a single device, which significantly reduces capital expenses (capex).[168] URFCs can operate in two configurations,[158] constant gas (CG) and constant electrode (CE). The CE configuration has been studied more in recent years, [25,158,169,170] and is capable of higher efficiency than CG, but at the expense of lower lifetimes since the individual electrodes are exposed to a larger range of potentials.[169] The CG configuration, while sacrificing efficiency, is capable of longer lifetimes and much faster switching times. In this paper, we focus on the CG configuration, illustrated in Figure 5.1, where both oxygen reactions (eqs. 5.1 and 5.2): reduction (ORR) and evolution (OER), occur at one electrode, and both hydrogen reactions (eqs. 5.3 and 5.4): oxidation (HOR) and evolution (HER), occur at the opposite electrode.

$$\text{ORR: } O_2 + 4H^+ + 4e^- \rightarrow 2H_2O \tag{5.1}$$

$$\text{OER: } 2H_2O \rightarrow O_2 + 4H^+ + 4e^- \tag{5.2}$$

$$\text{HOR: } 2H_2 \rightarrow 4H^+ + 4e^- \tag{5.3}$$

$$\text{HER: } 4H^+ + 4e^- \rightarrow 2H_2 \tag{5.4}$$

As a result of this configuration, the device itself does not have a fixed anode and cathode; rather, the O_2 electrode acts as the cathode during FC operation and the anode during WE operation, while the H_2 electrode acts as the anode during FC operation and the cathode during WE operation. Operating in this configuration minimizes the switchover time between FC and WE operation and minimizes combustion risk by completely isolating H_2 and O_2.

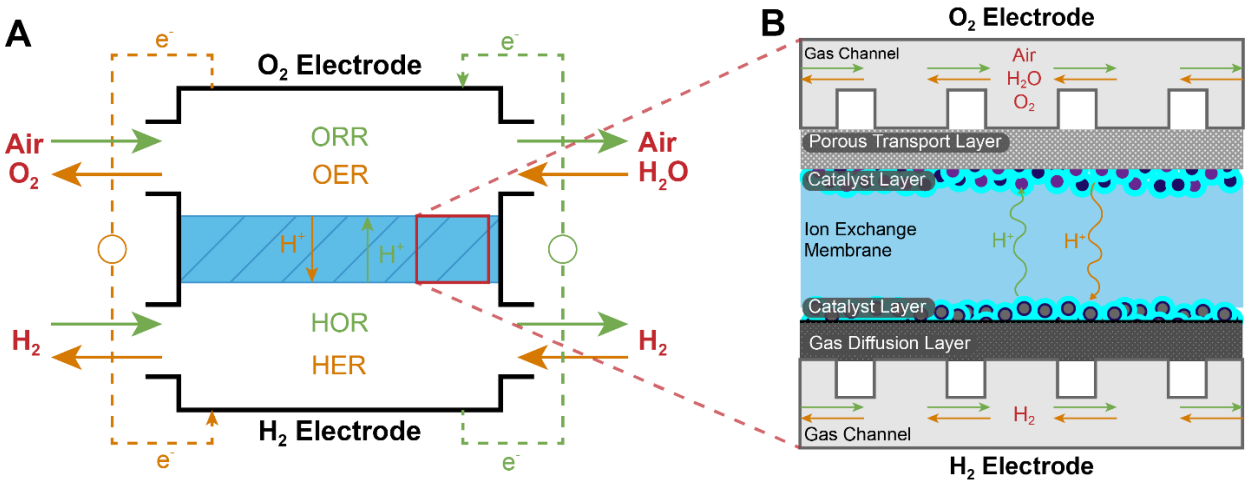

Figure 5.1: (a) Vapor-URFC schematic for constant-gas mode. (b) a cross section of the MEA used in the vapor-URFC. The water shown entering in the oxygen electrode is vapor phase and a hydrogen inlet is not needed for HER but could be fed in.

As shown in Figure 1b, a PEM-URFC consists of a membrane-electrode assembly (MEA), including two electrodes separated by the proton-exchange membrane (PEM). PEM devices typically employ perfluorinated sulfonic-acid membranes (PFSA) comprised of an inert polymer backbone and side chains terminated with sulfonic-acid groups that absorb water, thereby creating channels through which protons can be transported between the two electrodes. At each electrode there is a transport layer, either carbon gas-diffusion layer (GDL) or titanium porous-transport layer (PTL), to facilitate the transport of gaseous species to and from the catalyst layer where the electrochemical reactions take place. The catalyst layers for the hydrogen and oxygen electrodes are comprised of catalysts, ionomer, and open pores. The oxygen-electrode catalyst layer must have two catalysts, one for OER and one for ORR. In contrast, the hydrogen-electrode catalyst uses one catalyst, Pt/C, which catalyzes both HOR and HER. Thus far, research in the URFC field has been generally aimed at developing catalysts and tuning their structures,[171–173] integrated catalyst-layer structures,[74,166,170,174] porous-transport layers,[41,175,176] and membrane chemistry.[142] These factors also contribute to the overall cell efficiency and performance.[41,174]

The conventional URFC uses a liquid feed, which provides enough water for optimal proton conduction through the membrane and assures there is enough water for the reaction and hydration in WE operation. Using water vapor as a feed in place of liquid water eliminates the need for ultra-high purity deionized water, thereby simplifying operation and reducing operating and capital costs (opex and capex, respectively) at the expense for higher ohmic and transport losses through the membrane and cell. Removing the need of ultra-pure water also eliminates the need of ion-exchange resins for water purification and pumps.[177,178] Additionally, bubble formation in liquid-water fed WE complicates transport within the system by introducing multiphase flow. Vapor-fed operation eliminates these complexities and also removes the need for liquid water to be purged from the system when switching from WE to FC operation. While vapor-fed WE generates higher mass-transport overpotentials than liquid-fed,[145] the FC operation would be at an advantage as

water management would be better controlled and pore-flooding at the start of operation would be avoided.[179–184] Water management is important for these technologies and will be complicated by differential pressurization and need to be optimized, especially as electrolysis and fuel-cell modes have divergent criteria. While vapor operation can simplify to a certain extent, there are other materials solutions such as including amphiphilic diffusion layers and actively removing water from the feed. Additionally, humid ambient air can be used as a feed in both operating modes, supplying oxygen during FC operation and water vapor during WE operation. This operation eliminates the need for water purification and minimizes the switch-over time between operating modes, which brings the vapor-URFC on par with a typical battery for the balance of plant. The only storage needed is for the hydrogen gas.

This simplified operation makes the vapor URFC an attractive device in scenarios where small-scale, high-density, long-term energy storage is necessary. The advantages in such scenarios may outweigh the performance penalty incurred by using water vapor as a feed due to greater ohmic losses within the MEA. Namely, this device shows exceptional promise for off-grid energy storage in humid environments, as well as for energy storage on spacecraft and extraterrestrial habitats, where size and weight are critical constraints.

Currently there is a gap in the literature for investigating vapor-fed URFCs, their operating capabilities, and their applications. In this chapter, we baseline the performance of a vapor-fed URFC and explore how different membrane ion-exchange capacities and feed relative humidities enhance or inhibit the cell performance, specifically the roundtrip efficiency. Additionally, we apply durability protocols to assess the lifetime of such a cell. Finally, exploring two applications: off-grid and extraterrestrial, we demonstrate this device's feasibility for operation and identify additional optimization parameters.

5.3 Methods

5.3.1 Catalyst-Coated-Membrane Fabrication

Catalyst inks are comprised of catalyst particles, solvent, and ionomer. The catalyst inks for each electrode are detailed in Table 5.1. The H_2 electrode inks contain Pt/C (46.2 wt% Pt on HSC, Tanaka, Japan), with a 1:1 n-propanol (200 proof, Koptec, Pennsylvania, USA) to deionized (DI) water (18.2 MΩ, Milli-Q, EMD Millipore, Massachusetts, USA) mixture, by volume. The ionomer used was a 5 wt% Nafion™ dispersion (D521, Chemours, Delaware, USA) with an ionomer to carbon ratio of 0.6. The O_2 electrode inks contain a mixture of iridium black (SA=100, Tanaka, Japan) and platinum black (Tanaka, Japan) and used a 2:1:1 n-propanol:water:ethanol solvent mixture. The same ionomer was used in the O_2 electrode ink as the H_2 electrode ink, but the ionomer to catalyst ratio was 0.116.[74] For the H_2 electrode ink, the vial was manually shaken before sonicating in a bath sonicator (M1800, Branson, Connecticut, USA) equipped with a chiller (Grant) for 30 min at 10°C. For the O_2 electrode ink, the vial was manually shaken and sonicated using a probe-tip sonicator (CPX500, Cole-Parmer, Illinois, USA) with the vial submerged in an ice bath and covered with parafilm to prevent solvent evaporation during sonication.

Table 5.1: The catalyst recipe for the hydrogen electrode and oxygen electrode.

Component	**H_2 Electrode Ink**	**O_2 Electrode Ink**
Pt/C (46.2 wt% Pt)	65.22 mg	n/a
Platinum Black	n/a	25.00 mg
Iridium Black	n/a	25.00 mg
H_2O	17.60 g	10.00 g
N-propanol	16.08 g	14.09 g
Ethanol	n/a	7.89 g
Nafion™ D521	422.61 mg	116 mg

The Nafion™ (NR-212, Chemours, Delaware USA) and Aquivion® (E87-05S; E98-05S, Solvay, Belgium) PFSA membranes were conditioned by boiling in DI water at 100°C for one hour before being allowed to cool to room temperature and stored in DI water.

To prepare a 5 cm^2 catalyst-coated membrane (CCM), the membrane was placed on a protective fiberglass sheet and heated on the hotplate of the ultrasonic spray-coater (Sono-Tek Exacta Coater, New York, USA) under a Teflon-coated fiberglass mask and a rubber gasket. The membrane was dried at 80°C under vacuum prior to spraying the catalyst ink. For the H_2 electrode, 10 mL of ink was sprayed at a deposition rate of 0.3 mL min^{-1} to achieve a catalyst loading of 0.3 mg cm^{-2}. For the O_2 electrode, 30 mL of ink was sprayed at a deposition rate of 0.35 mL min^{-1} to achieve a total catalyst loading of 1 mg cm^{-2}.

5.3.2 Cell Assembly

Carbon-paper gas-diffusion layers (GDLs) with a microporous layer (MPL) (Sigracet 29BC, Fuel Cell Store, Texas, USA) were used for the H_2 electrode, and titanium porous-transport layers (Ti-PTL) (NEL Hydrogen, Connecticut) were used for the O_2 electrode. The Ti-PTLs were soaked in a dilute Teflon solution and dried on a vacuum hot plate at 100°C to deposit the desired amount of PTFE, 5 wt%, onto the PTL. The PTLs were then baked in a tube furnace at 400°C in Argon to crystalize the PTFE. PTFE gaskets (McMaster-Carr, Illinois, USA) were used on both sides, the PTFE gasket is thickness matched to the Ti-PTL, and 20% compression of the carbon GDL. Electrochemical cells from Fuel Cell Technologies (FCT, New Mexico, USA) equipped with graphite serpentine flow fields and gold-plated copper current collectors were used for testing. Graphite serpentine flow fields were used to assure no leaks are occurring in the system and when tested and compared to titanium flow fields, there was no change in performance. Graphite flow

fields showed minimal oxidation under the testing conditions and duration on both the H_2 and O_2 sides.[145]

5.3.3 Cell Testing

A potentiostat (Biologic, France) with electrochemical-impedance-spectroscopy capabilities and a 20 A booster was used for all electrochemical tests, and a fuel-cell test stand (FCT) was used to regulate cell operating conditions and feed gases. The cell was heated with FCT rod heaters, and a thermocouple in the endplate of the cell was used to maintain the cell at 80°C throughout testing. The gas feed lines were maintained at 85°C throughout testing, and DI water was used to humidify the gases before being fed to the cell. To note, these tests are run to assure better membrane hydration on the cathode and the humidity remains at 100% RH. However, in actual operation, running the system with high humidity on the hydrogen side would require an extra step of drying the system and could lead to lower overall system efficiency.

Prior to FC testing, the cell was conditioned by running chronoamperometry (CA) at 100 mV cell potential for 16 to 20 hr until the current stabilizes with air flowing at 700 mL min^{-1} at the O_2 electrode and H_2 flowing at 300 mL min^{-1} at the H_2 electrode, and no applied backpressure. The flow rates were then increased to 1000- and 450-mL min^{-1} at the oxygen and hydrogen electrodes, respectively, and the backpressure at both electrodes was set to 21 lb in^{-2}. High stoichiometric feeds were used to test the system to maintain differential conditions. For example, the stoichiometric feed was 5 for hydrogen and 10 for air at 1 A cm^{-2}. However, it is important to note that these are not practical operating conditions. To assess FC performance, a series of constant current holds were carried out: 1 min current holds were used for current densities below 0.2 A cm^{-2}, and 3 min current holds were used for current densities at or above 0.2 A cm^{-2}. The current was ramped up in steps of 20 mA cm^{-2} or 200 mA cm^{-2}, within the kinetic or ohmic regimes, respectively. The cell potential was averaged across the last 30 s of each step and across the ramp-up and ramp-down to generate a polarization curve. Electrochemical impedance was measured at every current density to generate a Nyquist plot, where the intercept with the real axis is the reported high-frequency resistance (HFR) of the cell

For WE testing, the flow rates were set to 450 mL min^{-1} of N_2 (corresponding to a stoichiometric feed of 10 at 1 A cm^{-2}) at the O_2 electrode and 100 mL min^{-1} of H_2 at the H_2 electrode. Flowing H_2 during electrolysis operation helps establish a stable reference electrode. Performance was assessed in a similar manner as FC mode, with the current increased stepwise from 5 mA cm^{-2} until the cell potential reached 2.1 V before ramping back down. Polarization curves were generated using the same method as FC polarization curves. The data analysis was performed using a Python code to generate the polarization curve, HFR, and Tafel slope.[185]

Accelerated-stress tests (ASTs) were performed on the down-selected MEA to assess the durability and stability of the vapor URFCs.[186,187] A sawtooth cycling profile was used, with the potential limits set to 0.55 and 1.55 V and a scan rate of 300 mV sec^{-1}.[168] These limits were chosen as they correspond to current densities of approximately –1 and 1 A cm^{-2}, respectively. At regular and convenient intervals, the cycling was stopped, and FC and WE performance were assessed using

the methods described above. The cycling continued until the cell no longer achieved a current density of 1 A cm^{-2} in either FC or WE mode, which was designated as end of test (EOT).

5.4 Results and Discussion

5.4.1 Liquid-Water vs. Water-Vapor Performance

To compare URFC performance with a liquid-water feed to that with a water-vapor feed for WE operation, CCMs were prepared with a Nafion™ 1100 membrane. Since the FC operation is usually operated with highly humidified gases, we initially compare the WE performance. As illustrated in Figure 5.2, the performance using a water-vapor feed is significantly reduced compared to that using liquid water. The vapor-fed URFC requires 1.78 V at 1.0 A cm^{-2} where the liquid-fed URFC reached the same current density at 1.54 V. One major difference between the two feeds is the HFR. The HFR increases with increasing current density for the vapor-fed cell, indicating larger ohmic losses at elevated current densities. The HFR for the liquid-fed cell remains low and constant (0.09 Ω cm^2). Compared to Chapter 4, the vapor electrolysis is majorly improved due to the thinner membrane (50 vs 180 μm). Consistently with the previous chapter, vapor electrolysis shows higher ohmic losses due to membrane dehydration and localized mass-transport limitations in the catalyst layer.[145] Regardless, the vapor-fed URFC achieved 42% roundtrip efficiency (RTE, calculations are in the SI) at 1 A cm^{-2}. The liquid-fed cell can achieve >50% for the RTE at 1 A cm^{-2}, although engenders a more complicated balance of plant and switching time between operation modes.

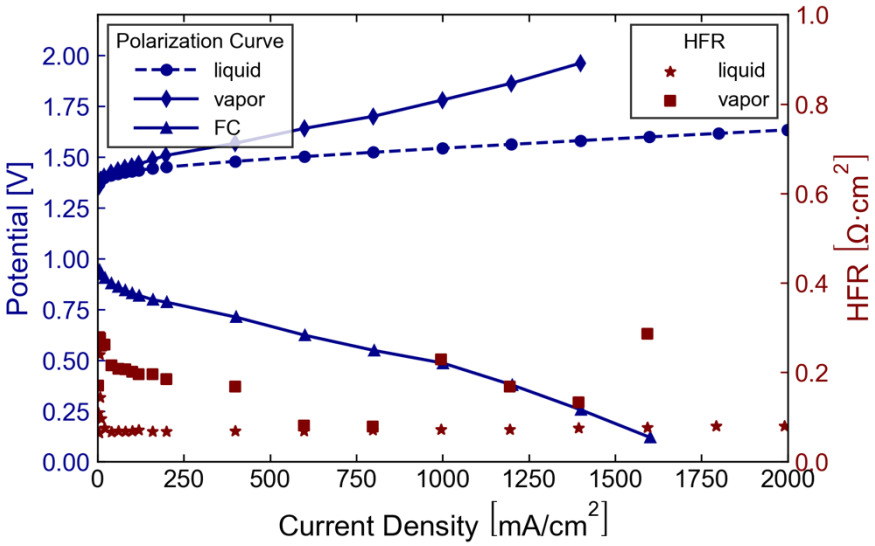

Figure 5.2: Vapor WE performance is compromised relative to the liquid WE due to greater ohmic losses. The left axis corresponds to WE performance, and the right axis shows the WE HFR.

5.4.2 Membrane comparison (1100 vs. 980 vs. 870)

While maintaining a constant membrane thickness (50 μm), we explore the effects of equivalent weight (EW) on URFC performance and efficiency using 3 membranes (Table 5.2). A membrane's EW is equal to the moles of water per ionic group, which is inversely proportional to the ion-exchange capacity.[142] Lower EW membranes were expected to improve device performance because the higher fraction of ionic groups should lead to high water uptake and thereby improve membrane hydration.[142] Better membrane hydration reduces ohmic losses across the membrane, resulting in lower overpotential. However, as shown in Table 5.2, Nafion™ 1100 exhibited the best performance of the three membranes tested, achieving 42% ± 2% RTE at 1 A cm^{-2}, and the polarization curves and HFR for each of the membranes are shown in the Figure 5.3. The trend continues in the direction of lower EW leading to higher overpotentials. The HFR for Aquivion® 870 was significantly higher than that for both Nafion™ 1100 and Aquivion® 980, suggesting that higher ohmic losses can account for the majority of the poor performance of this membrane. However, the HFRs for Aquivion® 980 and Nafion™ 1100 were similar for FC operation, differing some in WE operation. While the HFR differs in WE operation, other factors may result in the poorer performance of Aquivion® 980. Those factors may include different mass transport within the MEA or membrane swelling impacting the amount of electrochemically active catalyst in the layer, as the lower the EW results in higher swelling.[188,189] Additionally, using the Nafion ionomer in the catalyst layer with Aquivion membranes could lead to a mass transport loss due to the ionomer/membrane interface.

Table 5.2: The equivalent weight, cell RTE (%), and HFR [Ω cm^2] for all three membranes at 1 A cm^{-2}

Membrane	**Equivalent Weight [g/mol]**	**RTE [%] at 1 A cm^{-2}**	**HFR [Ω cm^2] at 1 A cm^{-2} in FC operation**	**HFR [Ω cm^2 at 1 A cm^{-2} in WE operation**
Nafion™	1100	42%	0.120	0.093
Aquivion®	980	32%	0.123	0.124
Aquivion®	870	35%	0.224	0.165

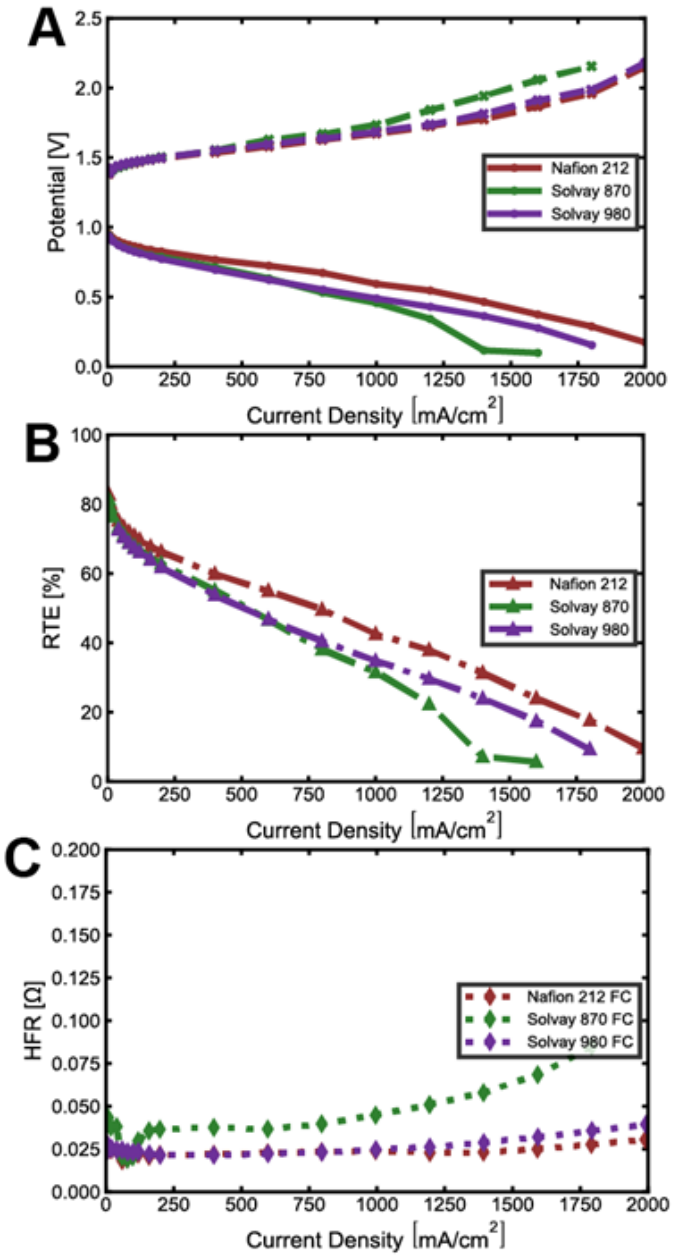

Figure 5.3. (a) Polarization curves during both FC (solid) and WE (dashed) operation for MEAs using the three membranes tested (Solvay is the same as Aquivion). (b) RTE for MEAs using the three membranes tested. (c) HFR during WE operation for the MEAs using the three membranes.

5.4.3 Relative-Humidity Experiments

Regardless of whether the performance loss associated with the Aquivion® membranes can be attributed to membrane swelling or an interfacial loss, reducing the amount of water available as reactant should result in performance loss for a system. Ideally, real-life applications would result

in the cells operating at less than 100% relative humidity (RH). Quantifying the loss due to the reduction in water availability can provide a guide for lower-humidity applications. Therefore, all three membranes were tested at RHs ranging from 52 to 122% RH at 80°C to gain insight into the importance of the rate of water fed into the vapor-fed URFC and the comparison to the liquid electrolyzer. As discussed earlier, decreasing membrane hydration increases ohmic overpotentials and in vapor-fed system is dependent on the vapor pressure. As shown in Figure 5.4 for Nafion™ 1100, the difference in potential were minimal at higher RHs, including the oversaturated case at 122%. The oversaturated test did not result in performance enhancement approaching the liquid electrolysis. Instead, oversaturated feed resembles the 100% RH vapor electrolysis, which indicates that although there is more water available to react, the system is still limited by other factors. The higher RH could lead to some condensing in the channels of the cell and the local RH at the MEA may be lower, something to explore in future work and is out of the scope of this paper.

As expected, the largest loss in performance is observed for the 52% RH test, showing a non-monotonic increase in potential with current density. Decreasing the RH reduces the amount of water available for the OER and membrane hydration. This decrease in water content manifests in the decrease in RTE from 42% at 100% RH to 37% RTE at 52% RH. Across the full range of RHs, Nafion™ 1100 exhibited the best performance relative to either Aquivion® membrane, regardless of the RH. Nafion™ 1100 exhibited an RTE of 37% at 52% RH, while Aquivion® 870 had an RTE of 33% at 122% RH. The difference between these tests could is revealed when comparing the EW and the respective HFR, as shown in Table 5.2, revealing that for higher EW membranes, less water is available to react in the vapor phase even at higher RHs.

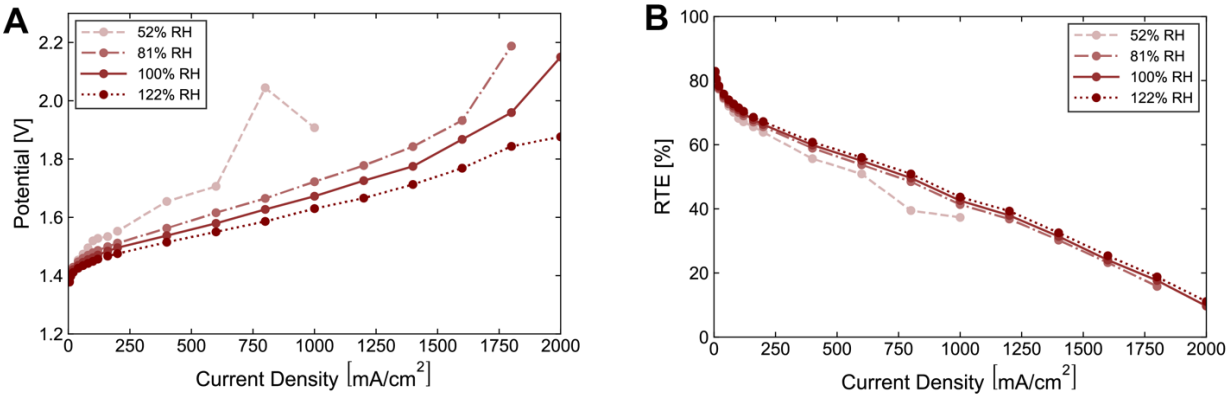

Figure 5.4: a) Nafion™ 1100 WE performance between 81 to 122% RH, with a significant decrease at 52% RH. b) RTE for the different RH feeds.

5.4.4 Durability

ASTs were used to assess device durability and to mimic start-up/shut-down or different duty cycles for these systems at both 100% RH and 75% RH to observe two different durability cases, shown in Figure 5.5. Although beginning-of-test (BOT) performance is similar for the 100% and 75% case (42% and 38% RTE, respectively), degradation occurs more rapidly at 75% RH as the lower humidity is a stressor in FC and WE operation. As seen in Figure 5.5a at 100% RH, the cell retained 78% of BOT performance after 7,000 charge/discharge cycles and 52% of BOT performance after 20,000 cycles, with EOT after 50,000 cycles. EOT is defined here as the point at which the cell could no longer sustain a current density of 1 A cm^{-2} for either test. In Figure 5.5b, at 75% RH, the cell retained 76% of BOT performance after 1,000 charge/discharge cycles and 37% of BOT performance after 7,000 cycles, with EOT after 20,000 cycles. Converting these cycle lifetimes into temporal lifetimes depends on the duty cycle in operation. For example, assuming a daily duty cycle resulting from load-shifting solar power in off-grid applications, the 100% and 75% RH cells would retain approximately 75% of BOT performance after 19 years and 3 years, respectively.

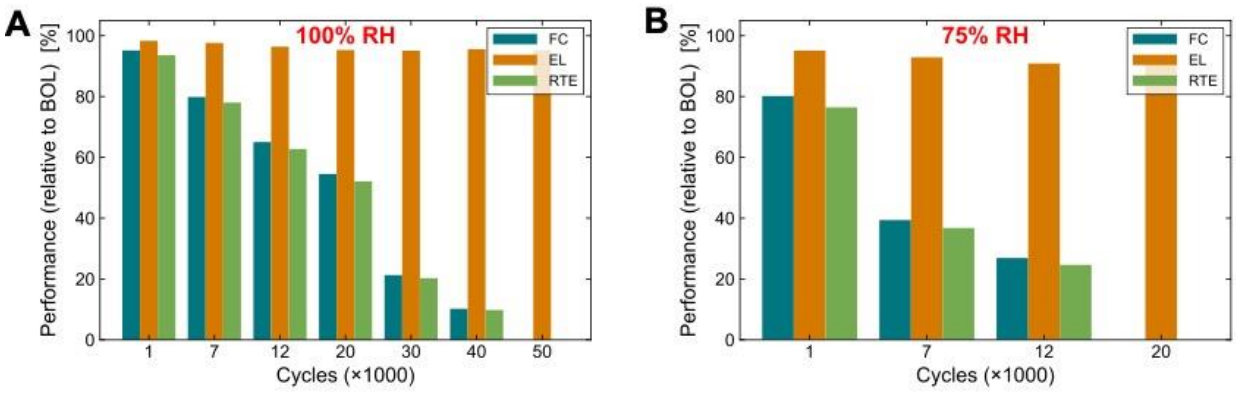

Figure 5.5: AST cycles and performance compared to beginning of life (BOT) for the vapor-URFC at (a) 100% RH and (b) 75% RH.

In both cases, WE performance remained constant for the duration of the AST, indicating that a loss of FC performance drives efficiency loss.[168] As shown in Figure S5.1, the voltage-loss breakdown for the FC performance indicates the kinetic and mass-transport loss is a large fraction of the voltage loss seen at EOT (Figure S5.2 shows the WE operation applied-voltage breakdown). We acknowledge that the AST protocol may not account for all degradation mechanisms that would occur during a realistic 24-hour charge/discharge cycle; however, these results are promising and suggest that this type of device could be used for the applications discussed in this chapter.

5.4.5 Impact of oxygen carrier gas

The vapor-URFC is most desirable for off-grid or extraterrestrial applications as the balance of plant is minimized and can provide on-demand hydrogen and electricity. For off-grid applications, operating at ambient humidity is necessary, since the air would not be humidified further before feeding it to the URFC. However, as shown in Figure 5.4, the limitation on the electrolyzer performance is already drastic at 52% RH. These losses seen at 52% RH could be mitigated by controlling water management within the cell and better utilization of the catalyst layer.[145] Further optimization of the MEA and technoeconomic analysis is required for fully understanding how this technology can be used as an off-grid long-term energy storage system. It should be noted that water recycling concepts that capture and use water generated during FC operation for increasing ambient RH during WE, or connections to local water sources, could help ameliorate these concerns although at a cost of system complexity.

When evaluating different applications, such as extraterrestrial, the feed gas at the oxygen electrode is another consideration. Humidifying air or carbon dioxide as a carrier gas could be other opportunities to utilize different ambient feeds. As shown in Figure 5.6a, at 100% RH, there was no significant change in RTE when air was used during WE operation in place of N_2, indicating that it is not necessary to switch from air to an inert gas at the O_2 electrode when switching from FC to WE operation in this mode. Shown in Figure 5.6a, the electrolyzer polarization curves increased by 55 mV at 1 A cm^{-2} when using air versus nitrogen, which can be accounted for the small change in diffusivity.[145] By maintaining constant gas flows at both electrodes, the device will be much simpler and more reliable for off-grid energy storage.

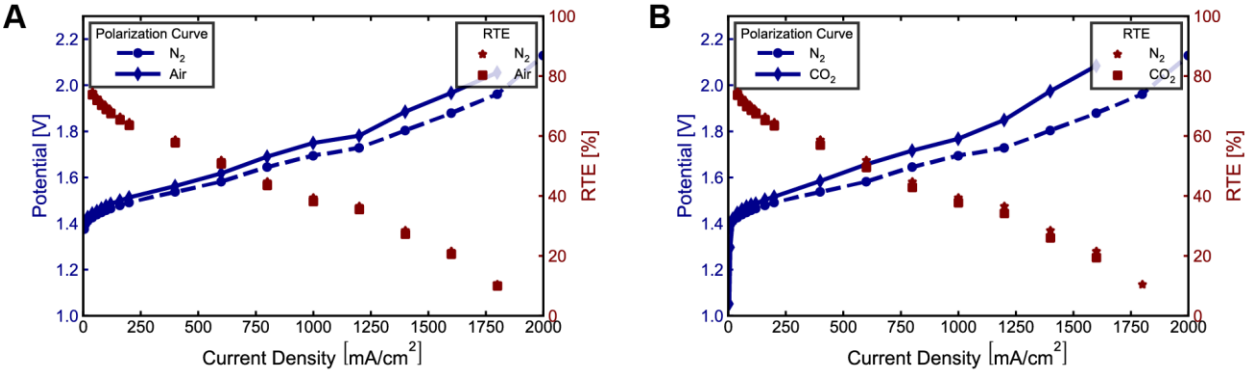

Figure 5.6: The electrolyzer polarization curve and RTEs for vapor-URFC with a) nitrogen and air at the oxygen electrode and b) carbon dioxide and nitrogen. The FC performance remains the same for these tests.

For applications in spacecraft and extraterrestrial habitats, it would be desirable to use humid CO_2 as a carrier gas during WE. Air would be a precious resource and repurposing captured CO_2 from human respiration would eliminate the need for carrying a source of nitrogen and all of the requisite supporting equipment (tanks, *etc*.). Additionally, operating at lower RH is better since water is also a limited resource. Figure 5.6b shows at both 100% RH, there was no significant change in RTE when CO_2 was used during WE operation in place of N_2, indicating that CO_2 is a viable

carrier gas for water vapor during WE operation. A disadvantage to using CO_2 as the feed gas is when the URFC is run at high pressures, hydrogen could potentially interact with CO_2 and lead to catalyst poisoning via the water gas shift reaction; further testing with CO_2 as the pressurized feed gas is required to assure catalyst poisoning does not happen. Additionally, it may be desirable to use either air or pure O_2 during FC operation depending on the availability of gases and/or to improve device performance.

5.5 Summary

In this chapter, we presented a parametric study of vapor-URFC components and operating conditions, focusing on membrane EW, the feed RH, and the oxygen-electrode carrier gas. We found that a higher EW membrane correlates with improved device performance, most likely as a result of better water transport and less swelling of the membranes during operation. When operating at 100% RH, the vapor-URFC achieved an RTE of 42 ± 2%, which is comparable to state-of-the-art for vapor-URFC to date. The device still achieved 37% RTE at 52% RH, indicating that the device is robust over a range of RHs. The vapor-URFC exhibited excellent long-term stability and sustained 1 A cm^{-2} for 50,000 and 20,000 AST cycles at 100 and 75% RH, respectively. The device performance was also agnostic to the oxygen electrode carrier gas, which emphasizes the flexibility of this device to fit niche markets. Specifically, proof-of-concept results using O_2, N_2, and CO_2 as carrier gases demonstrate the viability of the vapor-URFC for off-grid and extra-terrestrial applications.

5.6 Supplemental Information

5.6.1 Round-Trip-Efficiency (RTE) Calculation

The overall cell reaction in the URFC is

$$\mathrm{H_2} + \frac{1}{2}\mathrm{O_2} \leftrightharpoons \mathrm{H_2O} \tag{S5.1}$$

Where the reversible potential of the overall reaction is given by the Nernst Equation[190]

$$E_{rev}(T,P) = E^0_{rev} + \frac{RT}{2F} ln\left[\frac{\mathrm{a_{H_2}} \cdot \sqrt{\mathrm{a_{O_2}}}}{\mathrm{a_{H_2O}}}\right] \tag{S5.2}$$

The activities of gaseous species,a_{H_2} and a_{O_2}, are defined by

$$a_j = \frac{P_j}{P_0} \tag{S5.3}$$

where P_j is the partial pressure of species j, and P_0 is the standard pressure of 1 bar. The activity of liquid water, a_{H_2O}, is taken to be one by convention.[190] The reversible potential at standard conditions, E^0_{rev}, is[191]

$$E^0_{rev} = 1.2291\,V - 0.0008456(T - 298.15\,K) \tag{S5.4}$$

The fuel cell efficiency is calculated by[168]

$$Eff_{FC} = \frac{V_{measured}}{E_{rev}(T,P)} \tag{S5.5}$$

where $E_{rev}(T,P)$ at the testing conditions is calculated to be 1.168 V.

The electrolyzer efficiency is calculated by[168]

$$Eff_{WE} = \frac{E_{rev}(T,P)}{V_{measured}} \tag{S5.6}$$

where $E_{rev}(T,P)$ is the thermoneutral potential of 1.42 V.[192]

The RTE is calculated thus from[168]

$$RTE = Eff_{FC} \cdot Eff_{WE} \tag{S5.7}$$

5.6.2 Relative-Humidity Calculation

Relative humidity is defined as[193]

$$RH = \frac{P_{H_2O}}{P_{H_2O}^{sat}} \tag{S5.8}$$

where, in this case, P_{H_2O} is the saturation vapor pressure of H_2O at the dew point temperature, and $P_{H_2O}^{sat}$ is the saturation vapor pressure of H_2O at the URFC operating temperature. We use the August-Roche-Magnus formula to approximate these vapor pressures from temperature (T)[194]

$$P^{sat} = 6.1094\, exp\left(\frac{17.625T}{T + 243.04}\right) \tag{S5.9}$$

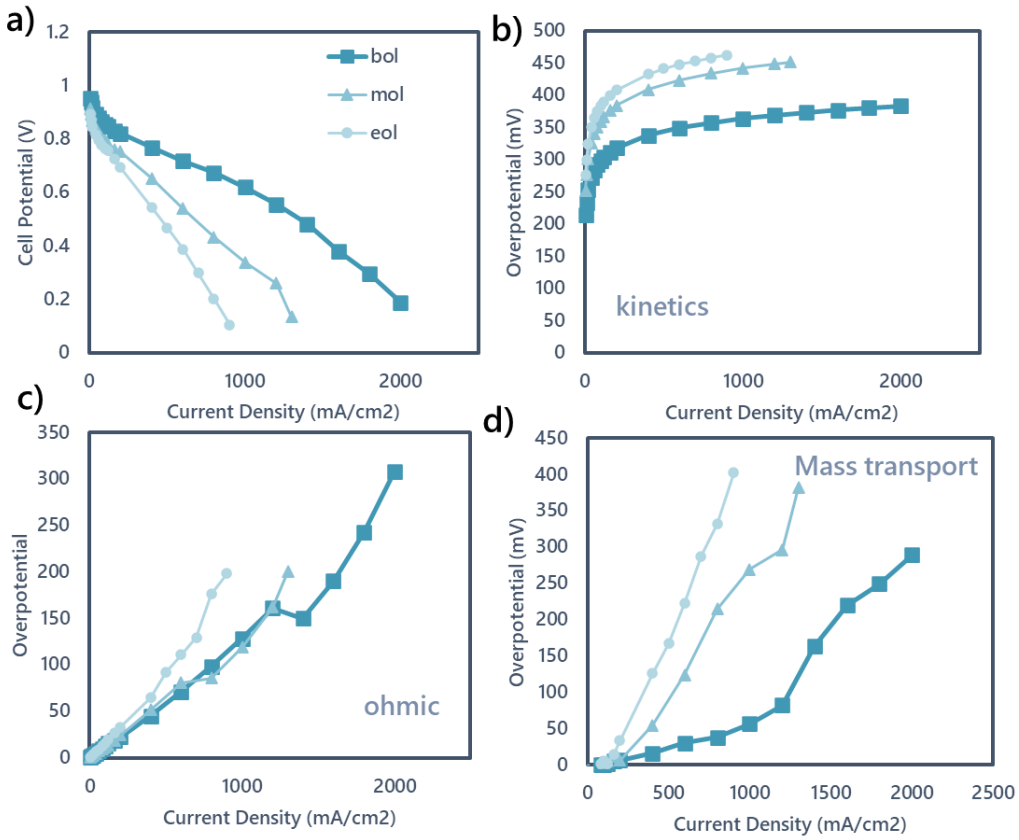

Figure S5.1: Voltage-loss breakdown in FC operation for the beginning of test (BOT, squares), middle of test (MOT, triangles) and end of test (EOT, circles). The polarization curves are shown in a. The overpotentials are shown for (b) kinetics, (c) ohmic, and (d) mass transport.

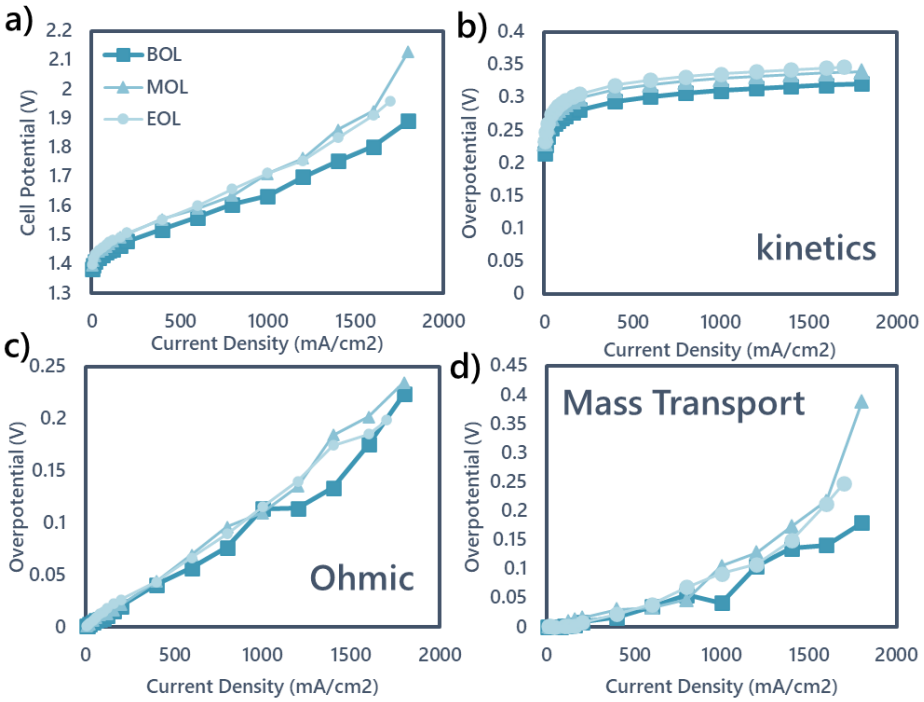

Figure S5.2: Applied-voltage breakdown in WE operation for the beginning of test (BOT, squares), middle of test (MOT, triangles) and end of test (EOT, circles). The polarization curves are shown in (a). The overpotentials are shown for (b) kinetics, (c) ohmic, and (d) mass transport.

6. Electrochemical Oxidation of Methane to Methanol in Membrane Electrode Assemblies[†]

6.1 Abstract

High rate and high yield, direct conversion of methane to methanol has been a long-sought objective. Partial oxidation by thermal catalysis is possible but suffers from a rapid loss in methanol selectivity with increasing methane conversion. More recently, the electrochemical oxidation of methane, using water, rather than oxygen, as the oxidizing agent has been considered in both aqueous electrolyte systems and membrane-electrode assemblies (MEAs). While promising results have been demonstrated using MEAs, the absence of key metrics of system performance make it hard to compare and contrast the results of different investigators. This chapter examines why MEAs are well suited for the electrochemical oxidation of methane, defines the metrics for assessing MEA performance, reviews the progress in the field, and reports on preliminary experimental findings. An analysis of the challenges in finding suitable electrocatalysts is included with the aim of guiding the search for electrocatalysts that would be both active and selective for the conversion of methane to methanol.

[†] Portions of this chapter were previously published as "Fornaciari, J.C.; Primc, D.; Kawashima, K.; Wygant, B.R.; Verma, S.; Mullins, C. B.; Bell, AT; Weber, A.Z. A Perspective on the Electrochemical Oxidation of Methane to Methanol in Membrane Electrode Assemblies. ACS Energy Letters 2020, 5, 9, 2954–2963" and are adapted with permission form all co-authors.

6.2 Introduction

There has been a longstanding interest in identifying processes for the direct conversion of methane to chemicals and fuels due to geographic availability and affordable cost of natural gas.[40,195] The current approach to methane conversion to products is indirect. Methane is steam reformed to synthesis gas, a mixture of CO and H_2, which is then used to produce products via either methanol or Fischer-Tropsch synthesis. While used today to produce methanol, indirect methane conversion is energetically unattractive for production of transportation fuels and chemicals.[195] We note as well that indirect methane conversion processes (e.g., methanol production) have a high CO_2 footprint because not all of the combusted methane is converted to synthesis gas.[40,195] These considerations have motivated the search for processes that enable the direct oxidation of methane to products, such as methanol or formaldehyde (Eqs. 6.1 and 6.2):

$$\mathrm{CH_{4(g)}} + \frac{1}{2}\mathrm{O_{2(g)}} \rightarrow \mathrm{CH_3OH_{(\mathit{l})}} \qquad \Delta G^0 = -115\ \mathrm{kJ/mol} \qquad (6.1)$$

$$\mathrm{CH_{4(g)}} + \mathrm{O_{2(g)}} \rightarrow \mathrm{CH_2O_{(\mathit{g})}} + \mathrm{H_2O_{(\mathit{l})}} \qquad \Delta G^0 = -296\ \mathrm{kJ/mol} \qquad (6.2)$$

$$\mathrm{CH_{4(g)}} + \mathrm{O_{2(g)}} \rightarrow \mathrm{CO_{2(g)}} + 2\mathrm{H_2O_{(\mathit{l})}} \qquad \Delta G^0 = -818\ \mathrm{kJ/mol} \qquad (6.3)$$

Thermal partial oxidation of methane over a catalyst is difficult to achieve because the Gibbs Free Energy for the complete combustion of methane to CO_2 and H_2O (Eq. 6.3) is considerably more favorable than that for the partial combustion to methanol and formaldehyde. The high temperatures needed to activate methane create further complications because formaldehyde decomposes to CO and H_2 and methanol can undergo complete combustion. Consequently, high selectivity to formaldehyde and methanol are only attainable at low methane conversions.[56,58,196] Given the difficulties associated with the thermal partial oxidation of methane, interest has arisen in examining the possibility of oxidizing methane to methanol electrochemically at low temperatures (< 150°C) using water (vapor) as the oxidant. We note that in the case of electrochemical oxidation, using water as the oxidant, the difference in Gibbs Free Energy for the oxidation of methane to methanol differs from that for the full oxidation to CO_2 by only 9 kJ mol^{-1} (Eqs. 6.4-6.6). This small difference in energy suggests that it may be possible to achieve selectivity to methanol at appreciable conversion levels using an appropriate electrocatalyst. In addition, we are entering an era of more affordable electrical energy produced from renewable sources (e.g., wind and solar), and thus electrochemical processes are increasingly attractive in terms of cost as well as the potential for lowering the CO_2 footprint for traditional thermochemical conversions (e.g., methane to methanol). In this chapter, we discuss the partial oxidation of methane to methanol via electrochemical systems, and focus on a potential system, a membrane-electrode assembly (MEA). The progress in this field is also reviewed. Furthermore, we provide recommendations for selecting electrocatalytic materials for efficient methane-to-methanol conversion.

$$CH_{4(g)} + H_2O_{(l)} \rightarrow CH_3OH_{(l)} + H_{2(g)} \qquad \Delta G^0 = 121 \text{ kJ/mol} \qquad (6.4)$$

$$CH_{4(g)} + H_2O_{(g)} \rightarrow CH_2O_{(g)} + 3H_{2(g)} \qquad \Delta G^0 = 178 \text{ k J/mol} \qquad (6.5)$$

$$CH_{4(g)} + 2H_2O_{(l)} \rightarrow CO_{2(g)} + 4H_{2(g)} \qquad \Delta G^0 = 130 \text{ k J/mol} \qquad (6.6)$$

Different electrochemical systems have been explored for the electrochemical oxidation of methane to methanol. As illustrated in Figure 6.1, these fall into two main types.[39,197–210] The simplest is an aqueous electrolyte cell comprising working and counter electrodes (or anode and cathode) immersed in an aqueous electrolyte, as shown in Figure 6.1a, and, in some cases, may include a third electrode, a reference electrode, to define the working and counter electrodes relative to the electrolyte. The working electrode could also be a gas-diffusion electrode, which helps distribute the gas product more efficiently (Figure 6.1a). Since we can differentiate between the working and the counter electrode, we call these arrangements half-cells.

While aqueous electrolyte cells are useful for rapid evaluation of catalyst activity and selectivity at the working electrode, they cannot achieve the high current densities required for industrial processes (200 to 1000 mA cm^{-2}). This limitation is because of poor mass transfer of methane dissolved in the electrolyte and low solubility of nonpolar methane in aqueous electrolytes limit the current density to < 20 mA cm^{-2}.[37,57,211] Product separation is also concerns for aqueous systems because soluble products may undergo complete oxidation.[37] A method for avoiding this is to distill these products from the electrolyte.[39] Since methanol has a boiling point of 65°C,[212] it can be selectively evaporated from aqueous electrolytes by elevating the aqueous electrolyte temperature (~ 80°C).[39] However, elevated temperature lowers the methane solubility in aqueous electrolytes, and hinders the achievement of high current densities. We note that while distillation might be used for exploratory scale studies, this separation method would not be useful in practice because the energy costs for separation would outweigh the fuel value of the products. MEAs, which are illustrated in Figure 6.1b, offer a means to overcome these limitations.

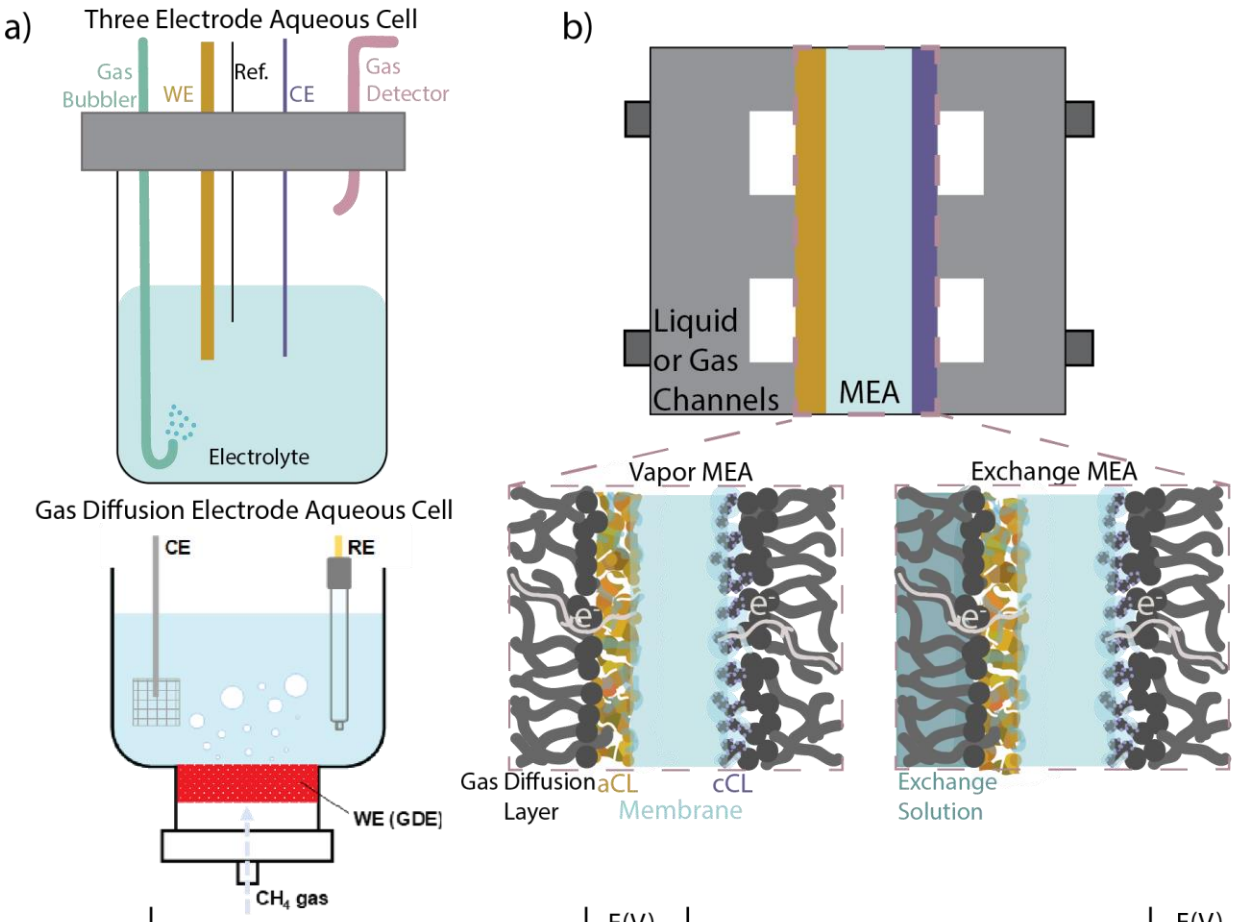

	PEM	E(V) vs SHE	HEM	E(V) vs SHE
Anode Reactions:	$CH_4 + H_2O \rightarrow CH_3OH + 2H^+ + 2e^-$	0.58	$CH_4 + 2OH^- \rightarrow CH_3OH + 2H_2O + 2e^-$	-0.18
	$2H_2O \rightarrow O_2 + 4H^+ + 4e^-$	1.23	$4OH^- \rightarrow O_2 + 2H_2O + 4e^-$	-0.40
Cathode Reactions:	$O_2 + 4H^+ + 4e^- \rightarrow 2H_2O$	1.23	$O_2 + 2H_2O + 4e^- \rightarrow 4OH^-$	-0.40
	$2H^+ + 2e^- \rightarrow 2H_2$	0.00	$H_2O + 2e^- \rightarrow H_2 + 2OH^-$	-0.83

Figure 6.1: a) Half-cell set ups for three-electrode and gas diffusion electrode aqueous test cells. b) The testing MEA cell and in the insets, the vapor membrane electrode assembly and the exchange membrane electrode assembly. The desired and potential reactions are shown below for the PEM and HEM cases.

The MEA architecture can be either fully vapor-fed or have a liquid electrolyte solution (e.g., KOH) fed on one or both sides of the cell, to help regulate the pH and microenvironment around the catalyst.[37,57] The key feature of the MEA architecture is efficient reactant and product transport to and from the catalyst layer and minimal ohmic loss through the membrane. MEAs have been used successfully for fuel cells, electrolyzers (see previous chapters), and other energy-conversion technologies, and are, therefore, a potentially ideal architecture for the partial oxidation of methane to methanol. As shown in the insets in Figure 6.1b, the MEA consists of an ionically conducting separator or membrane on one side of which is an anode catalyst layer (aCL) and on the other side is a cathode catalyst layer (cCL). The ion-conducting medium between the two CLs can be a

ceramic or a polymer (proton- or anion-conducting), typically ~ 100 μm thick. Gas-diffusion layers (GDLs) are located on the outside of the CLs to enhance transport of reactants and products as well as facilitate electron transport to and from the CLs. To assure sufficient transport of ions to and from the catalyst nanoparticles in the CLs, the catalyst nanoparticles are coated with an ionomer, which typically has properties similar to those of the membrane separator. The ionomer also provides a bridge for ion transport to the membrane. The porous CLs and GDLs can are also termed gas diffusion electrodes (GDEs) which can be used in both aqueous and gas fed systems.[37] Note that the complete oxidation of the products can be suppressed by moderating the cell temperature as well as accelerating the mass transport of methanol away from the electrode surface.[197,213,214] Methanol transport can also be enhanced through electrode surface shapes and reactant gas flow.[213–215]

The two most critical parts of an MEA are the catalyst and the ion-conducting medium, i.e., ionomer and membrane. The ionomer and the membrane often set the upper limit on the MEA operating temperature and must exhibit high ionic and electronic conductivity in order to minimize internal impedance of the cell. Both ceramics and polymers have been used as membranes, and each type has its advantages and disadvantages. A ceramic membrane must be operated at elevated temperatures, typically 100 to 300°C in order to exhibit adequate ionic conductivities of 0.06 to 0.2 S cm^{-1}, respectively.[216] Operation at elevated temperatures can be advantageous, since it facilitates the activation of methane; however, preventing full oxidation may be more difficult.[217] A disadvantage of ceramic separators is their brittleness, which can limit their service life due to cracking and result in long startup and shutdown times. On the positive side, though, ceramic separators exhibit minimal product crossover.[216,218] Polymeric membranes can achieve a conductivity of ~ 0.1 S cm^{-1} at ambient temperatures but in order to do so they must be fully hydrated.[142,217] This limits their operating temperature to below 100°C and requires maintaining the membrane in a hydrated state.[142] Moreover, polymeric membranes generally have a methanol crossover issue, although this could be advantageous in recovering methanol without further oxidation.[219] Typically, proton-exchange membranes (PEMs) (e.g., Nafion and sulfonated poly (ether ether ketone) (SPEEK)) are used since they have higher stability and are commercially mature.[142,220] A further advantage of PEMs is that they have been optimized for integration into an MEA. This includes well-established methods for fabricating the CLs using PEM ionomer dispersions. Hydroxide-exchange membranes (HEMs) or carbonate-exchange MEAs face stability and low conductivity issues. While researchers can mitigate the conductivity issue by using the exchange-MEA illustrated in Figure 6.1b, improving the stability and durability of these membranes remains the subject of ongoing research.[221]

Figure 6.1 lists the reactions that can occur during methane oxidation and their standard potentials (vs. standard hydrogen electrode (SHE)) in acidic and basic conditions. In Figure 6.1, the activation of methane to methanol occurs at the anode, where the competing reaction is the oxidation of water if at oxidizing potentials. To minimize the oxidation of methanol, the anode catalyst should have a low activity for the full oxidation for the following reactions,

$$CH_3OH + H_2O \rightarrow CO_2 + 6\,H^+ + 6\,e^- \qquad U = 0.046\ V\ vs\ SHE \quad (6.7)$$

or

$$CH_3OH + 6OH^- \rightarrow CO_2 + 5\,H_2O + 6\,e^- \qquad U = 0.03\ V\ vs\ SHE \quad (6.8)$$

for an MEA containing a PEM or a HEM, respectively. Therefore, the selective production of CH_3OH requires that the anode catalyst be much more active for methane than methanol oxidation. We discuss how these requirements might be met in more detail below.

The reactions listed in the table associated in Figure 6.1 show that either electrochemical system can be operated in galvanic or electrolytic mode. In the first case (galvanic), the protons produced at the anode react with O_2 to form H_2O, via the oxygen-reduction reaction (ORR), and in the second case (electrolytic) the protons combine and to release H_2, via the hydrogen-evolution reaction (HER), at the cathode. The advantage of operating in the galvanic mode is the cell can generate electricity through the spontaneous reactions and that the cell voltage never reaches highly oxidizing potentials, thereby mitigating the competing reactions at the anode (i.e., the oxygen-evolution reaction (OER) typically requires a potential of > 1.5 V due to kinetic issues as discussed in Chapter 3). However, operation in the galvanic mode requires two demanding reactions, the oxidation of methane to methanol at the anode and the ORR at the cathode. The sluggish ORR can limit the maximum current density within the MEA and the excess O_2 feed could crossover and further oxidize products at the anode. By contrast, in the electrolytic mode, the HER is a facile reaction and can establish a stable counter electrode potential, providing a clear reference potential to which one can relate the potential for product formation at the anode. Operation in the electrolytic mode requires a supply of electricity to drive the reactions, although hydrogen is produced as a valuable byproduct.

6.3 Evaluation of Cell Performance

In this section, we discuss the metrics for evaluating the performance of an MEA for the case of anodic activation of methane in a PEM MEA. An overall metric for the performance of an MEA is the energy efficiency (EE), which is defined as the amount of methanol produced by the cell compared to the electrical energy consumed. The EE is the product of the coulombic efficiency (CE) and the voltaic efficiency (VE),

$$\mathrm{EE} = \mathrm{VE} \times \mathrm{CE} \tag{6.9}$$

Both CE and VE are influenced by the transport of species and the number of reactions occurring at a single electrode as well as the operating conditions of the cell (cell potential, temperature, feed flow rate, etc.). In terms of the transport processes, since there are many fluxes in a MEA, it is important to identify them and understand their origin. As shown in Figure 6.2 for the PEM MEA, water vapor and CH_4 move through the aGDL to the aCL under the influence of diffusion and convection, whereas CH_3OH moves from the aCL in the opposite direction via the same processes. Electrons released in the reaction producing CH_3OH are transported via the carbon fibers in the aGDL to the anode current collector, whereas protons move from the aCL to the membrane via the connecting ionomer. The protons in the membrane move to the cCL by migration and diffusion because of the gradient in proton concentration and electric field. A part of the total proton flux is associated with water and methanol and hence both species move via electro-osmosis towards the cathode. At the cathode side of the membrane, the protons are reduced by electrons flowing from the cathode current collector, resulting in the generation of H_2, which then is transported through the cCL and cGDL by diffusion and convection. The H_2O and CH_3OH associated with protons

moving through the membrane are released in the cCL and may diffuse through the cGDL to the cathode flow channel. In the case of CH_3OH, electro-osmosis contributes to the crossover of this species driven by the concentration gradient in CH_3OH.

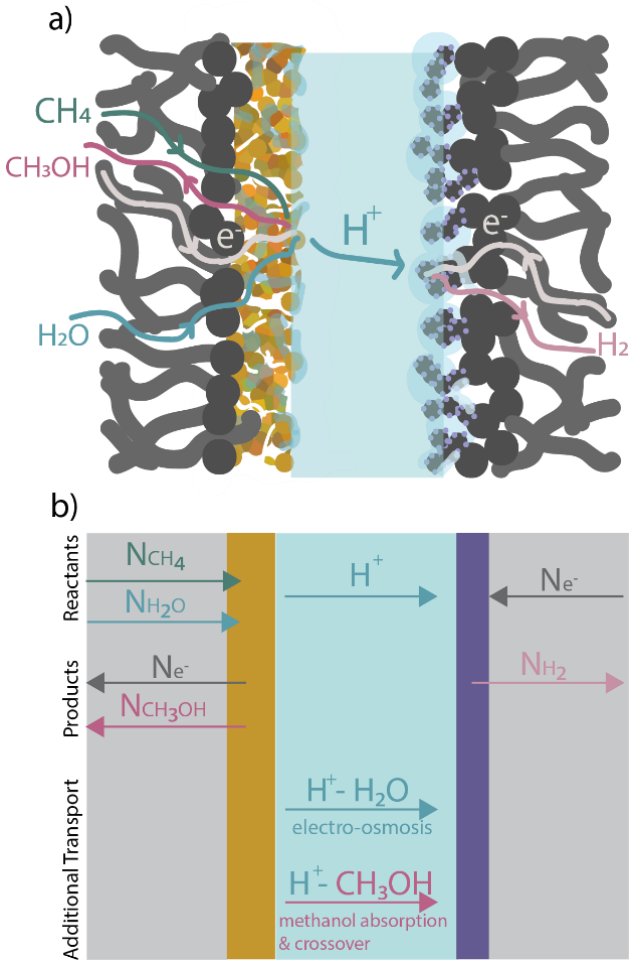

Figure 6.2: a) Gas and ion flows through the PEM MEA during electrolytic operation. b) Fluxes of each individual reactant and product and additional transport mechanisms.

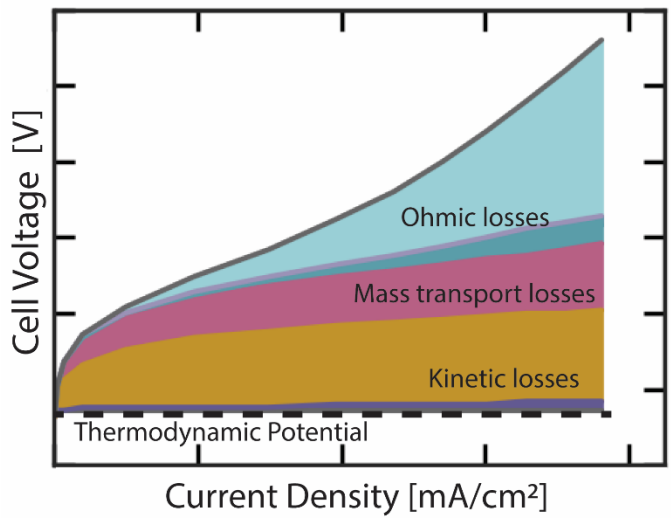

Figure 6.3: Distribution of overpotentials within the MEA vs. current density for an electrolytic cell. The three main components are ohmic losses, mass transport losses, and kinetic losses. Thermodynamic potential is the minimum free energy required to drive the reaction. (Adapted from Ref.[145]).

The transport phenomena described above impact the VE, which is a ratio of the thermodynamic potential related to its Gibbs Free Energy (0.58 V vs. SHE), the black dashed line in Figure 6.3, to the applied cell potential,

$$\mathrm{VE} \equiv \frac{\mathrm{V_{thermo}}}{\mathrm{V_{applied}}}. \tag{6.10}$$

Eq. 6.10 is defined for the electrolytic operation, for galvanic mode, the VE is defined as the inverse. As shown in Figure 6.3, the extra potential required to drive the desired reaction, above the thermodynamic potential, is related to irreversible losses, termed overpotentials. It should be noted that for galvanic operation, similar overpotentials exist, limiting the amount of energy and product generated. As shown in Figure 6.3, it is clear that the VE decreases nonlinearly with increasing current density. The largest overpotential is related to the reaction kinetics at the anode (the yellow band) and cathode (the purple band) and is often logarithmic with current density (Figure 6.3). The kinetic losses can be mitigated by increasing the total surface area of the electrocatalysts or developing more efficient electrocatalysts, as discussed below. As noted in Figure 6.2, the transport of species results in mass-transport overpotentials, shown by the pink band in Figure 6.3, due to concentration changes that occur between the gas channel and the reaction site. These mass-transport losses are far away from limiting current density, and respond more linearly; at limiting-current-density conditions, the mass-transport losses will have more rapid increase in voltage with increasing current density. Ion and electron transport through the CLs and the membrane result in ohmic losses. These losses can increase nonlinearly with increasing current density as the degree of hydration in the membrane and ionomer change the conductivity of these components. Since membrane and ionomer hydration depend on the transport of water, the ohmic losses are coupled to mass transfer. Both ohmic and mass-transport losses can be minimized by changing operating conditions (e.g., raising the temperature) or using thinner

membranes; however, there are tradeoffs such as reactant or product crossover, material stability, etc.

The CE is related to how much of the current is used for the methane to methanol reaction after accounting for side reactions including possible crossover and reduction of the produced methanol back to methane,

$$\mathrm{CE} = \frac{i_{\mathrm{methanol}} - i_{\mathrm{crossover}}}{i_{\mathrm{T}}} = \mathrm{FE} - \frac{i_{\mathrm{crossover}}}{i_{\mathrm{T}}}, \tag{6.11}$$

where i_{T} is the total current density and i_{methanol} is the partial current density for methanol produced at the anode, determined using Faraday's law. Thus, if all of the produced methanol crosses the membrane and converts to methane, one has only designed an electrochemical methane pump. If there is no crossover or the methanol does not reduce back to methane (which, typically, has been the case), then CE becomes the same as the faradaic efficiency (FE). For the methanol reactions, as shown in Figure 6.1, the FE can be less than unity due to other reactions at the anode such as the OER.

In Eq. 6.11, $i_{\mathrm{crossover}}$ is not easily measured, and thus CE is usually evaluated by measuring the total methanol flux and comparing that to the equivalent total flux if all of the current was converted to methanol using Faraday's law,

$$\mathrm{CE} = \frac{\mathrm{N_{methanol}}}{\frac{i_{\mathrm{T}}}{2F}} \tag{6.12}$$

where $\mathrm{N_{methanol}}$ is the total methanol flux leaving the cell in the liquid and gas states for both electrodes and F is Faraday's constant. Determination of the total flux of methanol and ability to close the overall carbon balance requires measurement of the concentrations in both the gas and liquid exit streams, as well as the volumetric flow rate of these streams. Furthermore, the total volumetric flowrate out of the cell compartments cannot be assumed to be the same as the inlet flowrate because during the course of the reactions the overall gas flux can change, as can water and other species transporting across the membrane (see Figure 6.2). For this reason, the measurement of the exact flowrate exiting the cell must be known to obtain an accurate measure of the molar flowrate of products. Such a measurement can be accomplished through various flow meters and calibrated devices, provided any condensable constituents are removed or accounted for (*e.g.*, using water traps). This precise measurement is particularly important at high current densities for which a large fraction of the reactants are consumed, since using the inlet flowrate can lead to inaccurate FEs.[222] Similarly, one may also be interested in the residence time of the gases in the cell, which can be obtained by knowing the free volume of the cell and the inlet flowrate. This is typically more important for half-cells than MEAs since the free volume of the latter is mainly in the channels and backing layers, and is really only a concern for high conversion rates.

The intricacies highlighted above demonstrate the complexities in determining VE, CE, and EE. This is further exacerbated by different types of electrochemical evaluations including sweep voltammetry (cyclic or linear) or chronoamperometry/chronopotentiometry. In particular, sweep studies are transient and do not necessarily allow for steady-state conditions, thereby resulting in

perhaps erroneous calculations for VE and CE, especially in terms of product detection and accumulation under steady-state conditions. Consistent, uniform, and detailed protocols and metadata that ameliorate the above concerns are required to help advance this difficult field. These recommendations include explicitly stating the voltage (and a reference potential or the counter electrode), the current density, and the duration of the experiments, the voltage and corresponding current density at which the products are obtained; a complete carbon balance for the entire cell including the flowrate and concentration of each species. Ancillary data such as the high-frequency cell resistance, measured using electrochemical-impedance spectroscopy, and an explicit statement of CE, VE, and EE should be reported, to provide comparisons between different cells and catalysts.

6.4 Literature on Electrochemical Methane-to-Methanol Conversion Devices.

Table 6.1 summarizes the results of published studies reporting the low temperature electrochemical oxidation of methane to methanol in both MEAs and half-cells (Figure 6.1), and several review papers have been published that complement the table for other conditions (i.e. higher temperature, various products, etc.).[56,58,196] It is readily apparent that the performance metrics provided by each set of authors is incomplete, making it difficult to assess the current status of the field. This conclusion is in complete agreement with that reached in a recent review by Mostaghimi *et. al*.[58] For example, only six of the fourteen articles report both the current density and the voltage at which methanol is detected, and none report the EE. If the cathode voltage is measured relative to a reference electrode and is compensated for the electrolyte resistance, then the voltage at which all reactions occur is known at the anode. This separation of voltage is possible to do for aqueous electrolyte systems, and is shown for the half-cells that are referenced to a specific potential. In the case of MEAs, the cell voltage is comprised of many components, as shown in Figure 6.3, and determining the separate components is nontrivial. Consequently, the total cell voltage is the only basis for comparing one study to another. Since it is impossible to make definitive comparisons of the results reported with different electrochemical cells, we review what has been learned through the literature, emphasizing full-cell MEA devices. The half-cell systems are only useful for assessing the performance of different electrocatalysts.

None of the reports of exchange-MEAs, using either a hydroxide or carbonate solution fed to the cell, have shown good selectivity or efficiency for methanol formation. Moreover, none have realized current densities higher than ~20 mA cm^{-2}.[200–204,206] Also, carbonate-exchange-MEAs produced various products besides methanol, including formic acid, formaldehyde, ethanol, ethers, etc.[202–204,206] These exchange-MEAs have also been used to test catalysts that are not stable in acidic conditions, such as Ni, Co, and Fe. However, a notable limitation of alkaline or hydroxide MEAs is membrane stability.

Gas fed-MEAs for anodic oxidation of methane, using various metal oxides (i.e., V_2O_5, CrO, Mn_2O_3, Fe_2O_3, CoO, and MoO_3) and metals (i.e., Ru, Pd, Ag, and Au) supported on SnO_2 have been tested at 100°C.[197] Using a ceramic proton conductor, $Sn_{0.9}In_{0.1}P_2O_7$, a current density of only 10 mA cm^{-2} is achieved. Among the tested materials, V_2O_5 supported on SnO_2 exhibited the highest methanol selectivity, 88.4%. The concentrations of methanol and carbon dioxide under these conditions were 0.0306% and 0.0040% (reported in terms of the outlet stream makeup),

respectively, at a total current density of 2 mA cm^{-2}, and no other species, such as carbon monoxide and oxygen, were detected. With increasing current density (~ 10 mA cm^{-2}), the methanol percent concentration decreased, while the carbon-dioxide one increased, indicating the progressive oxidation of methanol. An MEA with the same ceramic proton conductor, but introducing methane to the cathode side of the cell and using PdAu/C, CuO_x-PdAu/C, and Pt/C as the electrocatalysts were examined for methane activation.[198,199] In this configuration, a methanol selectivity of 60% at 400 mA cm^{-2} was achieved at 50°C; however, the methane conversion was only 0.012%. By increasing the temperature to 250°C, the conversion increased to 0.38% but the methanol selectivity decreased to 6.3%.[198] The authors also reported the rate of CO_2 evolution, which for the PdAu/C catalyst was an order of magnitude higher than the rate of methanol formation. At 250°C, CO_2 and methanol were formed at a rate of 6 and 0.4 μmol h^{-1} cm^{-2}, respectively. As the conversion of methane increased, CO_2 was the principal product formed. Gas-fed, proton conducting MEAs have shown the most promising results to date for the evolution of methanol. While systems using ceramic separators are able to oxidize methane to methanol, we believe that there is a greater potential for MEAs based on polymeric proton conductors because they operate at lower temperatures, which should favor methanol formation over complete oxidation.[58]

Table 6.1: Low Temperature Electrochemical Methane Oxidation, experimental findings. Energy efficiency and voltage efficiency was not reported for any of the following experimental results.

Products formed	**Potential (V)**	**Current Density ($mAcm^{-2}$)**	**Electrolyte/ Membrane**	**Temp. (°C)**	**Electrode (Catalyst/ Support)**	**CH_3OH Selectivity (CS)/CE**	**Half or Full Cell**	**Oxidant**	**Ref**
CH_3OH, CO_2	0.9	4	$Sn_{0.9}In_{0.1}P_2O_7$	100	V_2O_5/SnO_2-PTFE Anode	88.4% (CS) 61.4% (CE)	Full Cell (PEM)	H_2O	[197]
CH_3OH, CO_2	---	400	$Sn_{0.9}In_{0.1}P_2O_7$	50	PdAu/C Cathode	60.0% (CS)	Full Cell (PEM)	O_2	[198]
CH_3OH, CO_2	---	---	$Sn_{0.9}In_{0.1}P_2O_7$	300	CuO_x-PdAu/C Cathode	~ 100% (CS)	Full Cell (PEM)	O_2	[199]
CH_3OH,	0.4-0.5	---	Nafion 117	85 (anode) 80 (cathode)	Pt/C Cathode	---	Full Cell (PEM)	H_2O_2	[200]
CH_3OH	0.3	---	6.0 M KOH/Nafion 117	25 (anode) 80 (cathode)	Pd/C Anode, Pt/C Anode, Ni/C Anode	---	Full Cell (HEM)	OH^-	[201]
CH_3OH	---	---	KOH + H_2O (Catholyte)/ Membrane	160	MO_x Anode (M = Mn, Fe, Ni, Os, or Pt)	---	Full Cell (HEM)	OH^-	[202]
CH_3OH, CO_2	---	< 10	KOH + H_2O (Catholyte) /Daramic Anion Exchange Membrane	25-160	MO_x Anode (M = Ni, Co, Cu, Ag Pt, Au, Ce, Pb, Fe, Mn, Zn or Combinations)	---	Full Cell (HEM)	OH^-	[203]
CH_3OH, HCHO, CO, HCOOH, CH_3CH_2OH, CH_3COOH, CH_3COCH_3,	2.0	21	1.0 M Na_2CO_3 + DMF/Ralex AM-PAD Anion Exchange Membrane	40	NiO-ZrO_2 Anode	---	Full Cell (CO_3EM)	CO_3^{2-}	[204]

CH_3CHO HCH_3									
CH_3OH, CH_2O, CH_3CH_2OH, C_2H_4O, C_3H_8O, C_3H_6O	2.0 vs. Pt	< 10	0.5 M Na_2CO_3	RT	Co_3O_4-ZrO_2/CP-Nafion 117 Anode	---	Half Cell (CO_3EM)	CO_3^{2-}	205,206
CH_3OH, HCHO	2.0 vs. SCE	---	0.1 M Na_2SO_4	RT	TiO_2-RuO_2-V_2O_5/PTFE Anode	57% (CE)	Half cell (GDE)	H_2O (OH^-)	207
CH_3OH, HCHO, HCOOH	2.1 vs. SCE	13	0.1 M Na_2SO_4	RT	TiO_2-RuO_2/PTFE Anode	30% (CE)	Half Cell (GDE)	H_2O (OH^-)	208
CH_3OH	0.75 vs. Ag/AgCl	62	1.0 M KOH	80	$Ni(OH)_2$-NiOOH/ Ni Foam Anode	---	Half Cell (TEC)	OH^-	39
CH_3OH, C_2H_5OH	-0.2/0.64 vs. Ag/AgCl (pulsed potential)	---	0.5 M $HClO_4$	25	Pd/Graphite Anode	---	Half Cell (TEC)	H_2O	209
CH_3OSO_3H, CH_3SO_3H	2.0 vs. SSE (~1.29 vs. RHE)	≤ ~ 4.5	$PdSO_4$ in 95-98% H_2SO_4 (ionic catalyst)	80-140	FTO Anode	---	Half Cell (TEC)	H_2SO_4, SO_3	210

RT: room temperature; CP: carbon paper; FTO: fluorine-doped tin oxide glass; PEM: proton-exchange membrane; HEM: hydroxide-exchange membrane; CO_3EM: carbonate-exchange membrane; GDE: gas-diffusion electrode; TEC: three-electrode cell.

6.5 Current Status and Recommendations on Electrocatalysts

In all of the work on methane oxidation reported in Table 6.1, the basis for selecting the electrocatalysts chosen is not well articulated. The most common feature is that many of the materials chosen are known to be active for OER or methanol-to-CO_2 oxidation reaction in either acidic, neutral, or alkaline electrolytes, with the majority in acidic conditions and limited studies with neutral or alkaline ones. [200–208] However, no rationalization is given for why these materials should be active for methane oxidation.

To help with the search for potential catalysts, it would be very useful to have a theoretical framework to help guide the search. To this end, Arnason *et al.* calculated the Gibbs Free Energy

of each adsorbed species for electrochemical methane oxidation and OER occurring on a number of metal oxides and MX-enes.[213] The two reactions are envisioned to proceed as shown in Figure 6.4. Both reactions begin with the formation of an adsorbed hydroxide group, which then undergoes dehydrogenation to produce an adsorbed oxygen atom (O*). Atomic surface oxygen then reacts with water to form a hydroperoxide group, a precursor to O_2, or with methane to form methanol. Figure 6.4 shows the calculated free energies for the third step in the OER, the formation of a surface oxyhydroxide (blue), and the activation of methane to form methanol (pink) for a series of metal oxides at open-circuit potential. The smaller the endergonicity of each step the more easily this step will occur, i.e., the lower the minimum anode potential required for the reaction to proceed. For the preferential formation of methanol over O_2, the Gibbs Free Energy for the reaction leading to methanol should be lower than that leading to O_2 via –OOH groups. Accordingly, catalysts such as SnO_2, TiO_2, V_2O_5, RhO_2, and PtO_2 would seem to be the most promising candidates for methanol formation. Interestingly, some of the electrocatalysts that have been tested experimentally (in Table 6.1) align with the predictions shown in this theoretical work (Figure 6.4).

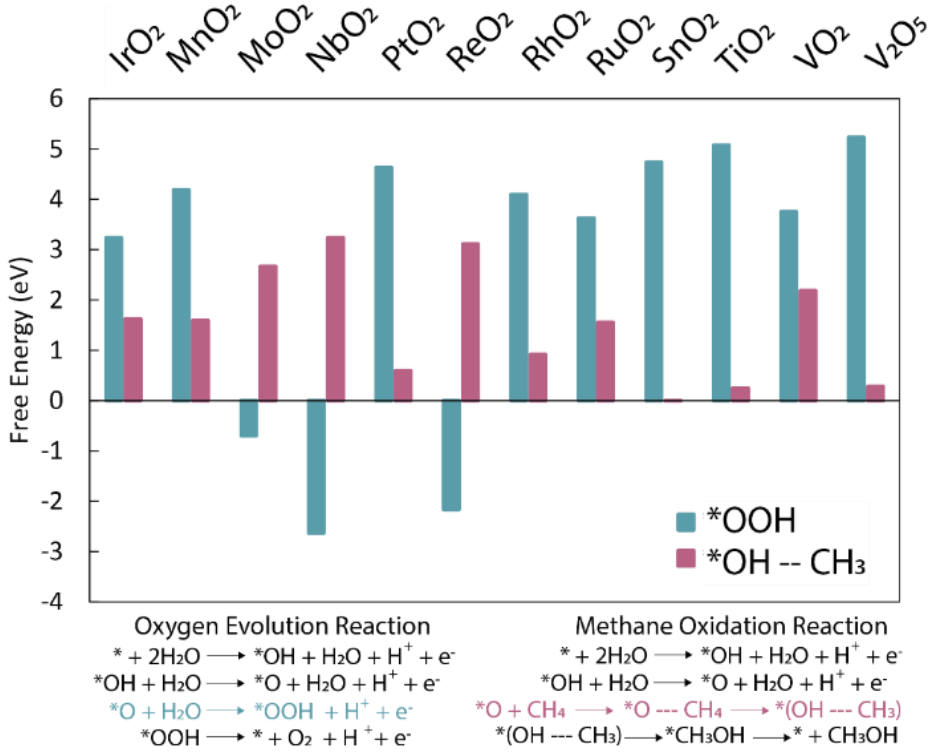

Figure 6.4: Free energies of various metal oxides for the third step in the water oxidation process and methane activation step. The steps for oxygen evolution and methane activation are shown below. Data from Ref. [213].

As noted above, Lee *et al*. used V_2O_5 supported on SnO_2 in a ceramic MEA. This system exhibited the highest selectivity (88.4% at 0.03% conversion) to methanol reported to date.[197] During electrocatalysis, partially reduced vanadium species ($V^{4+}O_2$) act as the active site for generating

reactive oxygen species ($O_2^{\cdot-}$ and $O^{\cdot-}$) in V_2O_5. These species are able to both chemisorb methane and partially oxidize it to methanol. The authors suggest that both methanol and CO_2 are formed at the surface of ceramic, gas fed-MEA anodes, by separate reaction pathways. For methanol, they propose that active oxygen species, such as surface $O_2^{\cdot-}$ and $O^{\cdot-}$, may be the primary participants in the partial oxidation of methane to methanol, in agreement with Figure 6.4. For CO_2, they propose that highly active oxygen species in the form of an OH^* surface site are responsible for full oxidation of methane to CO_2, which is also proposed by Yamakata *et al.* and Heo *et al.* for various hydrocarbons.[217,223] Accordingly, this hypothesis suggests that CO_2 formation could be suppressed by reducing the amount of OH^* generated during cell operation, thereby improving efficiency. However, they noted that a different support may be needed as SnO_2 may promote full oxidation of methane to carbon dioxide.[197]

Another study that compliments the theoretical work is that of Rocha *et al.*, who investigated TiO_2-RuO_2/PTFE and TiO_2-RuO_2-V_2O_5/PTFE for the anodic oxidation of methane to methanol in 0.1 M Na_2SO_4 into which methane was fed through a GDE.[207,208] Their electrocatalysts achieved a 57% FE towards methanol. Methanol and other byproducts were envisioned to form via two pathways, one involving active oxygen species (e.g., $O_2^{\cdot-}$ and $O^{\cdot-}$) and the other involving methane oxidation via a Ru/V redox couple, wherein the transition metals undergo valance transitions.[208] For the latter route, RuO_2 has two active redox couples, Ru^{4+}/Ru^{6+} and Ru^{3+}/Ru^{4+}. These redox couples are able to promote the generation of both methanol and formic acid, as shown below:

$$CH_4 + Ru^{6+}O_2^{2+} \rightarrow CH_3–Ru^{5+}O^{2+} + H^+ \rightarrow CH_3OH + Ru^{4+}O^{2+} \quad (6.13)$$

$$CH_4 + 2Ru^{6+}O_2^{2+} \rightarrow Ru^{5+}O_2^{+}–CH_2–Ru^{5+}O_2^{+} + 2H^+ \quad (6.14)$$

$$Ru^{5+}O_2^{+}–CH_2–Ru^{5+}O_2^{+} \rightarrow Ru^{4+}O^{+}–O–CH_2–O–Ru^{4+}O^{+} \rightarrow HCOOH + 2Ru^{3+}O^{+} \quad (6.15)$$

Conversely, V_2O_5 possesses only one redox couple, V^{4+}/V^{5+}, which may not generate sufficient electrons to form the double bond needed to generate both formic acid and formaldehyde.

$$CH_4 + V_2^{5+}O_4^{2+} \rightarrow CH_3–V_2^{4+}O_4^{2+} + H^+ \rightarrow CH_3OH + V_2^{4+}O_3^{2+} \quad (6.16)$$

Consequently, TiO_2-RuO_2-V_2O_5/PTFE can selectively oxidize methane to methanol, whereas RuO_2 bestows electrical conductivity to the GDE on which the catalyst is supported.

Based on both experiments and theory, we can envision that a selective electrocatalyst for methane oxidation to methanol should be composed of two phases: a minor phase, having a moderate activity for the first two steps in the OER, and a major phase capable of methane activation. The concept is that oxygen atoms derived from the activation of water on the minority phase would rapidly transfer to the majority phase chosen for its ability to activate methane. By balancing the activation of water and methane, it should be possible to minimize the formation of molecular O_2. The last requirement is that newly formed methanol is rapidly removed from contact with the electrocatalyst in order to prevent its complete oxidation to CO_2. This might be done by diffusion of the methanol though the membrane of an MEA to the anode side. Since the anode catalyst generates H_2, it is important the catalyst that facilitates this process not reduce methanol to methane and water.

In addition to composition, catalyst structure can also influence catalyst activity and selectivity. Therefore, the search for potential catalysts for the selective oxidation of methane to methanol should also include efforts on catalyst characterization. This requirement is particularly important for the development of a multiphase-, bifunctional-electrocatalyst. Such a catalyst requires in-depth investigation of the interfaces between its active phases, since these characteristics will control the transport of atomic O species between the phases. Accordingly, proper evaluation of the structural, morphological, and redox properties of the catalyst needed to obtain a complete understanding of how water and methane are activated.

Currently, the phase and structure of electrocatalysts is sometimes reported, but further work is required in order to trace back catalyst activity to catalyst structure. Many reports include basic structural characterization accomplished with X-ray diffraction (XRD). However, reporting the local crystal structure of the catalysts and correlating it to the catalyst's activity has to be considered as well. Further structural characterization will reveal the amorphous or crystalline nature of the material and identify exposed crystal planes. In addition to XRD, various techniques can be employed to gather further information, including Raman spectroscopy, high-resolution transmission electron microscopy, and X-ray photoelectron spectroscopy. For example, catalysts of the same phase that differ in the exposed crystallographic planes may show differences in their activities for methane oxidation and even lead to different products. For example, studies on iridium oxide catalysts for the OER have shown variations in activities depending on whether the compound is amorphous or crystalline.[224] Likewise Liang *et al.* demonstrated that specific facets of iridium oxide are active for methane oxidation.[225] Similar findings have also been demonstrated by Ma *et al.* showed that methane oxidation to carbon monoxide depends on specific facets of a platinum catalyst.[205] For bifunctional catalysts, not only differences in the facets exposed by each component but also the interactions between the surfaces of different materials (i.e., coherency of the lattices or the occurrence of mixed oxidational states) may lead to synergistic catalytic effects.[197–199,204–208] It should be noted that bifunctional catalysts may become unstable when operated at high current densities and, therefore, their structure and composition must be assessed after use as well as prior to use.

6.6 Experimental Efforts in a PEM MEA

6.6.1 Catalyst Screening and Membrane-Electrode-Assembly Testing

In efforts to see just how well a PEM MEA is able to convert methane to methanol, iridium oxide was used at the first catalyst. To make and test the MEAs, the procedure described in Chapter 4 was followed and the same cathode catalyst ink and loading was used. With this baseline assembly, the faradaic efficiency was calculated based on the above discussion. In Figure 6.5, we show the (a) polarization curve for feeding the methane and argon into the MEA and (b) the oxygen faradaic efficiency. As shown in Figure 6.5b, the oxygen faradaic efficiency is 100%, within error, using an iridium oxide catalyst.

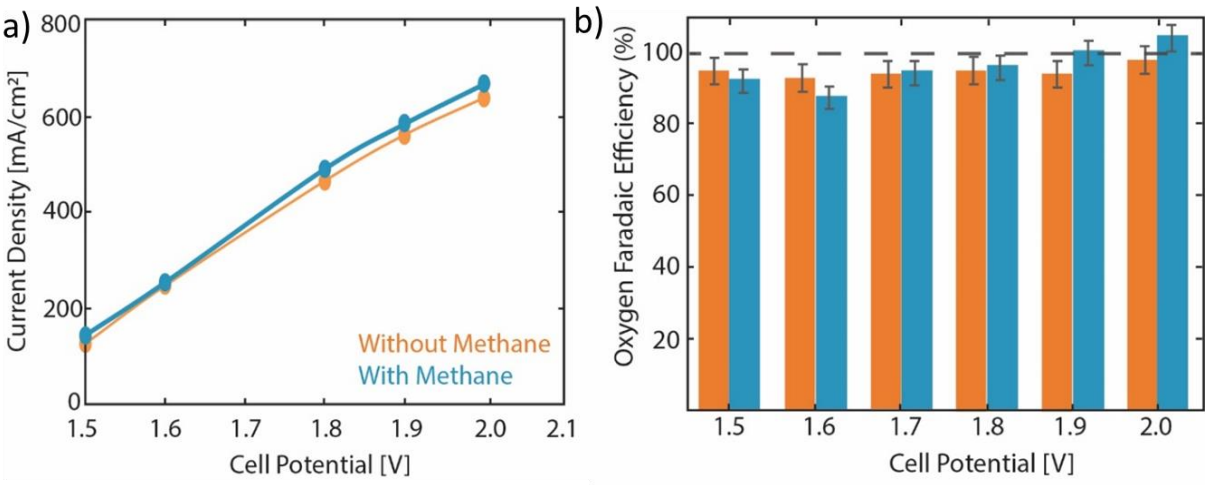

Figure 6.5: Testing Parameters: Flow rate: 200 ccm both sides, electrochemical test sweeping the voltage from 1.5 V – 2.0 V, at 2 min holds. Electrode Properties: Anode: Iridium Oxide (1 mg cm^{-2}), CH_4 or Ar with water vapor, Ti GDL. Cathode: Pt (0.3 mg cm^{-2}), 2% H_2 in Ar with water vapor, carbon GDL. Membrane: boiled Nafion, 183 mm dry.

The importance of calculating the faradaic efficiency is two-fold. One, the calculation shows that even though we have a slight increase in performance when feeding methane (i.e. more current for a given cell potential), we are not seeing any new products. We can account for this increase in current density due to the increased diffusivity of water within methane gas, as shown in Chapter 4 for helium. While the difference in current density is at most 50-mA cm^{-2}, comparable to what some previous results show for a methane system, we do not see a significant change in the faradaic efficiency due to changes in diffusivity. Secondly, this calculation demonstrates the importance of inlet flowrate. Due to the amount of water entering the system and being converted, the flowrate out of the system is crucial and could lead to erroneous results in the system.

The FE can be calculated via the following equation:

$$\mathrm{FE} = \frac{c_i\, Q\, n_{e-} F}{i_T A}. \tag{6.17}$$

The FE is dependent on the concentration of the reactant *i* (c_i), which is water for this system, the volumetric flow rate (Q), the number of electrons in the reaction (n_{e^-}), Faraday's constant (F), the total current density (i_T) and the active area of the MEA (A). If the concentration or the volumetric flow rate is off, then the FE can be drastically miscalculated. Flow meters were used to assure that volumetric flowrate was accurate. Best practices of checking the flowrate and establishing an 100% FE for a single reaction must be done before introducing more reactions into the system.

Since the FE exhibited 100% for both argon and methane, the tests indicated iridium oxide is not active for methane activation, which agrees with Figure 6.4. Other catalysts were chosen to be tested based on literature research (from Table 6.1) and promising results based on theoretical calculations (from Figure 6.4). The electrocatalysts that were tested are shown in Table 6.2.

Table 6.2: The electrocatalysts tested for methane partial oxidation at > 1.5V

Electrocatalyst Tested	Particle Size	Products Formed
IrO_2	~50-100 nm	O_2, trace amounts of CO_2
Pt	~5-10 nm	O_2
60% Pd/C	~50 nm	CO_2*
40% Ru/C	~50 nm	CO_2*, O_2
VOx	n/a	CO_2
Synthesized Vanadium nanoparticles	10-20 nm	None
Synthesized mesoporous vanadium	20 nm	None
Pt/Ru nanoparticles	~50 nm	O_2
SnO_2	12 nm	O_2
TiO_2	10 nm	O_2
IrO_2/SnO_2	1-2 nm IrO_2, and 12 nm SnO_2	O_2
IrO_2/TiO_2	3-5 nm IrO_2 on 10 nm TiO_2	O_2

Most catalysts observed little to know products formed besides oxygen. Even bifunctional catalysts that were predicted to be better methane-activation catalysts instead of oxygen-evolution catalysts did not yield high current densities or carbon products, as shown in Figure 6.6. Oxygen evolution is the most predominant reaction within these systems and unfortunately methane activation is still an important problem to be solved. Something to note, for each of these catalysts the ionomer:catalyst ratio was held constant (0.116%, optimized for iridium black) and the solvents stayed the same as well. However, from findings in Chapter 2 we know that the solvent composition can play an important role in the ink's morphology and the overall structure of the CL. Further work should be done to identify the electrocatalyst behaviors and once down selected, CL optimization accomplished.

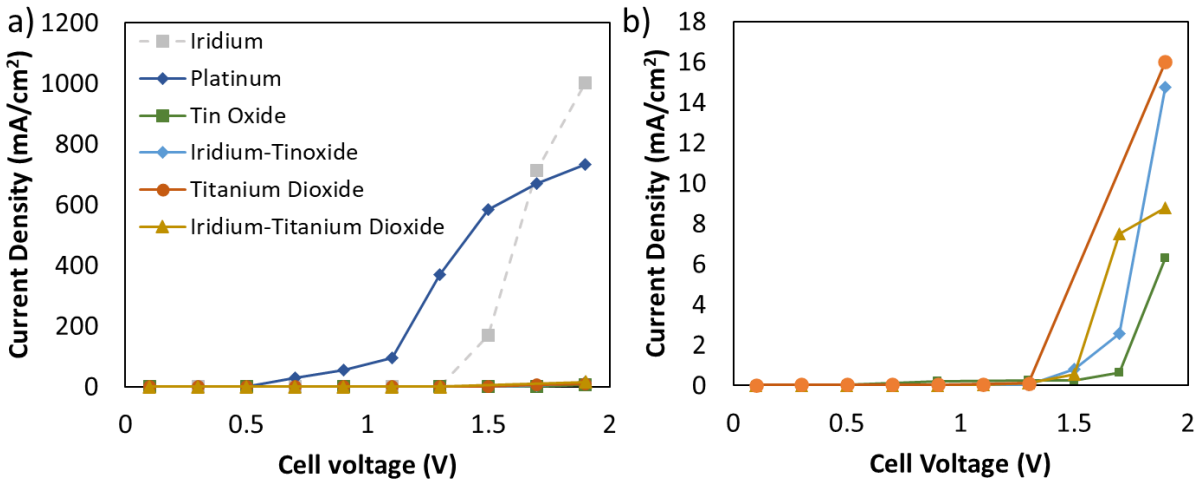

Figure 6.6: Polarization curves for the various catalysts up to (a) 1200 mA cm^{-2} and (b) a magnified portion of a, only going up to 18 mA cm^{-2} from 0 to 2 V. Each of these membrane electrode assemblies were coated with the catalyst with a target loading of 1 mg cm^{-2} on a boiled Nafion 117 membrane. Pt/C at 0.3 mg cm^{-2} was the cathode.

6.6.2 Methanol Crossover through the Membrane

Through the testing of these different catalysts, there is a chance that methanol could have been made but in very small quantities. Outside the detection limits of gas chromatography and mass spectroscopy, the methanol would not be able to be detected. However, with MEAs using Nafion, the methanol could be absorbed into the membrane. Studies have shown Nafion prefers to absorb methanol over water and other alcohols[142]. For every sulfonic-acid site, approximately twenty-one moles of methanol are absorbed in the membrane. Additionally, methanol can move with protons like water does via diffusion and electro-osmosis. Therefore, at low current densities, methanol could be trapped in the membrane or moved to the cathode, and, without proper detection, could be missed.

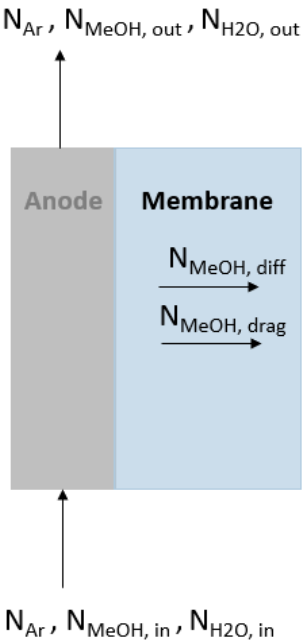

Figure 6.7: Schematic of the flux of methanol (N_{MeOH}) and water (N_{H2O}) when fed into the anode compartment. Argon was the carrier gas; 4% methanol vapor was fed in and the stream was saturated with water vapor at 100% RH at 80 °C.

Experiments were conducted to observe if methanol does crossover to the cathode. Feeding in a small amount of methanol to the anode, with no potential applied there was no crossover to the cathode even at longer periods of time (> 30 min). When the potential was applied, methanol was seen at the cathode via gas chromatography. This result shows that the methanol produced on the anode could be preserved via crossover to the cathode. Forcing methanol to crossover to the cathode could avoid complete oxidation and leverage new design for methane MEAs.

6.7 Summary and Conclusions

The work reported to date on the electrochemical partial oxidation of methane has shown that while this approach is promising, these are still very early days for the field. More active and selective electrocatalysts that minimize the conversion of methanol to undesired byproducts are required. The reported studies show that a high selectivity to methanol at low methane conversion rates is achievable, but the methanol selectivity rapidly decreases as the methane conversion rate increases needed for practical applications. These findings are similar to those reported for the thermal oxidation of methane. What is not clear is to what extent the observed trend of methanol selectivity and methane conversion can be altered by proper design of the electrochemical cell and electrocatalyst. We also note that using water as the oxidant greatly reduces the thermodynamic driving force for the complete oxidation of methane relative to its partial oxidation to methanol.

The published electrochemical studies of methane oxidation have used both aqueous/nonaqueous electrolyte cells (i.e., half-cells) and MEAs (i.e., full-cells), the latter of which have distinct advantages. MEAs are capable of achieving the high current densities (>> 100 mA cm^{-2}) needed for a commercially viable technology. Within this chapter, we have detailed the factors affecting the performance of these systems, such as the mode of operation, the microenvironment tested (i.e. acidic vs. alkaline), and the nature of the membrane (polymer versus ceramic). The critical metrics, i.e. the EE, CE, and VE, need to be carefully measured and reported in order to have a basis for comparing different electrochemical systems. Electrocatalyst discovery remains the main obstacle within the field and both experiments and theory suggest that bifunctional catalysts hold the greatest promise. Characterization of intrinsic electrocatalytic material properties, such as the crystal phase structure and the interactions between different metals or phases, are crucial to further understanding the mechanism for methane activation and selectivity towards methanol.

Taking what has been used within the literature and the work done on the MEAs throughout this dissertation, experiments were performed, attempting to partially oxidize methane to methanol using various promising catalysts from theory. While the initial test did not show the promising results we hoped, we can build off of them with better catalyst-layer fabrication and unique engineering of the system to accomplish this challenge. In summary, this chapter provides an approach for systematic approach for understanding the issues associated with the development of electrocatalysts and electrochemical systems for the partial oxidation of methane.

7. Summary & Outlook

Electrolytic devices are going to play a huge role in decarbonizing different sectors for a clean-energy future. This dissertation shows numerous experiments and simulations evaluating transport phenomena in various electrolytic devices, whether for hydrogen and oxygen evolution or other (electro)chemical transformations. This dissertation would not have been completed without the use of an MEA. MEAs are the future of these electrolytic devices with the advantage of low resistances, direct delivery of reactants to the catalyst layers, and balancing multiple phases and multiple scales at the same time. Throughout this dissertation, an MEA was used for specific applications as well as for simplified studies to better understand various phenomena. Working under operating conditions and in a multi-phase environment teaches the community the impact on the OER and other chemical reactions.

The OER was the main focus of the majority of the chapters in this dissertation (Chapter 2-5). While this dissertation did not focus on new electrocatalysts or traditional kinetic studies, it did focus on how transport can play a significant role on the performance of the OER. This coupled interaction between the reaction and species movement is essential for each of the chapters covered here. Within these chapters, the reaction was studied within operating conditions to get a detailed idea of the performance of iridium oxide within an MEA.

This dissertation highlights where there are inefficiencies in the systems, where there can be improvements in the existing state-of-the-art devices, and what needs to be determined before these systems are used for more complex chemistries. This dissertation shows the recurring outcomes and findings:

(1) *Local transport of species in the porous electrode or at the catalyst site greatly impacts cell inefficiencies.* Reducing overpotentials within the membrane-electrode assembly is crucial. Ways to reduce the overpotential include adding more catalyst, thinning the membranes, and adding a concentrated supporting electrolyte, but at various costs to the system. However, by manipulating within a small window, so as not to increase the catalyst loading or keep the same catalyst species, this dissertation shows increased transport of species within the layers can help reduce the overpotentials. Within Chapters 2 and 3, local transport near the catalyst surface shows a significant impact on the voltages the cells see and how they operate. A better understanding of how to control the transport with the structure or the transport near the surface of the catalyst is highlighted on several occasions throughout this dissertation.

(2) Water has a dual role in both the reaction and the membrane electrode assembly. In Chapters 4 and 5 of this dissertation, water vapor was used as the feed for the electrolyzer and the performance of the cells suffered. However, both of these chapters exhibited the best performance to date of a vapor electrolyzer and vapor-fed unitized regenerative fuel cell, respectively. Changing the amount of water delivered does not only change how much water is available to react in the oxygen-evolution reaction but also limits how much water there is to hydrate the membrane. The complexity of water and its role is a central theme throughout this dissertation and is specifically highlighted in those two chapters.

Additionally, in Chapter 3, changing the supporting electrolytes for the anolyte demonstrated the importance of the bulk fluid on the performance and durability of the cell. While this dissertation mostly focused on acidic and alkaline water electrolysis, these themes can be applied to carbon-dioxide reduction and other electrochemical systems.

(3) *Electrolytic devices can be used for complex reactions and help to decarbonize the hard-to-decarbonize sectors*. While the majority of this dissertation focuses on hydrogen production, much of the work in Chapters 2-4 is foundational and can translate to more complex reactions and applications. The work done in these three chapters could be seen as a "model" system for more complex reactions, such as the methane-to-methanol highlighted in Chapter 6 and carbon-dioxide or nitrogen reduction. Decarbonization is not going to be easy, and while hydrogen alone cannot solve all these problems, the applications for seasonable energy storage (Chapter 5) or chemical production via electrochemistry (Chapter 6) could be innovative ways for a clean energy future.

These conclusions highlight the different length scales that transport plays a role in, spanning from the microscale to the macroscale. Transport phenomena are one way to engineer these systems within a window of material constraints. Peering into this window helps to show the physical limitations as well as the physical meaning to improve these systems. The various studies shown in the five chapters of this dissertation include systematic studies, model-like systems, and experiments that are both applied and fundamental. Electrolytic devices will be essential in the deep-decarbonization of the industrial, power, and transportation sectors.

7.1 Future Directions

The water electrolysis field as a whole, particularly for PEMWE and LAWE, is at the point where commercialization is a large priority. In order to achieve the Hydrogen Shot goal, there needs to be harmony between scaling these systems and understanding the research and development needs. Overall, for the more mature parts of the field, identifying the driving the forces for the catalyst layer structure while using commercially relevant techniques is vital for the community. Additionally, this entire dissertation focuses on iridium oxide, a PGM material that is very limited in supply. The field needs to address how used iridium oxide can be recycled for a longer lifespan. Lastly, the OER has been well studied and more efforts need to be done in the electrocatalysis field and carrying over findings and understanding from OER to these harder electrochemical reactions.

While this dissertation explored many of the nuances in electrolytic devices, it is just a starting point. Many additional studies can be contemplated to expand and directly build upon the work in this dissertation.

(1) Explore the relationship between ink and structure for viscous inks. Viscous inks are becoming more important for fuel cells and electrolyzers since they are more industrially relevant. However, as shown in Chapter 2 and the literature, the particle/particle, particle/ionomer, and particle/solvent interactions change based on higher percent-solids. From the work done in Chapter 2, viscous inks could build off of that by using acoustic analyzers to measure the particle-size distributions and vary components such as solvent

or ionomer content. Additionally, comparing different fabrication methods could be useful to determine if the ink or the technique changes the structure of the catalyst layer. Since the viscous inks are normally coated via doctor blade or slot die, the structure is expected to be quite different than the layer-by-layer deposition via spraying coating, and yield different contact and interactions with the porous-transport layers and the membrane.

(2) *Explore the impact of different loadings and/or ionomer content and their impact on catalyst-layer structure.* As shown in Chapter 2, there is a direct correlation between the solvent ratio and catalyst-layer structure. Further work in this area is required though to understand the driving forces and disambiguate their contributions. Thus, systematic studies are required including keeping the solvent ratio the same, but changing the amount of ionomer and determining how the aggregates change and how the ionomer is distributed. Another aspect would be to evaluate lower loadings, which have less through-plane structure. Looking at lower loadings will provide an idea of catalyst-layer utilization as well as the impact of catalyst-layer structure on that utilization.

(3) *Test vapor electrolyzer and unitized regenerative fuel cells at relevant pressures and duty cycles.* The two chapters on vapor electrolysis (Chapter 4 and Chapter 5) look specifically at a narrow range of catalyst loading and operating conditions. Especially for real-world applications, testing these systems at relevant pressures and duty cycles needs to be explored. Determining if hydrogen crossover is going to be a limitation in these systems and determining how to mitigate the crossover will be crucial for these technologies. Especially as interest grows in the unitized regenerative fuel cell field, finding niche applications at relevant pressure would be influential.

(4) *Investigate the use-case of seawater vapor as the feed to a vapor electrolyzer and explore the durability and pitfalls.* Chapters 4 and 5 explore water vapor, but only from deionized water. Seawater electrolysis has been explored by many people, but salts and contaminants prevent seawater from ever being a useful feed for electrolysis. However, water vapor from seawater could be another way to leverage this plentiful feed source. The temperature and relative humidity would be significantly different than what is shown in Chapter 4, so optimization of the catalyst layer and membrane-electrode assembly would have to be made, but this specific application could be important for offshore hydrogen production.

(5) *Study nickel or other alkaline relevant catalysts to explore how the microkinetics change and what are the main barriers.* The advantage of alkaline or near-neutral electrolysis and photoelectrochemistry is the chance to use non-precious-group-metal catalysts. While this entire dissertation focused on iridium oxide as the main catalyst, using iridium oxide at the scale the government and the world want to scale hydrogen to is not possible—there is not enough iridium to reach that demand. However, nickel is a good substitute for alkaline systems but less is understood at the surface level. Understanding how the microkinetics and local transport would impact these systems, how the mechanism may change, and how it differs from iridium oxide could be beneficial to the community.

(6) Electrocatalyst synthesis and testing for methane to methanol partial oxidation. As stated in Chapter 6, the number one need for the partial oxidation of methane to methanol is an effective catalyst. While the literature has stated that some electrocatalysts have been able to achieve this tremendous feat, none have done it at high enough current densities. More work needs to be undergone to test these catalysts before they become incorporated into complex membrane-electrode assemblies. Thus, testing the kinetics using representative electroanalytical techniques is important to first screen the catalysts. Developing a high-throughput way to test catalysts is one way to make a lot of catalysts, or try a lot of commercial catalysts, and then start to integrate the one that performs the best into the catalyst layer.

8. Nomenclature

Abbreviations

LAWE	Liquid Alkaline Water Electrolysis
PEMWE	Proton-Exchange-Membrane Water Electrolysis
MEA	Membrane electrode assembly
GDL	Gas-diffusion layer
PTL	Porous-transport layer
CL (aCL or cCL)	Catalyst layer (anode or cathode)
PGM	Platinum Group Metal
HEMWE	Hydroxide-Exchange-Membrane water electrolysis
HEM	Hydroxide Exchange Membrane
OER	Oxygen Evolution Reaction
URFC	Unitized Regenerative Fuel Cell
HER	Hydrogen-evolution reaction
DLS	Dynamic Light Scattering
CCM	Catalyst-coated membrane
XRF	X-Ray Fluorescence
CP	Chronopotentiometry
HFR	High Frequency Resistance
AVB	Applied-voltage breakdown
FIB-SEM	Focused-Ion-Beam Scanning Electron Microscopy
ECSA	Electrochemical Surface Area
SHE	Standard hydrogen electrode, 0.0 V
DFT	Density Function Theory
DIW	Deionized Water
SEL	Supporting Electrolyte
RDE	Rotating Disk Electrode
RHE	Reversible Hydrogen Electrode
EIS	Electrochemical Impedance Spectroscopy
LSV	Linear Sweep Voltammetry

BV	Butler-Volmer Kinetics
FCT	Fuel-Cell Technologies
MPL	Microporous layer
MT	Mass transport
PEM	Proton-exchange membrane
RH	Relative humidity
RFC	Reversible Fuel Cell
FC	Fuel Cell
WE	Water Electrolyzer
CG	Constant Gas
CE	Constant Electrode
ORR	Oxygen Reduction Reaction
HOR	Hydrogen Oxidation Reaction
PFSA	Perfluorinated Sulfonic-Acid Membranes
CA	Chronoamperometry
AST	Accelerated Stress Tests
EOT	End of Test
RTE	Roundtrip Efficiency
EW	Equivalent Weight
BOT	Beginning of Test
GDE	Gas Diffusion Electrode
EE	Energy Efficiency
VE	Voltage Efficiency
FE	Faradaic Efficiency
XRD	X-Ray Diffraction

Roman

E_{cell}	Overall Cell Voltage
E_{rev}	Reversible Cell Potential
b	Tafel slope
i_o	Exchange Current density, mA cm^{-2}
i	Current density, mA cm^{-2}

R_{tot}	Total Resistance, Ohms cm^2
I	Total Current, mA
K_{eff}	Effective Transport Property (e.g., permeability or diffusivity
K	Bulk Transport Property
r_i	Net Rate of Formation of Species i
a_i	Activity of a species, where i can be water, proton, hydroxide, or oxygen
k_{fi}	Forward Reaction Rate Coefficient for reaction i
A	Pre-Exponential Factor (Ch.3), Area, cm^2 (Ch. 6)
k_B	Boltzmann Constant
T	Temperature, °C
n_i	Number of electrons
ΔE_{0V}	Activation Energy , for 0 V free energy change
k_{ri}	Reversible Reaction Rate Coefficient for reaction i
$\Delta G_{rxn,0V}$	Gibbs Free Energy of reaction at 0 V
N_i	Molar Flux of species i
v_z *or* v_r	Velocity Profile in the z or r direction, respectively
D_i	Diffusion Coefficient of Species i, $m^2\ s^{-1}$
C_o	Initial concentration, mol m^{-3}
D^{eff}	Effective diffusivity, $m^2\ s^{-1}$
F	Faraday's Constant, 96485 C mol^{-1}
i_{max}^{D}	Diffusional maximum current density, A cm^{-2}

i_{max}	Maximum current density, A cm^{-2}
$N_{H_2O,PEM}$	Molar water flux in the membrane, mol $cm^{-2}s^{-1}$
t_{PTL}	Thickness of the porous transport layer, m
U^{ref}	Nernstian thermodynamic potential, V
V	Applied Voltage, V
$i_{crossover}$	Crossover Current Density
i_T	Total Current Density
Q	Volumetric Flow Rate, mL min^{-1}

Greek

η_i	Overpotential in a domain i, V
ε	Porosity
τ	Tortuosity
θ_j	Surface Absorbed Species, j, which can be OH, O, OOH, or an empty site (*)
β	Transfer coefficient (Ch. 3), Normalized water flux within the membrane (Ch. 4)
α	Diffusion coefficient, $mol^2 J^{-1}$ cm s
λ	Membrane water content, mol H_2O/mol SO_3^-
μ_{H_2O}	Water electrochemical potential
ξ	Electro-osmotic coefficient

9. References

(1) De Luna, P.; Hahn, C.; Higgins, D.; Jaffer, S. A.; Jaramillo, T. F.; Sargent, E. H. What Would It Take for Renewably Powered Electrosynthesis to Displace Petrochemical Processes? *Science* **2019**, *364* (6438), eaav3506. https://doi.org/10.1126/science.aav3506.

(2) Williams, J. H.; Jones, R. A.; Haley, B.; Kwok, G.; Hargreaves, J.; Farbes, J.; Torn, M. S. Carbon-Neutral Pathways for the United States. *AGU Advances* **2021**, *2* (1). https://doi.org/10.1029/2020AV000284.

(3) Kumar, V.; Shrivastava, R. L.; Untawale, S. P. Solar Energy: Review of Potential Green & Clean Energy for Coastal and Offshore Applications. *Aquatic Procedia* **2015**, *4*, 473–480. https://doi.org/10.1016/j.aqpro.2015.02.062.

(4) Braff, W. A.; Mueller, J. M.; Trancik, J. E. Value of Storage Technologies for Wind and Solar Energy. *Nature Clim Change* **2016**, *6* (10), 964–969. https://doi.org/10.1038/nclimate3045.

(5) Harvard University; Mcelroy, M. B.; Chen, X.; Harvard University. Wind and Solar Power in the United States: Status and Prospects. *CSEE JPES* **2017**, *3* (1), 1–6. https://doi.org/10.17775/CSEEJPES.2017.0002.

(6) Lantz, E.; Hand, M. Past and Future Cost of Wind Energy: Preprint. 10.

(7) Dehghani-Sanij, A. R.; Tharumalingam, E.; Dusseault, M. B.; Fraser, R. Study of Energy Storage Systems and Environmental Challenges of Batteries. *Renewable and Sustainable Energy Reviews* **2019**, *104*, 192–208. https://doi.org/10.1016/j.rser.2019.01.023.

(8) Dowling, J. A.; Rinaldi, K. Z.; Ruggles, T. H.; Davis, S. J.; Yuan, M.; Tong, F.; Lewis, N. S.; Caldeira, K. Role of Long-Duration Energy Storage in Variable Renewable Electricity Systems. *Joule* **2020**, *4* (9), 1907–1928. https://doi.org/10.1016/j.joule.2020.07.007.

(9) Schiffer, Z. J.; Manthiram, K. Electrification and Decarbonization of the Chemical Industry. *Joule* **2017**, *1* (1), 10–14. https://doi.org/10.1016/j.joule.2017.07.008.

(10) Baldwin, R.; Pham, M.; Leonida, A.; McElroy, J.; Nalette, T. Hydrogen□oxygen Proton-Exchange Membrane Fuel Cells and Electrolyzers. *Journal of Power Sources* **1990**, *29* (3–4), 399–412. https://doi.org/10.1016/0378-7753(90)85013-3.

(11) Weber, A. Z.; Borup, R. L.; Darling, R. M.; Das, P. K.; Dursch, T. J.; Gu, W.; Harvey, D.; Kusoglu, A.; Litster, S.; Mench, M. M.; Mukundan, R.; Owejan, J. P.; Pharoah, J. G.; Secanell, M.; Zenyuk, I. V. A Critical Review of Modeling Transport Phenomena in Polymer-Electrolyte Fuel Cells. *J. Electrochem. Soc.* **2014**, *161* (12), F1254–F1299. https://doi.org/10.1149/2.0751412jes.

(12) Kushner, D. I.; Crothers, A. R.; Kusoglu, A.; Weber, A. Z. Transport Phenomena in Flow Battery Ion-Conducting Membranes. *Current Opinion in Electrochemistry* **2020**, *21*, 132–139. https://doi.org/10.1016/j.coelec.2020.01.010.

(13) Kusoglu, A. The Many Colors of Hydrogen. *The Electrochemical Society Interface* **2021**, 7.

(14) Pivovar, B.; Rustagi, N.; Satyapal, S. Hydrogen at Scale (H_2@Scale): Key to a Clean, Economic, and Sustainable Energy System. *Electrochem. Soc. Interface* **2018**, *27* (1), 47–52. https://doi.org/10.1149/2.F04181if.

(15) Pivovar, B. S.; Ruth, M. F.; Myers, D. J.; Dinh, H. N. Hydrogen: Targeting $1/Kg in 1 Decade. *The Electrochemical Society Interface* **2021**, 7.

(16) Barbir, F. PEM Electrolysis for Production of Hydrogen from Renewable Energy Sources. *Solar Energy* **2005**, *78* (5), 661–669. https://doi.org/10.1016/j.solener.2004.09.003.

(17) Dincer, I.; Acar, C. Innovation in Hydrogen Production. *International Journal of Hydrogen Energy* **2017**, *42* (22), 14843–14864. https://doi.org/10.1016/j.ijhydene.2017.04.107.
(18) Holladay, J. D.; Hu, J.; King, D. L.; Wang, Y. An Overview of Hydrogen Production Technologies. *Catalysis Today* **2009**, *139* (4), 244–260. https://doi.org/10.1016/j.cattod.2008.08.039.
(19) Saeedmanesh, A.; Mac Kinnon, M. A.; Brouwer, J. Hydrogen Is Essential for Sustainability. *Current Opinion in Electrochemistry* **2018**, *12*, 166–181. https://doi.org/10.1016/j.coelec.2018.11.009.
(20) Ayers, K.; Danilovic, N.; Harrison, K.; Xu, H. PEM Electrolysis, a Forerunner for Clean Hydrogen. *The Electrochemical Society Interface* **2021**, 7.
(21) Carmo, M.; Fritz, D. L.; Mergel, J.; Stolten, D. A Comprehensive Review on PEM Water Electrolysis. *International Journal of Hydrogen Energy* **2013**, *38* (12), 4901–4934. https://doi.org/10.1016/j.ijhydene.2013.01.151.
(22) Rashid, M.; Mesfer, M. K. A.; Naseem, H.; Danish, M. Hydrogen Production by Water Electrolysis: A Review of Alkaline Water Electrolysis, PEM Water Electrolysis and High Temperature Water Electrolysis. *4* (3), 14.
(23) Miller, E.; Randolph, K.; Peterson, D. The HydroGEN Consortium: Foundational Early Stage Water-Splitting Research Supporting Diversification of the Domestic Hydrogen Supply Chain. *Current Opinion in Electrochemistry* **2018**, *12*, 196–201. https://doi.org/10.1016/j.coelec.2018.11.018.
(24) Ardo, S.; Fernandez Rivas, D.; Modestino, M. A.; Schulze Greiving, V.; Abdi, F. F.; Alarcon Llado, E.; Artero, V.; Ayers, K.; Battaglia, C.; Becker, J.-P.; Bederak, D.; Berger, A.; Buda, F.; Chinello, E.; Dam, B.; Di Palma, V.; Edvinsson, T.; Fujii, K.; Gardeniers, H.; Geerlings, H.; H. Hashemi, S. M.; Haussener, S.; Houle, F.; Huskens, J.; James, B. D.; Konrad, K.; Kudo, A.; Kunturu, P. P.; Lohse, D.; Mei, B.; Miller, E. L.; Moore, G. F.; Muller, J.; Orchard, K. L.; Rosser, T. E.; Saadi, F. H.; Schüttauf, J.-W.; Seger, B.; Sheehan, S. W.; Smith, W. A.; Spurgeon, J.; Tang, M. H.; van de Krol, R.; Vesborg, P. C. K.; Westerik, P. Pathways to Electrochemical Solar-Hydrogen Technologies. *Energy Environ. Sci.* **2018**, *11* (10), 2768–2783. https://doi.org/10.1039/C7EE03639F.
(25) Grigoriev, S. A.; Millet, P.; Porembsky, V. I.; Fateev, V. N. Development and Preliminary Testing of a Unitized Regenerative Fuel Cell Based on PEM Technology. *International Journal of Hydrogen Energy* **2011**, *36* (6), 4164–4168. https://doi.org/10.1016/j.ijhydene.2010.07.011.
(26) Sadhasivam, T.; Dhanabalan, K.; Roh, S.-H.; Kim, T.-H.; Park, K.-W.; Jung, S.; Kurkuri, M. D.; Jung, H.-Y. A Comprehensive Review on Unitized Regenerative Fuel Cells: Crucial Challenges and Developments. *International Journal of Hydrogen Energy* **2017**, *42* (7), 4415–4433. https://doi.org/10.1016/j.ijhydene.2016.10.140.
(27) Advanced Liquid Alkaline Water Electrolysis Experts Meeting. 39.
(28) Shiva Kumar, S.; Himabindu, V. Hydrogen Production by PEM Water Electrolysis – A Review. *Materials Science for Energy Technologies* **2019**, *2* (3), 442–454. https://doi.org/10.1016/j.mset.2019.03.002.
(29) Pivovar, B. 2011 Alkaline Membrane Fuel Cell Workshop Final Report. *Renewable Energy* **2012**, 28.
(30) Abbasi, R.; Setzler, B. P.; Lin, S.; Wang, J.; Zhao, Y.; Xu, H.; Pivovar, B.; Tian, B.; Chen, X.; Wu, G.; Yan, Y. A Roadmap to Low-Cost Hydrogen with Hydroxide Exchange

Membrane Electrolyzers. *Adv. Mater.* **2019**, *31* (31), 1805876. https://doi.org/10.1002/adma.201805876.
(31) Fortin, P.; Khoza, T.; Cao, X.; Martinsen, S. Y.; Oyarce Barnett, A.; Holdcroft, S. High-Performance Alkaline Water Electrolysis Using Aemion™ Anion Exchange Membranes. *Journal of Power Sources* **2020**, *451*, 227814. https://doi.org/10.1016/j.jpowsour.2020.227814.
(32) Li, D.; Motz, A. R.; Bae, C.; Fujimoto, C.; Yang, G.; Zhang, F.-Y.; Ayers, K. E.; Kim, Y. S. Durability of Anion Exchange Membrane Water Electrolyzers. *Energy Environ. Sci.* **2021**, *14* (6), 3393–3419. https://doi.org/10.1039/D0EE04086J.
(33) Liu, J.; Kang, Z.; Li, D.; Pak, M.; Alia, S. M.; Fujimoto, C.; Bender, G.; Kim, Y. S.; Weber, A. Z. Elucidating the Role of Hydroxide Electrolyte on Anion-Exchange-Membrane Water Electrolyzer Performance. *J. Electrochem. Soc.* **2021**, *168* (5), 054522. https://doi.org/10.1149/1945-7111/ac0019.
(34) Pivovar, B.; Kim, Y. *2019 Anion Exchange Membrane Workshop Summary Report*; NREL/TP--5900-77240, 1660106, MainId:26186; 2020; p NREL/TP--5900-77240, 1660106, MainId:26186. https://doi.org/10.2172/1660106.
(35) Kiessling, A.; Fornaciari, J. C.; Anderson, G.; Peng, X.; Gerstmayr, A.; Gerhardt, M. R.; McKinney, S.; Serov, A.; Kim, Y. S.; Zulevi, B.; Weber, A. Z.; Danilovic, N. Influence of Supporting Electrolyte on Hydroxide Exchange Membrane Water Electrolysis Performance: Anolyte. *J. Electrochem. Soc.* **2021**, *168* (8), 084512. https://doi.org/10.1149/1945-7111/ac1dcd.
(36) Kiessling, A.; Fornaciari, J. C.; Anderson, G.; Peng, X.; Gerstmayr, A.; Gerhardt, M.; McKinney, S.; Serov, A.; Weber, A. Z.; Kim, Y. S.; Zulevi, B.; Danilovic, N. Influence of Supporting Electrolyte on Hydroxide Exchange Membrane Water Electrolysis Performance: Catholyte. *J. Electrochem. Soc.* **2022**, *169* (2), 024510. https://doi.org/10.1149/1945-7111/ac4fed.
(37) Higgins, D.; Hahn, C.; Xiang, C.; Jaramillo, T. F.; Weber, A. Z. Gas-Diffusion Electrodes for Carbon Dioxide Reduction: A New Paradigm. *ACS Energy Lett.* **2019**, *4* (1), 317–324. https://doi.org/10.1021/acsenergylett.8b02035.
(38) Lazouski, N.; Chung, M.; Williams, K.; Gala, M. L.; Manthiram, K. Non-Aqueous Gas Diffusion Electrodes for Rapid Ammonia Synthesis from Nitrogen and Water-Splitting-Derived Hydrogen. *Nat Catal* **2020**, *3* (5), 463–469. https://doi.org/10.1038/s41929-020-0455-8.
(39) Fornaciari, J. C.; Primc, D.; Kawashima, K.; Wygant, B. R.; Verma, S.; Spanu, L.; Mullins, C. B.; Bell, A. T.; Weber, A. Z. A Perspective on the Electrochemical Oxidation of Methane to Methanol in Membrane Electrode Assemblies. *ACS Energy Lett.* **2020**, *5* (9), 2954–2963. https://doi.org/10.1021/acsenergylett.0c01508.
(40) Zakaria, Z.; Kamarudin, S. K. Direct Conversion Technologies of Methane to Methanol: An Overview. *Renewable and Sustainable Energy Reviews* **2016**, *65*, 250–261. https://doi.org/10.1016/j.rser.2016.05.082.
(41) Bender, G.; Carmo, M.; Smolinka, T.; Gago, A.; Danilovic, N.; Mueller, M.; Ganci, F.; Fallisch, A.; Lettenmeier, P.; Friedrich, K. A.; Ayers, K.; Pivovar, B.; Mergel, J.; Stolten, D. Initial Approaches in Benchmarking and Round Robin Testing for Proton Exchange Membrane Water Electrolyzers. *International Journal of Hydrogen Energy* **2019**, *44* (18), 9174–9187. https://doi.org/10.1016/j.ijhydene.2019.02.074.

(42) Mayyas, A. T.; Ruth, M. F.; Pivovar, B. S.; Bender, G.; Wipke, K. B. *Manufacturing Cost Analysis for Proton Exchange Membrane Water Electrolyzers*; NREL/TP-6A20-72740, 1557965; 2019; p NREL/TP-6A20-72740, 1557965. https://doi.org/10.2172/1557965.
(43) University of California, Berkeley; Wei, M.; Lipman, T.; Mayyas, A.; Chien, J.; Chan, S.; Gosselin, D.; Breunig, H.; Stadler, M.; McKone, T.; Beattie, P.; Chong, P.; Colella, W.; James, B. *A Total Cost of Ownership Model for Low Temperature PEM Fuel Cells in Combined Heat and Power and Backup Power Applications*; LBNL-6772E, 1163271; 2014; p LBNL-6772E, 1163271. https://doi.org/10.2172/1163271.
(44) An, L.; Wei, C.; Lu, M.; Liu, H.; Chen, Y.; Scherer, G. G.; Fisher, A. C.; Xi, P.; Xu, Z. J.; Yan, C. Recent Development of Oxygen Evolution Electrocatalysts in Acidic Environment. *Adv. Mater.* **2021**, *33* (20), 2006328. https://doi.org/10.1002/adma.202006328.
(45) Suen, N.-T.; Hung, S.-F.; Quan, Q.; Zhang, N.; Xu, Y.-J.; Chen, H. M. Electrocatalysis for the Oxygen Evolution Reaction: Recent Development and Future Perspectives. *Chem. Soc. Rev.* **2017**, *46* (2), 337–365. https://doi.org/10.1039/C6CS00328A.
(46) Tahir, M.; Pan, L.; Idrees, F.; Zhang, X.; Wang, L.; Zou, J.-J.; Wang, Z. L. Electrocatalytic Oxygen Evolution Reaction for Energy Conversion and Storage: A Comprehensive Review. *Nano Energy* **2017**, *37*, 136–157. https://doi.org/10.1016/j.nanoen.2017.05.022.
(47) Hughes, J. P.; Clipsham, J.; Chavushoglu, H.; Rowley-Neale, S. J.; Banks, C. E. Polymer Electrolyte Electrolysis: A Review of the Activity and Stability of Non-Precious Metal Hydrogen Evolution Reaction and Oxygen Evolution Reaction Catalysts. *Renewable and Sustainable Energy Reviews* **2021**, *139*, 110709. https://doi.org/10.1016/j.rser.2021.110709.
(48) Lee, Ch.; Lee, J. K.; Zhao, B.; Fahy, K. F.; Bazylak, A. Transient Gas Distribution in Porous Transport Layers of Polymer Electrolyte Membrane Electrolyzers. *J. Electrochem. Soc.* **2020**, *167* (2), 024508. https://doi.org/10.1149/1945-7111/ab68c8.
(49) Satjaritanun, P.; O'Brien, M.; Kulkarni, D.; Shimpalee, S.; Capuano, C.; Ayers, K. E.; Danilovic, N.; Parkinson, D. Y.; Zenyuk, I. V. Observation of Preferential Pathways for Oxygen Removal through Porous Transport Layers of Polymer Electrolyte Water Electrolyzers. *iScience* **2020**, *23* (12), 101783. https://doi.org/10.1016/j.isci.2020.101783.
(50) Peng, X.; Satjaritanun, P.; Taie, Z.; Wiles, L.; Keane, A.; Capuano, C.; Zenyuk, I. V.; Danilovic, N. Insights into Interfacial and Bulk Transport Phenomena Affecting Proton Exchange Membrane Water Electrolyzer Performance at Ultra-Low Iridium Loadings. *Adv. Sci.* **2021**, *8* (21), 2102950. https://doi.org/10.1002/advs.202102950.
(51) Hatzell, K. B.; Dixit, M. B.; Berlinger, S. A.; Weber, A. Z. Understanding Inks for Porous-Electrode Formation. *J. Mater. Chem. A* **2017**, *5* (39), 20527–20533. https://doi.org/10.1039/C7TA07255D.
(52) Dixit, M. B.; Harkey, B. A.; Shen, F.; Hatzell, K. B. Catalyst Layer Ink Interactions That Affect Coatability. *J. Electrochem. Soc.* **2018**, *165* (5), F264–F271. https://doi.org/10.1149/2.0191805jes.
(53) Berlinger, S. A.; Garg, S.; Weber, A. Z. Multicomponent, Multiphase Interactions in Fuel-Cell Inks. *Current Opinion in Electrochemistry* **2021**, *29*, 100744. https://doi.org/10.1016/j.coelec.2021.100744.
(54) Khandavalli, S.; Park, J. H.; Kariuki, N. N.; Zaccarine, S. F.; Pylypenko, S.; Myers, D. J.; Ulsh, M.; Mauger, S. A. Investigation of the Microstructure and Rheology of Iridium

Oxide Catalyst Inks for Low-Temperature Polymer Electrolyte Membrane Water Electrolyzers. *ACS Appl. Mater. Interfaces* **2019**, *11* (48), 45068–45079. https://doi.org/10.1021/acsami.9b14415.

(55) Alia, S. M.; Reeves, K. S.; Baxter, J. S.; Cullen, D. A. The Impact of Ink and Spray Variables on Catalyst Layer Properties, Electrolyzer Performance, and Electrolyzer Durability. *J. Electrochem. Soc.* **2020**, *167* (14), 144512. https://doi.org/10.1149/1945-7111/abc746.

(56) Xie, S.; Lin, S.; Zhang, Q.; Tian, Z.; Wang, Y. Selective Electrocatalytic Conversion of Methane to Fuels and Chemicals. *Journal of Energy Chemistry* **2018**, *27* (6), 1629–1636. https://doi.org/10.1016/j.jechem.2018.03.015.

(57) Weng, L.-C.; Bell, A. T.; Weber, A. Z. Towards Membrane-Electrode Assembly Systems for CO_2 Reduction: A Modeling Study. *Energy Environ. Sci.* **2019**, *12* (6), 1950–1968. https://doi.org/10.1039/C9EE00909D.

(58) Bagherzadeh Mostaghimi, A. H.; Al-Attas, T. A.; Kibria, M. G.; Siahrostami, S. A Review on Electrocatalytic Oxidation of Methane to Oxygenates. *J. Mater. Chem. A* **2020**, *8* (31), 15575–15590. https://doi.org/10.1039/D0TA03758C.

(59) Taie, Z.; Peng, X.; Kulkarni, D.; Zenyuk, I. V.; Weber, A. Z.; Hagen, C.; Danilovic, N. Pathway to Complete Energy Sector Decarbonization with Available Iridium Resources Using Ultralow Loaded Water Electrolyzers. *ACS Appl. Mater. Interfaces* **2020**, *12* (47), 52701–52712. https://doi.org/10.1021/acsami.0c15687.

(60) Schmidt, J.; Gruber, K.; Klingler, M.; Klöckl, C.; Ramirez Camargo, L.; Regner, P.; Turkovska, O.; Wehrle, S.; Wetterlund, E. A New Perspective on Global Renewable Energy Systems: Why Trade in Energy Carriers Matters. *Energy Environ. Sci.* **2019**, *12* (7), 2022–2029. https://doi.org/10.1039/C9EE00223E.

(61) Davis, S. J.; Lewis, N. S.; Shaner, M.; Aggarwal, S.; Arent, D.; Azevedo, I. L.; Benson, S. M.; Bradley, T.; Brouwer, J.; Chiang, Y.-M.; Clack, C. T. M.; Cohen, A.; Doig, S.; Edmonds, J.; Fennell, P.; Field, C. B.; Hannegan, B.; Hodge, B.-M.; Hoffert, M. I.; Ingersoll, E.; Jaramillo, P.; Lackner, K. S.; Mach, K. J.; Mastrandrea, M.; Ogden, J.; Peterson, P. F.; Sanchez, D. L.; Sperling, D.; Stagner, J.; Trancik, J. E.; Yang, C.-J.; Caldeira, K. Net-Zero Emissions Energy Systems. *Science* **2018**, *360* (6396), eaas9793. https://doi.org/10.1126/science.aas9793.

(62) Mazloomi, K.; Gomes, C. Hydrogen as an Energy Carrier: Prospects and Challenges. *Renewable and Sustainable Energy Reviews* **2012**, *16* (5), 3024–3033. https://doi.org/10.1016/j.rser.2012.02.028.

(63) Department of Interface Chemistry and Surface Engineering, Max-Planck-Institut für Eisenforschung GmbH, Max-Planck-Strasse 1, 40237 Düsseldorf, Germany; Schalenbach, M. A Perspective on Low-Temperature Water Electrolysis – Challenges in Alkaline and Acidic Technology. *Int. J. Electrochem. Sci.* **2018**, 1173–1226. https://doi.org/10.20964/2018.02.26.

(64) Alia, S. M.; Rasimick, B.; Ngo, C.; Neyerlin, K. C.; Kocha, S. S.; Pylypenko, S.; Xu, H.; Pivovar, B. S. Activity and Durability of Iridium Nanoparticles in the Oxygen Evolution Reaction. *J. Electrochem. Soc.* **2016**, *163* (11), F3105–F3112. https://doi.org/10.1149/2.0151611jes.

(65) Berlinger, S. A.; McCloskey, B. D.; Weber, A. Z. Understanding Binary Interactions in Fuel-Cell Catalyst-Layer Inks. *ECS Trans.* **2017**, *80* (8), 309–319. https://doi.org/10.1149/08008.0309ecst.

(66) Khandavalli, S.; Park, J. H.; Kariuki, N. N.; Myers, D. J.; Stickel, J. J.; Hurst, K.; Neyerlin, K. C.; Ulsh, M.; Mauger, S. A. Rheological Investigation on the Microstructure of Fuel Cell Catalyst Inks. *ACS Appl. Mater. Interfaces* **2018**, *10* (50), 43610–43622. https://doi.org/10.1021/acsami.8b15039.
(67) Khandavalli, S.; Iyer, R.; Park, J. H.; Myers, D. J.; Neyerlin, K. C.; Ulsh, M.; Mauger, S. A. Effect of Dispersion Medium Composition and Ionomer Concentration on the Microstructure and Rheology of Fe–N–C Platinum Group Metal-Free Catalyst Inks for Polymer Electrolyte Membrane Fuel Cells. *Langmuir* **2020**, *36* (41), 12247–12260. https://doi.org/10.1021/acs.langmuir.0c02015.
(68) Lei, C.; Yang, F.; Macauley, N.; Spinetta, M.; Purdy, G.; Jankovic, J.; Cullen, D. A.; More, K. L.; Kim, Y. S.; Xu, H. Impact of Catalyst Ink Dispersing Solvent on PEM Fuel Cell Performance and Durability. *J. Electrochem. Soc.* **2021**, *168* (4), 044517. https://doi.org/10.1149/1945-7111/abf2b0.
(69) Orfanidi, A.; Rheinländer, P. J.; Schulte, N.; Gasteiger, H. A. Ink Solvent Dependence of the Ionomer Distribution in the Catalyst Layer of a PEMFC. *J. Electrochem. Soc.* **2018**, *165* (14), F1254–F1263. https://doi.org/10.1149/2.1251814jes.
(70) Ren, H.; Meng, X.; Lin, Y.; Shao, Z. Structural Stability of Catalyst Ink and Its Effects on the Catalyst Layer Microstructure and Fuel Cell Performance. *Journal of Power Sources* **2022**, *517*, 230698. https://doi.org/10.1016/j.jpowsour.2021.230698.
(71) Taning, A. Z.; Lee, S.; Woo, S.; Park, S.-H.; Bae, B.; Yim, S.-D. Characterization of Solvent-Dependent Ink Structure and Catalyst Layer Morphology Based on Ink Sedimentation Dynamics and Catalyst-Ionomer Cast Films. *J. Electrochem. Soc.* **2021**, *168* (10), 104506. https://doi.org/10.1149/1945-7111/ac2c13.
(72) Yang, D.; Zhu, S.; Guo, Y.; Tang, H.; Yang, D.; Zhang, C.; Ming, P.; Li, B. Control of Cluster Structures in Catalyst Inks by a Dispersion Medium. *ACS Omega* **2021**, *6* (48), 32960–32969. https://doi.org/10.1021/acsomega.1c05026.
(73) Welch, C.; Labouriau, A.; Hjelm, R.; Orler, B.; Johnston, C.; Kim, Y. S. Nafion in Dilute Solvent Systems: Dispersion or Solution? *ACS Macro Lett.* **2012**, *1* (12), 1403–1407. https://doi.org/10.1021/mz3005204.
(74) Bernt, M.; Gasteiger, H. A. Influence of Ionomer Content in IrO_2 /TiO_2 Electrodes on PEM Water Electrolyzer Performance. *J. Electrochem. Soc.* **2016**, *163* (11), F3179–F3189. https://doi.org/10.1149/2.0231611jes.
(75) Schuler, T.; Chowdhury, A.; Freiberg, A. T.; Sneed, B.; Spingler, F. B.; Tucker, M. C.; More, K. L.; Radke, C. J.; Weber, A. Z. Fuel-Cell Catalyst-Layer Resistance via Hydrogen Limiting-Current Measurements. *J. Electrochem. Soc.* **2019**, *166* (7), F3020–F3031. https://doi.org/10.1149/2.0031907jes.
(76) Gerhardt, M. R.; Pant, L. M.; Bui, J. C.; Crothers, A. R.; Ehlinger, V. M.; Fornaciari, J. C.; Liu, J.; Weber, A. Z. Method—Practices and Pitfalls in Voltage Breakdown Analysis of Electrochemical Energy-Conversion Systems. *J. Electrochem. Soc.* **2021**, *168* (7), 074503. https://doi.org/10.1149/1945-7111/abf061.
(77) Hartig-Weiß, A.; Bernt, M.; Siebel, A.; Gasteiger, H. A. A Platinum Micro-Reference Electrode for Impedance Measurements in a PEM Water Electrolysis Cell. *J. Electrochem. Soc.* **2021**, *168* (11), 114511. https://doi.org/10.1149/1945-7111/ac3717.
(78) Bratsch, S. G. Standard Electrode Potentials and Temperature Coefficients in Water at 298.15 K. *Journal of Physical and Chemical Reference Data* **1989**, *18* (1), 1–21. https://doi.org/10.1063/1.555839.

(79) Kumano, N.; Kudo, K.; Suda, A.; Akimoto, Y.; Ishii, M.; Nakamura, H. Controlling Cracking Formation in Fuel Cell Catalyst Layers. *Journal of Power Sources* **2019**, *419*, 219–228. https://doi.org/10.1016/j.jpowsour.2019.02.058.
(80) Holdcroft, S. Fuel Cell Catalyst Layers: A Polymer Science Perspective. *Chem. Mater.* **2014**, *26* (1), 381–393. https://doi.org/10.1021/cm401445h.
(81) Susac, D.; Berejnov, V.; Hitchcock, A. P.; Stumper, J. STXM Study of the Ionomer Distribution in the PEM Fuel Cell Catalyst Layers. *ECS Trans.* **2011**, *41* (1), 629–635. https://doi.org/10.1149/1.3635596.
(82) Alia, S. M.; Hurst, K. E.; Kocha, S. S.; Pivovar, B. S. Mercury Underpotential Deposition to Determine Iridium and Iridium Oxide Electrochemical Surface Areas. *J. Electrochem. Soc.* **2016**, *163* (11), F3051–F3056. https://doi.org/10.1149/2.0071611jes.
(83) Zhao, S.; Yu, H.; Maric, R.; Danilovic, N.; Capuano, C. B.; Ayers, K. E.; Mustain, W. E. Calculating the Electrochemically Active Surface Area of Iridium Oxide in Operating Proton Exchange Membrane Electrolyzers. *J. Electrochem. Soc.* **2015**, *162* (12), F1292–F1298. https://doi.org/10.1149/2.0211512jes.
(84) Wang, M.; Wang, Z.; Gong, X.; Guo, Z. The Intensification Technologies to Water Electrolysis for Hydrogen Production – A Review. *Renewable and Sustainable Energy Reviews* **2014**, *29*, 573–588. https://doi.org/10.1016/j.rser.2013.08.090.
(85) Nouri-Khorasani, A.; Tabu Ojong, E.; Smolinka, T.; Wilkinson, D. P. Model of Oxygen Bubbles and Performance Impact in the Porous Transport Layer of PEM Water Electrolysis Cells. *International Journal of Hydrogen Energy* **2017**, *42* (48), 28665–28680. https://doi.org/10.1016/j.ijhydene.2017.09.167.
(86) Zenyuk, I. V.; Parkinson, D. Y.; Connolly, L. G.; Weber, A. Z. Gas-Diffusion-Layer Structural Properties under Compression via X-Ray Tomography. *Journal of Power Sources* **2016**, *328*, 364–376. https://doi.org/10.1016/j.jpowsour.2016.08.020.
(87) Lee, J. K.; Lee, C.; Fahy, K. F.; Zhao, B.; LaManna, J. M.; Baltic, E.; Jacobson, D. L.; Hussey, D. S.; Bazylak, A. Critical Current Density as a Performance Indicator for Gas-Evolving Electrochemical Devices. *Cell Reports Physical Science* **2020**, *1* (8), 100147. https://doi.org/10.1016/j.xcrp.2020.100147.
(88) Mabuchi, T.; Huang, S.-F.; Tokumasu, T. Dispersion of Nafion Ionomer Aggregates in 1-Propanol/Water Solutions: Effects of Ionomer Concentration, Alcohol Content, and Salt Addition. *Macromolecules* **2020**, *53* (9), 3273–3283. https://doi.org/10.1021/acs.macromol.9b02725.
(89) Leonard, E.; Shum, A. D.; Danilovic, N.; Capuano, C.; Ayers, K. E.; Pant, L. M.; Weber, A. Z.; Xiao, X.; Parkinson, D. Y.; Zenyuk, I. V. Interfacial Analysis of a PEM Electrolyzer Using X-Ray Computed Tomography. *Sustainable Energy Fuels* **2020**, *4* (2), 921–931. https://doi.org/10.1039/C9SE00364A.
(90) Ahmad, H.; Kamarudin, S. K.; Minggu, L. J.; Kassim, M. Hydrogen from Photo-Catalytic Water Splitting Process: A Review. *Renewable and Sustainable Energy Reviews* **2015**, *43*, 599–610. https://doi.org/10.1016/j.rser.2014.10.101.
(91) Chu, S.; Majumdar, A. Opportunities and Challenges for a Sustainable Energy Future. *Nature* **2012**, *488* (7411), 294–303. https://doi.org/10.1038/nature11475.
(92) Badwal, S. P. S.; Giddey, S. S.; Munnings, C.; Bhatt, A. I.; Hollenkamp, A. F. Emerging Electrochemical Energy Conversion and Storage Technologies. *Front. Chem.* **2014**, *2*. https://doi.org/10.3389/fchem.2014.00079.

(93) Arminio-Ravelo, J. A.; Jensen, A. W.; Jensen, K. D.; Quinson, J.; Escudero-Escribano, M. Electrolyte Effects on the Electrocatalytic Performance of Iridium-Based Nanoparticles for Oxygen Evolution in Rotating Disc Electrodes. *ChemPhysChem* **2019**, *20* (22), 2956–2963. https://doi.org/10.1002/cphc.201900902.
(94) Reier, T.; Nong, H. N.; Teschner, D.; Schlögl, R.; Strasser, P. Electrocatalytic Oxygen Evolution Reaction in Acidic Environments - Reaction Mechanisms and Catalysts. *Adv. Energy Mater.* **2017**, *7* (1), 1601275. https://doi.org/10.1002/aenm.201601275.
(95) Naito, T.; Shinagawa, T.; Nishimoto, T.; Takanabe, K. Recent Advances in Understanding Oxygen Evolution Reaction Mechanisms over Iridium Oxide. *Inorg. Chem. Front.* **2021**, *8* (11), 2900–2917. https://doi.org/10.1039/D0QI01465F.
(96) Xiang, C.; Weber, A. Z.; Ardo, S.; Berger, A.; Chen, Y.; Coridan, R.; Fountaine, K. T.; Haussener, S.; Hu, S.; Liu, R.; Lewis, N. S.; Modestino, M. A.; Shaner, M. M.; Singh, M. R.; Stevens, J. C.; Sun, K.; Walczak, K. Modeling, Simulation, and Implementation of Solar-Driven Water-Splitting Devices. *Angew. Chem. Int. Ed.* **2016**, *55* (42), 12974–12988. https://doi.org/10.1002/anie.201510463.
(97) Jafari, T.; Moharreri, E.; Amin, A.; Miao, R.; Song, W.; Suib, S. Photocatalytic Water Splitting—The Untamed Dream: A Review of Recent Advances. *Molecules* **2016**, *21* (7), 900. https://doi.org/10.3390/molecules21070900.
(98) Kistler, T. A.; Larson, D.; Walczak, K.; Agbo, P.; Sharp, I. D.; Weber, A. Z.; Danilovic, N. Integrated Membrane-Electrode-Assembly Photoelectrochemical Cell under Various Feed Conditions for Solar Water Splitting. *J. Electrochem. Soc.* **2019**, *166* (5), H3020–H3028. https://doi.org/10.1149/2.0041905jes.
(99) Cook, T. R.; Dogutan, D. K.; Reece, S. Y.; Surendranath, Y.; Teets, T. S.; Nocera, D. G. Solar Energy Supply and Storage for the Legacy and Nonlegacy Worlds. *Chem. Rev.* **2010**, *110* (11), 6474–6502. https://doi.org/10.1021/cr100246c.
(100) Park, E. J.; Maurya, S.; Hibbs, M. R.; Fujimoto, C. H.; Kreuer, K.-D.; Kim, Y. S. Alkaline Stability of Quaternized Diels–Alder Polyphenylenes. *Macromolecules* **2019**, *52* (14), 5419–5428. https://doi.org/10.1021/acs.macromol.9b00853.
(101) Jensen, A. W.; Sievers, G. W.; Jensen, K. D.; Quinson, J.; Arminio-Ravelo, J. A.; Brüser, V.; Arenz, M.; Escudero-Escribano, M. Self-Supported Nanostructured Iridium-Based Networks as Highly Active Electrocatalysts for Oxygen Evolution in Acidic Media. *J. Mater. Chem. A* **2020**, *8* (3), 1066–1071. https://doi.org/10.1039/C9TA12796H.
(102) Alia, S. M.; Anderson, G. C. Iridium Oxygen Evolution Activity and Durability Baselines in Rotating Disk Electrode Half-Cells. *J. Electrochem. Soc.* **2019**, *166* (4), F282–F294. https://doi.org/10.1149/2.0731904jes.
(103) Anderson, G. C.; Pivovar, B. S.; Alia, S. M. Establishing Performance Baselines for the Oxygen Evolution Reaction in Alkaline Electrolytes. *J. Electrochem. Soc.* **2020**, *167* (4), 044503. https://doi.org/10.1149/1945-7111/ab7090.
(104) Ghoshal, S.; Pivovar, B. S.; Alia, S. M. Evaluating the Effect of Membrane-Ionomer Combinations and Supporting Electrolytes on the Performance of Cobalt Nanoparticle Anodes in Anion Exchange Membrane Electrolyzers. *Journal of Power Sources* **2021**, *488*, 229433. https://doi.org/10.1016/j.jpowsour.2020.229433.
(105) Dickens, C. F.; Kirk, C.; Nørskov, J. K. Insights into the Electrochemical Oxygen Evolution Reaction with Ab Initio Calculations and Microkinetic Modeling: Beyond the Limiting Potential Volcano. *J. Phys. Chem. C* **2019**, *123* (31), 18960–18977. https://doi.org/10.1021/acs.jpcc.9b03830.

(106) Over, H. Surface Chemistry of Ruthenium Dioxide in Heterogeneous Catalysis and Electrocatalysis: From Fundamental to Applied Research. *Chem. Rev.* **2012**, *112* (6), 3356–3426. https://doi.org/10.1021/cr200247n.
(107) Nishimoto, T.; Shinagawa, T.; Naito, T.; Takanabe, K. Microkinetic Assessment of Electrocatalytic Oxygen Evolution Reaction over Iridium Oxide in Unbuffered Conditions. *Journal of Catalysis* **2020**, *391*, 435–445. https://doi.org/10.1016/j.jcat.2020.09.007.
(108) Singh, M. R.; Goodpaster, J. D.; Weber, A. Z.; Head-Gordon, M.; Bell, A. T. Mechanistic Insights into Electrochemical Reduction of CO_2 over Ag Using Density Functional Theory and Transport Models. *Proc Natl Acad Sci USA* **2017**, *114* (42), E8812–E8821. https://doi.org/10.1073/pnas.1713164114.
(109) Peng, J.; Roy, A. L.; Greenbaum, S. G.; Zawodzinski, T. A. Effect of CO2 Absorption on Ion and Water Mobility in an Anion Exchange Membrane. *Journal of Power Sources* **2018**, *380*, 64–75. https://doi.org/10.1016/j.jpowsour.2018.01.071.
(110) Felgenhauer, M.; Hamacher, T. State-of-the-Art of Commercial Electrolyzers and on-Site Hydrogen Generation for Logistic Vehicles in South Carolina. *International Journal of Hydrogen Energy* **2015**, *40* (5), 2084–2090. https://doi.org/10.1016/j.ijhydene.2014.12.043.
(111) Vincent, I.; Kruger, A.; Bessarabov, D. Development of Efficient Membrane Electrode Assembly for Low Cost Hydrogen Production by Anion Exchange Membrane Electrolysis. *International Journal of Hydrogen Energy* **2017**, *42* (16), 10752–10761. https://doi.org/10.1016/j.ijhydene.2017.03.069.
(112) Li, D.; Park, E. J.; Zhu, W.; Shi, Q.; Zhou, Y.; Tian, H.; Lin, Y.; Serov, A.; Zulevi, B.; Baca, E. D.; Fujimoto, C.; Chung, H. T.; Kim, Y. S. Highly Quaternized Polystyrene Ionomers for High Performance Anion Exchange Membrane Water Electrolysers. *Nat Energy* **2020**, *5* (5), 378–385. https://doi.org/10.1038/s41560-020-0577-x.
(113) Vincent, I.; Bessarabov, D. Low Cost Hydrogen Production by Anion Exchange Membrane Electrolysis: A Review. *Renewable and Sustainable Energy Reviews* **2018**, *81*, 1690–1704. https://doi.org/10.1016/j.rser.2017.05.258.
(114) Man, I. C.; Su, H.; Calle-Vallejo, F.; Hansen, H. A.; Martínez, J. I.; Inoglu, N. G.; Kitchin, J.; Jaramillo, T. F.; Nørskov, J. K.; Rossmeisl, J. Universality in Oxygen Evolution Electrocatalysis on Oxide Surfaces. *ChemCatChem* **2011**, *3* (7), 1159–1165. https://doi.org/10.1002/cctc.201000397.
(115) Rossmeisl, J.; Qu, Z.-W.; Zhu, H.; Kroes, G.-J.; Nørskov, J. K. Electrolysis of Water on Oxide Surfaces. *Journal of Electroanalytical Chemistry* **2007**, *607* (1–2), 83–89. https://doi.org/10.1016/j.jelechem.2006.11.008.
(116) Exner, K. S.; Over, H. Beyond the Rate-Determining Step in the Oxygen Evolution Reaction over a Single-Crystalline IrO_2 (110) Model Electrode: Kinetic Scaling Relations. *ACS Catal.* **2019**, *9* (8), 6755–6765. https://doi.org/10.1021/acscatal.9b01564.
(117) Fornaciari, J. C.; Weng, L.-C.; Alia, S. M.; Zhan, C.; Pham, T. A.; Bell, A. T.; Ogitsu, T.; Danilovic, N.; Weber, A. Z. Mechanistic Understanding of PH Effects on the Oxygen Evolution Reaction. *Electrochimica Acta* **2022**, *405*, 139810. https://doi.org/10.1016/j.electacta.2021.139810.
(118) Lee, Y.; Suntivich, J.; May, K. J.; Perry, E. E.; Shao-Horn, Y. Synthesis and Activities of Rutile IrO_2 and RuO_2 Nanoparticles for Oxygen Evolution in Acid and Alkaline Solutions. *J. Phys. Chem. Lett.* **2012**, *3* (3), 399–404. https://doi.org/10.1021/jz2016507.

(119) Giordano, L.; Han, B.; Risch, M.; Hong, W. T.; Rao, R. R.; Stoerzinger, K. A.; Shao-Horn, Y. PH Dependence of OER Activity of Oxides: Current and Future Perspectives. *Catalysis Today* **2016**, *262*, 2–10. https://doi.org/10.1016/j.cattod.2015.10.006.
(120) Hashiba, H.; Weng, L.-C.; Chen, Y.; Sato, H. K.; Yotsuhashi, S.; Xiang, C.; Weber, A. Z. Effects of Electrolyte Buffer Capacity on Surface Reactant Species and the Reaction Rate of CO_2 in Electrochemical CO_2 Reduction. *J. Phys. Chem. C* **2018**, *122* (7), 3719–3726. https://doi.org/10.1021/acs.jpcc.7b11316.
(121) Kuo, D.-Y.; Kawasaki, J. K.; Nelson, J. N.; Kloppenburg, J.; Hautier, G.; Shen, K. M.; Schlom, D. G.; Suntivich, J. Influence of Surface Adsorption on the Oxygen Evolution Reaction on IrO_2 (110). *J. Am. Chem. Soc.* **2017**, *139* (9), 3473–3479. https://doi.org/10.1021/jacs.6b11932.
(122) Axnanda, S.; Crumlin, E. J.; Mao, B.; Rani, S.; Chang, R.; Karlsson, P. G.; Edwards, M. O. M.; Lundqvist, M.; Moberg, R.; Ross, P.; Hussain, Z.; Liu, Z. Using "Tender" X-Ray Ambient Pressure X-Ray Photoelectron Spectroscopy as A Direct Probe of Solid-Liquid Interface. *Sci Rep* **2015**, *5* (1), 9788. https://doi.org/10.1038/srep09788.
(123) Favaro, M.; Xiao, H.; Cheng, T.; Goddard, W. A.; Yano, J.; Crumlin, E. J. Subsurface Oxide Plays a Critical Role in CO_2 Activation by Cu(111) Surfaces to Form Chemisorbed CO_2, the First Step in Reduction of CO_2. *Proc Natl Acad Sci USA* **2017**, 201701405. https://doi.org/10.1073/pnas.1701405114.
(124) Qian, J.; Ye, Y.; Yang, H.; Yano, J.; Crumlin, E. J.; Goddard, W. A. Initial Steps in Forming the Electrode–Electrolyte Interface: H_2O Adsorption and Complex Formation on the Ag(111) Surface from Combining Quantum Mechanics Calculations and Ambient Pressure X-Ray Photoelectron Spectroscopy. *J. Am. Chem. Soc.* **2019**, *141* (17), 6946–6954. https://doi.org/10.1021/jacs.8b13672.
(125) Henkensmeier, D.; Najibah, M.; Harms, C.; Žitka, J.; Hnát, J.; Bouzek, K. Overview: State-of-the Art Commercial Membranes for Anion Exchange Membrane Water Electrolysis. *Journal of Electrochemical Energy Conversion and Storage* **2021**, *18* (2), 024001. https://doi.org/10.1115/1.4047963.
(126) Li, G.-F.; Divinagracia, M.; Labata, M. F.; Ocon, J. D.; Abel Chuang, P.-Y. Electrolyte-Dependent Oxygen Evolution Reactions in Alkaline Media: Electrical Double Layer and Interfacial Interactions. *ACS Appl. Mater. Interfaces* **2019**, *11* (37), 33748–33758. https://doi.org/10.1021/acsami.9b06889.
(127) Pavel, C. C.; Cecconi, F.; Emiliani, C.; Santiccioli, S.; Scaffidi, A.; Catanorchi, S.; Comotti, M. Highly Efficient Platinum Group Metal Free Based Membrane-Electrode Assembly for Anion Exchange Membrane Water Electrolysis. *Angew. Chem. Int. Ed.* **2014**, *53* (5), 1378–1381. https://doi.org/10.1002/anie.201308099.
(128) Weng, L.-C.; Bell, A. T.; Weber, A. Z. Modeling Gas-Diffusion Electrodes for CO_2 Reduction. *Phys. Chem. Chem. Phys.* **2018**, *20* (25), 16973–16984. https://doi.org/10.1039/C8CP01319E.
(129) Buttler, A.; Spliethoff, H. Current Status of Water Electrolysis for Energy Storage, Grid Balancing and Sector Coupling via Power-to-Gas and Power-to-Liquids: A Review. *Renewable and Sustainable Energy Reviews* **2018**, *82*, 2440–2454. https://doi.org/10.1016/j.rser.2017.09.003.
(130) Shaner, M. R.; Atwater, H. A.; Lewis, N. S.; McFarland, E. W. A Comparative Technoeconomic Analysis of Renewable Hydrogen Production Using Solar Energy. *Energy Environ. Sci.* **2016**, *9* (7), 2354–2371. https://doi.org/10.1039/C5EE02573G.

(131) Dai, W.; Wang, H.; Yuan, X.-Z.; Martin, J. J.; Yang, D.; Qiao, J.; Ma, J. A Review on Water Balance in the Membrane Electrode Assembly of Proton Exchange Membrane Fuel Cells. *International Journal of Hydrogen Energy* **2009**, *34* (23), 9461–9478. https://doi.org/10.1016/j.ijhydene.2009.09.017.
(132) Majlan, E. H.; Rohendi, D.; Daud, W. R. W.; Husaini, T.; Haque, M. A. Electrode for Proton Exchange Membrane Fuel Cells: A Review. *Renewable and Sustainable Energy Reviews* **2018**, *89*, 117–134. https://doi.org/10.1016/j.rser.2018.03.007.
(133) Pant, L. M.; Yang, Z.; Perry, M. L.; Weber, A. Z. Development of a Simple and Rapid Diagnostic Method for Polymer-Electrolyte Fuel Cells. *J. Electrochem. Soc.* **2018**, *165* (6), F3007–F3014. https://doi.org/10.1149/2.0011806jes.
(134) Stucki, S.; Scherer, G. G.; Schlagowski, S.; Fischer, E. PEM Water Electrolysers: Evidence for Membrane Failure in 100kW Demonstration Plants. 9.
(135) Andolfatto, F.; Durand, R.; Michas, A.; Millet, P.; Stevens, P. Solid Polymer Electrolyte Water Electrolysis: Electrocatalysis and Long-Term Stability. *International Journal of Hydrogen Energy* **1994**, *19* (5), 421–427. https://doi.org/10.1016/0360-3199(94)90018-3.
(136) Seh, Z. W.; Kibsgaard, J.; Dickens, C. F.; Chorkendorff, I.; Nørskov, J. K.; Jaramillo, T. F. Combining Theory and Experiment in Electrocatalysis: Insights into Materials Design. *Science* **2017**, *355* (6321), eaad4998. https://doi.org/10.1126/science.aad4998.
(137) Spurgeon, J. M.; Lewis, N. S. Proton Exchange Membrane Electrolysis Sustained by Water Vapor. *Energy Environ. Sci.* **2011**, *4* (8), 2993. https://doi.org/10.1039/c1ee01203g.
(138) Giesbrecht, P. K.; Müller, A. M.; Read, C. G.; Holdcroft, S.; Lewis, N. S.; Freund, M. S. Vapor-Fed Electrolysis of Water Using Earth-Abundant Catalysts in Nafion or in Bipolar Nafion/Poly(Benzimidazolium) Membranes. *Sustainable Energy Fuels* **2019**, *3* (12), 3611–3626. https://doi.org/10.1039/C9SE00672A.
(139) Dresp, S.; Dionigi, F.; Klingenhof, M.; Strasser, P. Direct Electrolytic Splitting of Seawater: Opportunities and Challenges. *ACS Energy Lett.* **2019**, *4* (4), 933–942. https://doi.org/10.1021/acsenergylett.9b00220.
(140) Kumari, S.; Turner White, R.; Kumar, B.; Spurgeon, J. M. Solar Hydrogen Production from Seawater Vapor Electrolysis. *Energy Environ. Sci.* **2016**, *9* (5), 1725–1733. https://doi.org/10.1039/C5EE03568F.
(141) Haussener, S.; Xiang, C.; Spurgeon, J. M.; Ardo, S.; Lewis, N. S.; Weber, A. Z. Modeling, Simulation, and Design Criteria for Photoelectrochemical Water-Splitting Systems. *Energy Environ. Sci.* **2012**, *5* (12), 9922. https://doi.org/10.1039/c2ee23187e.
(142) Kusoglu, A.; Weber, A. Z. New Insights into Perfluorinated Sulfonic-Acid Ionomers. *Chem. Rev.* **2017**, *117* (3), 987–1104. https://doi.org/10.1021/acs.chemrev.6b00159.
(143) Ito, H.; Maeda, T.; Nakano, A.; Takenaka, H. Properties of Nafion Membranes under PEM Water Electrolysis Conditions. *International Journal of Hydrogen Energy* **2011**, *36* (17), 10527–10540. https://doi.org/10.1016/j.ijhydene.2011.05.127.
(144) Heremans, G.; Bosserez, T.; Martens, J. A.; Rongé, J. Stability of Vapor Phase Water Electrolysis Cell with Anion Exchange Membrane. *Catalysis Today* **2019**, *334*, 243–248. https://doi.org/10.1016/j.cattod.2018.10.007.
(145) Fornaciari, J. C.; Gerhardt, M. R.; Zhou, J.; Regmi, Y. N.; Danilovic, N.; Bell, A. T.; Weber, A. Z. The Role of Water in Vapor-Fed Proton-Exchange-Membrane Electrolysis. *J. Electrochem. Soc.* **2020**, *167* (10), 104508. https://doi.org/10.1149/1945-7111/ab9b09.

(146) Balliet, R. J.; Newman, J. Cold Start of a Polymer-Electrolyte Fuel Cell I. Development of a Two-Dimensional Model. *J. Electrochem. Soc.* **2011**, *158* (8), B927. https://doi.org/10.1149/1.3592430.
(147) Zenyuk, I. V.; Das, P. K.; Weber, A. Z. Understanding Impacts of Catalyst-Layer Thickness on Fuel-Cell Performance via Mathematical Modeling. *J. Electrochem. Soc.* **2016**, *163* (7), F691–F703. https://doi.org/10.1149/2.1161607jes.
(148) Gerhardt, M. R.; Pant, L. M.; Weber, A. Z. Along-the-Channel Impacts of Water Management and Carbon-Dioxide Contamination in Hydroxide-Exchange-Membrane Fuel Cells: A Modeling Study. *J. Electrochem. Soc.* **2019**, *166* (7), F3180–F3192. https://doi.org/10.1149/2.0171907jes.
(149) Kreuer, K.-D. The Role of Internal Pressure for the Hydration and Transport Properties of Ionomers and Polyelectrolytes. *Solid State Ionics* **2013**, *252*, 93–101. https://doi.org/10.1016/j.ssi.2013.04.018.
(150) Zawodzinskijr, T.; Springer, T.; Uribe, F.; Gottesfeld, S. Characterization of Polymer Electrolytes for Fuel Cell Applications. *Solid State Ionics* **1993**, *60* (1–3), 199–211. https://doi.org/10.1016/0167-2738(93)90295-E.
(151) Weber, A. Z.; Newman, J. Transport in Polymer-Electrolyte Membranes. *Journal of The Electrochemical Society* 15.
(152) Weber, A. Z. Gas-Crossover and Membrane-Pinhole Effects in Polymer-Electrolyte Fuel Cells. *J. Electrochem. Soc.* **2008**, *155* (6), B521. https://doi.org/10.1149/1.2898130.
(153) Schalenbach, M.; Carmo, M.; Fritz, D. L.; Mergel, J.; Stolten, D. Pressurized PEM Water Electrolysis: Efficiency and Gas Crossover. *International Journal of Hydrogen Energy* **2013**, *38* (35), 14921–14933. https://doi.org/10.1016/j.ijhydene.2013.09.013.
(154) Schalenbach, M.; Hoefner, T.; Paciok, P.; Carmo, M.; Lueke, W.; Stolten, D. Gas Permeation through Nafion. Part 1: Measurements. *J. Phys. Chem. C* **2015**, *119* (45), 25145–25155. https://doi.org/10.1021/acs.jpcc.5b04155.
(155) Krishan, O.; Suhag, S. An Updated Review of Energy Storage Systems: Classification and Applications in Distributed Generation Power Systems Incorporating Renewable Energy Resources. *Int J Energy Res* **2019**, *43* (12), 6171–6210. https://doi.org/10.1002/er.4285.
(156) Gür, T. M. Review of Electrical Energy Storage Technologies, Materials and Systems: Challenges and Prospects for Large-Scale Grid Storage. *Energy Environ. Sci.* **2018**, *11* (10), 2696–2767. https://doi.org/10.1039/C8EE01419A.
(157) Gabbasa, M.; Sopian, K.; Fudholi, A.; Asim, N. A Review of Unitized Regenerative Fuel Cell Stack: Material, Design and Research Achievements. *International Journal of Hydrogen Energy* **2014**, *39* (31), 17765–17778. https://doi.org/10.1016/j.ijhydene.2014.08.121.
(158) Paul, B.; Andrews, J. PEM Unitised Reversible/Regenerative Hydrogen Fuel Cell Systems: State of the Art and Technical Challenges. *Renewable and Sustainable Energy Reviews* **2017**, *79*, 585–599. https://doi.org/10.1016/j.rser.2017.05.112.
(159) Wang, Y.; Leung, D. Y. C.; Xuan, J.; Wang, H. A Review on Unitized Regenerative Fuel Cell Technologies, Part-A: Unitized Regenerative Proton Exchange Membrane Fuel Cells. *Renewable and Sustainable Energy Reviews* **2016**, *65*, 961–977. https://doi.org/10.1016/j.rser.2016.07.046.
(160) Wang, Y.; Leung, D. Y. C.; Xuan, J.; Wang, H. A Review on Unitized Regenerative Fuel Cell Technologies, Part B: Unitized Regenerative Alkaline Fuel Cell, Solid Oxide Fuel

Cell, and Microfluidic Fuel Cell. *Renewable and Sustainable Energy Reviews* **2017**, *75*, 775–795. https://doi.org/10.1016/j.rser.2016.11.054.
(161) Millet, P.; Ngameni, R.; Grigoriev, S. A.; Fateev, V. N. Scientific and Engineering Issues Related to PEM Technology: Water Electrolysers, Fuel Cells and Unitized Regenerative Systems. *International Journal of Hydrogen Energy* **2011**, *36* (6), 4156–4163. https://doi.org/10.1016/j.ijhydene.2010.06.106.
(162) Ito, H.; Miyazaki, N.; Ishida, M.; Nakano, A. Efficiency of Unitized Reversible Fuel Cell Systems. *International Journal of Hydrogen Energy* **2016**, *41* (13), 5803–5815. https://doi.org/10.1016/j.ijhydene.2016.01.150.
(163) Yoshida, T.; Kojima, K. Toyota MIRAI Fuel Cell Vehicle and Progress Toward a Future Hydrogen Society. *Interface magazine* **2015**, *24* (2), 45–49. https://doi.org/10.1149/2.F03152if.
(164) Hunsom, M.; Kaewsai, D.; Kannan, A. M. Recent Developments in Bifunctional Air Electrodes for Unitized Regenerative Proton Exchange Membrane Fuel Cells – A Review. *International Journal of Hydrogen Energy* **2018**, *43* (46), 21478–21501. https://doi.org/10.1016/j.ijhydene.2018.09.152.
(165) Choi, S.; Davenport, T. C.; Haile, S. M. Protonic Ceramic Electrochemical Cells for Hydrogen Production and Electricity Generation: Exceptional Reversibility, Stability, and Demonstrated Faradaic Efficiency. *Energy Environ. Sci.* **2019**, *12* (1), 206–215. https://doi.org/10.1039/C8EE02865F.
(166) Peng, X.; Taie, Z.; Liu, J.; Zhang, Y.; Peng, X.; Regmi, Y. N.; Fornaciari, J. C.; Capuano, C.; Binny, D.; Kariuki, N. N.; Myers, D. J.; Scott, M. C.; Weber, A. Z.; Danilovic, N. Hierarchical Electrode Design of Highly Efficient and Stable Unitized Regenerative Fuel Cells (URFCs) for Long-Term Energy Storage. *Energy Environ. Sci.* **2020**, *13* (12), 4872–4881. https://doi.org/10.1039/D0EE03244A.
(167) Duan, C.; Kee, R.; Zhu, H.; Sullivan, N.; Zhu, L.; Bian, L.; Jennings, D.; O'Hayre, R. Highly Efficient Reversible Protonic Ceramic Electrochemical Cells for Power Generation and Fuel Production. *Nat Energy* **2019**, *4* (3), 230–240. https://doi.org/10.1038/s41560-019-0333-2.
(168) N. Regmi, Y.; Peng, X.; C. Fornaciari, J.; Wei, M.; J. Myers, D.; Z. Weber, A.; Danilovic, N. A Low Temperature Unitized Regenerative Fuel Cell Realizing 60% Round Trip Efficiency and 10000 Cycles of Durability for Energy Storage Applications. *Energy & Environmental Science* **2020**, *13* (7), 2096–2105. https://doi.org/10.1039/C9EE03626A.
(169) Ahn, J.; Holze, R. Bifunctional Electrodes for an Integrated Water-Electrolysis and Hydrogen-Oxygen Fuel Cell with a Solid Polymer Electrolyte. *J Appl Electrochem* **1992**, *22* (12), 1167–1174. https://doi.org/10.1007/BF01297419.
(170) Grigoriev, S. A.; Millet, P.; Dzhus, K. A.; Middleton, H.; Saetre, T. O.; Fateev, V. N. Design and Characterization of Bi-Functional Electrocatalytic Layers for Application in PEM Unitized Regenerative Fuel Cells. *International Journal of Hydrogen Energy* **2010**, *35* (10), 5070–5076. https://doi.org/10.1016/j.ijhydene.2009.08.081.
(171) Sadhasivam, T.; Palanisamy, G.; Roh, S.-H.; Kurkuri, M. D.; Kim, S. C.; Jung, H.-Y. Electro-Analytical Performance of Bifunctional Electrocatalyst Materials in Unitized Regenerative Fuel Cell System. *International Journal of Hydrogen Energy* **2018**, *43* (39), 18169–18184. https://doi.org/10.1016/j.ijhydene.2018.08.035.

(172) Chen, G.; Bare, S. R.; Mallouk, T. E. Development of Supported Bifunctional Electrocatalysts for Unitized Regenerative Fuel Cells. *J. Electrochem. Soc.* **2002**, *149* (8), A1092–A1099. https://doi.org/10.1149/1.1491237.
(173) Wang, Y.-J.; Fang, B.; Wang, X.; Ignaszak, A.; Liu, Y.; Li, A.; Zhang, L.; Zhang, J. Recent Advancements in the Development of Bifunctional Electrocatalysts for Oxygen Electrodes in Unitized Regenerative Fuel Cells (URFCs). *Progress in Materials Science* **2018**, *98*, 108–167. https://doi.org/10.1016/j.pmatsci.2018.06.001.
(174) da Silva, G. C.; Mayrhofer, K. J. J.; Ticianelli, E. A.; Cherevko, S. Dissolution Stability: The Major Challenge in the Regenerative Fuel Cells Bifunctional Catalysis. *J. Electrochem. Soc.* **2018**, *165* (16), F1376–F1384. https://doi.org/10.1149/2.1201816jes.
(175) Omrani, R.; Shabani, B. Review of Gas Diffusion Layer for Proton Exchange Membrane-Based Technologies with a Focus on Unitised Regenerative Fuel Cells. *International Journal of Hydrogen Energy* **2019**, *44* (7), 3834–3860. https://doi.org/10.1016/j.ijhydene.2018.12.120.
(176) Ito, H.; Abe, K.; Ishida, M.; Hwang, C. M.; Nakano, A. Effect of Through-Plane Polytetrafluoroethylene Distribution in a Gas Diffusion Layer on a Polymer Electrolyte Unitized Reversible Fuel Cell. *International Journal of Hydrogen Energy* **2015**, *40* (46), 16556–16565. https://doi.org/10.1016/j.ijhydene.2015.09.102.
(177) Xiang, C.; Papadantonakis, K. M.; Lewis, N. S. Principles and Implementations of Electrolysis Systems for Water Splitting. *Mater. Horiz.* **2016**, *3* (3), 169–173. https://doi.org/10.1039/C6MH00016A.
(178) Ursua, A.; Gandia, L. M.; Sanchis, P. Hydrogen Production From Water Electrolysis: Current Status and Future Trends. *Proc. IEEE* **2012**, *100* (2), 410–426. https://doi.org/10.1109/JPROC.2011.2156750.
(179) Grimm, M.; Hellmann, M.; Kemmer, H.; Kabelac, S. Water Management of PEM Fuel Cell Systems Based on the Humidity Distribution in the Anode Gas Channels. *Fuel Cells* **2020**, *20* (4), 477–486. https://doi.org/10.1002/fuce.202000070.
(180) Kandlikar, S. G. Microscale and Macroscale Aspects of Water Management Challenges in PEM Fuel Cells. *Heat Transfer Engineering* **2008**, *29* (7), 575–587. https://doi.org/10.1080/01457630801922246.
(181) Berg, P.; Promislow, K.; St. Pierre, J.; Stumper, J.; Wetton, B. Water Management in PEM Fuel Cells. *J. Electrochem. Soc.* **2004**, *151* (3), A341. https://doi.org/10.1149/1.1641033.
(182) Nguyen, T. V.; Knobbe, M. W. A Liquid Water Management Strategy for PEM Fuel Cell Stacks. *Journal of Power Sources* **2003**, 10.
(183) Zhang, C.; Zhou, W.; Zhang, L.; Chan, S. H.; Wang, Y. An Experimental Study on Anode Water Management in High Temperature PEM Fuel Cell. *International Journal of Hydrogen Energy* **2015**, *40* (13), 4666–4672. https://doi.org/10.1016/j.ijhydene.2015.02.037.
(184) Kim, M.; Jung, N.; Eom, K.; Yoo, S. J.; Kim, J. Y.; Jang, J. H.; Kim, H.-J.; Hong, B. K.; Cho, E. Effects of Anode Flooding on the Performance Degradation of Polymer Electrolyte Membrane Fuel Cells. *Journal of Power Sources* **2014**, *266*, 332–340. https://doi.org/10.1016/j.jpowsour.2014.04.092.
(185) Garg, S.; Fornaciari, J.; Weber, A.; Danilovic, N. Fuelcell: A Python Package and Graphical User Interface for Electrochemical Data Analysis. *JOSS* **2021**, *6* (59), 2940. https://doi.org/10.21105/joss.02940.

(186) Lim, C.; Ghassemzadeh, L.; Van Hove, F.; Lauritzen, M.; Kolodziej, J.; Wang, G. G.; Holdcroft, S.; Kjeang, E. Membrane Degradation during Combined Chemical and Mechanical Accelerated Stress Testing of Polymer Electrolyte Fuel Cells. *Journal of Power Sources* **2014**, *257*, 102–110. https://doi.org/10.1016/j.jpowsour.2014.01.106.
(187) Rodgers, M. P.; Bonville, L. J.; Kunz, H. R.; Slattery, D. K.; Fenton, J. M. Fuel Cell Perfluorinated Sulfonic Acid Membrane Degradation Correlating Accelerated Stress Testing and Lifetime. *Chem. Rev.* **2012**, *112* (11), 6075–6103. https://doi.org/10.1021/cr200424d.
(188) Kusoglu, A.; Kienitz, B. L.; Weber, A. Z. Understanding the Effects of Compression and Constraints on Water Uptake of Fuel-Cell Membranes. *J. Electrochem. Soc.* **2011**, *158* (12), B1504. https://doi.org/10.1149/2.097112jes.
(189) Arthurs, C.; Kusoglu, A. Compressive Creep of Polymer Electrolyte Membranes: A Case Study for Electrolyzers. *ACS Appl. Energy Mater.* **2021**, *4* (4), 3249–3254. https://doi.org/10.1021/acsaem.0c03024.
(190) Newman, J. S.; Thomas-Alyea, K. E. *Electrochemical Systems*, 3rd ed.; J. Wiley: Hoboken, N.J, 2004.
(191) Harrison, K. W.; Remick, R.; Martin, G. D. Hydrogen Production: Fundamentals and Case Study Summaries; Preprint. 21.
(192) Huang, S.-Y.; Ganesan, P.; Jung, H.-Y.; Popov, B. N. Development of Supported Bifunctional Oxygen Electrocatalysts and Corrosion-Resistant Gas Diffusion Layer for Unitized Regenerative Fuel Cell Applications. *Journal of Power Sources* **2012**, *198*, 23–29. https://doi.org/10.1016/j.jpowsour.2011.09.071.
(193) Seader, J. D.; Henley, E. J.; Roper, D. K. *Separation Process Principles: Chemical and Biochemical Operations*, 3rd ed.; Wiley: Hoboken, NJ, 2011.
(194) Alduchov, O. A.; Eskridge, R. E. Improved Magnus FOrm Approximation of Saturation Vapor Pressure. *Journal of Applied Meteorology and Climatology* **1996**, *35* (4), 601–609. https://doi.org/10.1175/1520-0450(1996)035<0601:IMFAOS>2.0.CO;2.
(195) Ravi, M.; Ranocchiari, M.; van Bokhoven, J. A. The Direct Catalytic Oxidation of Methane to Methanol-A Critical Assessment. *Angew. Chem. Int. Ed.* **2017**, *56* (52), 16464–16483. https://doi.org/10.1002/anie.201702550.
(196) Meng, X.; Cui, X.; Rajan, N. P.; Yu, L.; Deng, D.; Bao, X. Direct Methane Conversion under Mild Condition by Thermo-, Electro-, or Photocatalysis. *Chem* **2019**, *5* (9), 2296–2325. https://doi.org/10.1016/j.chempr.2019.05.008.
(197) Lee, B.; Hibino, T. Efficient and Selective Formation of Methanol from Methane in a Fuel Cell-Type Reactor. *Journal of Catalysis* **2011**, *279* (2), 233–240. https://doi.org/10.1016/j.jcat.2010.12.020.
(198) Tomita, A.; Nakajima, J.; Hibino, T. Direct Oxidation of Methane to Methanol at Low Temperature and Pressure in an Electrochemical Fuel Cell. *Angew. Chem. Int. Ed.* **2008**, *47* (8), 1462–1464. https://doi.org/10.1002/anie.200703928.
(199) Lee, B.; Sakamoto, Y.; Hirabayashi, D.; Suzuki, K.; Hibino, T. Direct Oxidation of Methane to Methanol over Proton Conductor/Metal Mixed Catalysts. *Journal of Catalysis* **2010**, *271* (2), 195–200. https://doi.org/10.1016/j.jcat.2010.01.011.
(200) Nandenha, J.; Piasentin, R. M.; Silva, L. M. G.; Fontes, E. H.; Neto, A. O.; de Souza, R. F. B. Partial Oxidation of Methane and Generation of Electricity Using a PEMFC. *Ionics* **2019**, *25* (10), 5077–5082. https://doi.org/10.1007/s11581-019-03186-z.

(201) Santos, M. C. L.; Nunes, L. C.; Silva, L. M. G.; Ramos, A. S.; Fonseca, F. C.; Souza, R. F. B.; Neto, A. O. Direct Alkaline Anion Exchange Membrane Fuel Cell to Converting Methane into Methanol. *ChemistrySelect* **2019**, *4* (39), 11430–11434. https://doi.org/10.1002/slct.201902421.
(202) Fan, Q. (73) Assignee: Gas Technology Institute, Des Plaines,. 10.
(203) Fan, Q. (54) NON-FARADAIC ELECTROCHEMICAL. 8.
(204) Spinner, N.; Mustain, W. E. Electrochemical Methane Activation and Conversion to Oxygenates at Room Temperature. *J. Electrochem. Soc.* **2013**, *160* (11), F1275–F1281. https://doi.org/10.1149/2.071311jes.
(205) Ma, M.; Jin, B. J.; Li, P.; Jung, M. S.; Kim, J. I.; Cho, Y.; Kim, S.; Moon, J. H.; Park, J. H. Ultrahigh Electrocatalytic Conversion of Methane at Room Temperature. *Adv. Sci.* **2017**, *4* (12), 1700379. https://doi.org/10.1002/advs.201700379.
(206) Ma, M.; Oh, C.; Kim, J.; Moon, J. H.; Park, J. H. Electrochemical CH4 Oxidation into Acids and Ketones on ZrO2:NiCo2O4 Quasi-Solid Solution Nanowire Catalyst. *Applied Catalysis B: Environmental* **2019**, *259*, 118095. https://doi.org/10.1016/j.apcatb.2019.118095.
(207) Rocha, R. S.; Reis, R. M.; Lanza, M. R. V.; Bertazzoli, R. Electrosynthesis of Methanol from Methane: The Role of V2O5 in the Reaction Selectivity for Methanol of a TiO2/RuO2/V2O5 Gas Diffusion Electrode. *Electrochimica Acta* **2013**, *87*, 606–610. https://doi.org/10.1016/j.electacta.2012.09.113.
(208) Rocha, R. S.; Camargo, L. M.; Lanza, M. R. V.; Bertazzoli, R. A Feasibility Study of the Electro-Recycling of Greenhouse Gases: Design and Characterization of a (TiO2/RuO2)/PTFE Gas Diffusion Electrode for the Electrosynthesis of Methanol from Methane. *Electrocatal* **2010**, *1* (4), 224–229. https://doi.org/10.1007/s12678-010-0029-7.
(209) Scharifker, B.; Eduvigis, S. (54) ELECTROCATALYST FOR THE OXDATION OF METHANE AND AN ELECTROCATALYTIC PROCESS. 9.
(210) O'Reilly, M. E.; Kim, R. S.; Oh, S.; Surendranath, Y. Catalytic Methane Monofunctionalization by an Electrogenerated High-Valent Pd Intermediate. *ACS Cent. Sci.* **2017**, *3* (11), 1174–1179. https://doi.org/10.1021/acscentsci.7b00342.
(211) Durst, J.; Rudnev, A.; Dutta, A.; Fu, Y.; Herranz, J.; Kaliginedi, V.; Kuzume, A.; Permyakova, A. A.; Paratcha, Y.; Broekmann, P.; Schmidt, T. J. Electrochemical CO_2 Reduction – A Critical View on Fundamentals, Materials and Applications. *chimia (aarau)* **2015**, *69* (12), 769–776. https://doi.org/10.2533/chimia.2015.769.
(212) Ott, J.; Gronemann, V.; Pontzen, F.; Fiedler, E.; Grossmann, G.; Kersebohm, D. B.; Weiss, G.; Witte, C. Methanol. In *Ullmann's Encyclopedia of Industrial Chemistry*; Wiley-VCH Verlag GmbH & Co. KGaA, Ed.; Wiley-VCH Verlag GmbH & Co. KGaA: Weinheim, Germany, 2012; p a16_465.pub3. https://doi.org/10.1002/14356007.a16_465.pub3.
(213) Arnarson, L.; Schmidt, P. S.; Pandey, M.; Bagger, A.; Thygesen, K. S.; Stephens, I. E. L.; Rossmeisl, J. Fundamental Limitation of Electrocatalytic Methane Conversion to Methanol. *Phys. Chem. Chem. Phys.* **2018**, *20* (16), 11152–11159. https://doi.org/10.1039/C8CP01476K.
(214) Seidel, Y. E.; Schneider, A.; Jusys, Z.; Wickman, B.; Kasemo, B.; Behm, R. J. Transport Effects in the Electrooxidation of Methanol Studied on Nanostructured Pt/Glassy Carbon Electrodes. *Langmuir* **2010**, *26* (5), 3569–3578. https://doi.org/10.1021/la902962g.

(215) Márquez-Montes, R. A.; Collins-Martínez, V. H.; Pérez-Reyes, I.; Chávez-Flores, D.; Graeve, O. A.; Ramos-Sánchez, V. H. Electrochemical Engineering Assessment of a Novel 3D-Printed Filter-Press Electrochemical Reactor for Multipurpose Laboratory Applications. *ACS Sustainable Chem. Eng.* **2020**, *8* (9), 3896–3905. https://doi.org/10.1021/acssuschemeng.9b07368.
(216) Heo, P.; Kajiyama, N.; Kobayashi, K.; Nagao, M.; Sano, M.; Hibino, T. Proton Conduction in Sn0.95Al0.05P2O7–PBI–PTFE Composite Membrane. 6.
(217) Heo, P.; Ito, K.; Tomita, A.; Hibino, T. A Proton-Conducting Fuel Cell Operating with Hydrocarbon Fuels. *Angew. Chem. Int. Ed.* **2008**, *47* (41), 7841–7844. https://doi.org/10.1002/anie.200801667.
(218) Paschos, O.; Kunze, J.; Stimming, U.; Maglia, F. A Review on Phosphate Based, Solid State, Protonic Conductors for Intermediate Temperature Fuel Cells. *J. Phys.: Condens. Matter* **2011**, *23* (23), 234110. https://doi.org/10.1088/0953-8984/23/23/234110.
(219) Li, W.; Manthiram, A.; Guiver, M. D. Acid–Base Blend Membranes Consisting of Sulfonated Poly(Ether Ether Ketone) and 5-Amino-Benzotriazole Tethered Polysulfone for DMFC. *Journal of Membrane Science* **2010**, *362* (1–2), 289–297. https://doi.org/10.1016/j.memsci.2010.06.059.
(220) Merle, G.; Wessling, M.; Nijmeijer, K. Anion Exchange Membranes for Alkaline Fuel Cells: A Review. *Journal of Membrane Science* **2011**, *377* (1–2), 1–35. https://doi.org/10.1016/j.memsci.2011.04.043.
(221) Hickner, M. A.; Herring, A. M.; Coughlin, E. B. Anion Exchange Membranes: Current Status and Moving Forward. *J. Polym. Sci. Part B: Polym. Phys.* **2013**, *51* (24), 1727–1735. https://doi.org/10.1002/polb.23395.
(222) Ma, M.; Clark, E. L.; Therkildsen, K. T.; Dalsgaard, S.; Chorkendorff, I.; Seger, B. Insights into the Carbon Balance for CO_2 Electroreduction on Cu Using Gas Diffusion Electrode Reactor Designs. *Energy Environ. Sci.* **2020**, *13* (3), 977–985. https://doi.org/10.1039/D0EE00047G.
(223) Yamanaka, I.; Hasegawa, S.; Otsuka, K. Partial Oxidation of Light Alkanes by Reductive Activated Oxygen over the (Pd-Black + VO(Acac)2/VGCF) Cathode of H2–O2 Cell System at 298 K. *Applied Catalysis A: General* **2002**, *226* (1–2), 305–315. https://doi.org/10.1016/S0926-860X(01)00916-4.
(224) Gao, J.; Xu, C.-Q.; Hung, S.-F.; Liu, W.; Cai, W.; Zeng, Z.; Jia, C.; Chen, H. M.; Xiao, H.; Li, J.; Huang, Y.; Liu, B. Breaking Long-Range Order in Iridium Oxide by Alkali Ion for Efficient Water Oxidation. *J. Am. Chem. Soc.* **2019**, *141* (7), 3014–3023. https://doi.org/10.1021/jacs.8b11456.
(225) Liang, Z.; Li, T.; Kim, M.; Asthagiri, A.; Weaver, J. F. Low-Temperature Activation of Methane on the IrO_2 (110) Surface. *Science* **2017**, *356* (6335), 299–303. https://doi.org/10.1126/science.aam9147.